TECHNISCHE UNIVERSITÄT MÜNCHEN

Lehrstuhl für Ingenieurgeologie

Pre-survey suitability analysis of the differential and persistent scatterer synthetic aperture radar interferometry method for deformation monitoring of mass movements and subsidence

Dipl.-Geol. Univ. Simon Manuel Plank, MSc (GIS)

Vollständiger Abdruck der von der Fakultät für Bauingenieur- und Vermessungswesen der Technischen Universität München zur Erlangung des akademischen Grades eines

Doktor-Ingenieurs (Dr.-Ing.)

genehmigten Dissertation.

Vorsitzender: Univ.-Prof. Dr.techn. Roland Pail

Prüfer der Dissertation:

1. Univ.-Prof. Dr.rer.nat. Kurosch Thuro
2. Univ.-Prof. Dr.-Ing. habil. Richard Hans Georg Bamler
3. Hon.-Prof. Dr.-Ing. Günter Strunz

Die Dissertation wurde am 10.07.2012 bei der Technischen Universität München eingereicht und durch die Fakultät für Bauingenieur- und Vermessungswesen am 19.11.2012 angenommen.

Acknowledgments

I would like to thank my supervisor Prof. Dr. Kurosch Thuro (Chair for Engineering Geology, Technische Universität München TUM) for his great support and the opportunity to work on this interesting research topic. I also gratefully appreciate Dr. John Singer (Chair of Engineering Geology, ETH Zürich) for his helpful guidance and fruitful discussions on this work. Many thanks go to Prof. Dr. Richard Bamler, director of the Remote Sensing Technology Institute (IMF) at the DLR, for the motivating discussions and his advices. I also want to thank Prof. Dr. Günter Strunz (DFD, DLR) for his helpful suggestions.

Special thanks go to Mr. Christian Minet (IMF, DLR) for his very helpful tips and for answering my questions. I also want to thank Dr. Michael Eineder, Mr. Nico Adam, Mr. Alessandro Parizzi (IMF, DLR), Dr. Stefan Auer and Dr. Stefan Gernhardt (both Remote Sensing Technology, TUM) for their great advices.

Many thanks to Dr. Alessandro Ferretti (Tele-Rilevamento Europa T.R.E) for the motivating discussion at the Fringe 2011 workshop and for providing the PS-targets data of several sites.

Sincere thanks are also due to Dr. Pablo d'Angelo (IMF, DLR) for his advices on orthorectification, to Mr. Martin Huber and Mr. Achim Roth (DFD, DLR) for information about the Geocoded Incidence Angle Mask and the geocoding of SAR images, to Dr. Ulrich Haas and Mr. Karl Meyer (Bavarian State Office for Environment LfU) for the allocation of the georisk data in Bavaria.

I thank Dr. Michael Riedmann and Dr. Oliver Lang (both Astrium Infoterra), Mr. Werner Liebhart (IMF, DLR), Dr. Michael Foumelis (University of Athens) and Mr. Miguel Caro Cuenca (Delft University of Technology) for providing the PS-targets data of the sites. I also want to thank ESA for providing the KOMPSAT-2 data (Cat-1 project 8377), DLR for providing the TerraSAR-X data (Project GEO_1026), the European Space Imaging company for providing the WorldView-2 data and NASA for providing the ASTER data. I gratefully acknowledge the Universität Bayern e.V. for financial support.

Simon Manuel Plank
Munich, November 2012

Abstract

The remote sensing technique differential synthetic aperture radar interferometry (D-InSAR) and its further development persistent scatterer interferometry (PS-InSAR) are powerful methods for detection and monitoring of deformation of the Earth‘s crust – such as subsidence and landslides – with an accuracy up to a few millimeters. However, the factors listed below strongly complicate the application of these radar interferometry methods.

(a) Due to the radar specific imaging geometry, areas behind steep slopes are not achieved by the radar pulse (shadowing), while other areas show an overlap of radar responses from different ground positions (layover). D-InSAR cannot be applied in areas affected by these effects. (b) Moreover, D-InSAR applications in areas covered with dense vegetation are very complicated. (c) Reliable PS-InSAR processing requires a stack of at least 15 to 50 SAR images. Therefore, its processing is time-consuming and expensive. PS-InSAR can only successfully be applied if there is a sufficiently high number of scatterers of high coherent values (long-term constant backscattering properties) – so-called persistent scatterers (PS) – within the site. An estimation of these PS prior to the processing of several SAR images is very complicated.

The goal of this dissertation is the development of methods that enable an objective feasibility assessment of the D-InSAR and PS-InSAR techniques prior to the SAR acquisition. Therefore, the seven methods explained below were developed and then validated using real SAR data.

The first topic deals with the development of a geographical information system (GIS) procedure that accurately predicts the areas in which layover and shadowing will occur, prior to SAR recording of the area of interest. Furthermore, as radar can only measure movements in its line-of-sight direction, additionally the measurable percentage of movement of a potential landslide is calculated in this procedure. For both, the layover-shadow-simulation and the calculation of the measurable percentage of movement, a GIS toolbox consisting of complex GIS models that were expanded by several Python and VBA scripts were developed.

As the land cover of the site has a very high influence on the applicability of D-InSAR, this thesis presents the classification of the main types of the land cover regarding this influence, based on the SAR sensor’s characteristics. Based on a European wide land cover dataset, this classification of the D-InSAR applicability was applied for the entire continent.

The methods developed in the first topic of this dissertation were exemplary applied at a site in the Bavarian Alps, Germany and validated with real SAR data.

As reliable PS-InSAR application requires a high number of PS within the site, the second topic of this work presents the development of three new methods for PS-estimation prior to SAR acquisition. In empirical approaches freely available or low-cost land cover and optical remote sensing data as well as topographic maps and OpenStreetMap data are compared with results of real PS-InSAR processing of several sites.

The first PS-estimation method is based on freely available land cover datasets of global (GlobCover) and continental (CORINE) coverage. To be able to compare the PS-density (PS/km²) of sites recorded by different SAR sensors (different spatial resolution) and processed by different PS-InSAR algorithms, the so-called relative PS-density method was developed in this work. The validation of the land cover based PS-estimation with processed

PS-targets (results of real SAR data) shows a very good conformity of the estimated and processed PS-density, when using high spatial resolution land cover data (e.g. CORINE). For lower spatial resolution land cover data (e.g. GlobCover), a relatively good match in the validation is achieved.
The second method uses the well-known normalized difference vegetation index (NDVI) calculated from optical remote sensing data in an entirely new approach – the estimation of PS. The NDVI based PS-estimation procedure enables for each pixel of the NDVI image the calculation of the probability to get a PS at a certain NDVI value. This thesis shows that the method is very well suited in areas covered with sparse vegetation, when using free available middle spatial resolution optical data (e.g. Landsat and ASTER). For world-wide application of the NDVI based PS-estimation method – even in areas of denser vegetation coverage – high spatial resolution optical sensors are required.
The third PS-estimation method is based on topographic maps and OpenStreetMap data. In this method, besides the density of the estimated PS-targets also (a) their distances between each other is calculated and classified regarding to the applicability for PS-InSAR processing and (b) their dispersion within the site is analyzed. The results of the PS-estimation procedure are validated using real (processed) PS-datasets.
To guarantee wide usability of the methods 17 PS and 9 DS&PS (distributed scatterers) datasets of 13 sites from different climate zones and land cover are used: Cairo (Egypt), Budapest (Hungary), Bavaria (Germany), Aschau am Inn (Germany), North Germany, Netherlands, two sites in the Aosta Valley (Italy) and five sites in Piedmont (Italy).
The third section of this thesis is one step further towards PS-InSAR processing. Based on real SAR data, the minimum number of SAR images required for a meaningful PS-detection is determined. This enables to test whether the number of to be expected PS-targets of the area of interest is high enough for a subsequent PS-InSAR processing, prior to ordering the entire stack of SAR data. Based on a reference PS-detection applied to a stack of 81 co-registered ERS SAR images, the effects on PS-detection when continuously reducing the number of SAR images in the stack is examined. Two experiments are applied. The first one uses a constant false alarm rate detector (CFAR) and the second one examines the relationship of correctly and falsely detected PS at different thresholds depending on the number of SAR images used. The results show that around 8 SAR images are required for reliable PS-detection, prior to ordering the entire stack of SAR data.
The procedures developed in this dissertation enable objective pre-survey estimation of the potential applicability of the SAR interferometry techniques for deformation monitoring, prior to the costly investment of a radar survey. These procedures can be used for a wide area feasibility assessment, which is very interesting for geological surveys and the companies executing the InSAR processing for them.

Zusammenfassung

Die Fernerkundungsmethode differentielle Radarinterferometrie (D-InSAR) und ihre Weiterentwicklung Persistent Scatterer Interferometrie (PS-InSAR) ermöglichen die millimetergenaue Erfassung und Überwachung von Deformationen der Erdkruste – wie Setzungen und Hangbewegungen. Aber durch nachfolgend genannte Faktoren wird die Anwendbarkeit dieser Radarinterferometrie Methoden stark erschwert.
(a) Durch die radarspezifische Aufnahmegeometrie werden z.B. Bereiche hinter steilen Bergen nicht von den Radarwellen erfasst (Radarschatten); andere Bereiche zeigen wiederum eine Überlagerung von Radarechos verschiedener Objekte am Erdboden (Layover). In Gebieten, die von diesen Effekten betroffen sind, kann das D-InSAR Verfahren nicht angewendet werden. (b) Des Weiteren erschwert dichte Vegetation im Untersuchungsgebiet die Anwendung von D-InSAR. (c) Bei der PS-InSAR Methode werden mindestens 15 bis 50 Radaraufnahmen benötigt, wodurch die Prozessierung sehr zeitaufwändig und teuer wird. PS-InSAR kann nur dann erfolgreich angewendet werden, wenn im Untersuchungsgebiet eine ausreichend hohe Anzahl an Streuern mit hohen Kohärenzwerten (Langzeit konstante Rückstreuungseigenschaften) – sogenannte Persistent Scatterers (PS) – vorhanden ist. Eine Abschätzung dieser PS vor einer Prozessierung vieler Radaraufnahmen ist sehr schwierig.
Ziel dieser Dissertation ist deshalb die Entwicklung von Methoden, die eine objektive Überprüfung der Anwendbarkeit der D-InSAR und PS-InSAR Verfahren vor einer Radaraufnahme ermöglichen. Dazu wurden die sieben nachfolgend kurz erläuterten Methoden entwickelt und anschließend mittels echter Radardaten validiert.
Der erste Schwerpunkt behandelt die Entwicklung eines auf einem Geographischen Informationssystem (GIS) basierenden Verfahrens, das – vor einer Radaraufnahme des Untersuchungsgebiets – eine genaue Abschätzung der Gebiete ermöglicht, wo Layover oder Shadow auftreten wird. Des Weiteren wird in diesem Verfahren, da mit Radar nur Bewegungen in dessen Blickrichtung gemessen werden können, der messbare Anteil einer potentiellen Hangbewegung bestimmt. Für die Layover-Shadow Simulation und die Berechnung des messbaren Bewegungsanteils wurde eine GIS Toolbox, bestehend aus umfangreichen GIS Modellen und erweitert durch mehrere Python und VBA Skripte, entwickelt.
Da die Landbedeckung des Testgebiets einen sehr großen Einfluss auf die Anwendbarkeit des D-InSAR Verfahrens hat, wird in dieser Arbeit, basierend auf den SAR Sensor Eigenschaften, die Klassifikation der Hauptlandbedeckungsarten bezüglich dieses Einflusses präsentiert. Basierend auf einem europaweiten Landbedeckungsdatensatz wurde die Klassifikation der Anwendbarkeit des D-InSAR Verfahrens auf den ganzen Kontinent angewandt.
Die im ersten Schwerpunkt dieser Dissertation entwickelten Methoden wurden beispielhaft in einem Testgebiet in den Bayerischen Alpen angewendet und mit einer echten Radaraufnahme validiert.
Da zur erfolgreichen Anwendung von PS-InSAR eine hohe Anzahl von PS im Untersuchungsgebiet benötigt wird, zeigt der zweite Schwerpunkt dieser Arbeit die Entwicklung dreier neuer Methoden zur PS Abschätzung vor einer Radaraufnahme. In empirischen Ansätzen werden freiverfügbare bzw. kostengünstige Landbedeckungs- und optische Fernerkundungsdaten sowie topographische Karten und OpenStreetMap Daten mit den Ergebnissen echter PS-InSAR Prozessierungen verschiedener Testgebiete verglichen.
Die erste PS-Abschätzungsmethode basiert auf freiverfügbaren Landbedeckungsdaten mit globaler (GlobCover) und kontinentaler (CORINE) Abdeckung. Um den Vergleich der PS-

Dichte (PS/km²) von Testgebieten, die mit verschiedenen Radarsensoren (unterschiedliche räumliche Auflösung) aufgenommen und mit verschiedenen PS-InSAR Algorithmen prozessiert wurden, zu ermöglichen, wurde in dieser Arbeit die sogenannte relative PS-Dichte entwickelt. Die Validierung der auf Landbedeckungsdaten basierenden PS-Abschätzung mit prozessierten PS (Ergebnisse echter Radardaten) zeigt bei der Verwendung von räumlich hochauflösenden Landbedeckungsdaten (z.B. CORINE) eine sehr gute Übereinstimmung zwischen der abgeschätzten und der prozessierten PS-Dichte. Räumliche gröber aufgelöste Landbedeckungsdaten (z.B. GlobCover) zeigen in der Validierung eine relative gute Übereinstimmung.
Die zweite Methode nutzt den weit verbreiteten aus optischen Fernerkundungsdaten berechneten Vegetationsindex NDVI in einem ganz neuen Ansatz – der Abschätzung von PS. Die auf dem NDVI basierende PS-Abschätzungsmethode ermöglicht für jeden Pixel des NDVI Bildes die Berechnung der Wahrscheinlichkeit bei einem bestimmten NDVI Wert auf einen PS zu treffen. Diese Arbeit zeigt, dass die Methode bei Verwendung von freiverfügbaren optischen Sensoren mittlerer räumlicher Auflösung (z.B. Landsat und ASTER) sehr gut in Gebieten mit spärlicher Vegetation funktioniert. Für eine weltweite Anwendung der auf NDVI basierenden PS-Abschätzungsmethode – auch in Gebieten mit dichterer Vegetation – werden räumlich hoch auflösende optische Sensoren benötigt.
Die dritte PS-Abschätzungsmethode verwendet topographische Karten und OpenStreetMap Daten. Bei dieser Methode werden neben der Dichte der abgeschätzten PS auch (a) ihre Distanzen untereinander berechnet und bezüglich der Anwendbarkeit des PS-InSAR Verfahrens klassifiziert und (b) ihre Verteilung im Untersuchungsgebiet analysiert. Die Ergebnisse der PS-Abschätzung werden mit echten (prozessierten) PS-Datensätzen validiert.
Um eine breite Anwendbarkeit der Methoden zu ermöglichen werden 17 PS und 9 DS&PS (distributed scatterers) Datensätze von 13 Testgebieten aus unterschiedlichen Klimazonen und mit verschiedener Landbedeckung verwendet: Kairo (Ägypten), Budapest (Ungarn), Bayern, Aschau am Inn, Norddeutschland, Niederlande, zwei Testgebiete im Aostatal (Italien) und fünf Testgebiete in Piemont (Italien).
Der dritte Schwerpunkt dieser Arbeit ist einen Schritt näher in Richtung PS-InSAR Prozessierung. Basierend auf echten Radardaten wird die Mindestanzahl an SAR Aufnahmen ermittelt, die für eine sinnvolle Abschätzung von PS benötigt werden. Hiermit wird es möglich zu überprüfen, ob die Anzahl an zu erwartenden PS hoch genug ist, bevor der gesamte Stapel an SAR Daten für die anschließende PS-InSAR Prozessierung bestellt wird. Ausgehend von einer Referenz PS-Detektion angewandt auf einen Stapel von 81 ko-registierten ERS SAR Aufnahmen, werden die Auswirkungen der kontinuierlichen Reduzierung der Anzahl der SAR Aufnahmen im Stapel auf die PS-Detektion untersucht. Es werden zwei Experimente durchgeführt. Das erste basiert dabei auf einem konstanten Fehlalarmrate-Detektor (constant false alarm rate detector, CFAR). Im zweiten Experiment wird das Verhältnis von richtig und falsch detektierten PS für verschiedene Grenzwerte in Abhängigkeit der Anzahl der verwendeten SAR Aufnahmen untersucht. Die Arbeit zeigt, dass etwa 8 SAR Aufnahmen für eine Abschätzung der PS im Interessensgebiet notwendig sind, bevor die restlichen SAR Daten für die anschließende PS-InSAR Prozessierung in Auftrag gegeben werden.
Die in dieser Dissertation entwickelten Verfahren ermöglichen eine objektive Vorabüberprüfung der Anwendbarkeit der Methoden der Radarinterferometrie zur Deformationsüberwachung, bevor eine aufwändige Radarvermessung in Auftrag gegeben wird. Mit diesen Verfahren ist eine Eignungsprüfung großer Gebiete möglich, was besonders für Geologische Dienste und die Unternehmen, die die InSAR Prozessierung für diese ausführen, interessant ist.

Contents

List of figures

List of tables

List of abbreviations

ALOS	Advanced Land Observing Satellite
AOI	Area of Interest
ASAR	Advanced Synthetic Aperture Radar, ENVISAT sensor
ASTER	Advanced Spaceborne Thermal Emission and Reflection Radiometer
ATKIS	Amtliches Topographisch-Kartographisches Informationssystem
BIS	Bodeninformationssystem, Soil information system
CGIAR	Consultative Group on International Agricultural Research
CFAR	Constant False Alarm Rate
CORINE	Coordination of Information on the Environment
DBF	Data Base File
DEM	Digital Elevation Model
D-InSAR	Differential SAR Interferometry
DLR	Deutsches Zentrum für Luft- und Raumfahrt, German Aerospace Center
DS	Distributed Scatterer
EEA	European Environmental Agency
ENVISAT	Environmental Satellite
ERS	European Remote Sensing Satellite
ESA	European Space Agency
ETM+	Enhanced Thematic Mapper Plus, Landsat 7 sensor
FAO	Food Agricultural Organization
GB D-InSAR	Ground Based D-InSAR
GIM	Geocoded Incidence Angle Mask
GIS	Geographical Information System
GOFC-GOLD	Global Observation of Forest and Land Cover Dynamics
GPS	Global Positioning System
IGBP	International Geosphere-Biosphere Program
InSAR	SAR Interferometry
IRS-P6	ResourceSAT-1, part of Indian Remote Sensing Satellite series
JRC	Joint Research Center
KOMPSAT-2	Korea Multi-Purpose Satellite-2
LCCS	Land Cover Classification System
MERIS	Medium Resolution Imaging Spectrometer, ENVISAT optical sensor
MS	Multispectral
NASA	National Aeronautics and Space Administration

NDVI	Normalized Difference Vegetation Index
NIR	Near Infrared
NNA	Nearest Neighbor Analysis
OSM	OpenStreetMap
PALSAR	Phase Array type L-band Synthetic Aperture Radar
PPA	Point Pattern Analysis
PS	Persistent Scatterer
PS-InSAR	Persistent Scatterer SAR Interferometry
RADAR	RAdio Detection And Ranging
RAR	Real Aperture Radar
ROC	Receiver Operating Characteristic
SAR	Synthetic Aperture Radar
SCR	Signal-to-clutter-ratio
SPOT	Système Pour l'Observation de la Terre (French remote sensing satellite)
SRTM	Shuttle Radar Topography Mission
TM	Topographic Map
UN	United Nations
UNEP	United Nations Environment Program
UTM	Universal Transverse Mercator

List of symbols

A	Area of site
$B_{\perp}$	Perpendicular baseline
$B_{critical}$	Critical baseline
φ	Angle between absolute and perpendicular baseline
c	Velocity of light
λ	Wavelength
v	Frequency
t	Time between transmission and reception of radar pulse
τ	Radar pulse duration
θ	SAR incidence angle
R_a	Azimuth resolution
R_r	Range resolution
R_{gr}	Ground range resolution
R_s	Slant range distance
ΔR	Difference of slant range distance

ΔR_{def}	Deformation on the ground between the two SAR acquisitions
L	Antenna length (real)
L_{sa}	Antenna length (SAR)
ϑ_{ra}	Angular resolution in azimuth of real aperture radar
ϑ_{sa}	Angular resolution in azimuth of SAR
ϕ	Phase of radar signal
ϕ_{scatt1}, ϕ_{scatt2}	Backscattering properties of SAR 1, 2
ϕ_{int}	Interferometric phase of radar signal
ϕ_1	Phase of first SAR
ϕ_2	Phase of second SAR
ϕ_{def}	Deformation part of interferometric phase
ϕ_{dist}	Disturbing factors (e.g. phase errors due to orbit inaccuracies and noise)
ϕ_{topo}	Topographic part of interferometric phase
ϕ_{atm}	Atmospheric part of interferometric phase
Δx	Moving distance
Δh	Maximum topographic difference
ξ	Observer looking angle
z	Spatial resolution of DEM, pixel size
β	Angle between range and α
α	Slope's dip direction
ε	Angle between E-W-axis and range
h	Horizontal component of movement
δ	Reduced dip of slope
l	Footprint length
ω	Real dip of slope
v	Vertical component of movement
r	Real movement on the ground
ρ_1	Difference of ψ and δ
ρ_2	Sum of ψ and δ
ψ	90° - θ
m_{3D}	Measurable percentage of movement
η	Visual field of observers
SPOT	Base height of observer
OFFSETA	Height of observer (above base height)
AZIMUTH1, 2	Horizontal visual field of observers (angle)
VERT1, 2	Vertical visual field of observers (angle)

Ω	Complementary angle to VERT1, 2
$\Upsilon_{\Delta t}$	Temporal coherence
μ	Mean value
μ_a	Temporal mean value of amplitude
i, j	Integer values, $\in \mathbb{N}_0$
k	Factor
σ	Standard deviation
σ_a	Temporal standard deviation of amplitude
$\hat{\sigma}$	Estimated phase standard deviation
H	Hypothesis
S^2	Signal intensity
C^2	Clutter intensity
D_a	Normalized amplitude dispersion
$P(\cdot)$	Probability
P_M	Probability of missed hits
P_D	Probability of detection
P_F	Probability of false alarm
X	Random variable
N	Number of images
γ	SCR threshold
$\Delta\gamma$	Increment of γ
w	Some value of P_F
D	Detection rate
F	False alarm rate
d_{ij}	Euclidean distance between the points i and j
$d_{averaged}$	Average distance between empirical points
Q	Quotient of the averaged nearest neighbor distances of the empirical and random point patterns
$r_{averaged}$	Average distance between random points
M	Number of estimated points
x, y	x, y coordinate

1. Introduction

1.1 Motivation

Since the launch of the European Remote Sensing Satellites ERS-1 and 2 in 1991 and 1995, respectively, differential synthetic aperture radar interferometry (D-InSAR) has proven to be a powerful tool for detection and monitoring of deformations of the Earth's crust with centimeter accuracy (GABRIEL et al. 1989, MASSONNET et al. 1993). This European mission, supported amongst others by its successor mission ENVISAT (launch 2002), the Canadian missions Radarsat-1 and 2 (launch 1995 and 2007, respectively) and the German X-band mission TerraSAR-X (launch 2007), provide a large data archive. Besides the monitoring of earthquakes (MASSONNET et al. 1993, MEYER et al. 1998, RAUCOULES et al. 2010), volcanoes (MANZO et al. 2006), glaciers (SUNDAL et al. 2012) and subsidence (CARNEC & DELACOURT 2000, CHATTERJEE et al. 2003), D-InSAR has been successfully applied for landslide monitoring in several case studies (FRUNEAU et al. 1996, SQUARZONI et al. 2003, CATANI et al. 2005, COLESANTI & WASOWSKI 2006).

However, as landslides mainly occur in mountainous areas, the spatial distortions of SAR images caused by its 'range-azimuth' imaging geometry, negatively influence or even inhibit the application of D-InSAR at these regions. Layover – an overlapping of radar responses from different ground positions – and shadowing – areas in the radar shadow of steep slopes – are the main distortions (LILLESAND & KIEFER 2000, BARBIERI & LICHTENEGGER 2005, COLESANTI & WASOWSKI 2006).

The site's land cover also has a very important influence on the applicability of D-InSAR, requiring areas with high coherence. Coherence decreases with changes on the ground in the time between the radar acquisition dates, e.g. plant growth and movements of trees due to wind (WEGMÜLLER & WERNER. 1995, BAMLER & HARTL 1998, LU 2007, AHMED et al. 2011, CARTUS et al. 2011).

As these limiting factors of D-InSAR are usually only roughly estimated so far – sometimes leading to disappointing results when the actual SAR images are analyzed –, the first topic of this dissertation is the development of a procedure providing objective pre-survey estimation of the potential applicability of D-InSAR prior to the costly investment of a radar survey. This procedure is based on a geographical information system (GIS) and allows an accurate prediction of areas which will be affected by layover and shadowing. Furthermore, the percentage of movement of a potential landslide measurable by D-InSAR is calculated. Finally, depending on the SAR sensor wavelength, the main types of land cover within the footprint area are classified in terms of the applicability of D-InSAR.

The development of persistent scatterer synthetic aperture radar interferometry (PS-InSAR) by FERRETTI et al. (1999, 2000a, 2001) has overcome the 'coherence problem' of conventional D-InSAR and receives a sub-centimeter accuracy (KETELAAR 2009). Contrary to D-InSAR the deformation measurement is limited to specific points called persistent scatterers (PS). However, a high quality PS-InSAR processing is only possible with a stack containing at least 15 to 50 SAR images, depending on the site's land cover (FERRETTI et al. 2000b, COLESANTI et al. 2003a, HANSSEN 2005, CROSETTO et al. 2010, WASOWSKI et al. 2012). This high amount

of SAR images is a very critical cost factor when applying this method and the processing of the data is very time-consuming. Until now it is difficult to estimate the number of PS-targets and their distribution prior to the radar recording of the site and processing of several SAR images (COLESANTI et al. 2003b, COLESANTI & WASOWSKI 2006, CASCINI et al. 2009).

Therefore, the second topic of this dissertation deals with the development of three new methods for estimating possible PS prior to the acquisition of the SAR images of the area of interest. The goal of these pre-processing methods is to assess, whether the site's PS-density is high enough for successful PS-InSAR processing or whether the PS-density has to be artificially increased (e.g. by corner reflectors) – prior to the costly data acquisition.

The first PS-estimation method uses the freely available land cover data GlobCover, CORINE and Africover to calculate the PS-density of each single land cover class. The second method uses the normalized difference vegetation index (NDVI) computed from optical remote sensing data. The results show a strong correlation of the NDVI value and the PS-target distribution. Both methods were empirically developed by comparing the distribution of the results of PS-InSAR processing (processed, real PS) of several sites with land cover data and optical remote sensing data.

The third method uses freely available or low-cost topographic maps (TM) and OpenStreetMap (OSM) data to estimate the number of PS at a certain site. Furthermore, the distance between the estimated PS and their distribution within the site are determined and classified regarding to the usability for PS-InSAR processing. The results of the third PS estimation method are validated using processed PS-datasets.

By the selection of test areas with different climate and land cover a wide usability of the PS-estimation is guaranteed.

The pre-processing feasibility assessment of PS-InSAR for monitoring a certain site is extended by the third topic of this thesis, which investigates the determination of the minimum number of SAR images required for PS-detection. This topic deals with the number of SAR scenes needed for detection of PS-targets (PS-candidates) to test, whether the number of PS-targets of a certain site is high enough for a subsequent PS-InSAR processing, which of course then requires a higher number of SAR images. As a reference PS-detection was applied to a stack of 81 co-registered ERS scenes. Then, the number of SAR scenes of the stack was halved and again the PS-detection was applied optimized for a constant false alarm rate (CFAR). This procedure of halving the number of SAR images and PS-detection using a CFAR was continued until the number of SAR images of the stack was reduced to only one image. Additionally, a suitability criterion was used to guarantee that the number of correctly detected PS is at least as high as the number of falsely detected PS.

1.2 Objectives and state of the art

The overall topic of this dissertation is the development of pre-processing methods to enable the suitability evaluation of D-InSAR and PS-InSAR to monitor a certain site – prior to radar recording. The key question of the first main topic of this thesis can be formulated as:

1) 'Can D-InSAR be applied for monitoring a certain landslide?'

One major part of the first topic is the simulation of layover and shadow areas prior to the radar recording of the site. The GIS implementation of the developed layover and shadow simulation is a great advantage compared with approaches that can be found in the literature (e.g. EINEDER 2003, RAGGAM & GUTJAHR 2005). This GIS procedure is independent from the SAR sensor and can be applied for each incidence angle and orbit (ascending / descending). By executing the method several times using different parameters, one is able to figure out the best suited imaging parameters for monitoring a certain landslide by means of D-InSAR. As GIS is widely used in Earth sciences, the developed GIS procedure can also easily be used by geoscientists being non-experts in D-InSAR to carry out a first step evaluation whether D-InSAR can be used for monitoring a certain landslide – prior to the radar acquisition of the area of interest.

The algorithms developed in topic one consider the main factors when applying D-InSAR for landslide monitoring: Not only layover and shadow areas are predicted, but also the percentage of movement of a potential landslide measurable by D-InSAR is determined and the influence of the site's land cover is classified.

A great advantage of the methods developed is their usability for an area wide assessment, which is very interesting for e.g. geological surveys and the companies executing the D-InSAR processing for them.

However, as mentioned above, the methods developed in this dissertation are intended for a first step feasibility assessment whether D-InSAR can be used for monitoring a certain landslide. But these methods are not intended for replacing high functionality SAR software.

For topic two the following key question is formulated:

2) 'Can the PS-density of a site be estimated prior to its radar recording?'

The PS-technique is described in detail in FERRETTI et al. (1999, 2000a, 2001) and KAMPES (2006). Previous research for PS-estimation used already acquired SAR data. According to COLESANTI & WASOWSKI (2006), forecasting of the PS-density of a certain site prior to its radar recording and the processing of several SAR images is very difficult, "as the exact nature and physical principles of scatterers behavior are still insufficiently known" (see also COLESANTI et al. 2003b, CASCINI et al. 2009). This is especially true for rural areas, as only in urban areas there is a high number of PS-targets. The physical principles of PS-targets in urban area have been analyzed by FERRETTI et al. (2005), PERISSIN et al. (2006) and AUER et al.

(2011). REFICE et al. (2005) assume in their PS-InSAR processing algorithm high PS-density in urban area.

In this dissertation three new pre-processing methods are developed for PS-estimation prior to the radar recording of the site. To enable wide access, these GIS methods are based on freely available or low cost (a) land cover data, (b) optical remote sensing data and (c) topographic maps and OpenStreetMap data with mostly global coverage. For instance method (b) uses the well known NDVI (HOFFER 1978, HILDEBRANDT 1996, LILLESAND & KIEFER 2000:448, GUPTA 2003:572, ALBERTZ & WIGGENHAGEN 2009:284) for an entirely new approach – the estimation of PS.

Topic three covers the following key question:

3) 'How many SAR images are required for a meaningful PS-detection?'

According to the literature, PS-InSAR processing requires a stack of 15 to 50 or even more SAR images to enable useable results (FERRETTI et al. 2000b, COLESANTI et al. 2003a, HANSSEN 2005, CROSETTO et al. 2010, WASOWSKI et al. 2012). Until now there is little literature about the number of SAR images required for a useable PS-detection. In the third topic, this question is investigated by using a constant false alarm rate detector, which is a well known approach for automatic target detection in SAR images (e.g. ship detection; CRISP 2004, LÒPEZ-ESTRADA et al. 2004) and is here used in another way to examine the effects of continuously reducing the number of SAR images on PS-detection. The goal is to enable the user to do a first PS-detection with a small number of SAR images to test whether the PS-density of a certain site is high enough for a later PS-InSAR processing with a larger stack of images. As already mentioned above, PS-InSAR can be applied very well in urban areas because of its high PS-density (FERRETTI et al. 2000b). Contrary to this, in rural areas the PS-density is not always high enough for a successful PS-InSAR processing. Therefore, the most interesting areas for this research are rural areas, where the site of this study was chosen.

1.3 Structure of the dissertation

Figure 1 shows the structure of this dissertation. After an introduction including the motivation, state of the art and the objectives of the thesis, the sites and used datasets are described. Chapter 3 gives an overview on the basics of SAR and its interferometric applications D-InSAR and PS-InSAR. In chapter 4, the first topic of this dissertation presents the pre-survey feasibility assessment of the D-InSAR technique for landslide monitoring and contains (a) the development of a GIS tool for simulation of layover and shadowing (chapter 4.1), (b) the calculation of the percentage of movement measurable by InSAR (chapter 4.2) and (c) the classification of the main types of land cover regarding its influence on the applicability of D-InSAR for deformation monitoring (chapter 4.3). A summarized version of this first topic has been published in advance in PLANK et al. (2012). Using the description of the PS-InSAR method (chapter 3.4) chapter 5 deals with the second topic of this thesis, the estimation of PS prior to radar recording of the area of interest. To enable this estimation three procedures were developed based on (a) land cover data (chapter 5.1), (b) optical remote sensing data, more precisely on the NDVI calculated by this data (chapter 5.2) and (c) topographic maps (TM) and OpenStreetMap (OSM) data (chapter 5.3). For development and validation of these PS-estimation methods the datasets of the sites described in chapter 2 were used. In PLANK et al. (in review) a summarized version of the second topic has been published in advance. In the third topic of the dissertation (chapter 6) the minimum number of SAR images required for PS-detection is determined. The dissertation concludes with a summary, a discussion and an outlook on possible further work in the future. Finally, an appendix gives more detailed information on the data, codes and models used and developed in this thesis.

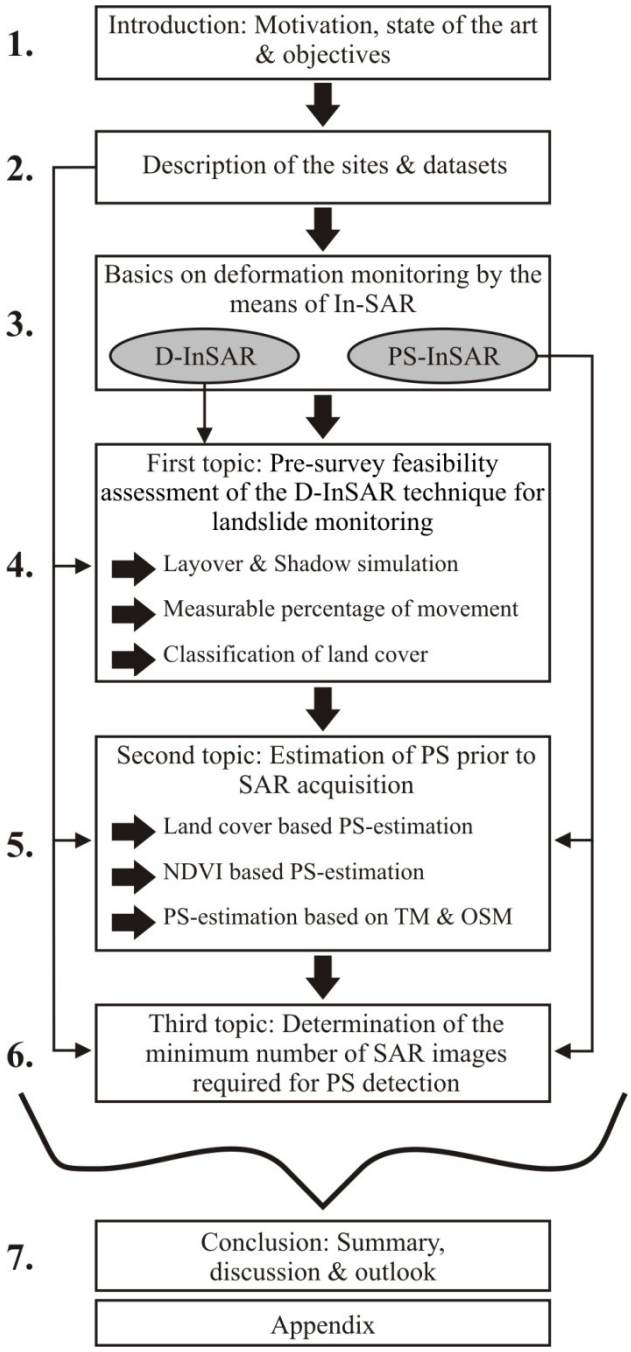

Fig. 1: The structure of the thesis.

2. Description of the sites and datasets

This chapter describes the sites and SAR datasets that were used in the development and validation of the methods described in the chapters 4, 5 and 6. Table 1 and figure 2 show the 14 sites: The city of Cairo (Egypt) and surrounding, the city of Budapest (Hungary), Bavaria (Germany), Aschau am Inn (Germany), the Sudelfeld (Germany), North Germany, Netherlands, two sites in the Aosta Valley (Italy) and five test areas in Piedmont (Italy).

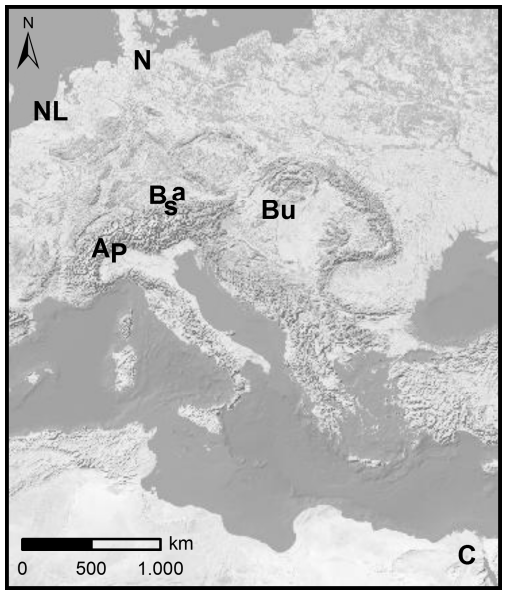

Fig. 2: Overview map of the sites North Germany (N), Netherlands (NL), Bavaria (B), Aschau am Inn (a), Sudelfeld (s), Budapest (Bu), Cairo (C), Aosta Valley (A; east and west) and the five Piedmont (P) sites: Domodossola, Novara, Ivrea, Omegna and Varallo. For detailed maps see AFig. 1 (appendix 1). © Background map ESRI.

a) Cairo, Egypt

The first site is the city of Cairo and surrounding characterized by a dry hot desert climate and a very flat terrain (AFig. 1a, appendix 1). The ca. 70 km times 45 km wide study area consist of three regions: the capital city Cairo (mainly built up by buildings with flat roofs), the temporary flooded Nile Delta and the surrounding stony and rocky desert. For this site the results of three PS-detection methods processed with 38 ENVISAT ASAR (Advanced Synthetic Aperture Radar) images were available[1]: Signal-to-clutter-ratio (SCR), thresholding on the amplitude dispersion (D_a) and the combination of both methods (These terms are further described in chapter 3.4).

As all the other sites are in Central or Eastern Europe (Budapest), respectively, they have a warm-moderate climate and sufficient precipitation in all months (humid) (PEEL et al. 2007).

b) Budapest, Hungary

The capital city of Hungary is the second site (ca. 13.4 km x 13.5 km; AFig. 1b, appendix 1). It is located in flat terrain. The main parts of this site are urban areas. For the Budapest site geocoded PS-targets of 43 TerraSAR-X StripMap mode data were used[2].

[1] Kindly provided by Dr. Michael Foumelis (University of Athens).
[2] Generously provided by Dr. Michael Riedmann and Dr. Oliver Lang (Astrium Infoterra).

c) Bavaria, Auschau am Inn and Sudelfeld

The Bavaria site is a ca. 100 km times 100 km large part of Upper Bavaria, Germany (AFig. 1c, appendix 1). Starting from the city of Augsburg in the northwest to the city of Munich in the east, it extends as far as the Bavarian Alps in the south. Beside these two large cities the main part of the site is rural area (farmland, followed by forest). The site is dominated by flat and hilly terrain. A small percentage of the site shows a stronger topographic relief at the northern boundary of the Alps. The PS-targets of the Bavaria site were processed using 81 ERS SAR images (ERS-1 & 2)[3].

In the third topic (chapter 6), a subset (ca. 6 km x 7 km) of this site is used. It is located in rural area between the lakes Ammersee, Pilsensee and Wörthsee and consists of ca. 40 % forest, 20 % water, 17 % farmland, 13 % settlement area (villages) and 10 % moor.

Approximately 40 km to the east of the Bavaria site there is the Aschau am Inn site (10 km x 12 km), characterized by flat terrain in rural area. The PS-targets of this site were processed by a 73 image stack of TerraSAR-X StripMap mode data[2].

The Sudelfeld site is ca. 30 km in the southeast of the Bavaria site. It is located between the city of Bayrischzell in the west and the city of Oberaudorf in the east. The site shows a mountainous topography and extends over ca. 5 km times 10 km. For the Sudelfeld site there was a geocoded TerraSAR-X High resolution Spotlight mode image available to validate the results of topic one (chapter 4).

d) North Germany

This site is an area of ca. 100 km times 100 km in North Germany, characterized by very flat terrain (AFig. 1d, appendix 1). Outside the big cities of Hamburg in the south and Lübeck in the east, this site is mainly dominated by rural area (mainly farmland). The PS-targets of the site were processed by using 34 ERS SAR images[3].

e) Netherlands

Approximately 400 km to the west of the North Germany site, there is the Netherland site, covering an area of ca. 80 km times 100 km from the cities of The Hague and Rotterdam in the north to the city of Antwerp in the south (AFig. 1e, appendix 1). The main land cover class of this very flat terrain is farmland. For the Netherlands site 75 ERS SAR images were used for the PS-InSAR processing[4].

f) Aosta Valley, northwest Italy

The Aosta Valley site (ca. 130 km x 75 km) is a west-east oriented valley in the Graian Alps in the northwestern part of Italy (AFig. 1f, appendix 1). This site displays sharp reliefs with the valley floor at the city of Aosta at ca. 583 m above sea level and the mountains Matterhorn and Monte Rosa (4478 and 4634 m above sea level, respectively) at the border to Switzerland in the north and the mountain Montblanc (4807 m) at the border to France in the west. The mountain Gran Paradiso (4061 m above sea level) towers in the south of the site. The Aosta Valley site consists of two Radarsat-1 footprints (each ascending and descending orbit). For the ascending orbit 102 SAR images and for the descending orbit 94 SAR images were used[5].

[3] Kindly provided by Mr. Werner Liebhart (DLR).
[4] Generously provided by Mr. Miguel Caro Cuenca (TU Delft).
[5] Kindly provided by Dr. Alessandro Ferretti (T.R.E.).

g) Sites in Piedmont, northwest Italy

The Piedmont sites are in the eastern neighborhood of the Aosta Valley site. The study area consists of five sites (all Radarsat-1)[5]: Ivrea (91 SAR images, 50 km x 60 km), Omegna (86 SAR images, 30 km x 93 km) and Varallo (92 SAR images, 35 km x 80 km) (all ascending orbit; AFig. 1h, appendix 1) and Domodossola (77 SAR images, 60 km x 90 km) and Novara (77 SAR images, 70 km x 55 km) (both descending orbit; AFig. 1g, appendix 1). All Piedmont sites are dominated by rural area.

For the sites in the Aosta Valley and in Piedmont additionally to 'normal' PS-targets also distributed scatterers (DS, SqueeSAR™) were available (FERRETTI et al. 2011) (cf. chapter 3.4).

Tab. 1: SAR datasets used

Site	Satellite	Mode	Track	Pass (Ascending, Descending)	Period
Aschau am Inn	TerraSAR-X	StripMap	131	A	2008-2011
Budapest	TerraSAR-X	StripMap	32	D	2008-2010
Sudelfeld	TerraSAR-X	HS	55	A	2009-04-08
Aosta Valley East	Radarsat-1	Standard	290	A	2003-2010
	Radarsat-1	Standard	340	D	2003-2010
Aosta Valley West	Radarsat-1	Standard	290	A	2003-2010
	Radarsat-1	Standard	340	D	2003-2010
Ivrea	Radarsat-1	Standard	290	A	2003-2009
Omegna	Radarsat-1	Standard	47	A	2003-2009
Varallo	Radarsat-1	Standard	290	A	2003-2009
Domodossola	Radarsat-1	Standard	97	D	2003-2009
Novara	Radarsat-1	Standard	97	D	2003-2009
Cairo	ENVISAT	Image	436	D	2003-2009
Bavaria	ERS-1 & 2	-	437	D	1992-2002
Netherlands	ERS-1 & 2	-	194	D	1992-2001
North Germany	ERS-1 & 2	-	129	A	1993-2000

3. Basics on deformation monitoring by the means of InSAR

This chapter gives a short overview of the basics on synthetic aperture radar and its interferometric techniques. In each section literature sources for further information are provided.

3.1 Synthetic aperture radar

RADAR – short for RAdio Detection And Ranging – uses the microwave region (wavelength λ: mm to dm) of the electromagnetic spectrum, while optical sensors use the visible and infrared part (λ: 0.4 µm to 1 mm). This larger wavelength of the radar sensor makes radar an all-weather technique, as only larger atmospheric changes in the time between radar acquisitions have a big influence on D-InSAR applications. Radar is able to work day and night, as the active instrument transmits a synthetically generated pulse to the Earth and receives its echo – independently of the solar radiation used by optical sensors (GUPTA 2003:5).

The mostly used frequency bands in civilian space-borne SAR missions are the L-band (frequency ν = 0.39 – 1.55 GHz), C-band (ν = 4.2 – 5.75 GHz) and X-band (ν = 5.75 – 10.90 GHz) (BARBIERI & LICHTENEGGER 2005:1.5). Radar sensors using higher frequencies (such as X and C-band) enable higher spatial resolution of the radar image, whereas lower frequencies (e.g. L-band) are less influenced by vegetation (BAMLER & HARTL 1998, BARBIERI & LICHTENEGGER 2005:4.3).

As shown in figure 3, imaging radar is a side-looking technique (range = viewing direction). Perpendicular to the flight direction (azimuth) of the air- or satellite-borne sensor a radar pulse is transmitted to the ground and its echo is received. The slant range distance R_s between the sensor and the object on the ground is measured according to equation 1, where c represents the velocity of light and t the two-way travel time of the signal from the sensor to the object on the ground and back to the sensor.

$$R_s = \frac{ct}{2} \qquad (1)$$

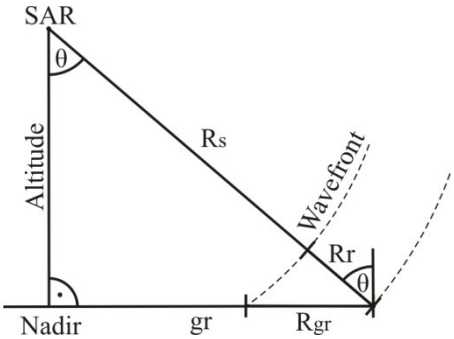

Fig. 3: Radar imaging geometry. Relationship between the spatial resolution in range direction R_r and ground range R_{gr} (modified after ALBERTZ & WIGGENHAGEN 2009:301).

The spatial resolution of an imaging system is the minimum distance at which one is able to distinguish two neighboring objects. The spatial resolution in range direction R_r depends on the pulse duration τ of the signal (Eq. 2).

$$R_r = \frac{c\tau}{2} \qquad (2)$$

To achieve R_{gr}, the spatial resolution on the ground in range direction, also the incidence angle θ has to be considered (Eq. 3). According to GUPTA (2003:326), to guarantee high enough power of the received signal for radar sensors flying at high altitude τ has to be larger (= decrease of R_{gr}) than for sensors flying at lower altitude.

$$R_{gr} = \frac{c\tau}{2\cos(90-\theta)} \qquad (3)$$

In azimuth direction the angular resolution ϑ_{ra} of a real aperture radar (RAR) sensor is determined by the wavelength λ of the transmitted radar pulse and the length of the antenna L (Eq. 4).

$$\vartheta_{ra} = \frac{\lambda}{L} \qquad (4)$$

The spatial resolution in azimuth direction $R_{a,RAR}$ also depends on R_s (Eq. 5, ALBERTZ & WIGGENHAGEN 2009:302).

$$R_{a,RAR} = R_s\vartheta_{ra} = \frac{\lambda R_s}{L} \qquad (5)$$

As $R_{a,RAR}$ decreases with increasing altitude and the corresponding longer distances to the objects on the ground, RAR systems have a very limited applicability. For instance, to achieve a spatial resolution of several meters, satellite-borne sensors would require L to be in the order of several kilometers, which is technically not realizable.

The synthetic aperture radar (SAR) technique overcomes these limitations and achieves high resolution with small antennas. As an object on the ground is recorded several times by succeeding radar recordings of the overflying sensor (Fig. 4), a synthetically enlarged antenna (synthetic aperture) is formed, which is many times longer than the real antenna (ALBERTZ & WIGGENHAGEN 2009:302-303). The radar echoes of the object on the ground show a different frequency shift, the so called Doppler frequency shift, being a function of the relative velocity of a transmitter (the radar sensor) and a reflector (the object on the ground). Using a wide antenna beam, echoes from objects in the area ahead of the sensor show higher frequencies, whereas returns from objects behind the satellite have lower frequencies (LILLESAND & KIEFER 2000:629).

The angular resolution ϑ_{sa} of a SAR of a length L_{sa} is (Eq. 6).

$$\vartheta_{sa} = \frac{\lambda}{2L_{sa}} \qquad (6)$$

The maximum lengths of L_{sa} is equal to the length of the flight pass at which the object on the ground is recorded (Eq 7).

$$L_{sa} = \vartheta_{ra}R_s = \frac{\lambda R_s}{L} \qquad (7)$$

Using the full synthetic aperture, the spatial resolution in azimuth direction $R_{a,SAR}$ at a certain R_s is achieved by combing equation 6 and 7 (Eq. 8). The important advantage of the SAR technique is the independence from the slant range distance R_s – therefore even with SAR

sensors operating at high altitude (space-borne) and using a small antenna high spatial resolution is achieved (ALBERTZ & WIGGENHAGEN 2009:303).

$$R_{a,SAR} = \vartheta_{sa} R_s = \frac{L}{2} \quad (8)$$

More detailed information about the SAR principle is provided in e.g. GEUDTNER (1995), BAMLER & HARTL (1998), HEIN (1998), WU (1998), FRANCESCHETTI & LANARI (1999), MÜLLENHOFF (2004), BARBIERI & LICHTENEGGER (2005) and COLESANTI & WASOWSKI (2006).

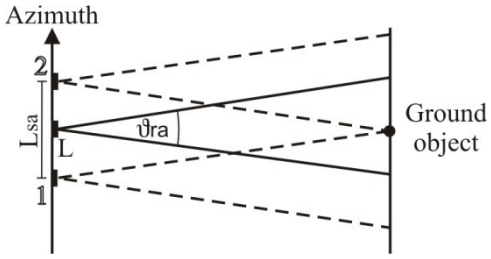

Fig. 4: Synthetic aperture radar (SAR) principle. The object on the ground is recorded several times by the satellite during its flyover. 1 marks the first sensing of the object, 2 the last sensing. Using the radar echoes recorded at different antenna positions a synthetically large antenna L_{sa} is formed (modified after LILLESAND & KIEFER 2000:628).

3.2 Interferometric application of SAR

In SAR interferometry (InSAR) two radar acquisitions recorded at two slightly different positions are used to generate a digital elevation model (DEM) of the Earth's surface (SCHWÄBISCH 1995, FRANCESCHETTI & LANARI 1999:11f., ROSEN et al. 2000, RABUS et al. 2003, FERRETTI et al. 2007:A18ff.). The phase ϕ of the chromatic radar wave is directly proportional to the travel way of the signal, which is $2R_s$ (double travel path: from the sensor to the ground and back to the sensor). As the distance from the second SAR sensor to the object on the ground is by the amount of ΔR larger than the corresponding distance from the first SAR, both sensors receive slightly different phase signals (Fig. 5, Eqs. 9 & 10).

$$\phi_1 = -\frac{4\pi}{\lambda} R_s + \phi_{scatt1} \quad (9)$$

$$\phi_2 = -\frac{4\pi}{\lambda} (R_s + \Delta R) + \phi_{scatt2} \quad (10)$$

Knowing the perpendicular baseline $B\perp$ between the two SAR sensors and the angle φ (angle between the absolute and perpendicular baseline; Fig. 5), ΔR can be calculated using equation 11.

$$\Delta R = B_\perp \tan \varphi \quad (11)$$

$B\perp$ should not exceed a certain threshold $B_{critical}$, at which the coherence equals to zero, as the change of the incidence angle θ becomes too large and the radar echoes from both SAR sensors become uncorrelated (Eq. 12, cf. 4.3.1, ZEBKER & VILLANSENOR 1992).

$$B_{critical} = \frac{\lambda R_s}{2R_r (\cos\theta)^2} \quad (12)$$

For constant backscattering properties at both acquisition times ($\phi_{scatt1} = \phi_{scatt2}$), the interferometric phase ϕ_{int} is the difference of ϕ_1 and ϕ_2 (Eq. 13). The backscattering properties can for instance be changed by growth of vegetation, movements due to wind or large atmospheric variations (BAMLER & HARTL 1998). These effects can be reduced by reducing the time between the two SAR acquisitions. For instance, in the TanDEM-X mission this time is reduced to zero, as two satellites simultaneously record the area of interest (BARTUSCH et al. 2009).

$$\phi_{int} = \phi_1 - \phi_2 = \frac{4\pi}{\lambda}\Delta R \quad (13)$$

As the phase of a radar echo can only be determined in modulo 2π, the interferometric phase ϕ_{int} is wrapped. Using the techniques of phase-unwrapping the phase can be transferred to absolute height values.

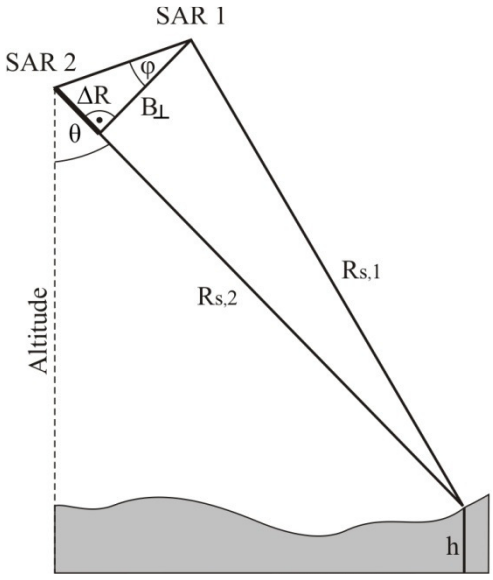

Fig. 5: Principle of InSAR. As the distance from the SAR 2 to the object on the ground is by the amount of ΔR longer than the distance from SAR 1 to the object ($R_{s,2} = R_{s,1} + \Delta R$), two different phase signals are recorded at the two SAR acquisitions. This phase difference can be used to determine the topographic height h of the object on the ground (modified after ALBERTZ & WIGGENHAGEN 2009:305).

3.3 Differential SAR interferometry

The goal of differential SAR interferometry (D-InSAR) is the measurement of deformations of the Earth's crust (GABRIEL et al. 1989, MASSONNET & FEIGL 1998, CHEN, Y. et al. 2002, ZHOU et al. 2009), such as earthquakes (e.g. MASSONNET et al. 1993, MEYER et al. 1998, RAUCOULES et al. 2010), volcanoes (e.g. MANZO et al. 2006), subsidence (e.g. CARNEC & DELACOURT 2000, CHATTERJEE et al. 2003) and landslides (e.g. FRUNEAU et al. 1996, SQUARZONI et al. 2003, CATANI et al. 2005, COLESANTI & WASOWSKI 2006). The deformation in the time between the two SAR acquisitions is measured with centimeter accuracy. The interferometric phase ϕ_{int} as shown in equation 13, is influenced by the topography of the footprint ϕ_{topo} (including the influence of the 'flat Earth'), atmospheric variations between the two acquisitions ϕ_{atm}, other disturbing factors ϕ_{dist} (such as phase errors due orbit inaccuracies and noise) and the deformation on the ground ϕ_{def} (Eq. 14).

$$\phi_{int} = \phi_{topo} + \phi_{atm} + \phi_{dist} + \phi_{def} \quad (14)$$

By using a DEM ϕ_{topo} can be excluded. This DEM can for example be generated by the method described in 3.2. The deformation on the ground ΔR_{def} is then be calculated according to equation 15 – after considering all disturbing factors as well as possible (FERRETTI et al. 2007:A23).

$$\phi_{def} = \frac{4\pi}{\lambda} \Delta R_{def} \quad (15)$$

The advantage of D-InSAR is the possibility of spatially continuously deformation measurement over wide areas. However, atmospheric influences can be misinterpreted as deformation signal (FERRETTI et al. 2001). Another very important limitation factor of the applicability of D-InSAR is temporal decorrelation (loss of coherence between the two SAR recordings), e.g. due plant growth and movements of trees due to wind (see chapter 4.3; WEGMÜLLER & WERNER 1995, BAMLER & HARTL 1998, COLESANTI & WASOWSKI 2006, LU 2007, AHMED et al. 2011, CARTUS et al. 2011).

3.4 Persistent scatterer SAR interferometry

To overcome the disadvantages of the conventional D-InSAR technique mentioned above, the so called persistent scatterer SAR interferometry (PS-InSAR) method was developed, which achieves an accuracy of 1 to 3 mm (FERRETTI et al. 1999, 2000a, 2001, COLESANTI et al. 2003, KAMPES 2006). PS-InSAR not only uses two SAR images, but a stack of at least 15 to 50 SAR images, depending on the site's land cover (FERRETTI et al. 2000a, COLESANTI et al. 2003a, HANSSEN 2005, CROSETTO et al. 2010, WASOWSKI et al. 2012). Deformation is measured at specific objects called persistent scatterers (PS), which are characterized by long-term constant backscattering properties (high coherence) of the radar signal. These PS-targets for instance are artificial objects such as buildings, which directly send the radar signal back to the satellite because of their geometry and orientation to the SAR sensor, and metallic objects such as power poles and railway tracks. Natural PS-targets can be generated by rock outcrops and single rock blocks. The newly developed SqueeSAR™ method uses not only 'normal' PS-targets, but also distributed scatterers (DS), which correspond to neighboring pixels sharing similar reflectivity values. DS are usually found at debris areas, non-cultivated land with short vegetation or desert areas. For a detailed description of SqueeSAR™ the reader is referred to FERRETTI et al. (2011).

PS-InSAR has successfully been applied for measuring e.g. subsidence (e.g. KIRCHNER 2005, WORAWATTANAMATEEKUL 2006, KETELAAR 2009, HUNG et al. 2011, HELENO et al. 2011, CIGNA et al. 2012), landslides (e.g. COLESANTI et al. 2003a, METTERNICHT et al. 2005, CASCINI et al. 2009, LAUKNES et al. 2010, BOVENGA et al. 2012) and tectonic deformation (e.g. MASSIRONI et al. 2009, VILARDO et al. 2009).

There are two major concepts for PS-detection. The first one uses the normalized amplitude dispersion D_a (FERRETTI et al. 2001), calculated by dividing the temporal standard deviation of the amplitude σ_a by the temporal mean of the amplitude μ_a of a certain pixel in a stack of SAR images (Eq. 16).

$$D_a = \frac{\sigma_a}{\mu_a} = \hat{\sigma}_\phi \quad (16)$$

The basic idea of this concept is that a pixel characterized by a high and more or the less constant amplitude value is assumed to show a low phase dispersion ($\hat{\sigma}_\phi$ = estimated phase standard deviation). Using this relationship it is possible to identify pixels with a coherent signal without analyzing the phase. A pixel is selected as PS (candidate), if its value for D_a is below a certain threshold (KAMPES 2006, KETELAAR 2009).

The second concept for PS-detection uses the signal-to-clutter-ratio (SCR), originally developed for SAR calibration with corner reflectors (FREEMAN 1992). The SCR is calculated by dividing the intensity of the signal (S^2) by the clutter (C^2), the intensity of the spatial neighborhood of the pixel (Eq. 17).

$$SCR = \frac{S^2}{C^s} \quad (17)$$

With intensity S^2 being the square of the amplitude.

According to ADAM et al. (2005), a high SCR value corresponds with a low phase error (Eq. 18).

$$\hat{\sigma}_\phi = \frac{1}{\sqrt{2SCR}} \quad (18)$$

Therefore, pixels exceeding a certain SCR threshold are detected as PS-targets.

The advantages of the PS-InSAR method are the possibility of estimating the atmospheric influence on the phase signal by processing a stack of SAR images (SÖRGEL 2006:7) and the generation of time series of the deformation for each PS-target. Also the problem of the temporal decorrelation can be overcome by this method – prerequisite is there is a high enough number of these PS-targets within the site. Therefore, one goal of this thesis is the estimation of the number of PS prior to SAR acquisition of the area of interest, to be able to test the applicability of PS-InSAR before ordering the expensive SAR images (see chapter 5).

4. Pre-survey feasibility assessment of the D-InSAR technique for landslide monitoring

The first topic of this work deals with the development of GIS-based tools enabling the user to accurately predict areas which will be affected by layover and shadowing, calculate the percentage of movement of a potential landslide measurable by D-InSAR and get information about the influence of the footprint's land cover on the applicability of this SAR technique. A summarized version of this first topic has been published in advance in PLANK et al. (2012). Here the procedures are presented in detail.

4.1 Layover & Shadow

4.1.1 Layover & Shadow effect

The imaging geometry of radar systems 'range-azimuth' causes several distortions in SAR images of areas with topographic relief. The range distance between two points in a radar image depends on the time delay of the received radar echoes (cf. chapter 3.1, Eq. 1). There are two types of distortions. Geometric distortions cause a disturbed imaging of the Earth's topography, whereas radiometric distortions change the intensity values (brightness) of the SAR image.

There are several types of geometric distortions (Fig. 6). Due to the lateral illumination of the Earth's surface, certain areas, e.g. behind mountains, are not reached by the radar pulse. These shadow areas appear black in the SAR image. Shadowing occurs at slopes oriented averse to the SAR sensor where the slope angle δ is greater than 90° minus the incidence angle θ.

Slopes leaning towards the SAR senor are shortened in the radar image. This foreshortening effect is caused by the shorter travel time of the radar pulse, as the slant range distance to an object on the inclined slope is shorter than to an object on flat terrain. As the entire backscatter of the slope is compressed into a smaller image part, these foreshortening areas appear brighter in the SAR image. Contrary to foreshortening is the elongation effect of slopes averse to the SAR senor, leading to darker image regions.

For slopes leaning towards the SAR sensor and with slope angles δ greater than the incidence angle θ, layover, an extreme form of foreshortening, appears. At very steep slopes the radar pulse first hits the summit of the mountain and then its foot. Therefore, the summit is imaged in front of the mountain's foot, leading to great geometric distortions in the radar image. As the radar echoes of the mountain's summit and of a point in front of the mountain are received at the same time, both signals are overlaid. These layover areas are characterized by very high intensity values (cf. foreshortening).

All these geometric distortions make the interferometric application very difficult or even prohibit them. As in shadow areas no signal of the ground is received and in layover areas radar echoes from different objects on the ground overlap, D-InSAR cannot be applied in these areas (LILLESAND & KIEFER 2000, GUPTA 2003, BARBIERI & LICHTENEGGER 2005, COLESANTI & WASOWSKI 2006).

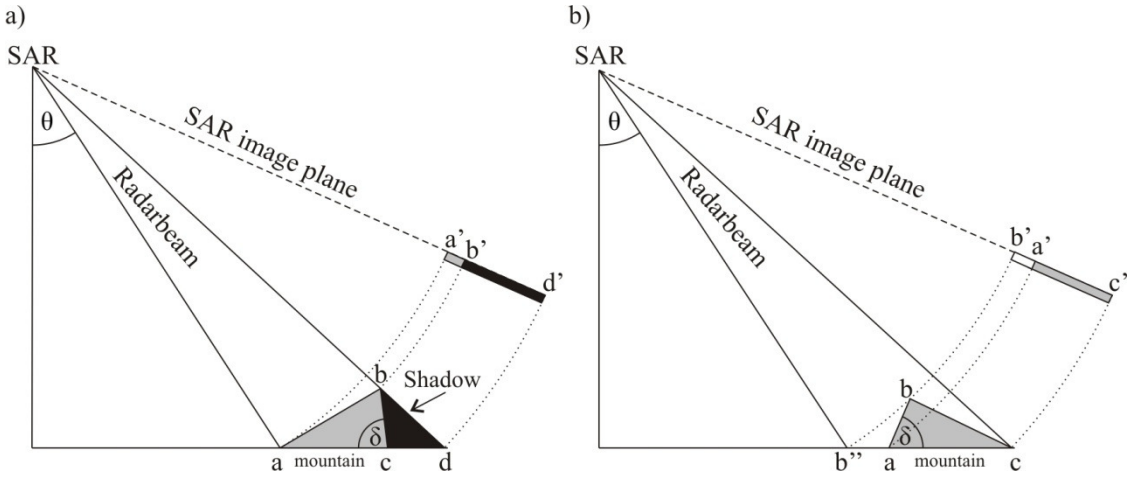

Fig. 6: **a) Foreshortening and shadowing. The slope leaning towards the SAR is shortened in the SAR image, due to the relatively short travel time between the points a and b. As the slope angle δ of the slope averse to the SAR sensor is greater than 90° - θ, this area is not achieved by the radar pulse and is therefore located in the radar shadow (points b to d). b) At the slope leaning towards the SAR with slope angle δ greater than θ the summit b of the mountain is recorded by the SAR before the mountain's foot a is imaged. Furthermore, the radar echoes from b'' and b are received at the same time and are therefore overlapped in the SAR image (layover) (modified after ALBERTZ & WIGGENHAGEN 2009:296-297).**

4.1.2 Layover-shadow-simulation method

As D-InSAR cannot be applied in layover and shadow areas (cf. chapter 4.1.1), it is very important to know whether the area of interest will be affected by these distortions prior to the costly SAR acquisition. Therefore, in this thesis a GIS-based tool was developed to precisely predict these areas. A basic version of this layover-shadow-simulation was developed in PLANK (2009). Here an expanded version is presented, allowing (a) more precise layover and shadow simulation and (b) faster execution of the procedure, due to its higher automatization level.

4.1.2.1 Description of the layover-shadow-simulation

In figure 7 the program sequence of the layover-shadow-simulation is shown. The main part of the program comprises a complex GIS-model, which is part of a toolbox developed with the model builder in ArcGIS® (Esri) and is expanded by several Python and VBA scripts (Tab. 2). The GIS procedure uses two observer points for each pixel of the DEM of the footprint area – one observer for layover- and one for shadow-simulation. The air- or satellite-borne radar sensor is simulated by these observer points. For the simulation following parameters and datasets are required as input: (a) the incidence angle at near range and far range, (b) the coordinates of the ground area (footprint) recorded by radar, (c) orbit information of the satellite (ascending or descending pass) and (d) a DEM of the footprint area and a certain surrounding. Information about the orbit of the satellite and the incidence angle are freely available at the online databases of the agencies operating the satellites. DEMs (at least Shuttle Radar Topography Mission (SRTM) DEMs, RABUS et al. 2003) can be downloaded free of charge at several websites (e.g. at the Consultative Group on International Agricultural Research (CGIAR) Consortium for Spatial Information: http://srtm.csi.cgiar.org).

Tab. 2: Developed ArcGIS® models and Python and VBA scripts (cf. chapter 4.1.2.2 & appendix 2 to 6)

ArcGIS® model / script	Short description	Chapter / Appendix
Model 'Get coordinates of points'	Calculates coordinates of footprint corners	Chapter 4.1.2.2 a)
Model '20 km buffer zone'	Creates 20 km buffer zone around footprint	Chapter 4.1.2.2 a)
Model 'layover-shadow-simulation' for large areas	Layover-shadow-simulation for sites where large DEMs are available	Chapter 4.1.2.2 b)
Model 'layover-shadow-simulation' for small areas	Layover-shadow-simulation for sites where small DEMs are available	Chapter 4.1.2.2 b)
VBA code 'rotation angle and footprint length'	Calculates the rotation angle and the footprint length, required for the simulation	Chapter 4.1.2.2 a), App. 2
Python code 'optimal moving distance'	Calculates the moving distance, required for the simulation	Chapter 4.1.2.2 a), App. 3
VBA code 'split lines'	Included within the ArcGIS® models	Chapter 4.1.2.2 b), App. 4
VBA code 'individual incidence angle'	Parameter calculation, included in models	Chapter 4.1.2.2 b), App. 5
VBA code 'observer's height'	Parameter calculation, included in models	Chapter 4.1.2.2 d), App. 6
VBA code 'observer's vertical visual field'	Parameter calculation, included in models	Chapter 4.1.2.2 d), App. 6
VBA code 'observer's horizontal visual field'	Parameter calculation, included in models	Chapter 4.1.2.2 d), App. 6

In the first step of the layover-shadow-simulation (Fig. 7), the footprint area is determined by using its four corner coordinates. Then, a test area for which the DEM is required is defined. Its size depends on the topographic relief Δh of the footprint area and its surroundings and the incidence angle θ and is automatically optimized to reduce computing time.

Low orbit Earth observation satellites fly on a near polar orbit with an inclination of a few degrees. As the orientation of the DEM pixels is fixed in the GIS and the simulation requires a constricted visual field of each observer (to guarantee that each observer only monitors the pixel dedicated to it), the DEM of the test area is rotated so its pixels are oriented parallel and its columns orthogonal to the range direction of the satellite (cf. section 4.1.2.2 a). Next, the two observer points (one for layover- and one for shadow-simulation) are generated for each pixel of the DEM (within the area of the footprint). Then, the layover observer points are moved away from the sensor and the shadow observer points are moved towards the satellite by the moving distance Δx, which depends on the same factors as the size of the test area and is calculated by equation 19.

$$\Delta x = \Delta h \tan \xi \quad (19)$$

Where Δh representing the maximum difference of the topography's height within the footprint area and a 20 km buffer zone, which enables the simulation of layover and shadow areas even at the edges of the footprint area. The buffer of 20 km is large enough to consider a height difference larger than 7,000 m based on the steepest incidence angle of TerraSAR-X (20°); more exactly on the corresponding observer looking angle 90° – 20° = 70° to consider layover. Therefore, worldwide applicability of the simulation is guaranteed.

The observer looking angle ξ requires a case differentiation to consider layover and shadow observers: $\xi = \theta$ for $\theta \geq (90° - \theta)$ or $\xi = 90° - \theta$ for $\theta < (90° - \theta)$, respectively (with θ = center incidence angle; Fig. 7).

To ensure that the observer points are looking at their correct pixels the moving distance Δx has to be an integer multiple of the DEM's pixel size (spatial resolution) z. This is imple-

mented by step by step increasing the integer value of Δx (= Δx_{int}) by the value of '1' until equation 20 is fulfilled.

$$\Delta x_{int} mod\ z = 0 \quad (20)$$

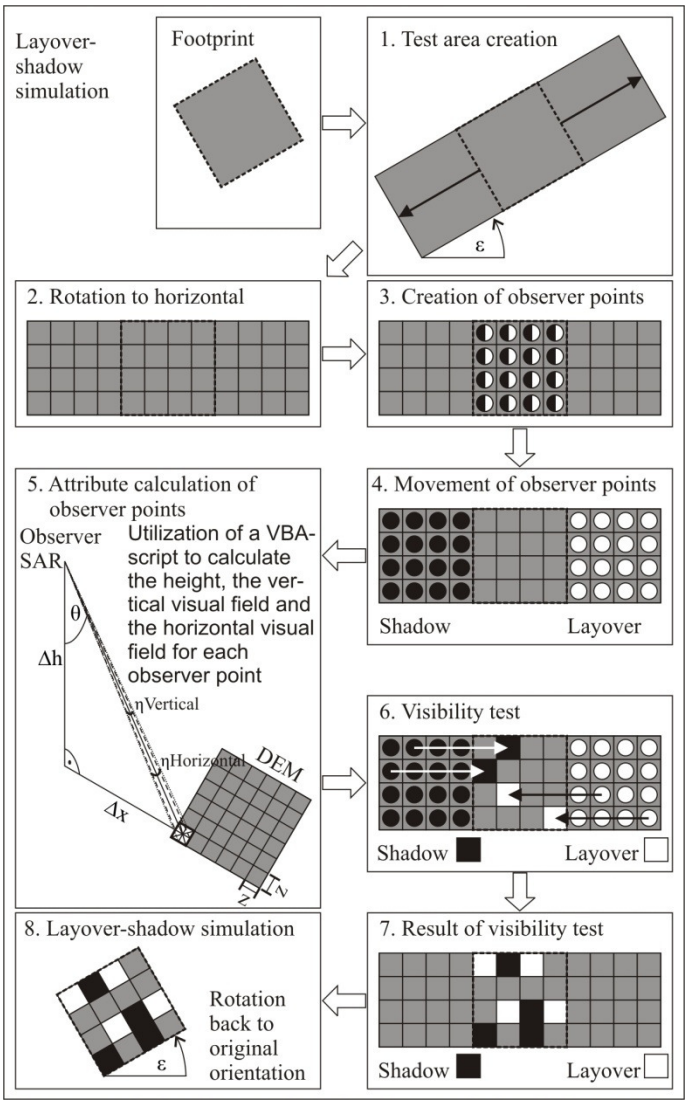

Fig. 7: The program sequence of the layover-shadow-simulation (modified after PLANK et al. 2012).

In the next step, using a VBA script (cf. appendix 5 & 6) the attributes of the observer points are calculated to constrict the visual field of the observer points to ensure that each observer only monitors the pixel dedicated to it. Thereby, the variation of the incidence angle from near range to far range is considered. Then, the visibility test is executed to test for each observer point whether it is able to 'see' its pixel or not. A pixel is affected by shadow or layover, if it cannot be seen by its shadow or layover observer, respectively. As a result of the layover-shadow-simulation a map of the footprint area precisely predicting the areas which will be affected by layover and shadowing is produced. In the last step, the layover-shadow map is backwards rotated to the original footprint orientation so that each pixel again has its original geographic coordinates.

One separate observer point for each DEM pixel is used (as described above), because of several advantages in comparison to the usage of one single observer point located at the real position of the SAR sensor and monitoring the entire footprint. The observer points have to be located inside the DEM because of GIS technical reasons. The high altitude of the satellite and the side-looking imaging geometry of SAR systems would lead to the requirement of a very large DEM when using the 'one-observer' method. This is technically realizable by synthetically enlarging the size of the DEM. However, there are two significant disadvantages: (a) the computation time of the simulation would strongly increase and (b) the accuracy of the layover-shadow-simulation would be reduced as such a large DEM could extend over several map projection zones. All data used has to be in or transferred to the same isogonal metrical coordinate system (e.g. Universal Transverse Mercator, UTM) to ensure a correct simulation. The method described here ensures that the distance between the observer and the DEM pixel is less than 20 km (see above).

4.1.2.2 Technical implementation in ArcGIS®

a) Preparation for the simulation

In this section the technical implementation of the layover-shadow-simulation in ArcGIS® is described. As already mentioned in section 4.1.2.1, the required parameters for the simulation are (a) the minimum (near range) and maximum (far range) incidence angle θ, (b) the pass direction (ascending (south to north) or descending pass (north to south); the simulation is programmed for 'right looking' satellites as this is the most common case – for 'left looking' SAR sensors the commands for shadow and layover have to be changed), (c) the coordinates of the four footprint corners and (d) a DEM covering the footprint and a buffer of at least 20 km (this buffer is not mandatory, as the simulation also works using smaller DEMs).

Using an ArcGIS® model, the coordinates of all footprint corner points are calculated. As mentioned in section 4.1.2.1, the DEM has to rotated so its pixels are oriented parallel and its columns orthogonal to the range direction of the satellite. The rotation angle ε is calculated by equation 21 (Fig. 8).

$$\varepsilon = \arctan\left(\frac{y_2 - y_1}{x_2 - x_1}\right) \quad (21)$$

The footprint length l is another important parameter (Eq. 22).

$$l = \sqrt{(x_2 - x_1)^2 + (y_2 - y_1)^2} \quad (22)$$

Both parameters ε and l can automatically be determined by using the developed VBA tool 'Calculate Angle and Length of Footprint' (see appendix 2).

For the calculation of the optimal moving distance Δx (section 4.1.2.1) two procedures are developed. The first one is an ArcGIS® model that creates a 20 km buffer zone around the site and cuts the DEM to this area. By subtracting the minimum height value from the maximum one within this area the parameter Δh, the maximum difference of height, is calculated. The succeeding calculation and optimization of Δx is done fully automatically in a Python script (appendix 3).

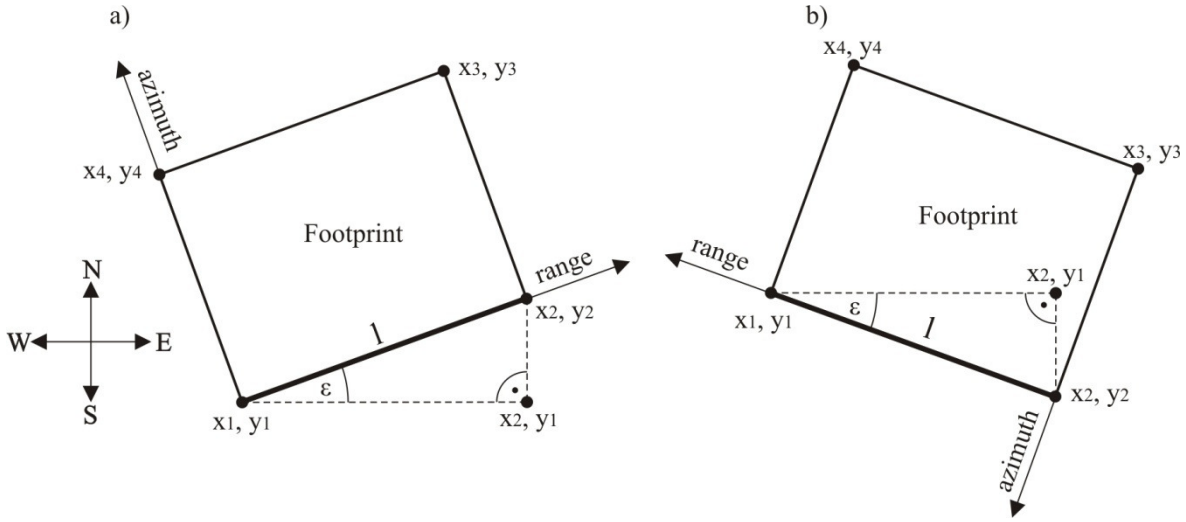

Fig. 8: Calculation of the rotation angle ε and footprint length l. a) ascending, b) descending pass.

b) ArcGIS® model for layover and shadow simulation

Two ArcGIS® models for the layover-shadow-simulation were developed. The first one is to be used for DEMs larger than the buffer zone of the optimal moving distance Δx around the outline of the footprint, whereas the second one is intended for smaller DEMs. Such smaller DEMs need to be synthetically enlarged before they can be used in the simulation, as the later *viewshed-operation* requires the observer points to be located inside the DEM (see chapter 4.1.2.1). Following parameters are required as input data:

- The DEM and its cell size z
- The footprint area as polygon shapefile
- The rotation angle ε (cf. Eq. 21): positive for an ascending pass and negative for a descending pass. The signs are the other way round for later backward rotation.
- The coordinates of the pivot point (lower left footprint corner, determined by the aforementioned ArcGIS® model).
- The resampling technique: For the continuous data of the DEM 'bilinear' interpolation should be used for the rotation (ARCGIS DESKTOP HELP 9.3 2009). For the backward rotation the resampling technique 'nearest' is best suited, as the result of the layover-shadow-simulation is discontinuous data (single values).
- The optimal moving distance (cf. Eqs. 19 & 20)
- The incidence angle at near range and at far range
- The x-coordinate of the Pivot-Point
- The length of the footprint l (cf. Eq. 22)
- Input pass: choose '1' for an ascending pass and '2' for a descending pass
- For moving the observers:
  Layover observer: for an ascending pass the optimal moving distance Δx has to be added to the x-coordinate of the pivot point. For a descending pass Δx has to be subtracted from the pivot point's x-coordinate. The parameters for ascending and descending pass are the other way round for shadow observers.

Next, the functionality of the model for the layover-shadow simulation of larger areas is described. In the first step, a 20 km *buffer* zone around the footprint polygon is created and the DEM is cut by 'extract by mask' to this buffer zone. Then, a further *buffer* of 1 km around the

footprint is generated and the DEM again is cut to this buffer zone (Footprint-Buff-DEM 1 km) to avoid any boundary effects in the later *viewshed-operation*. As DEM pixels have to be oriented parallel and the columns orthogonal to the range direction of the satellite, both fitted DEMs are *rotated* by the angle ε. Then, all cell values of the 'Footprint-Buff-DEM' (1 km) are transformed to integer values, which is necessary for the succeeding conversion of the raster to a polygon. Using the *extent* of the created 'DEM Footprint Polygon' a *Constant Raster* (all cell values = 0) is generated and converted to a polygon to get a north-south / east-west orientated polygon rectangle ('Extent Polygon Rotated Footprint').

Then, the outlines of the polygon are created by *Polygon to Line* and split into four single lines by *Split at Vertices*. After that, the field *BufferDist* is added to the attribute table of these lines (*Add Field*) and calculated (*Calculate Field*) based on the FID (feature identification number) of each line (appendix 4). The north and south edge of the rectangle get the value 100 m and the east and the west edge get the value of the previously determined Δx. Based on these values a *buffer* (with the attributes *side type*: left, dissolve type: all and end type: flat) is generated. The value '100 m' for the north and south edge is necessary to avoid GIS-technical bugs, occurring when the difference of the east-west and north-south values is too large. Next, this buffer and the previously created 'Extent Polygon Rotated Footprint' are merged (*Union*) and united to one raster (*Dissolve* with dissolve fields: ID_1) to get the mask of the test region.

Using this mask the previously rotated raster 'Testregion 20km' is cut (*Extract by Mask*) to achieve the test region DEM. In the next step, using *Raster to Points* to each pixel of the test region DEM one observer point is added and then cut to the area of the previously rotated 'DEM Footprint Polygon' (*Clip*) to get only observer points of the area of the rotated footprint and a small buffer of 1 km (to avoid any boundary effects in the later *viewshed-operation*). Then, the field SPOT (observer base height) is added to the attribute table of the observer points (a detailed description of SPOT can be found below, 4.1.2.2 c)) by *Add Field*. Each observer point gets the elevation value of its pixel by setting SPOT equal to the *Grid-code* of the DEM. The later *viewshed-operation* can only successfully be applied, if the base height of each observer has the same value as the elevation of the pixel it is observing. Afterwards, the observer points are *copied* to get one observer for shadow simulation and one for layover simulation for each pixel.

Then, the x and y coordinates of each observer are calculated. Another field for the footprint length l (see 4.1.2.2 a) is added and calculated. In the next step, the incidence angle θ at near range and at far range, the x-coordinate of the pivot point and the type of orbit (ascending/descending) are added to the attribute table of the observer points (*Add field*, *Calculate field*). To consider the variation of the incidence angle from near to far range, the individual incidence angle for each observer is calculated by a VBA-code (appendix 5).

Then, the optimal moving distance Δx and the raster cell size z of the DEM are added to the attribute table. After that, the height of the observers (OFFSETA), the vertical (VERT1 & 2) and the horizontal (AZIMUTH1 & 2) visual field are calculated for each single layover and shadow observer (appendix 6). The change of the incidence angle from near range to far range is considered by the individual heights of the observers depending on their x-coordinate (in range direction). The theory of this calculation is described below (see 4.1.2.2 d).

Then, the new x-coordinates of the observer points are calculated: the optimal moving distance Δx is added to the original x-coordinate in the case of a layover observer in an ascending pass and in the case of a shadow observer in a descending pass, whereas Δx is subtracted from the original x-coordinate in the case of a layover observer in a descending pass and in the case of a shadow observer in an ascending pass. Next, *Make XY Event Layer* is used to create a new layer at the changed xy-positions of the observer points. Thus the shadow observers are moved to the SAR and the layover observers are moved away from the SAR by the amount of Δx. After that, the moved observer points are copied (*Copy Feature Class*) to create applicable shapefiles (observer points) for the following *viewshed-operation*. The procedure described in this paragraph is executed twice: first for the layover observers and then for the shadow observers.

The next step in the layover-shadow-simulation is the visibility testing, which is applied twice: for the layover observers and for the shadow observers. Then, both computed 'viewshed-rasters' are *rotated* back to the original orientation of the footprint and are *reclassified* to correct rotation effects and to classify layover and shadow areas. Afterwards, both raster files are combined to one raster (*Mosaic*), which is then cut to the area of the footprint. Additionally, this raster is converted to a polygon (shapefile).

Next, the description of model for layover-shadow-simulation of smaller areas:

As in the case of the second model the DEM is smaller than the test region, some additional work has to be done in comparison to the first model: The first step is the creation of a 20 km buffer zone around the outline of the footprint polygon. Then, a *Constant Raster* is created using the same *Extent* as the buffer generated before and setting the cell size equal to the one of the used DEM. Afterwards, this *Constant Raster* is added to the DEM (*Plus*) with the *Extent* set equal to the sum of both (*Union of Inputs*). Then, this raster is *reclassified* setting 'NoData' to zero, afterwards rotated according to the first model and then transformed to integer values, which is necessary for the following conversion of the raster to a polygon. The remaining steps of the second model are equal to the first model.

c) Description of the SPOT attribute

As mentioned in the model description (4.1.2.2. b), the elevation value of each pixel is added as base height to the observer monitoring the pixel. This is necessary to avoid errors in the succeeding visibility test, which is based on a simple triangular relationship for the calculation of the observer height OFFSETA (see 4.1.2.2. d). The nadir[6]of the observer (A) and the observed pixel (B) have to be at the same elevation value to guarantee a correct observer height calculation. As shown in figure 9, if A and B are located at different elevation values, the wrong pixel is observed. This problem can be solved by adding the base height SPOT of the observer points to the height of the observer (OFFSETA).

[6] The nadir is the position on the ground with the shortest distance to the satellite (Fig. 3).

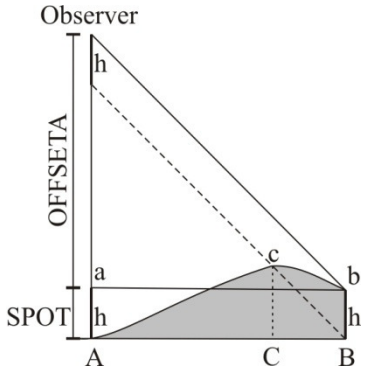

Fig. 9: **The base height of the observed pixel (= SPOT) has to be added to the height of the observer OFFSETA to ensure that the observer monitors the right pixel (B). If the SPOT is not added the wrong pixel is observed (C).**

d) The theory of the observer attributes calculation

In this section the calculation of the observer attributes height above base height SPOT (OFFSETA), the horizontal (AZIMUTH1 & AZIMUTH2) and the vertical visual field (VERT1 & VERT2) are described (cf. also appendix 6). These attributes guarantee that an observer only looks at its dedicated pixel.

The horizontal visual field AZIMUTH1 and AZIMUTH2

AZIMUTH1 is the beginning and AZIMUTH2 the end of the observer's horizontal visual field (Fig. 10). The horizontal visual field is equal to AZIMUTH2 minus AZIMUTH1. The calculation of AZIMUTH1 and …2 depends on the raster cell size z and the optimal moving distance Δx (Eq. 19) with $\Delta x_{S\ (Shadow)} = \Delta x_{L\ (Layover)}$ (Eq. 23 & 24)

Ascending pass, shadow:

$$AZIMUTH1_{Shadow,\ Asc} = 90° - \arctan\left(\frac{z}{2\Delta x}\right) \quad (23)$$

$$AZIMUTH2_{Shadow,\ Asc} = 90° + \arctan\left(\frac{z}{2\Delta x}\right) \quad (24)$$

The horizontal visual field for a layover observer is rotated by 180°:

$$AZIMUTH1_{Layover,\ Asc} = 180° + AZIMUTH1_{Shadow,\ Asc} \quad (25)$$

$$AZIMUTH2_{Layover,\ Asc} = 180° + AZIMUTH2_{Shadow,\ Asc} \quad (26)$$

In the case of a descending pass the positions of the layover and the shadow observers are changed. Then, the equations 23 and 24 are valid for a layover observer and the equations 25 and 26 for a shadow observer (descending).

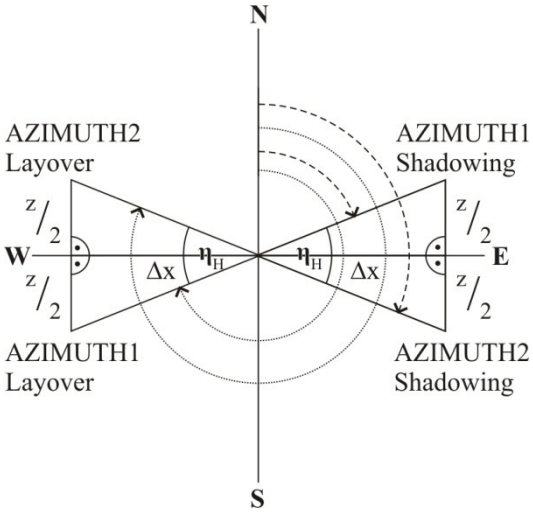

Fig. 10: **The horizontal visual field η_H of the observer (located in the center of the figure) is determined by the attributes AZIMUTH1 & 2 and is a function of optimal moving distance Δx and the cell size z.**

The observer's height (above base height) OFFSETA

The height of the observer points depends on the optimal moving distance Δx and the incidence angle θ. The figures 11a and b show the geometry for a shadow-observer and layover-observer, respectively. The equations 27 (shadow) and 28 (layover with observer looking angle $\xi = 90° - \theta$) are valid for both ascending and descending orbit.

$$OFFSETA_{Shadow} = \frac{\Delta x}{\tan\theta} \quad (27)$$

$$OFFSETA_{Layover} = \Delta x \tan\theta \quad (28)$$

The vertical visual field VERT1 and VERT2

Also the vertical visual field parameters, VERT1 and VERT2, are independent of the orbit. The figures 11a and b show the geometry for a shadow-observer and layover-observer, respectively. VERT1 represents the upper and VERT2 the lower limit of the vertical visual field. With (Eqs. 29 & 30)

$$VERT1_{Shadow} = 90° - \Omega_{1S} \quad (29)$$

$$VERT2_{Shadow} = 90° - \Omega_{2S} \quad (30)$$

and (Eqs. 31 & 32)

$$\tan\Omega_{1S} = \frac{\Delta x + \frac{z}{2}}{H_S} \quad (31)$$

$$\tan\Omega_{2S} = \frac{\Delta x - \frac{z}{2}}{H_S} \quad (32)$$

and using equation 27 it follows (with H_S = OFFSETA; multiplied by -1 because of the downward looking of the SAR; Eq. 33 & 34)

$$VERT1_{Shadow} = (-1)\left[90° - \arctan\left(\frac{\left(\Delta x + \frac{z}{2}\right)\tan\theta}{\Delta x}\right)\right] \quad (33)$$

$$VERT2_{Shadow} = (-1)\left[90° - \arctan\left(\frac{\left(\Delta x - \frac{z}{2}\right)\tan\theta}{\Delta x}\right)\right] \quad (34)$$

The equations 35 to 38 show the calculation for a layover observer. With $VERT1_{Layover} = \Omega_{1L}$ and $VERT2_{Layover} = \Omega_{2L}$ and therefore

$$\tan\Omega_{1L} = \frac{H_L}{\Delta x + \frac{z}{2}} \quad (35)$$

$$\tan\Omega_{2L} = \frac{H_L}{\Delta x - \frac{z}{2}} \quad (36)$$

and $H_L = OFFSETA_{Layover}$ (see Eq. 28) it follows (again '-1' because of the downward looking of the SAR)

$$VERT1_{Layover} = (-1)\left[\arctan\left(\frac{\Delta x \tan\theta}{\Delta x + \frac{z}{2}}\right)\right] \quad (37)$$

$$VERT2_{Layover} = (-1)\left[\arctan\left(\frac{\Delta x \tan\theta}{\Delta x - \frac{z}{2}}\right)\right] \quad (38)$$

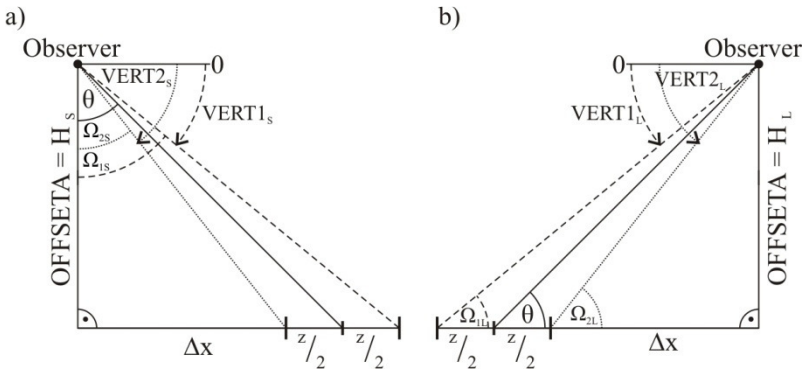

Fig. 11: The observer's height OFFSETA and vertical visual field determined by the attributes VERT1 & 2 are a function of the Δx and z. a) shadow observer, b) layover observer.

4.1.3 Layover & Shadow simulation results and validation

4.1.3.1 Simulation based on a C-band SRTM DEM

The validation of the previously described layover-shadow-simulation was carried out on data from the Sudelfeld site (cf. chapter 2 c) based on an 80 m SRTM DEM and afterwards compared with a real SAR image of TerraSAR-X (Fig. 12). As this image was recorded at a very steep incidence angle (ca. 25.8°), very strong layover, but no shadow occurs. As the site was acquired from an ascending pass and in right-looking mode, the illumination of the site is from west to east, causing strong layover areas on steep west facing slopes leaning towards the SAR sensor. The D-InSAR technique cannot be used for monitoring landslides in 8 % of the footprint area because of layover coverage.

Beside the enhanced ellipsoid corrected (geocoded) High-Resolution SpotLight Mode SAR image of TerraSAR-X, also the 'Geocoded Incidence Angle Mask' (GIM) was provided by the German Aerospace Center (DLR) (RAGGAM & GUTJAHR 2005). The GIM shows the layover calculated by DLR (processed layover), which is also the result of a model that is based on a DEM and several imaging parameters (e.g. incidence angle). The GIM was calculated by a DEM mosaic of a SRTM C-band DEM (spatial resolution: 3 arc seconds, which is ca. 62 m at the latitude of the Sudelfeld site) covering the northern part of the site and a SRTM X-band DEM (1 arc second; ca. 21 m spatial resolution at the site) covering the southern area.

Figure 12 shows a generally good match of the simulated and the processed layover. However, a closer look reveals that the simulated layover has a much rougher shape than the processed one. Moreover, not all areas of the processed layover are covered by the simulation. For the entire footprint area ca. 58 % of the processed layover area is detected by the simulation. This relatively low value and the aforementioned effects are caused by the lower spatial resolution of the DEM (80 m) used for the layover simulation in comparison to the DEM (ca. 21 m (SRTM X-band), respectively, ca. 62 m (SRTM C-band)) used for the processed layover (GIM) calculation. Setting the processed layover as a reference, the simulation shows an overestimation of ca. 17 %.

When restricting the validation area to the part of the site, where the C-band SRTM data was used for the calculation of the processed layover, it could be recognized that the detection rate of the simulation slightly increased to ca. 59 % of the processed layover. The value of overestimation is reduced to ca. 12 % for this case. At the X-band SRTM DEM area (south) of the site, the simulation detected only ca. 52 % of the processed layover and the overestimation increased to about 46 %. The detection rate of the simulation is much lower at the southern part than at the northern part of the site, as the difference of the spatial resolution of the DEM used for the simulation (80 m) and the DEMs used for the calculation of the processed layover is much higher at the southern part (X-band SRTM DEM, ca. 21 m) than at the northern part of the site (C-band SRTM DEM, ca. 62 m). The detection rate for the entire site (see above) is very close to the one of the C-band SRTM DEM area, as the majority (ca. 83 %) of the processed layover is located within this part of the site.

But, in spite of the low spatial resolution and the following low detection rate, the layover-shadow-simulation provides useable results for analysis on a regional scale. All main parts of the processed layover are correctly recognized at the simulation. The user can get an overview

of the anticipated layover-shadow-coverage of a SAR image for an entire footprint area. As the simulation can be executed at very low cost prior to radar recording – the underlying SRTM data is freely available (e.g. at the CGIAR Consortium for Spatial Information: http://srtm.csi.cgiar.org) – it has a great advantage in comparison to the processed layover provided by DLR, which is only available after ordering a geocoded SAR image.

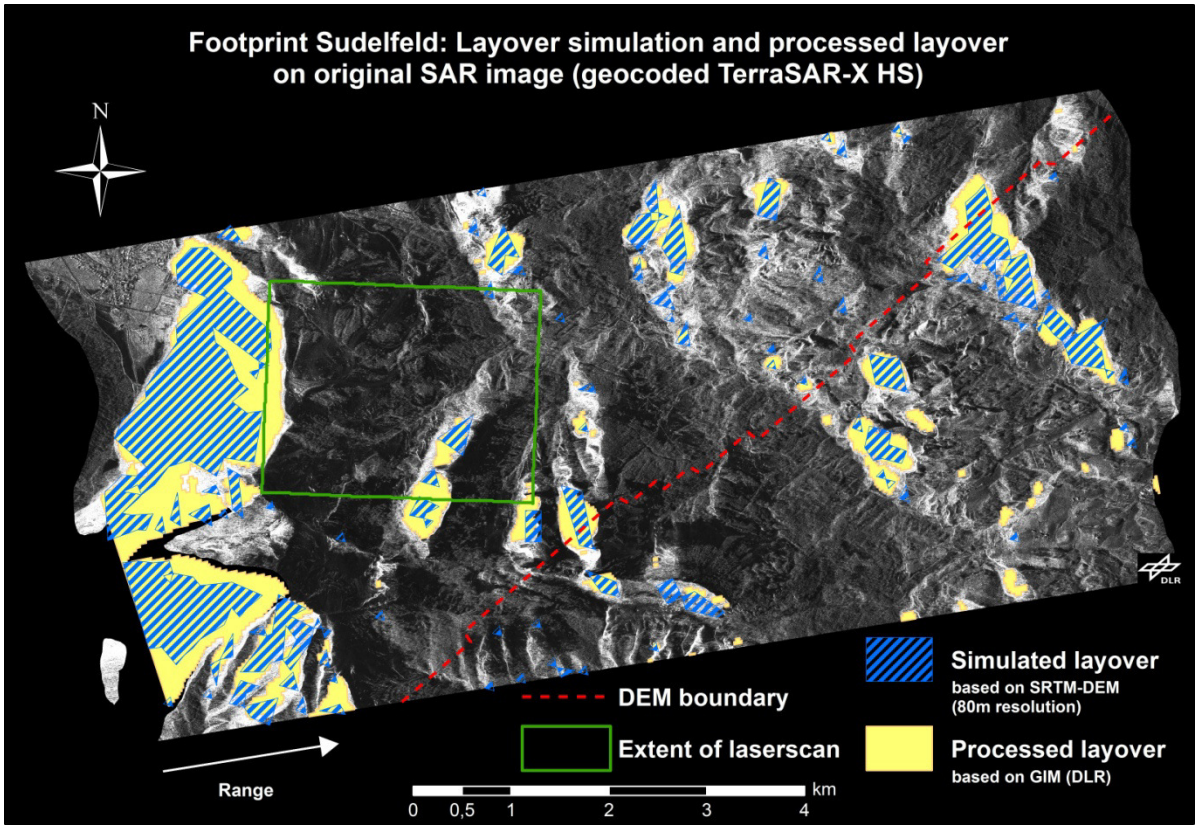

Fig. 12: **Layover simulation of footprint Sudelfeld based on an 80 m DEM. By comparing the simulated (blue) and the processed layover (yellow) one can recognize a generally good match. The red line marks the boundary of the DEMs used by DLR for the calculation of the processed layover: At the left part a C-band SRTM DEM (ca. 62 m spatial resolution) and on the right part an X-band SRTM DEM (ca. 21 m spatial resolution) was used. The TerraSAR-X data was provided by DLR (modified after PLANK et al. 2012).**

4.1.3.2 Simulation based on a high resolution laserscan DEM

Figure 13 shows the result of the layover-shadow-simulation of a part of the above mentioned footprint based on a 10 m spatial resolution laserscan DEM and compares it with the processed layover (GIM). Considering the entire area of the laserscan DEM, the simulation detected only ca. 55 % of the processed layover. However, as explained below in detail, strong differences between the laserscan DEM used for the simulation and the DEM used for the processed layover calculation by DLR could be determined.

At the southeastern part of the scene these differences are relatively low. At this area of the site a very good conformity of the simulated and the processed layover can be recognized: The simulation detected ca. 88 % of the processed layover. But in the east section of the image small dispersed areas of the simulated layover occur, which are not covered by processed layover. This is due to the distinctly higher spatial resolution of the DEM used for the simulation (10 m laserscan) in comparison to the DEM (C-band SRTM, ca. 62 m in the area of the

laserscan) used for the processed layover calculation by DLR. Due to the higher spatial resolution of the laserscan DEM, the results of the simulation are more detailed and closer to reality than the processed layover, which is also the result of a model and not absolutely the 'real' layover.

The west edge of the image shows a big mismatch between the simulation and the processed layover, which is caused by differences of both DEMs (laserscan DEM used for layover-shadow-simulation and the DEM used by DLR for the geocoding of the SAR image and the calculation of the processed layover). Comparing the laserscan DEM and the geocoded SAR image it was determined that the mountain ridge at the west side of the image (Fig. 13) is located at different positions in both DEMs. In the SAR image this mountain ridge is further to the east than in the laserscan DEM, causing a further eastward extent of the processed layover in comparison to the simulation. Due to the higher positioning accuracy of the laserscan in comparison to that of the SRTM DEM used by DLR, the simulated layover is closer to reality than the processed one.

Besides the aforementioned simulation based on the 10 m laserscan DEM, an additional simulation was also carried out by reducing the laserscan's spatial resolution to 62 m. In this way it was possible to compare the results of the simulation and the processed layover using DEMs of about the same spatial resolution. The simulation based on the 62 m laserscan DEM only detected the layover area in the southeastern part of the site. This is due to the aforementioned differences of the laserscan DEM and the DEM used by DLR for the calculation of the processed layover – especially at the west side of the site. At the southeastern part of the laserscan area ca. 78 % of the processed layover are detected by the simulation. However, as both DEMs (laserscan DEM and DEM used by DLR) are not completely identical (as mentioned above), the values of the validation (percentage of processed layover detected by the simulated one) are generally reduced. The simulation would show slightly higher values for the detection rate at completely identical DEMs for the processed and simulated layover.

A big advantage of the layover-shadow-simulation is that each type of DEM (even high spatial resolution laserscan DEMs) that is available for the site can easily be used in the simulation procedure. Contrary to this, the processed layover is based on SRTM DEMs of lower spatial resolution.

As laserscan data is only available in some regions and mostly quite costly, this high quality data is best used in single case studies. In general one can conclude: the higher the spatial resolution of the DEM used, the more detailed is the result of the simulation.

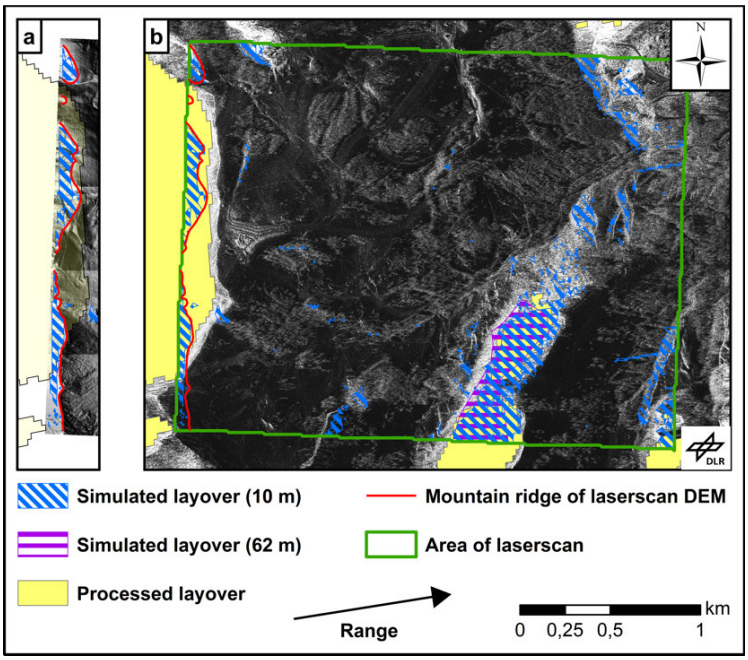

Fig. 13: **Layover simulations based on a 10 m and 62 m laserscan DEM, respectively (part of the footprint Sudelfeld, see Fig. 12). The comparison of the simulated layover (10 m blue; 62 m magenta) and the processed layover (yellow) show a very good match. The mismatch of the processed layover and the simulated layover on the left side is caused by the different position of the mountain ridge at the laserscan DEM (a) and at the SRTM DEM used for the processed layover calculation and the geocoding of the radar image by DLR (b). The TerraSAR-X data was provided by DLR (modified after PLANK et al. 2012).**

4.1.3.3 Application of the simulation for topic 2

The layover-shadow-simulation described in chapter 4.1.2 was also applied to a subset of the western Aosta Valley site (cf. chapter 2 f) based on a C-band SRTM DEM. Figure 14 shows the CORINE 2006 land cover (cf. chapter 5.1.1) and the geocoded DS&PS-targets of this site. Due to the steep incidence angle (ca. 33.68°) layover areas are the most dominant distortion, only small areas are affected by shadow. The simulation matches very well with the PS (&DS) processing, as the areas affected by layover or shadow contain almost no PS (&DS). The results of this simulation were used to exclude the areas affected by layover and shadowing from the calculations of the PS-estimation procedures based on land cover data (cf. chapter 5.1.3) and NDVI (cf. chapter 5.2.3).

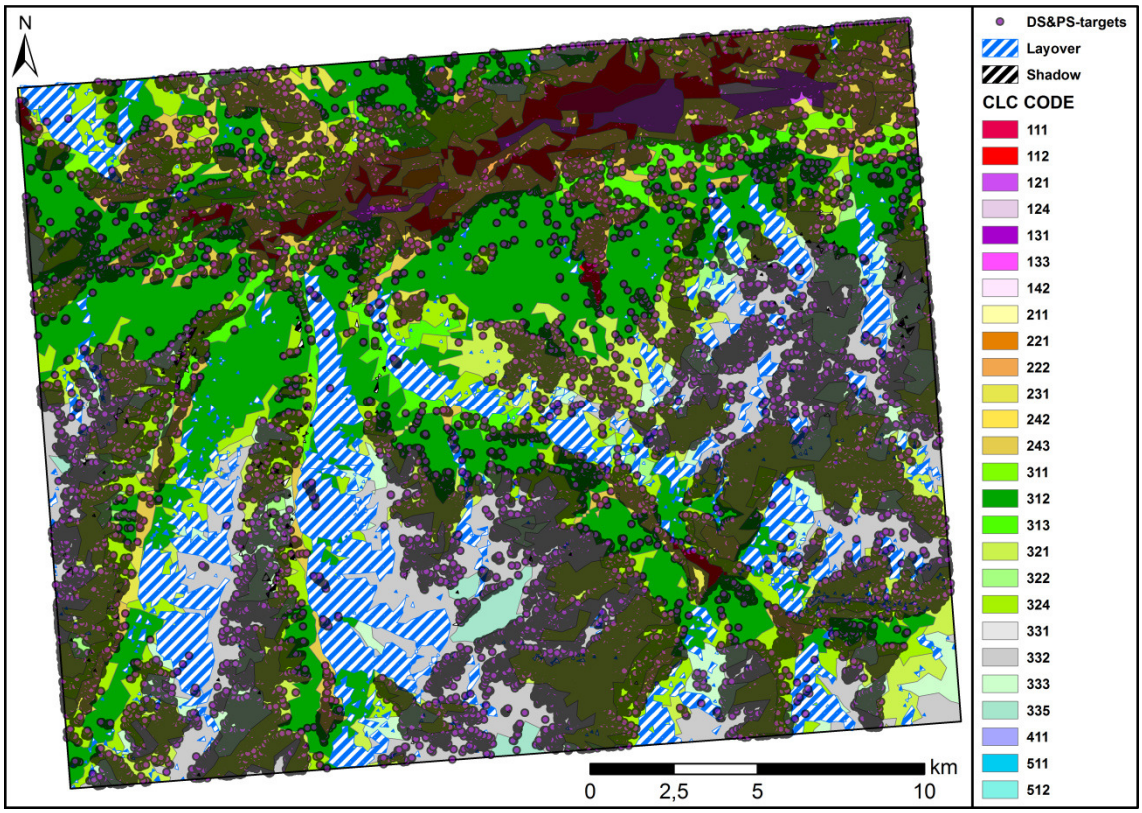

Fig. 14: **The layover-shadow-simulation of part of the western Aosta Valley site shows a very good conformity with the DS&PS-distribution within the site, as there are almost no DS&PS-targets in the area of predicted layover and shadowing. The CORINE CLC code is explained in figure 29.**

4.2 Measurable percentage of movement

4.2.1 Theory of measurable percentage of movement

This chapter describes the measurable percentage of movement, defined as the percentage of total movement of a potential landslide that can be detected from the satellite by the means of D-InSAR. The satellite is only able to measure movements occurring in its line-of-sight direction (CROSETTO et al. 2010). If the landslide's motion direction is parallel to the satellite line-of-sight, the measurable percentage of movement is 100 % of the real movement on the ground, whereas if the landslide's motion direction is parallel to the azimuth direction (flight pass of the satellite) this measurable percentage is reduced to 0 % (METTERNICHT et al. 2005).

As the basic simplifying assumption of the developed model is that a landslide moves down slope along the steepest gradient of the slope, this model is best suited for planar slides, translational slides and very slow flowing mass movements (e.g. avalanches and rock glaciers).

Rotational slides show a different behavior characterized by a high subsidence rate at the slide's head area, which is underestimated when calculating the measurable percentage of the vertical component of the movement when using a model of the terrain surface (DEM). At regional scale this limitation of the method is acceptable, but for local studies a more critical usage of the method is required. For such detailed examinations it is also possible to get correct estimations of the vertical component of the movement for rotational slides without changing the algorithm described below. In the case of availability of an approximation of the landslide's sliding surface one can use a model of the sliding surface instead of the DEM for the measurable percentage of the landslide's movement calculation. In this way the high subsidence rate at the slide's head area (at rotational slides) is considered by a steep gradient of the sliding surface at this area. Estimation of the depth and the shape of the sliding surface requires a geological model of the landslide, based on geological and geophysical investigations, such as seismic, geoelectric, etc.

The landslide type 'spreading' is characterized by a lateral movement in nearly flat terrain (BRUNSDEN et al. 1996). Therefore, the measurable percentage of movement of this landslide type is relatively low, especially at steep incidence angles.

Here, the percentage of a possible movement on the ground that can be detected by means of D-InSAR is calculated for given imaging parameters – prior to radar recording of the area of interest (PLANK 2009). The measurable percentage of movement depends on the satellite's orbit and incidence angle θ. Using this model one is able to choose the optimal orbit and incidence angle for monitoring a certain landslide. This model can also be applied to determine the optimal positions for corner reflectors in order to maximize the detectable percentage of the landslide's movement. These reflectors enable highly accurate deformation measurements (FROESE et al. 2008).

The calculations described below are executed in each raster cell of the DEM within the area of the footprint by a fully automated GIS-procedure (ArcGIS®). The measurable percentage of the horizontal and the vertical components of movement are separately calculated and afterwards multiplied.

The horizontal component of the measurable percentage of movement h depends on the satellite's orbit (ascending pass or descending pass); more precisely on the cosine of the angle β

(angle between range (satellite line-of-sight) and the slope's dip direction α (Fig. 15)). The angle β is a function of the slope's dip direction α and the angle ε (angle between the E-W-axis and range.

$$h_{Ascending} = |\cos\beta| \cdot 100\,\% = |\cos(90° - \alpha - \varepsilon)| \cdot 100\,\% \quad (39)$$

$$h_{Descending} = |\cos\beta| \cdot 100\,\% = |\cos(90° - \alpha + \varepsilon)| \cdot 100\,\% \quad (40)$$

From the equation 39 (ascending) & 40 (descending) it follows that the satellite is able to detect 100 % of the real movement on the ground, if the slope's dip direction is equal to the range. An increase of β leads to a decrease of h. For slopes with dip direction α parallel to azimuth direction, β is equal to 90° and the h is reduced to 0 %. Consequently, movements occurring in that direction cannot be monitored by D-InSAR (METTERNICHT et al. 2005).

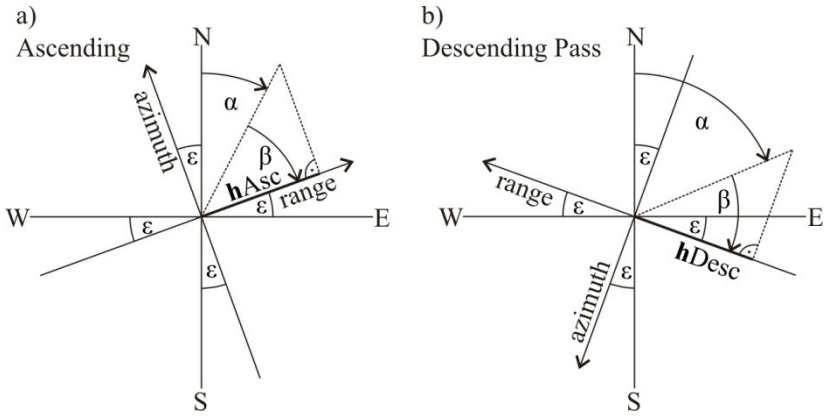

Fig. 15: The satellite is only able to measure movements in its line-of-sight (range). The measurable percentage of the horizontal component of the movement *h* depends on *α* (the slope's dip direction) and *ε* (the angle between the E-W-axis and range). a) ascending pass; b) descending pass (modified after PLANK et al. 2012).

The vertical part of the measurable percentage of movement is a function of the incidence angle θ and the reduced dip of the slope δ (slope angle in satellite line-of-sight direction). Here, slopes that are averse to the satellite and slopes oriented towards the SAR sensor have to be distinguished.

δ depends on the cosine of the angle β (cf. measurable percentage of the horizontal component of the movement) and on the real dip of slope ω (Eq. 41).

$$\delta = \arctan[\tan\omega \cos\beta] \quad (41)$$

In figure 16*a* the imaging geometry for slopes that are averse to the SAR sensor is shown. v_{averse} represents the measurable percentage of the vertical component of the movement, r the actual movement on the ground and ρ_1 the difference of the angle ψ (= 90° – θ) and δ.

$$v_{averse} = \cos\rho_1 \cdot 100\,\% = \cos(\psi - \delta) \cdot 100\,\% = \cos(90° - \theta - \delta) \cdot 100\,\% \quad (42)$$

According to equation (42) v_{averse} reaches its maximum value if 90° minus θ is almost equal to δ. However, it is not possible to detect completely 100 % of the total movement on the ground (e.g. a landslide), because if ψ is equal to δ shadowing already occurres. v_{averse} decreases with increasing ρ_1.

Figure 16b shows the imaging geometry for slopes oriented towards the radar sensor with ρ_2 being the sum of δ and ψ.

$$v_{towards} = \cos\rho_2 \cdot 100\,\% = \cos(\psi + \delta) \cdot 100\,\% = \cos(90° - \theta + \delta) \cdot 100\,\% \quad (43)$$

The measurable percentage of the vertical component of movement for slopes oriented towards the radar sensor ($v_{towards}$) is reduced to 0 % (no movement detection is possible), if the satellite's view is directly perpendicular to the slope surface ($\rho_2 = 90°$) (Eq. 43).

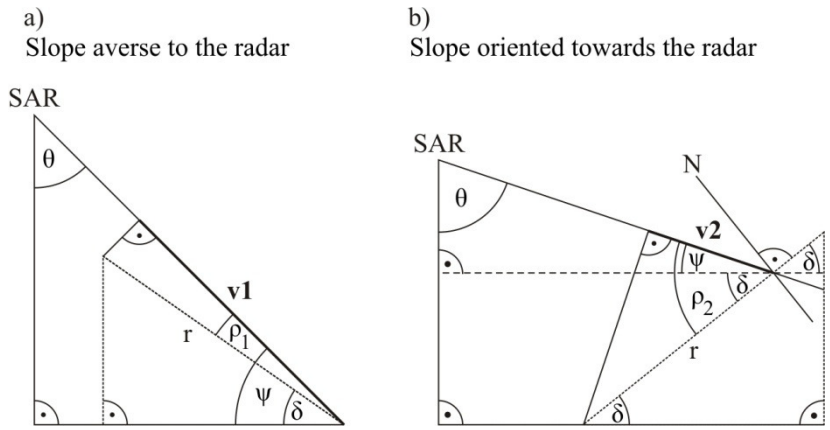

Fig. 16: The measurable percentage of the vertical component of movement v_{averse} (= *v1*) respectively $v_{towards}$ (= *v2*) depends on the reduced dip of slope δ (based on the satellites range direction) and the incidence angle θ. *r* is the total movement on the ground (e.g. a landslide). a) slope averse to the satellite; b) slope oriented towards the satellite (modified after PLANK et al. 2012).

By the multiplication of the horizontal component *h* and the vertical component *v* the three dimensional measurable percentage of movement m_{3D} is calculated (Eq. 44).

$$m_{3D} = hv \quad (44)$$

with: $h = h_{Ascending}$ resp. $h = h_{Descending}$ and $v = v_{averse}$ resp. $v = v_{towards}$

Both components *h* and *v* can achieve values from 0 % to 100 %. Therefore, the method described above, ensures that if one part of movement is zero, automatically the entire measurable percentage of movement (3D) becomes zero.

For flat areas the measurable percentage of movement is not calculated in this model. These areas are marked by a special signature.

When calculating the measurable percentage of movement it is also very important to consider the expected velocity of the landslide. According to METTERNICHT et al. (2005) and COLESANTI & WASOWSKI (2006), the displacement gradient between neighboring pixels of a SAR image has to be less than half the radar wavelength λ. Therefore, D-InSAR applications are limited to 'extremely slow' and 'very slow' landslides referring to the landslide velocity scale of CRUDEN & VARNES (1996). The maximum detectable displacement velocity for X- and C-band sensors is a few centimeters per month, e.g. 1.55 cm within 11 days (repeat cycle) or 2.8 cm within 35 days for TerraSAR-X (X-band: λ = 3.1 cm) or ENVISAT ASAR (C-band: λ = 5.6 cm), respectively. L-band sensors can monitor displacement velocities up to a decimeter per month (e.g. ALOS PALSAR λ = 23.6 cm, 46 days repeat cycle; Tab. 3).

Landslides characterized by velocities greater than one meter per year can for example be measured by image correlation techniques (e.g. normalized cross-correlation described by DEBELLA-GILO & KÄÄB 2011). A possibility for faster landslides up to 'slow' and 'moderate' (max. meters per day) might be ground-based (GB) D-InSAR (METTERNICHT et al. 2005, CORSINI et al. 2006).

Tab. 3: SAR satellites and maximum detectable displacement

Satellite, Sensor	Band	Wavelength [cm]	Repeat cycle [days]	Max. detectable displacement [cm] per month (30 days)
ERS-1, Active Microwave	C	5.6	35	2.4
ERS-2, Active Microwave	C	5.6	35	2.4
ENVISAT, ASAR	C	5.6	35	2.4
Radarsat-1, SAR	C	5.6	24	3.5
Radarsat-2, SAR	C	5.6	24	3.5
JERS-1, SAR	L	23.5	44	8.0
ALOS, PALSAR	L	23.6	46	7.7
TerraSAR-X, TSX-1	X	3.1	11	4.2

Source: ITC database of satellites and sensors (http://www.itc.nl/research/products/sensordb/AllSatellites.aspx).

4.2.2 Implementation in GIS

The model theoretically described in the previous chapter was implemented in the ArcGIS® model builder by creating one model for ascending pass and another one for descending. The calculation is done separately for each pixel inside the footprint. The description is valid for an ascending pass. The differences for a descending pass are written in [brackets].

The input parameters of both models are as follows

- A DEM of the footprint area

- The rotation angle ε (cf. Eq. 21)

- The center incidence angle θ

The final results of the model are the determination of flat areas ($\omega = 0°$) and the calculation of the three dimensional measurable percentage of movement.

First, the dip direction of the slope (*aspect*) is calculated for each DEM raster cell (pixel) within the footprint area. With *Greater Than Equal* (0) all non-flat areas are determined ($\omega \neq 0°$) and *reclassified* ('0' becomes 'NoData', '0-1' becomes '1' and 'NoData' remains 'NoData'). Then, *Aspect* is cut by the just reclassified raster (*Extract By Mask*) to get the *Aspect* of all non-flat areas.

Then, 90 *minus* the *aspect-value* is calculated for each pixel of the DEM. After that, the value of the ε is *subtracted* [*added*] from [to] the result of the previous calculation. Then, the *cosine* of the just calculated difference [sum] is computed. As ArcGIS® calculates with radiant, a *Single Output Map Algebra* containing the function cos(Delta div (180/pi)) was used to convert radiant to degrees. The modulus of this cosine is achieved by calculating its square (*Square*) and then the 2nd root (*Square Root*). The result of these calculations is *h*.

Next, all flat areas are determined (by *Equal* (-1) of *Aspect*) and *reclassified* ('0' becomes 'NoData', '0-1' becomes '1' and 'NoData' remains 'NoData').

Then, ω (*Slope*) is determined and its *tangent* is calculated. As this calculation has to be done in degrees, a *Single Output Map Algebra* (tan(Slope div (180/pi))) is executed. By *multiplying* the tangent of ω by *h*, determined above, one gets the tangent of δ, which is then transformed to δ by 'ATan' (= arctangent) and the multiplication by (=180/π).

The next step, distinguishes between slopes leaning towards the SAR sensor and slopes that are averse to it. First, the *Aspect* of the non-flat areas is *multiplied* by '0' ('Aspect 0') to get a raster with the same *extent* and raster cell size as the raster file *Aspect*. Then, to each raster cell the value '180' is *added*. Next, the value of ε is *subtracted* from [*added* to] each of these pixels. By *LessThanEqual* [*GreaterThanEqual*] all non-flat areas fulfilling the property 'Aspect $\leq (180 - \varepsilon)$' ['Aspect $\geq (180 - \varepsilon)$'] are detected.

In the next step, to each pixel of 'Aspect 0' the value '360' is *added* to achieve a raster file with the same *extent* as the raster file *Aspect* containing the value '360' in each pixel. Then, the value of ε is *subtracted* from this raster file. By *GreaterThanEqual* one gets all areas with 'Aspect $\geq (360 - \varepsilon)$' [For descending all areas with the property 'Aspect $\leq \varepsilon$' are identified by *LessThanEqual*]. Then, the areas 'Aspect $\leq (180 - \varepsilon)$' ['Aspect $\geq (180 - \varepsilon)$'] and the just determined areas 'Aspect $\geq (360 - \varepsilon)$' ['Aspect $\leq \varepsilon$'] are *added* up. As a result one gets a raster file*, covering all slopes that are averse to the SAR sensor. This raster file is *reclassified* ('0' becomes 'NoData', '0-1' becomes '1' and 'NoData' remains 'NoData') to receive a *mask*** of those slopes.

To detect all slopes leaning towards the satellite***, the raster file* is *reclassified* ('0' becomes '1', '0-1' becomes 'NoData' and 'NoData' remains 'NoData').

To receive the value of δ of slopes that are averse to the satellite, the raster file of δ is cut by the mask** (*Extract By Mask*). Then, the raster file δ is cut by the mask*** (*Extract By Mask*) to get δ of the slopes leaning towards the radar sensor.

To calculate v_{averse} the corresponding pixels of δ are *multiplied* by '-1', then the value '90' is *added* to each pixel and finally the value of θ is *subtracted*. Next, the *cosine* of the previous result is calculated using the *Single Output Map Algebra* cos(Sigma1 div (180/pi)). $v_{towards}$ is determined by *adding* the value '90' to the corresponding pixels of δ and subtracting θ. Afterwards, the *cosine* of the result above is calculated (in degree). Then, both raster files v_{averse} and $v_{towards}$ are united to one raster by *Mosaic* to get the value of v for the entire footprint area. The final step is the *multiplication* of the raster files h and v to achieve m_{3D}.

The results of the measurable percentage of movement calculation are shown in chapter 4.4.

4.3 The influence of land cover on D-InSAR

4.3.1 Decorrelation

For useable results of D-InSAR applications interferograms with high coherence are necessary. Coherence is a measure of correlation and describes the preservation of the phase in an interferogram generated by two SAR images (LÖFFLER et al. 2005:233). The range of values is from 0 to 1. Coherence can be used to test the quality of an interferogram, e.g. for DEM generation or displacement mapping, as low coherence (decorrelation) corresponds to noisy interferograms, which often makes phase unwrapping very difficult. To receive a meaningful interferogram, the coherence has to be as high as possible.

There are several types of decorrelation: (a) thermal decorrelation, caused by uncorrelated noise inside the radar sensor itself (LU 2007); (b) missregistration decorrelation, due to inaccurate registration of the two SAR images (FRANCESCHETTI & LANARI 1999); (c) spatial decorrelation, which occurs for too large baselines (when $B\perp \geq B_{critical}$, cf. Eq. 12) (ZEBKER & VILLANSENOR 1992); (d) Doppler centroid decorrelation, similar to spatial decorrelation, is caused by too large differences of the squint angle between both radar acquisition. This effect (d) can be avoided by a proper antenna steering (FRANCESCHETTI & LANARI 1999). (e) The interaction of the radar waves with the atmosphere can cause artefacts in the interferogram, as different water vapor contents at both acquisition times of the SAR images change the refraction index and cause different duration of the emitted microwave (GUPTA 2003:383).

(f) Temporal decorrelation is caused by changes on the ground in the time between the radar acquisition dates (GUPTA 2003, COLESANTI & WASOWSKI 2006). For instance, the Earth's surface changes by frost and dew cycles, snow and ice cover or melting, respectively. Areas that are bare of vegetation such as built-up areas and rocks have high coherence values (FRUNEAU et al. 1996, METTERNICHT et al. 2005, LU 2007), whereas areas covered by vegetation, especially forests (ZEBKER & VILLASENOR 1992, BAMLER & HARTL 1998, STROZZI et al. 2000), have low coherence values, e.g. due to plant growth and wind (WEGMÜLLER & WERNER 1995, CHEN, Y. et al. 2002, ROSIN & HERVÁS 2005, ROTT & NAGLER 2006, THIEL et al. 2009, AHMED et al. 2011, CARTUS et al. 2011). Therefore, coherence is strongly influenced by the land cover of the footprint area. This influence also depends on the properties of the radar sensor, especially the wavelength (BAMLER & HARTL 1998, BARBIERI & LICHTENEGGER 2005, BOVENGA et al. 2006). ZEBKER & VILLANSENOR (1992) developed a model for the temporal coherence $\Upsilon_{\Delta t}$ as a function of the wavelength λ for an independent Gaussian displacement of scatterers in a volume (e.g. a tree; Eq. 45).

$$\Upsilon_{\Delta t} = exp\left[-8\left(\frac{\pi}{\lambda}\right)^2\left(\sigma_y^2(\sin\theta)^2 + \sigma_z^2(\cos\theta)^2\right)\right] \quad (45)$$

With σ_y, σ_z representing the standard deviations of the movements in horizontal (y) and vertical (z) direction, respectively. $\Upsilon_{\Delta t}$ is independent of θ for σ_y equal σ_z as the term $(\sin\theta)^2 + (\cos\theta)^2 = 1$. Figure 17 shows $\Upsilon_{\Delta t}$ as a function of the displacement according to equation 45 for X, C and L-band. As reasonable interferogram quality requires coherence values $\Upsilon_{\Delta t} \geq 0.3$, only SAR sensors working with longer wavelengths, such as L-band, are suited for D-InSAR applications in densely vegetated areas. At shorter wavelengths (e.g. X and C-band) coherence decreases very fast with small movements (e.g. branches and leaves).

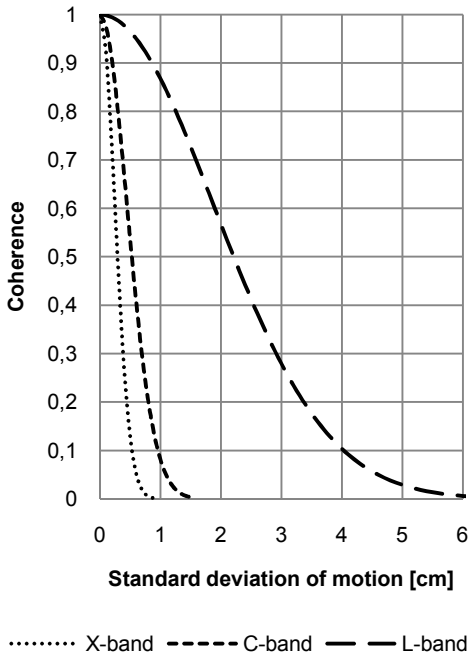

Fig. 17: Temporal coherence $\gamma_{\Delta t}$ as a function of the displacement for X-band (λ = 3.1 cm), C-band (λ = 5.6 cm) and L-band (λ = 23.6 cm) (Calculated using equation 45; modified after ZEBKER & VILLANSENOR 1992).

4.3.2 Classification of land cover regarding its influence on D-InSAR applications

As temporal decorrelation due to the site's land cover has a very high influence on the applicability of D-InSAR, an according classification of the main types of land cover was developed to get a quick and easy overview of this applicability. This thesis presents a further development of groundwork done in PLANK (2009). The classification accounts for the operational wavelength of the radar sensor and ranges in value from 1 (very suitable) to 6 (not at all suitable for D-InSAR applications) (Tab. 4). This classification can be applied to all land cover datasets that are available for the area of interest. In this work the CORINE Land Cover 2006 data is used (cf. chapter 5.1.1 for detailed description and appendix 7).

Tab. 4: Classification of the main types of land cover regarding the applicability of D-InSAR (from '1' = 'very well suitable' to '6' = 'not at all suitable')

Category	X-band (λ = 3.1 cm)	C-band (λ = 5.6 cm)	L-band (λ = 23.6 cm)
Continuous urban area	1	1	1
Discontinuous urban area and infrastructural work	1	1	2
Rocks	2	1	1
Alluvium	3	2	2
Pastures	4	3	2
Forest	6	5	3
Farmland	6	6	6
Water surfaces	6	6	6
Fast changing areas	6	6	6
Glaciers and perpetual snow	6	6	6

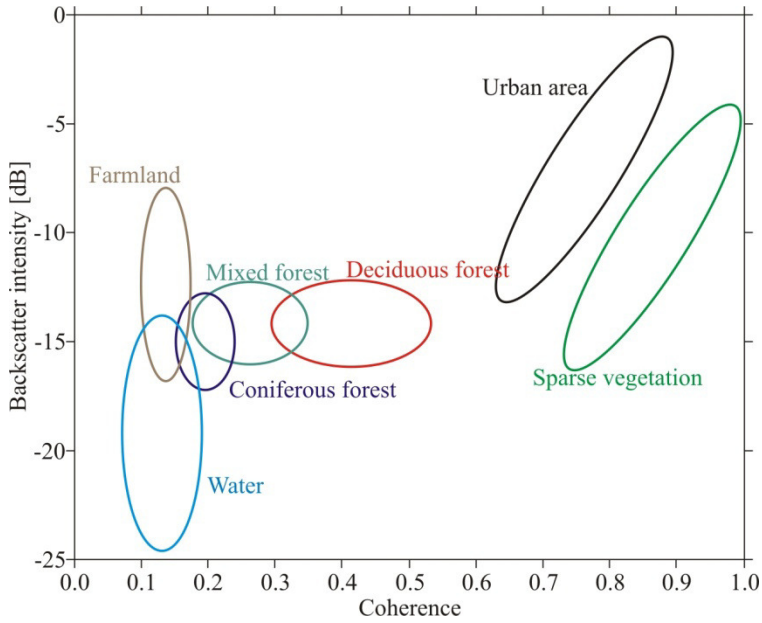

Fig. 18: Variation of the backscattering intensity as a function of the coherence for different land cover types (modified after BORGEAUD & WEGMÜLLER 1997).

a) Urban area and infrastructural work

According to STROZZI et al. (2000) and HANSSEN (2005), urban area, especially continuous urban area, has very high coherence values in all three X-, C- and L-band (e.g. for C-band: coherence values from 0.7 to 0.9, Fig. 18). Therefore, this land cover type is classified as 'very good applicability' of D-InSAR (value '1') in table 4. The single buildings of discontinuous urban area can very good be identified by X- and C-band sensors, due to their higher spatial resolution (value '1'). Whereas the lower spatial resolution L-band sensors are not as good as suited for monitoring single buildings (DAITO et al. 2004). Consequently, L-band is classified by the value '2'.

b) Rocks

According to FRUNEAU et al. (1996) and LU (2007), areas of bare rocks and rocks covered by short grass show sufficiently high coherence values for more than three years at C-band. As L-band is not influenced by low vegetation, the coherence values are even higher (ZEBKER & VILLANSENOR 1992). Consequently, this land cover class is classified by the value '1' in both wavelengths. As even low vegetation has a big influence on the coherence value in X-band, it is classified as '2' (Fig. 17).

c) Alluvium

Areas covered by debris, gravel or sand show a sufficiently high coherence value for a few months (at C-band; LU 2007). The land cover class gets the values '2' (C- and L-band) and '3' (X-band), as this time period is significantly shorter than the one for rocks. In X-band even smaller changes on the ground, such as rearrangement and reshaping of the surface structure caused by water or wind, decrease the coherence (Fig. 17).

d) Pastures

Meadows and pastures are classified with '3' in table 4, as radar waves in C-band are partially already scattered at leaves BAMLER & HARTL (1998). At the short-wave X-band this scattering effect is even stronger. Therefore, this land cover class is classified as '4' in X-band. The considerably longer wavelength of L-band penetrates even tall grass without any influences and is

only scattered at the substratum of the grass. The classification value would be '1' for rocky substratum, but as alluvium is more common, the value '2' is chosen (see above).

e) Forest

Forest areas are characterized by low coherence values (Fig. 18), caused by fast change of the geometrical configuration of the scatterers, especially movement due to wind (ZEBKER & VILLASENOR 1992, WEGMÜLLER &WERNER 1995, STROZZI et al. 2000, AHMED et al. 2011). Moreover, also growth of the vegetation and change of the soil moisture cause decorrelation (THIEL et al. 2009). Figure 18 shows higher coherence values for deciduous forest in comparison to coniferous forest, while mixed forest is in the middle of both. This difference is only valid in winter, as deciduous trees lose their leaves in autumn and are therefore less susceptible to wind in the cold season. The tree trunks and bare branches of deciduous forest are more stable scatterers. In summer both deciduous and coniferous forests have low coherence values, especially due to wind (BORGEAUD & WEGMÜLLER 1997). In X-band the coherence of forest is very low (value '6' in classification), as the short-wave X-band radar waves are already backscattered at the top canopy, which is very unstable due to wind (BAMLER & HARTL 1998; Figs. 17 and 19). Due to the slightly longer wavelength of C-band, there is mainly a volume scattering inside the canopy at the branches and leaves. As only an inferior part of the radar waves penetrates the treetop (Fig. 19), forest is classified as '5' in C-band. The long-wave L-band penetrates the canopy almost without being influenced by it (Fig. 19). Only the tree trunks and larger branches act as scatterers (BAMLER & HARTL 1998). As these are much less influenced by wind in comparison to leaves and smaller branches (scatterer sources for X- and C-band), L-band has a much higher coherence in forest areas and is therefore classified as '3' in table 4.

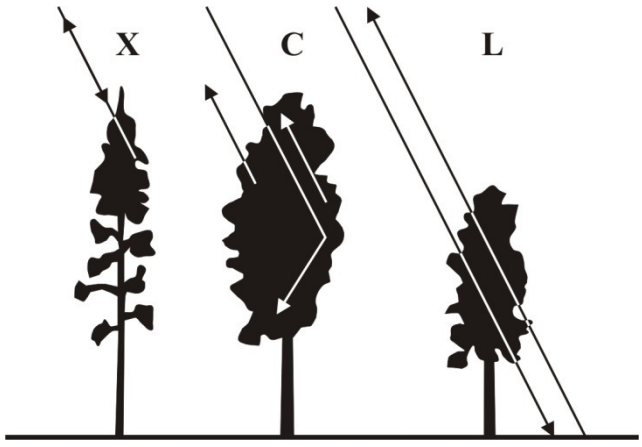

Fig. 19: Behavior of the radar waves as a function of the wavelength when interacting with vegetation (forest). At X-band the short-wave radar waves are already backscattered at the top of the canopy. At the slightly longer C-band there is mainly a volume scattering inside the canopy. Only longer wavelength such as the L-band can penetrate dense vegetation. Such long-wave radar pulses are only backscattered at the ground and at tree trunks (modified after BARBIERI & LICHTENEGGER 2005:4.3).

f) Farmland

Agricultural land show relatively high coherence values – as long as there are no changes on the ground (BORGEAUD & WEGMÜLLER 1997, METTERNICHT et al. 2005). This is mainly valid for winter. However, as already mentioned, accumulation and melting of snow and ice cause completely decorrelation within a few days (LU 2007). In summer there are great changes in the surface conditions on farmland due to cultivation (ploughing, harvesting, etc.) and plant

growth, causing low coherence values (WEGMÜLLER & WERNER 1995). Consequently, this land cover class is classified as '6' (in all bands).

g) Water surfaces

Calm water surfaces are always incoherent, as the radar pulse emitted by the SAR sensor is mirrored away from the satellite and no phase signal is received (LÖFFLER et al. 2005:233). Although turbulent water surfaces scatter the radar signal back to the satellite, completely decorrelation occurs, as their surface changes within tens of milliseconds due to wind (BAMLER & HARTL 1998, STROZZI et al. 2000). Therefore, D-InSAR cannot be applied at water surfaces (value '6' in the classification).

h) Fast changing areas

Due to the great changes in their backscattering properties in the time between two radar image recordings (up to several months for monitoring landslides), areas such as construction sites, dump sites and mineral extraction sites, etc. receive the value '6' (complete decorrelation).

i) Glaciers and perpetual snow

Glaciers and areas with perpetual snow show complete decorrelation within a few days, because of the movement of glaciers, but above all the accumulation, transfer and melting of snow and ice (LU 2007). Thus these areas are assigned the value '6' in all bands in the classification. For short time periods of a few days glacier movements can be monitored by conventional D-InSAR. However, the classification of table 4 was developed for slow moving landslides, where a monitoring period of several months is required.

The advantage of an L-band sensor is its applicability even in densely vegetated areas. However, its spatial resolution is much lower than that of an X- or C-band sensor (DAITO et al. 2004).

4.3.3 Application of the land cover classification regarding its influence on D-InSAR

As mentioned above, the developed land cover classification of table 4 was applied on the CORINE 2006 land cover data (see appendix 7). Three maps showing the D-InSAR applicability for X-, C- and L-band sensors based on land cover were developed for entire Europe – the coverage of the CORINE land cover data (Figs. 20a to 20d). The applicability of D-InSAR increases with increasing wavelength, especially for the long-wave L-band. The figures 21 to 24 show a zoom in on the figures 20a to 20d for the area of the footprint Sudelfeld. The green marked urban areas show the best applicability of D-InSAR. At the yellow colored areas (meadows and pastures) D-InSAR is relatively well suited. As large areas of the footprint are covered with forest, at the X and C-band classification wide regions are marked red ('6') and orange ('5'), respectively, representing a worse applicability of D-InSAR. These areas can only be monitored by long-wave SAR sensors, such as L-band ('3').

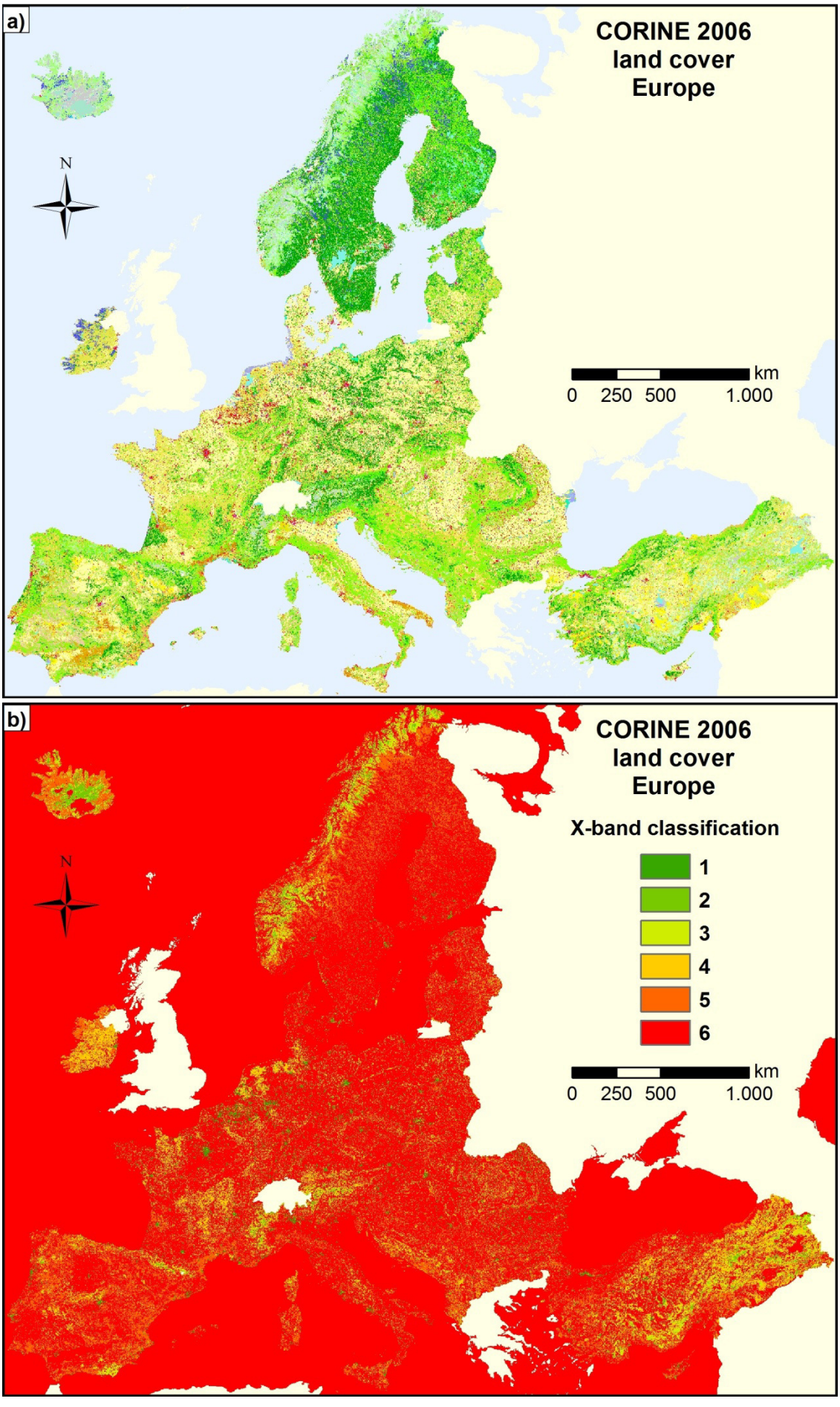
a)
CORINE 2006
land cover
Europe
N
km
0 250 500 1.000
b)
CORINE 2006
land cover
Europe
X-band classification
1
2
3
4
5
6
N
km
0 250 500 1.000

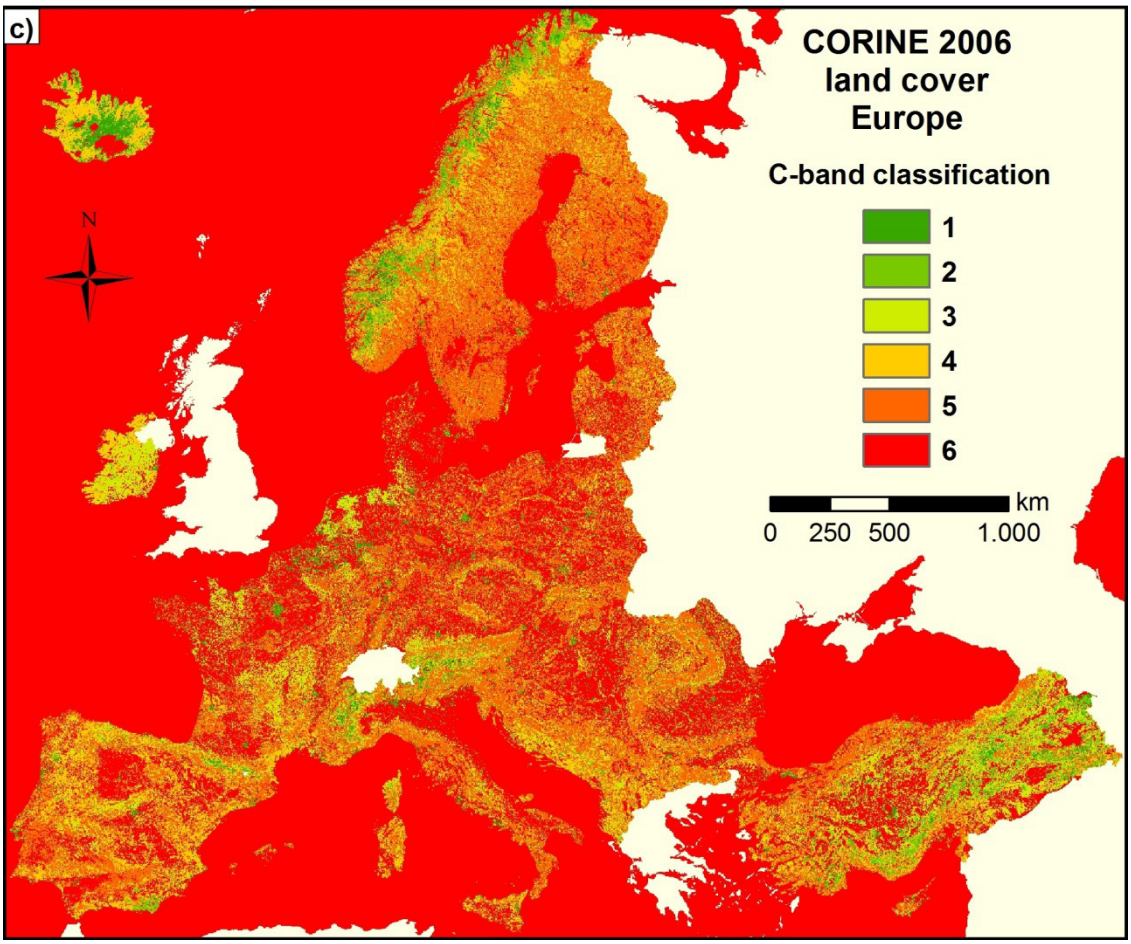
c)
CORINE 2006
land cover
Europe
C-band classification
1
2
3
4
5
6
N
km
0 250 500 1.000

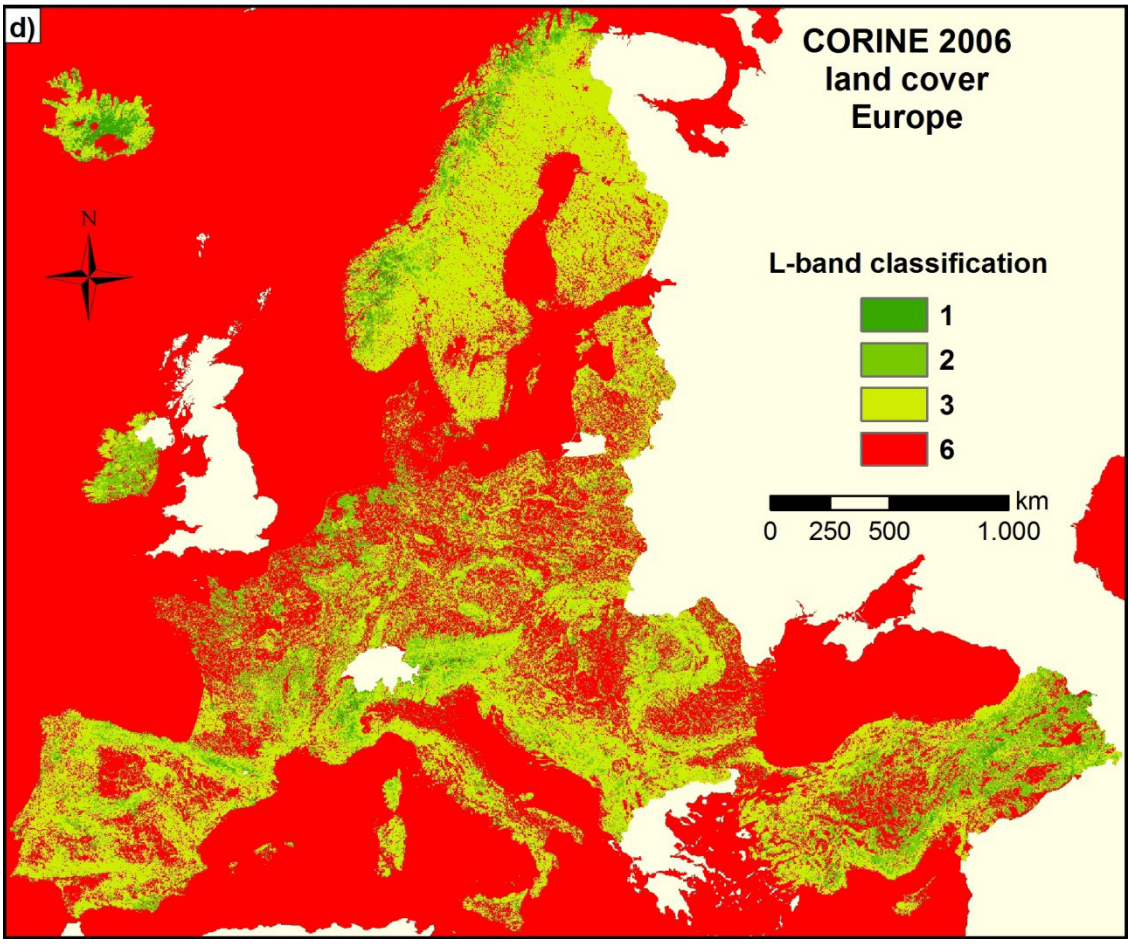
d)
CORINE 2006
land cover
Europe
L-band classification
1
2
3
6
N
km
0 250 500 1.000

Fig. 20: **CORINE 2006 land cover of Europe (a) and its classification for D-InSAR applicability using X-band (b), C-band (c) and L-band (d).**

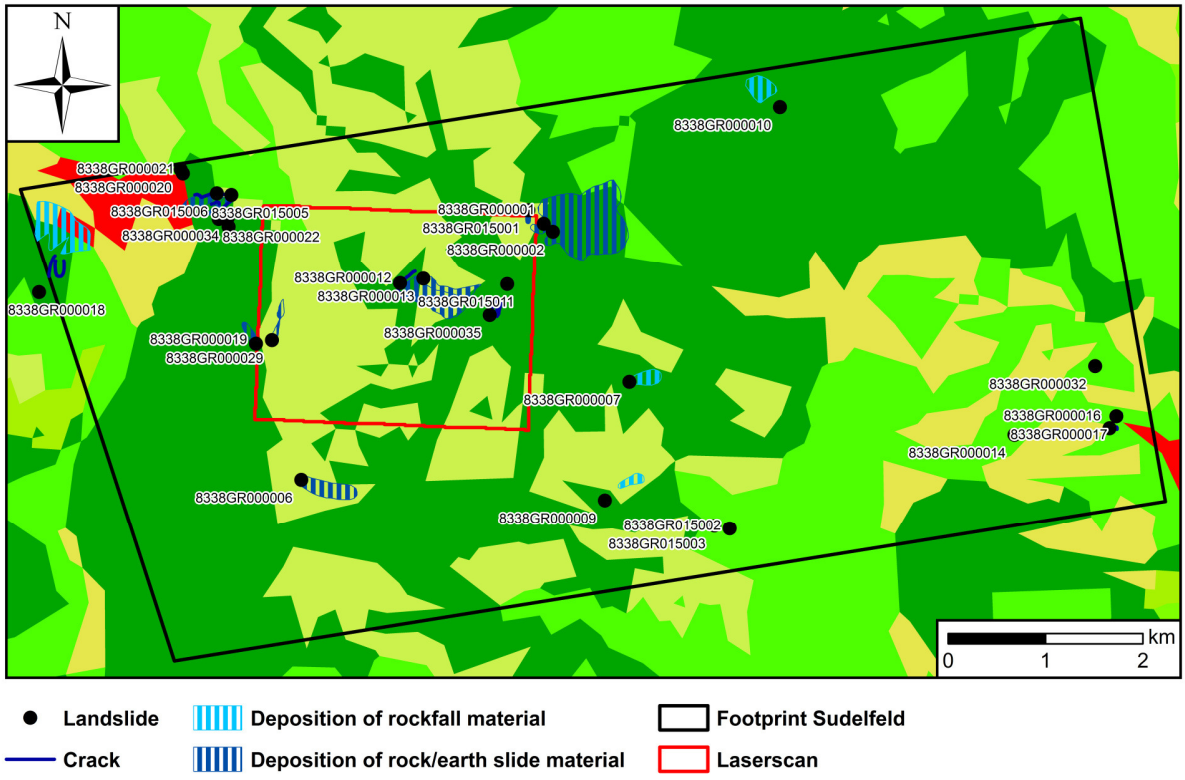

Fig. 21: **CORINE 2006 land cover Sudelfeld site (part of Fig. 20a).**

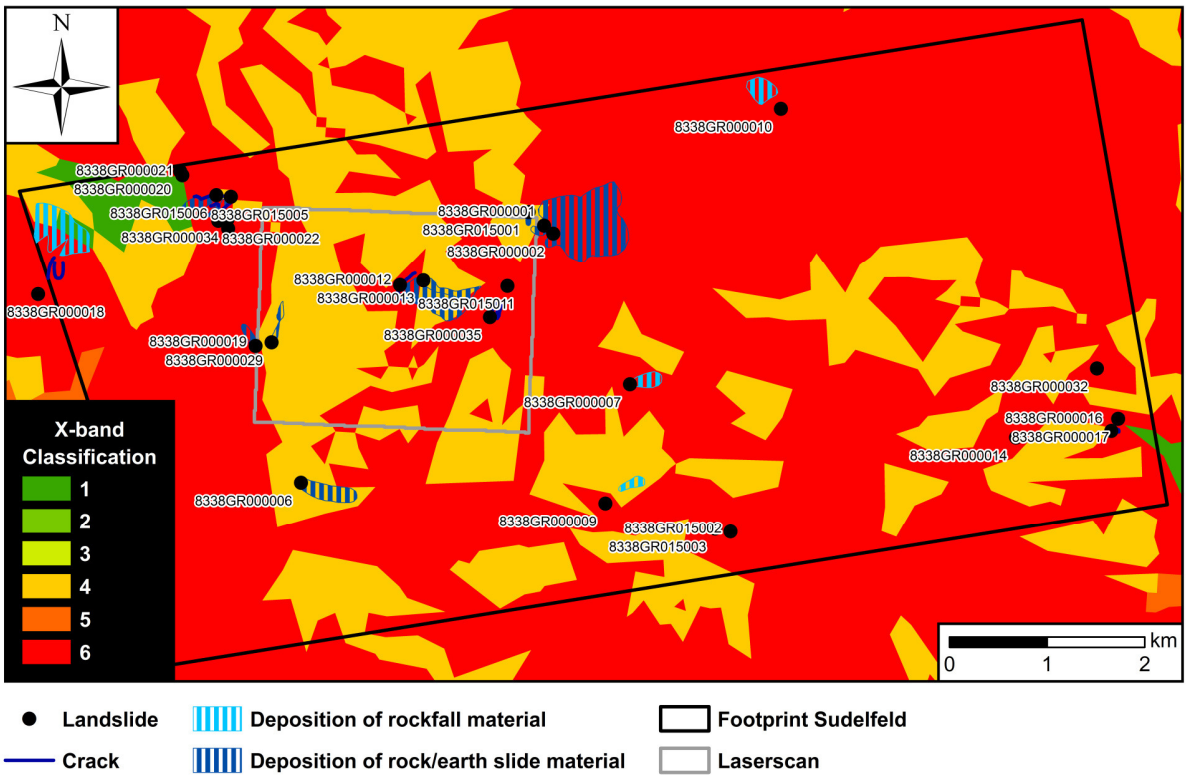

Fig. 22: **CORINE 2006 land cover of Sudelfeld site classified for D-InSAR applicability using X-band (part of Fig. 20b).**

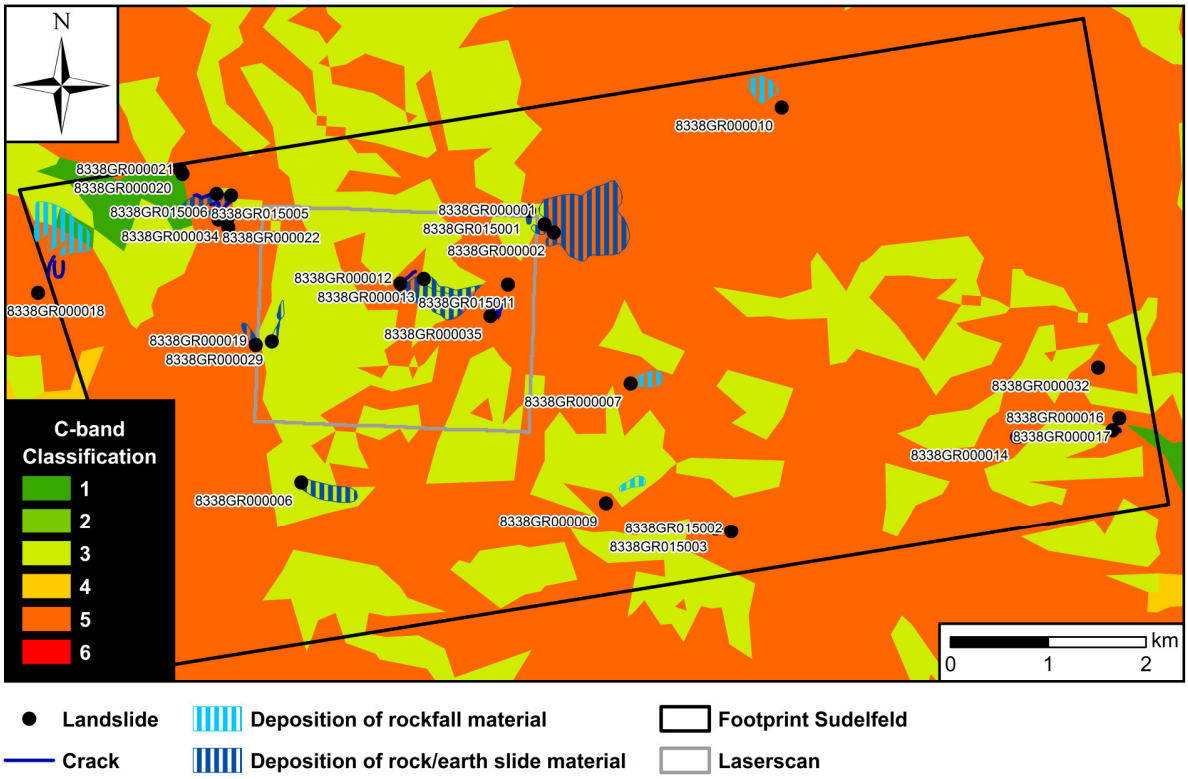

Fig. 23: **CORINE 2006 land cover of Sudelfeld site classified for D-InSAR applicability using C-band (part of Fig. 20c).**

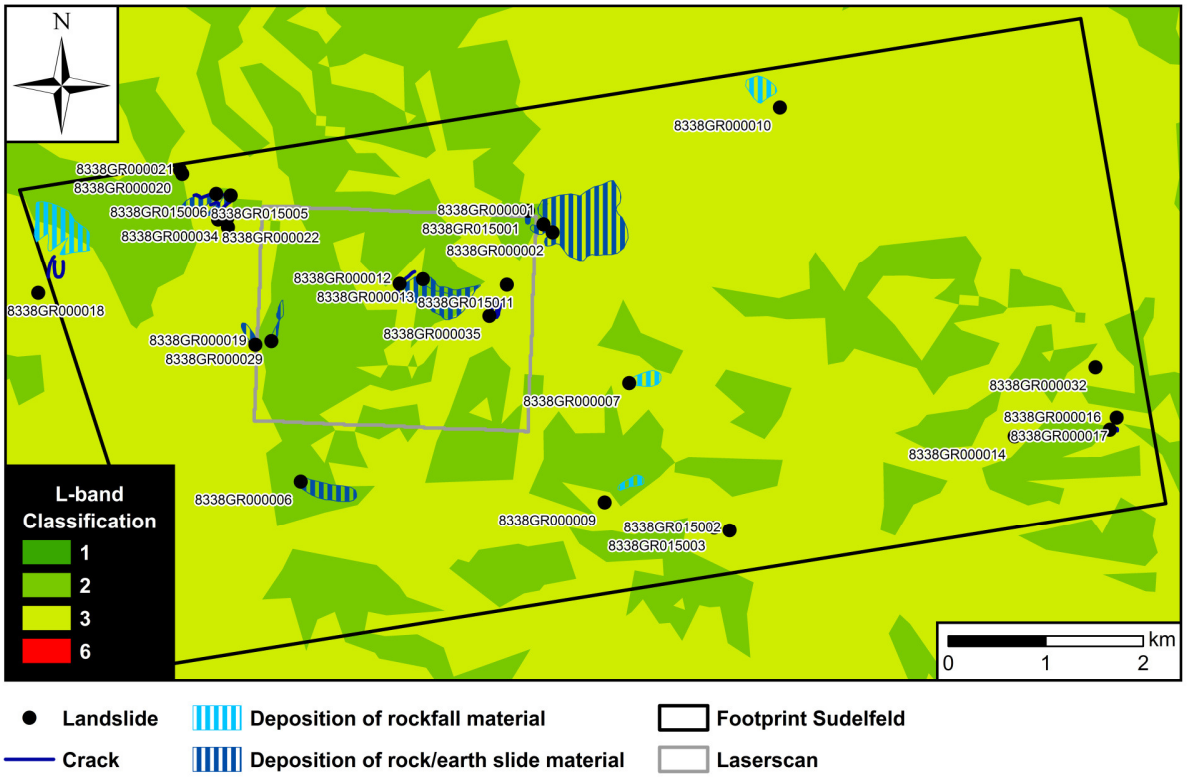

Fig. 24: **CORINE 2006 land cover of Sudelfeld site classified for D-InSAR applicability using L-band (part of Fig. 20d).**

4.4 Conclusion of the first topic

To answer the first key question of this dissertation – 'Can D-InSAR be applied for monitoring a certain landslide?' (cf. chapter 1.2), the final step of the analysis of the first topic, is the combination of the results of the layover-shadow-simulation (chapter 4.1), the calculation of the measurable percentage of movement (chapter 4.2) and the classification of the land cover regarding its influence on the applicability of D-InSAR (chapter 4.3). This combination enables to evaluate the applicability of D-InSAR for each single landslide within the area of a footprint prior to radar recording.

The developed procedures were applied at the Sudelfeld site and validated with real SAR data of TerraSAR-X. When using an 80 m spatial resolution DEM for the layover-shadow-simulation, the comparison with the processed layover / shadow (based on a DEM mosaic of 21 and 62 m spatial resolution, respectively) showed a generally good match. Although only about 58 % of the processed layover / shadow area were detected by the simulation, it provides useable results on regional scale, as all main parts of the processed layover / shadow areas are correctly recognized. Further investigations showed that the simulation detected about 78 % of the processed layover / shadow, when using a DEM of the same spatial resolution at the simulation as was used for the processed layover / shadow calculation. However, as both DEMs (the DEM used for the simulation and the one used for processed layover / shadow calculation) are not completely identical (Fig. 13), the values of the validation are slightly reduced.

The simulation based on a high resolution laserscan DEM (10 m spatial resolution) detected about 88 % of the processed layover / shadow. However, due to the very high spatial resolution of the laserscan DEM, the hereon based simulation showed even more details than the processed layover / shadow. Besides the aforementioned mismatches of the DEMs, it is important to notice that the processed layover / shadow are also the result of a model and not absolutely the 'real' layover / shadow. Depending of the spatial resolution of the DEM used, the simulation shows even better results (more details and closer to reality) than the processed layover / shadow.

The figures 25 & 26 show the combination of the layover-shadow-simulation and the calculation of the measurable percentage of movement for the Sudelfeld site including the landslides of the Bavarian georisk database (http://www.bis.bayern.de/bis). Table 5 shows the results of the analysis for these landslides and gives objective rating (from '1' = very well suitable, to '6' = unsuitable) of the anticipated applicability of the D-InSAR technique for landslide monitoring purposes.

The value '1' is for landslides that can be monitored by all three bands (X-, C- and L-band). An example for this value is the Aggenalm landslide (ID '…00012', cf. also Figs. 13 & 26), which is mainly covered by natural grassland. For the chosen imaging parameters, this landslide achieves a very high measurable percentage of movement (ca. 94 %) and is not affected by layover or shadowing. Therefore, D-InSAR can very well be used for monitoring the Aggenalm landslide.

The value '2' represents landslides, where SAR sensors working with C- and L-band can be applied, due to slightly denser vegetation. At landslides covered by high vegetation (e.g. for-

est) only long-wave sensors (e.g. L-band) enable successful D-InSAR applications (value '3'). For instance, the landslide ID '…00001' (Tab. 5) is covered with dense forest and can only be monitored by an L-band sensor. The values '4' (e.g. landslide ID '…15005', Tab. 5) and '5' (landslide ID '…00022') represent partly or full coverage by layover or shadow, respectively. Consequently, another incidence angle and or orbit are required to be able to monitor the landslide. Also landslides with a very low value of the measurable percentage of movement (< 20 %) and of too small size (only few image pixels) are classified with the value '5'.

Tab. 5: Applicability of the D-InSAR technique for a selection of the landslides of footprint Sudelfeld

Landslide ID	Type of movement	Layover (L), Shadow (S)	Measurable percentage of movement	Land cover class			Applicability of the D-InSAR technique
				X- band	C- band	L- band	
…00001	Slide	-	74.78 %	6	5	3	3
…00002	Slide	-	91.49 %	6	5	3	3
…00007	Fall	-	-	6	5	3	6
…00012	Slide	-	93.85 %	4	3	2	1
…00022	Slide	L (100 %)	45.25 %	6	5	3	5
…00029	Slide	-	92.57 %	4	3	2	1
…00032	Rockfall	-	-	6	5	3	6
…00034	Slide	-	45.66 %	6	5	3	3
…15005	Slide	L (70 %)	56.44 %	4 6	3 5	2 (35 %) 3 (65 %)	4

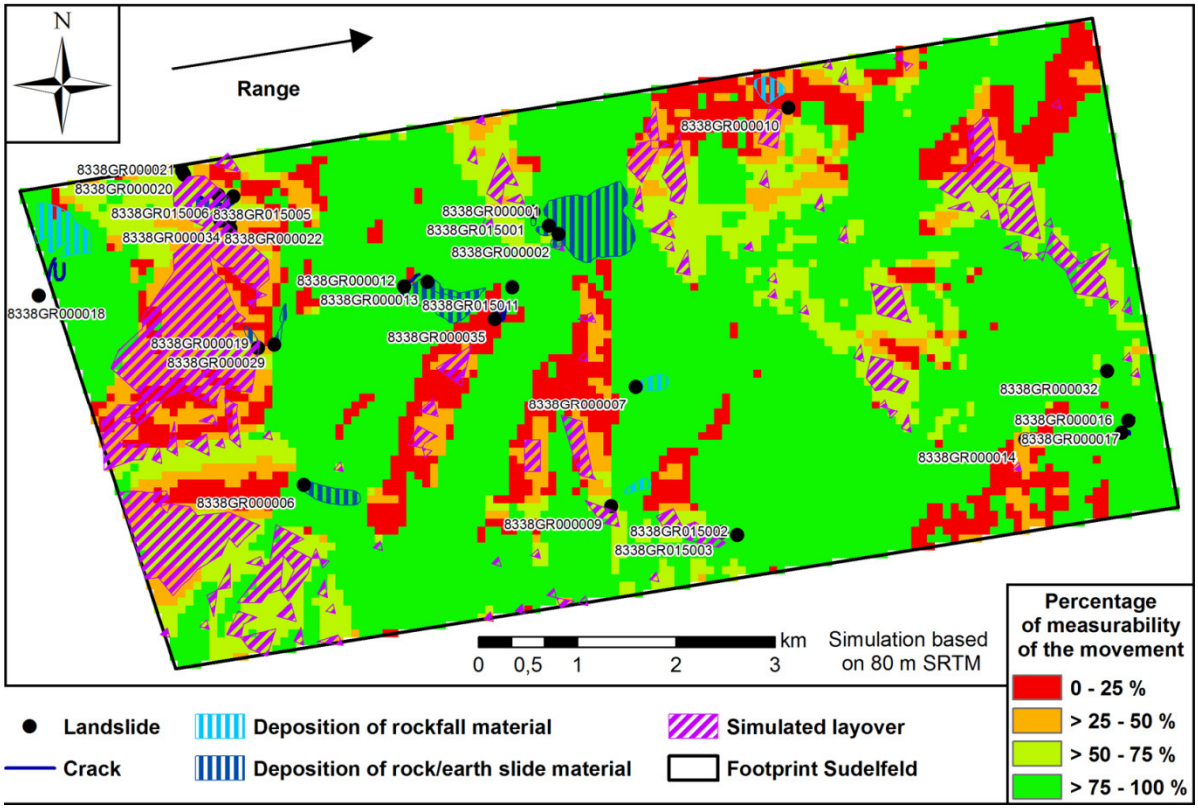

Fig. 25: Final result of footprint Sudelfeld: using this map one can estimate whether a landslide will be affected by layover and/or shadowing and which percentage of a potential (real) movement can be detected by the satellite, prior to the acquisition of the radar images for the area of interest. Landslides from Bavarian Georisk Database: http://www.bis.bayern.de/bis. © Bayerisches Landesamt für Umwelt, Bodeninformationssystem (BIS) (PLANK et al. 2012).

According to METTERNICHT et al. 2005, COLESANTI & WASOWSKI 2006 and CORSINI et al. 2006, D-InSAR can only be applied for the detection of slow movements (cf. chapter 4.2). Consequently, the measurable percentage of movement of faster landslides is not listed in table 5. Also landslides that belong to another type of movement such as 'fall' (e.g. rockfall) are excluded from the calculation of the measurable percentage of movement. This concerns for example the landslides ID '…00007' (fall) and '…00032' (rock fall; Tab. 5). As D-InSAR cannot be applied at such landslides, they are classified by the value '6'.

With the resulting information of the GIS procedure, presented in this first topic, stakeholders are able to easily evaluate whether D-InSAR can be applied for monitoring a certain area of interest. An iterated analysis for different SAR acquisition geometries makes it possible to decide which imaging geometry (incidence angle and orbit) will provide the best results. Moreover, other factors such as the spatial resolution of the radar sensor, data availability (repeat cycle) and atmospheric disturbances, need to be considered when deciding whether to use D-InSAR or not. By undertaking a pre-survey assessment of the expected data coverage and quality using the presented methods a first evaluation can be performed, delineating the areas in which D-InSAR is promising. Using the freely available SRTM DEMs reasonable results are archived only on a regional scale (e.g. an entire footprint). More detailed analysis (e.g. for positioning corner reflectors on a landslide) requires higher quality DEMs.

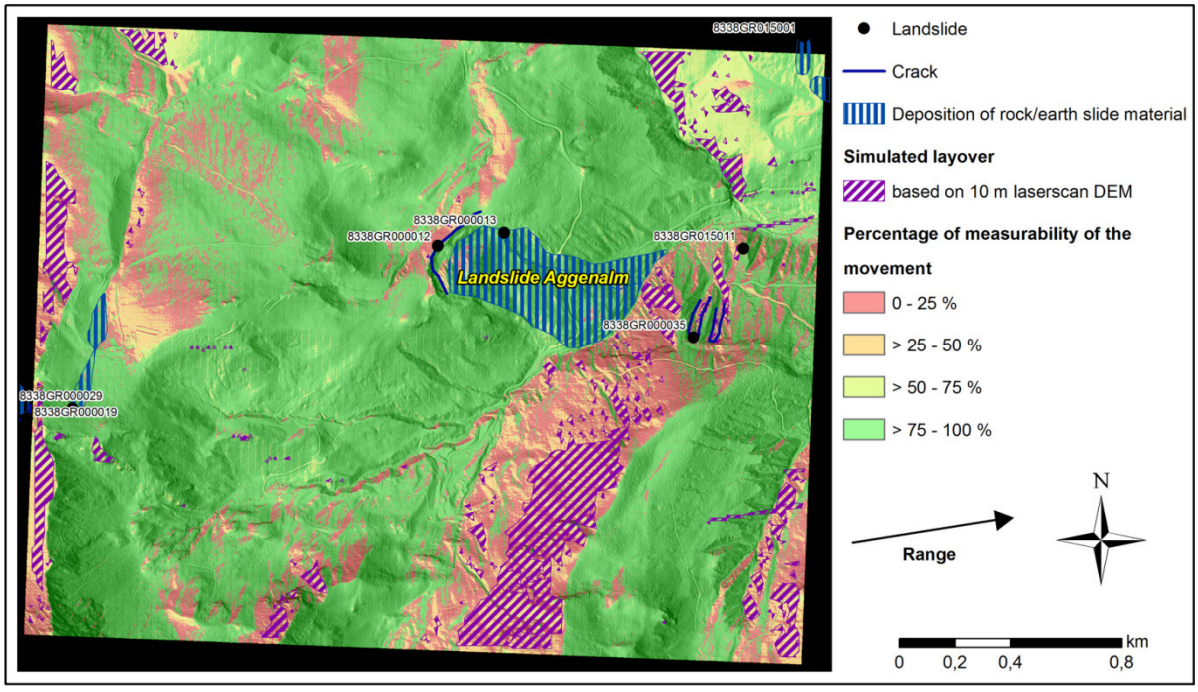

Fig. 26: Simulation of layover and measurable percentage of movement with landslides for the area of the laserscan (part of footprint Sudelfeld, cf. Figs. 12 & 13). The measurable percentage of movement in the area of the landslide Aggenalm is very high, since the landslide's motion direction is almost parallel to the satellite's range direction. Landslides from Bavarian Georisk Database: http://www.bis.bayern.de/bis. © Bayerisches Landesamt für Umwelt, Bodeninformationssystem (BIS) (PLANK et al. 2012).

5. Estimation of persistent scatterers prior to SAR acquisition

Persistent scatterer synthetic aperture radar interferometry (PS-InSAR) overcomes several limitations of the conventional D-InSAR method. One big improvement is the deformation measurement at specific objects called persistent scatterers (PS), which are characterized by long-term high coherence values of the radar signal. Thereby, also areas characterized by only punctual and not area wide high coherence values, as needed for conventional D-InSAR, enable deformation measurements. Moreover, using a stack of at least 15 to 50 SAR images allows an estimation of the atmospheric influence on the phase signal and its correction (chapter 3.4). However, this high amount of SAR images makes processing very time-consuming and expensive. Therefore, in this second topic of the work, three new methods for estimating PS prior to the radar recording of the area of interest using freely available or low-cost optical remote sensing data, land cover data, topographic maps and OpenStreetMap data are presented. In the procedure, the distance between the estimated PS is calculated and classified regarding to the applicability for PS-InSAR processing and the dispersion of the estimated PS within the site is analyzed. Then, results of the PS-estimation methods are validated using data of real PS-InSAR processing. Chapter 2 describes the sites and used SAR data. In PLANK et al. (in review) a summarized version of this second topic has already been published. Here, a more detailed version is presented.

5.1 PS-estimation based on land cover data

5.1.1 Freely available land cover data

The first pre-survey PS-estimation method uses freely available land cover data. Three types of land cover datasets with different ground coverage and spatial resolution are used. The first one is the GlobCover 2009 land cover dataset, which is characterized by a global coverage and a spatial resolution of 300 m. This dataset was derived by the classification of MERIS (Medium Resolution Imaging Spectrometer) data acquired at the time period January to December 2009. This sensor flies on board of the ENVISAT satellite. The dataset distinguishes 22 land cover classes. The GlobCover project is an ESA initiative which started in 2005 in partnership with the Joint Research Center (JRC), the European Environmental Agency (EEA), the Food Agricultural Organisation (FAO), the United Nations Environment Program (UNEP), the Global Observation of Forest and Land Cover Dynamics (GOFC-GOLD) and the International Geosphere-Biosphere Program (IGBP). The data processing included a set of corrections as cloud detection, atmospheric correction, geolocalisation and re-mapping. The classification of GlobCover is compatible with the United Nations (UN) Land Cover Classification System (LCCS). For more information about this land cover data and its download, the reader is referred to BONTEMPS et al. (2011) and http://ionia1.esrin.esa.int/.

The second land cover dataset used for the PS-density estimation is the year 2006 version of CORINE (Coordination of Information on the Environment) land cover data, which has a spatial resolution of 100 m. Due to its limited coverage to Europe, this land cover dataset was used for the twelve European sites. CORINE land cover is based on satellite data, such as IRS-P6 (part of Indian Remote Sensing satellite series), SPOT-4 and SPOT-5 MS (Système Pour l'Observation de la Terre, French remote sensing satellite), and topographic data (e.g. ATKIS - Amtliches Topographisch-Kartographisches Informationssystem – Germany). The

mapping scale of the data is 1:100,000. 44 land cover classes are distinguished. CORINE 2006 is available at: http://www.eea.europa.eu (KEIL et al. 2010).

For the Cairo site the Africover land cover data was used. The source of this dataset (for Egypt) are Landsat imagery (scale 1:100,000) which were acquired in 1997. The Africover project is part of the Global Land Cover Network initiative, which has been jointly launched by FAO and UNEP. The Project (period from 1995 to 2002) was undertaken in ten African countries: Burundi, Democratic Republic of Congo, Egypt, Eritrea, Kenya, Rwanda, Somalia, Sudan, Tanzania and Uganda. More information about Africover is available at http://www.africover.org.

5.1.2 Method of land cover based PS-estimation

This PS-estimation method is based on an empirical approach. Datasets of geocoded processed PS from sites of different climate zones and geographical regions (chapter 2) were compared with the land cover datasets described in chapter 5.1.1. As the goal of this method is to estimate the PS-density of a site prior to its radar recording, using the land cover datasets described above, for each single land cover class the number of processed PS-targets lying inside the land cover class and the entire area of the class (within the site) were calculated. Then, the processed PS-density (PS-targets per km²) was derived (Eq. 46).

$$PS\ density\left[\frac{PS}{km^2}\right] = \frac{Number\ of\ PS\ targets}{Area\ of\ land\ cover\ class[km^2]} \quad (46)$$

The calculation of equation 46 was done for each single site and land cover dataset using a model programmed with the ArcGIS® Model Builder supported by several SQL queries applied in MS Access® (see appendix 8 for the technical implementation). The single results for all the sites and land cover data are shown in detail in appendix 9.

As the sites were recorded by SAR sensors, working with different wavelengths, different imaging modes, etc., and the PS were processed with different PS-detection methods and algorithms, the absolute PS-density values of the sites show a strong variation within each land cover class (cf. appendix 9). To be able to compare the datasets of the different sites the so-called relative PS-density was developed in this work. This relative PS-density was derived by dividing the absolute PS-density values of all land cover classes within a site by the value of a certain reference class. Therefore, the relative PS-density of this reference class equals to '1'. All land cover classes with a relative PS-density less than '1' have a lower absolute PS-density and vice versa (see appendix 9, AFigs. 2 to 6).

The concept of the land cover based PS-estimation method is to use the graphs described in chapter 5.1.3 to estimate the absolute PS-density of all land cover classes within the area of interest, prior to its radar recording. Precondition for this method is an estimation of absolute PS-density of the reference class. As PS-InSAR has very often been successfully applied in urban areas (COLESANTI et al. 2003a, REFICE et al. 2005, COLESANTI & WASOWSKI 2006), there already exists a lot of information about the absolute PS-density values in urban area for different SAR sensors and PS processing algorithms. Therefore, the class 'urban area' was chosen as reference class for the relative PS-density method. It is important to notice, that the class 'urban area' is only required in the sites used for the calibration of the relative PS-

density (in this work). However, for a later application of this PS-estimation method urban area within the area of interest is not mandatory.

The GlobCover dataset was used for PS-datasets of the sites Aosta West (ascending and descending), Bavaria, Budapest, Cairo (containing 3 PS-datasets, see chapter 2a), Domodossola, Netherlands, Novara, North Germany, Omegna and Varallo. The sites Aosta Valley East and Aschau am Inn could not be considered for the GlobCover dataset, as in both sites the area of the reference class ('urban area') is very low (ca. 3 km², which is less than 0.25 % of the entire site area). At such small areas even very small changes of the number of PS-targets cause large variations of the PS-density. This could distort the results of the relative PS-density method. Consequently, these areas are not suitable for the calibration of the relative PS-density graphs (see above, cf. appendix 9).

For the CORINE dataset there is a sufficiently large percentage of urban area within each site, because of its higher spatial resolution. Therefore, all European sites were used – except for the Ivrea site, which was excluded from the calibration of both GlobCover and CORINE dataset to be used for validation of the results (chapter 5.1.4).

5.1.3 Results of land cover based PS-estimation

The AFigs. 2 to 6 (appendix 9) show the relative PS-density values for the GlobCover, CORINE 2006 and Africover land cover datasets, respectively. At most land cover classes the variation of the values is relatively small. However, some land cover classes show strong differences between the minimum and maximum value. These land cover classes are stronger influenced by the factors mentioned in the following than the majority of the land cover classes. These factors are the climate and topographic relief of the site, the wavelength of the SAR sensor and the PS-detection method used for PS-InSAR processing. To take these stronger influences on these land cover classes into account and to reduce the variation of their values, subclasses were generated for certain land cover classes.

Due to the low annual precipitation and resulting sparse vegetation, areas of arid climate are much better suited to form PS than humid areas (mostly higher vegetation density). Therefore, the sites were divided into areas of arid (precipitation < evaporation all-year; e.g. the Cairo site) and humid (precipitation > evaporation all-year; the European sites) climate. For instance, the annual precipitation of the Cairo site (ca. 29 mm/a) is very low compared to the Aosta Valley site (ca. 1863 mm/a). A very suitable source to determine the site's climate is the updated world map of the Köppen-Geiger climate classification developed by PEEL et al. (2007), which is freely available at http://www.hydrol-earth-syst-sci.net/11/1633/ 2007/hess-11-1633-2007-supplement.zip).

PS-InSAR applications are complicated in (humid) areas in high mountains (e.g. the Alps), which are characterized by (a) lots of snow and ice more than half a year, (b) very high annual precipitation (see above) and (c) strong geometrical distortions, such as the layover and shadowing effect (see chapter 4.1). Therefore, the next subclasses divide the sites in areas of high mountains (Alpine sites of Aosta Valley and Piedmont) and flat & hilly terrain (other sites) delimited by a 20° threshold for the mean slope (based on a SRTM DEM).

Depending on the spatial resolution of the SAR sensor used, objects of different size can work as PS-target. At high spatial resolution SAR sensors such as TerraSAR-X (StripMap mode or

higher spatial resolution), smaller objects of decimeter size on the ground possibly work as PS-target. Contrary to this, at C-band SAR data (in this work ERS, ENVISAT and Radarsat-1 (Standard mode) were used, Tab. 1), larger objects of meter size are required to form PS-targets. Consequently, two subcategories '…(for X-band)' and '…(for C-band)' were defined. As described in 5.1.3 b), only the class 'road & railroad' is affected by the wavelength of the SAR sensor.

The results of the PS-detection methods SCR and amplitude dispersion index D_a, which are described in chapter 3.4, show very strong differences at natural areas free of vegetation. At the SCR method only pixels of intensity values higher than their spatial neighborhood (clutter) are selected as PS (candidates; Eq. 17). Simply spoken, at the SCR method 'bright' pixels are selected as PS. Contrary to this, the D_a method investigates the relationship of the temporal standard deviation of the amplitude and the temporal mean of the amplitude of a certain pixel in a stack of SAR images (Eq. 16; KAMPES 2006). Therefore, this method not only selects 'bright' pixels. This difference of the PS-detection methods has a strong influence on the number of selected PS-targets at the vegetation free stony and rocky desert of the Cairo site. This land cover type is characterized by a very low value for the D_a, which is an indicator for low phase dispersion (high probability to form a PS). However, this rocky desert does not show very high intensity values in a SAR image (contrary to e.g. urban areas). Therefore, the application of the SCR method results in a much lower number of selected PS, than the application of the D_a method. For the corresponding land cover classes subclasses were generated to take this PS-detection method related differences into account.

a) GlobCover

The figures 27 and 28 show the average mean of the relative PS-density of the GlobCover dataset for 'normal' PS-targets (PS) and distributed scatterers (DS) and 'normal' PS-targets (DS&PS), respectively. As mentioned in the previous chapter (5.1.1) the GlobCover dataset has a global coverage, but a very general thematic classification of only 22 classes, which does not take the climatic differences of the sites into account: The GlobCover class 'bare areas' represents both the bare rock areas of the Alpine sites (Aosta Valley and Piedmont) and the desert areas of the Cairo site. Both regions have a very different climate. As mentioned above, the class 'bare areas' in the Alpine sites is not as suitable for PS-InSAR processing as the same land cover class in the arid climate Cairo site. Therefore, for the GlobCover class 'bare areas' the aforementioned climate based sub-classification was applied, by dividing the class into the subclasses 'bare areas, humid' representing the European sites and 'bare areas desert, arid' for the Cairo site.

For the Cairo site the results of three different PS-detection methods were available (cf. chapter 2 & 3.4). The GlobCover class 'bare areas' of the Cairo site shows very different values for the different PS-detection methods. The PS-detection method based on the D_a shows a twice as high value for the relative PS-density as the result for the SCR method, while the combination of both methods ranges in the mean of both (this effect was explained at the beginning of chapter 5.1.3). This strong variation for the GlobCover class 'bare areas' between the different PS-detection techniques was considered by the definition of a subcategory for each method.

The examination of the single relative PS-density values of the classes ‘sparse vegetation’ and ‘bare areas’ showed large differences between the values of the Alpine sites (Aosta Valley and Piedmont) and the other European (humid climate) sites (appendix 9, AFigs. 2 & 3). In the Alpine sites both land cover classes are mainly restricted to high mountainous areas. The mean inclination of slope was greater than 26.7°. As explained above, PS-InSAR is very difficult to apply in such high mountainous terrain. As opposed to this, at the other sites these two land cover classes are located in flat (inclination of slope < 2°) and hilly terrain. Therefore, the aforementioned threshold of 20° for the mean inclination of the slope was used to consider this ‘terrain-related’ difference. Two subcategories were defined: ‘... in flat and hilly terrain’ for the mean slope inclination being less or equal than 20° and ‘... in high mountains’ for the mean slope inclination being greater than 20°.

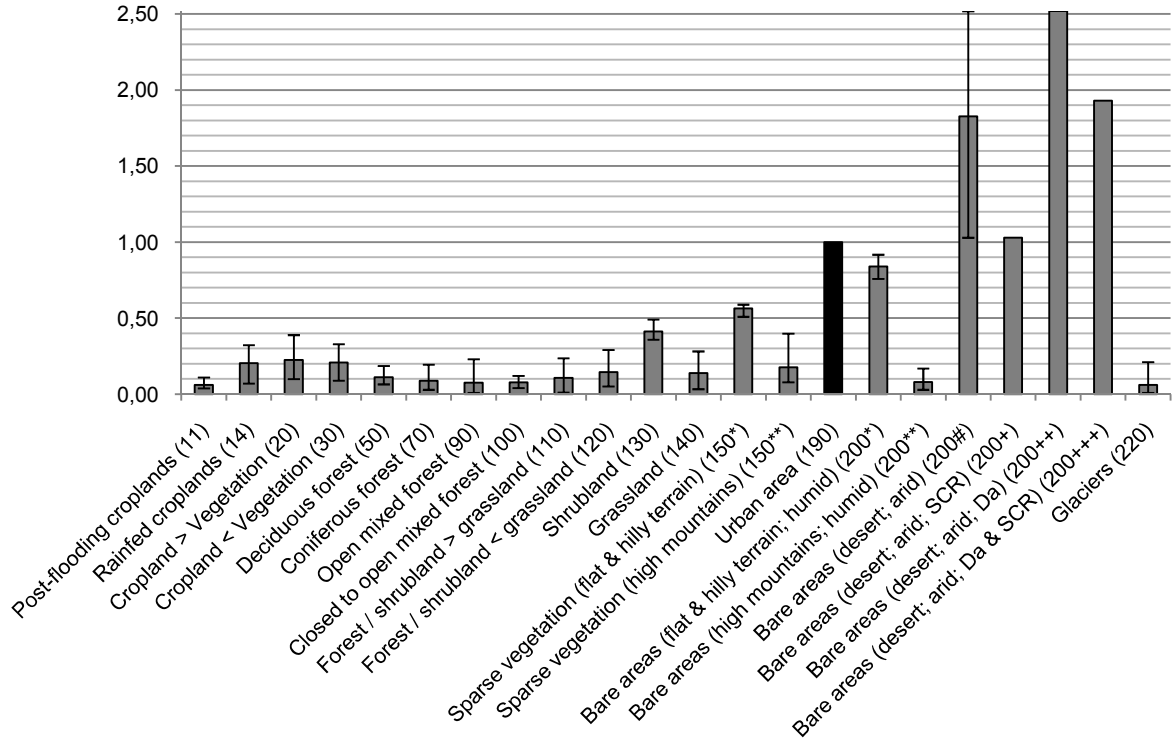

Fig. 27: GlobCover 2009 arithmetic mean of relative PS-density. The numbers show the ID of the GlobCover land cover classification. The small bars show the minimum and maximum values.

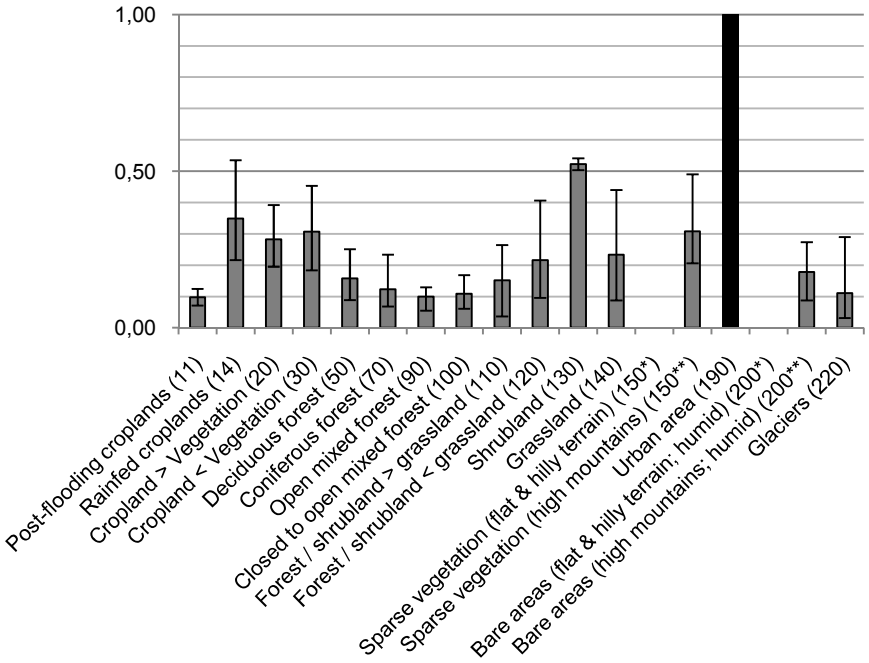

Fig. 28: GlobCover 2009 arithmetic mean of relative DS&PS-density. The numbers show the ID of the GlobCover land cover classification. The small bars show the minimum and maximum values. For the classes '150*' and '200*' (flat terrain) no data values were available, as all sites with DS&PS were located in high mountains.

b) CORINE

The figures 29 and 30 show the average mean of the relative PS-density values for the CORINE dataset for 'normal' PS-targets (PS) and distributed scatterers and 'normal' PS-targets (DS&PS), respectively. The land cover classes 'continuous urban area' (densely build-up area), 'industrial' and 'port areas' show high variability between the single values (appendix 9, AFigs 4 & 5), however as the values always are near or above the reference class 'discontinuous urban area', enough PS-targets can always be expected in these land cover classes.

AFig. 4 (appendix 9) shows that the relative PS-density of the class 'road & railroad' is twice as high for the Budapest site as for the other sites. As mentioned above, due to the smaller wavelength of X-band, which was used for the sites Budapest and Aschau am Inn (here this class is not represented), smaller objects of decimeter size on the ground, such as road signs and overhead line masts, possibly work as PS-target. As opposed to these two sites, at all other sites C-band SAR data was used (see chapter 2), requiring larger objects of meter size to work as PS-target. Therefore, the aforementioned sub-classification was applied to the CORINE land cover class 'road & railroad' by splitting it into the subcategories 'road & railroad (for X-band)' and 'road & railroad (for C-band)'.

The land cover classes 'mineral extraction', 'dump sites' and 'construction sites' show very large variations between the single values in AFig. 4 (appendix 9). As already mentioned in chapter 4.3.2. (h), at these classes occur strong changes within a short time period. Therefore, the time lag between the acquisition date of the SAR data and the recording date of the optical satellite data used for the classification of the CORINE data is very important. With increasing time lag, also the uncertainty of the relative PS-density increases. PS-InSAR is very difficult to apply at these classes due to their very high temporal variability.

AFig. 4 (appendix 9) shows high variations in the values of the class ‘sands’. This can be explained by the different geographic location of the sites containing this land cover class. At the Piedmont sites this class is located at riverbanks containing lots of rocks and buildings in the surrounding, which can work as PS-objects. Contrary to this, as the widely sandy North Sea beaches of the Netherland and North Germany sites contain no rocks and very rarely buildings, they show a very low PS-density. Therefore, the class ‘sands’ was divided into the two subcategories ‘sands (seashore)’ and ‘sands (riverbank)’. However, it is important to notice that the term ‘seashore’ represents widely sandy beaches with no rocks and only a few buildings (as at the German and Dutch North Sea coast). If the site is characterized by a coast containing significantly more rocks (more potential PS-targets) the relative PS-density values of the class ‘…(riverbank)’ should be used instead of the one of ‘…(seashore)’.

Similar to the corresponding classes of the GlobCover land cover dataset (see above), also for the CORINE classes ‘sparse vegetation’ and ‘bare rocks’ the two previously defined subclasses based on the 20° inclination of slope threshold were applied to these land cover classes: ‘… in high mountains’ with inclination of slope > 20° (Piedmont and Aosta Valley sites) and ‘… in flat and hilly terrain’ with inclination of slope < 20° (the other European sites). For the class ‘bare rocks’ only data from sites in high mountains were available.

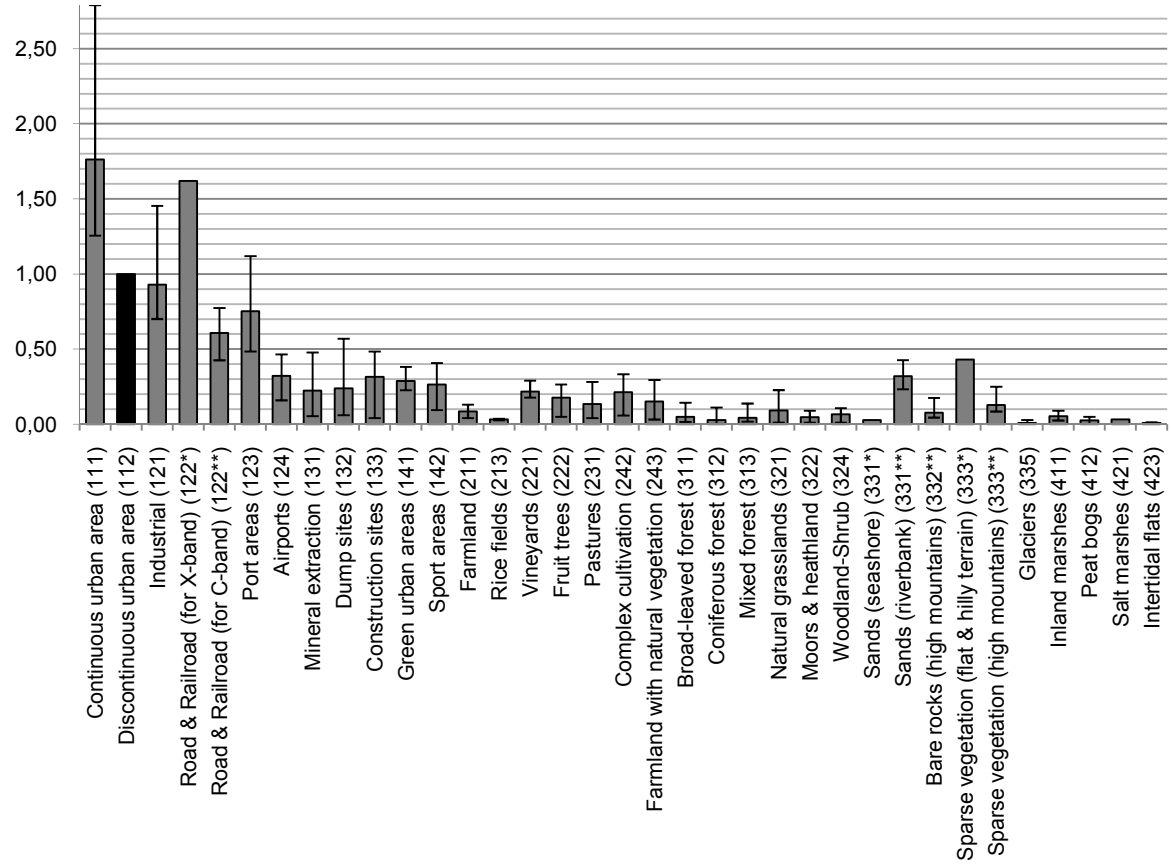

Fig. 29: CORINE 2006 arithmetic mean of relative PS-density. The numbers show the ID of the CORINE land cover classification. The small bars show the minimum and maximum values.

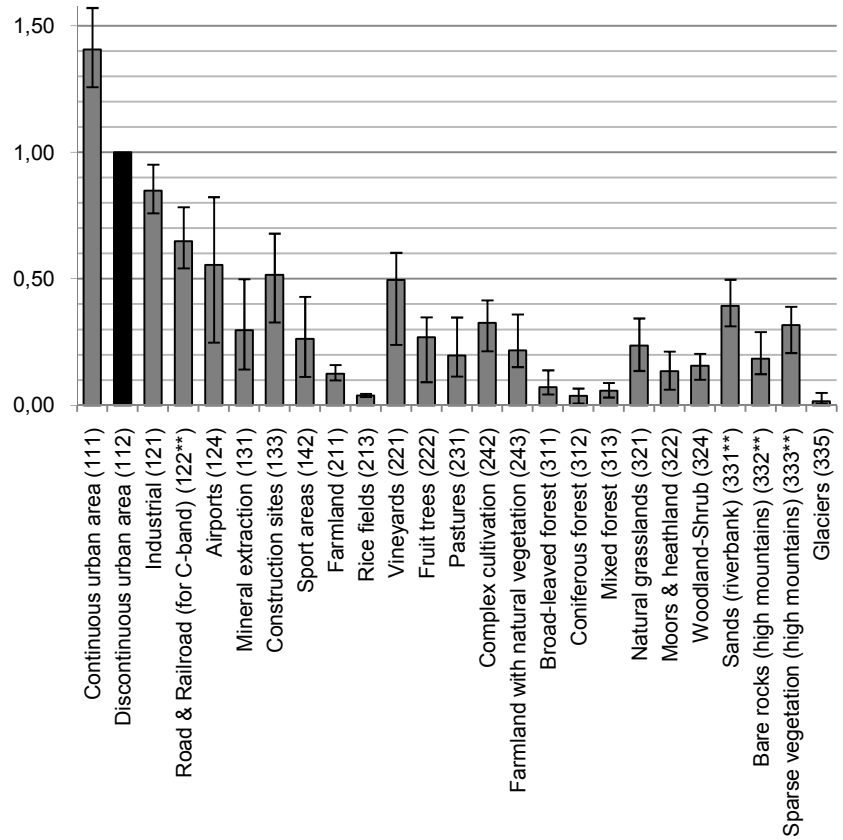

Fig. 30: CORINE 2006 arithmetic mean of relative DS&PS-density. The numbers show the ID of the CORINE land cover classification. The small bars show the minimum and maximum values.

c) Africover

As for the Africover land cover dataset only the three PS-target datasets of the Cairo site (chapter 3.4) were available, the results of the relative PS-density have to be perceived with great care. To achieve more meaningful results, data from several African sites would be required. Therefore, the results of Africover are only presented to give an incentive for future work and to show that higher spatial and thematic resolution land cover data (in comparison to the world wide available GlobCover data) is not only available for Europe.

The figure 31 shows a good conformity within all classes, except of the classes 'bare rock' and 'bare rock with thin sand layer'. The later show strong variations depending on the type of PS-detection method used (this effect was already explained at the beginning of chapter 5.1.3). The result for the PS-detection method based on the D_a is four times as high as the value of the SCR method (for the class 'bare rocks'). This difference is much lower at the classes 'bare rock with thin sand layer' and 'bare soil stony'. Therefore, the previously defined sub-classification for each PS-detection method was applied for the Africover classes 'bare rock' and 'bare rock with thin sand layer' (cf. also appendix 9, AFig. 6).

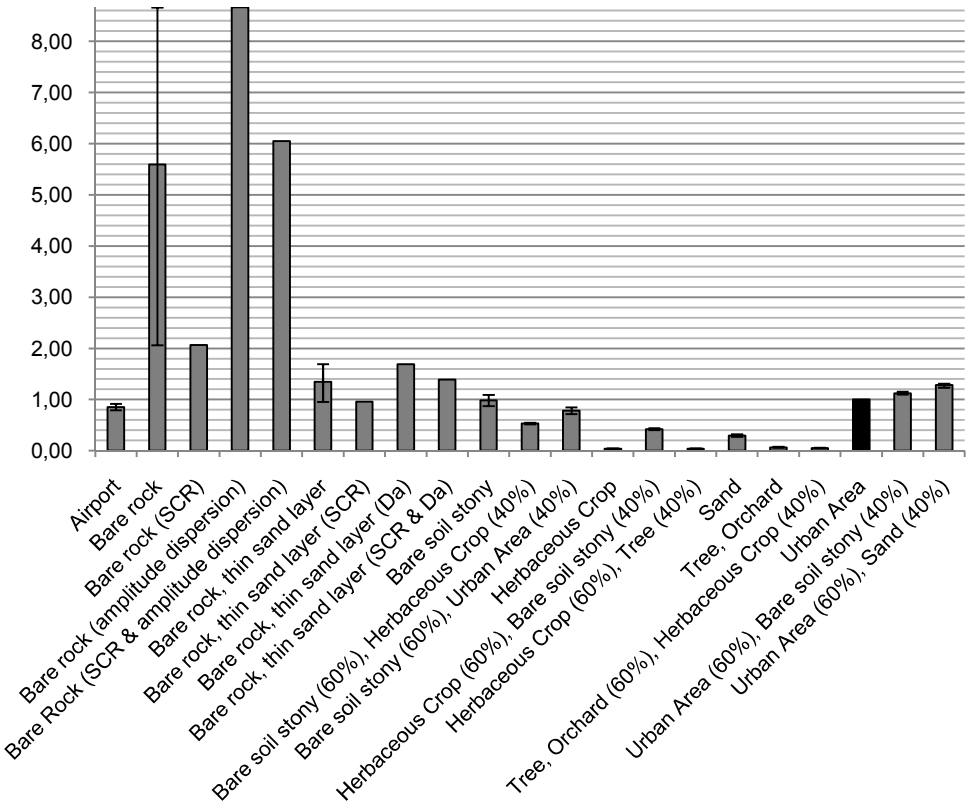

Fig. 31: Africover arithmetic mean of relative PS-density. The small bars show the minimum and maximum values.

5.1.4 Application and validation of the land cover based PS-estimation method

The land cover based PS-estimation method was applied at the Ivrea site for all four cases: GlobCover and CORINE for PS and DS&PS in each case. This was applied by multiplying the relative PS(DS)-density of each single land cover class of the figures 27 to 30, respectively, with the absolute value (PS- or DS&PS-density, respectively) of the reference class 'urban area' of the Omegna site. The sites Ivrea and Omegna were both recorded by Radarsat-1 and processed by the same or comparable PS-detection and processing algorithms. Therefore, both sites show similar values for the PS-density in the reference class 'urban area'. As both sites cover different geographical areas and belong to different tracks (also different incidence angles), the value of the reference class from the Omegna site can be used for the validation of the land cover PS-estimation at the Ivrea site.

5.1.4.1 Description of the method

The figures 32 and 33 show the processed PS and DS&PS-density (result of real SAR data) of the Ivrea site (see chapter 2), respectively. This density (unit PS/km²) was calculated by using a grid of 1 km cell size and counting the number of processed PS (DS) in each cell (ArcGIS® Hawth Tool *count points in polygon*).

The estimated PS(DS)-densities were calculated by multiplying each single value of the figures 27 to 30, respectively, with the absolute value (PS- or DS&PS-density, respectively) of the reference class 'urban area' (class '190' for GlobCover and '112' for CORINE, respectively) of the Omegna site. As the classes 'bare areas' and 'sparse vegetation' are located in mountainous terrain (inclination of slope > 20°) in the Ivrea site, the corresponding values for GlobCover ('high mountains, humid') were chosen. For the corresponding CORINE classes

'bare rocks' and 'sparse vegetation', the associated subclasses 'in high mountains' were applied, too. Additionally, as the Ivrea site was recorded by Radarsat-1 (chapter 2), the subclass 'road & railroad for C-band' was used. Finally, due to the inland location of the site, the subclass 'sands (riverbank)' was applied.

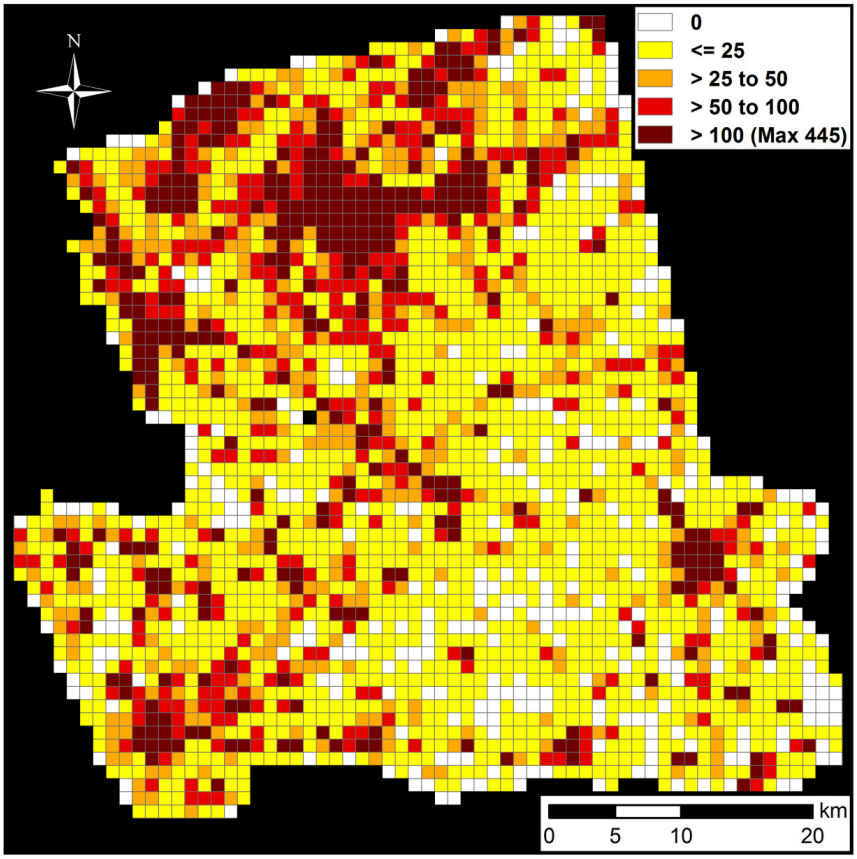

Fig. 32: Processed PS-density [PS/km²] Ivrea site.

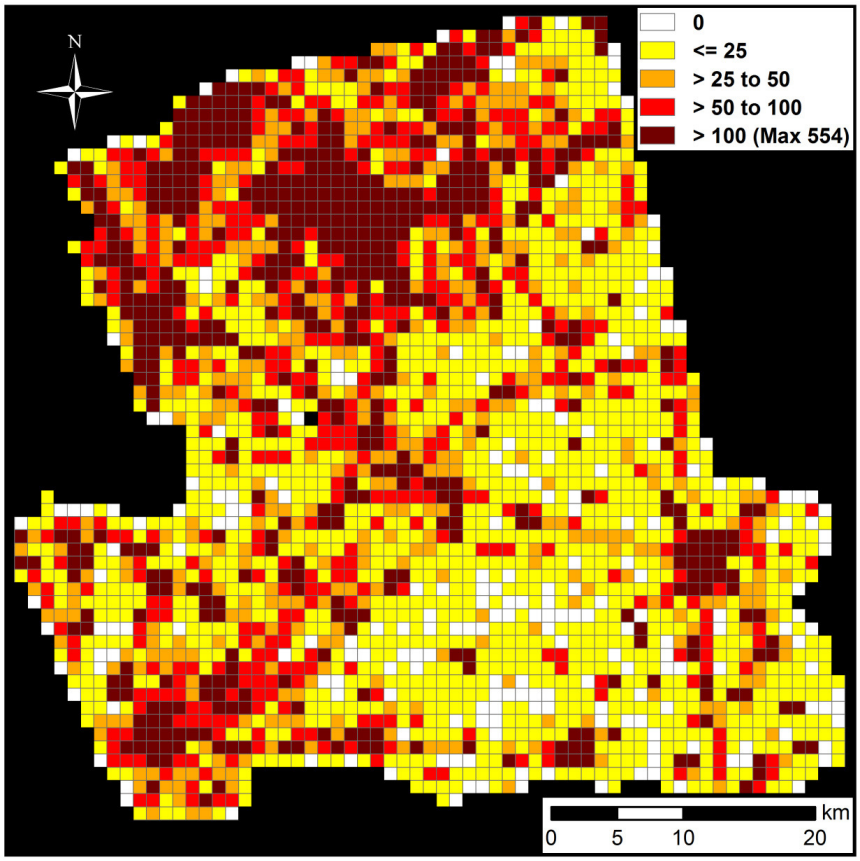

Fig. 33: Processed DS&PS-density [DS&PS/km²] Ivrea site.

5.1.4.2 Results of validation

Comparing the processed PS (DS) density (Figs. 32 & 33) with the land cover maps of GlobCover and CORINE (Figs. 34 & 35), one can clearly see a strong concentration of the processed PS (DS) at urban area (GlobCover class '190' and CORINE classes '111', '112', '121', '122' & '124') and in the northwestern part of the Ivrea site, which is covered by sparse vegetation (GlobCover class '150'; CORINE classes '332' (rock) & '333'). Both of these land cover types show a strong increase of the DS&PS-density compared to the PS-density.

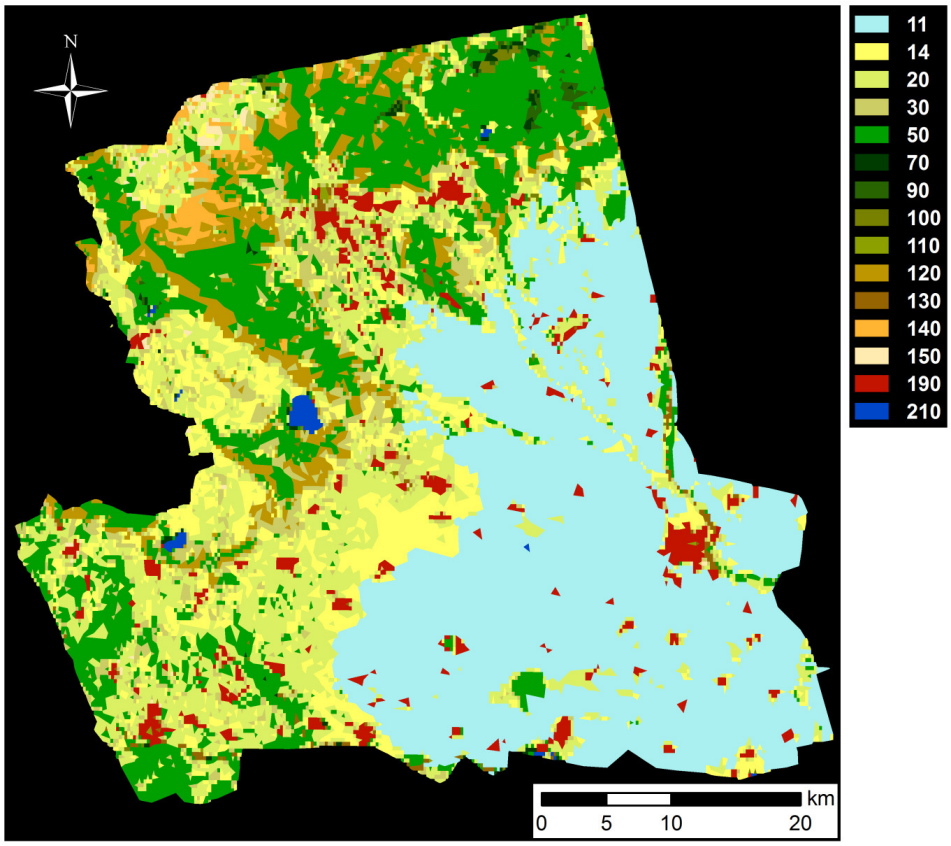

Fig. 34: **GlobCover 2009 land cover Ivrea site. (Legend: see Fig. 27).**

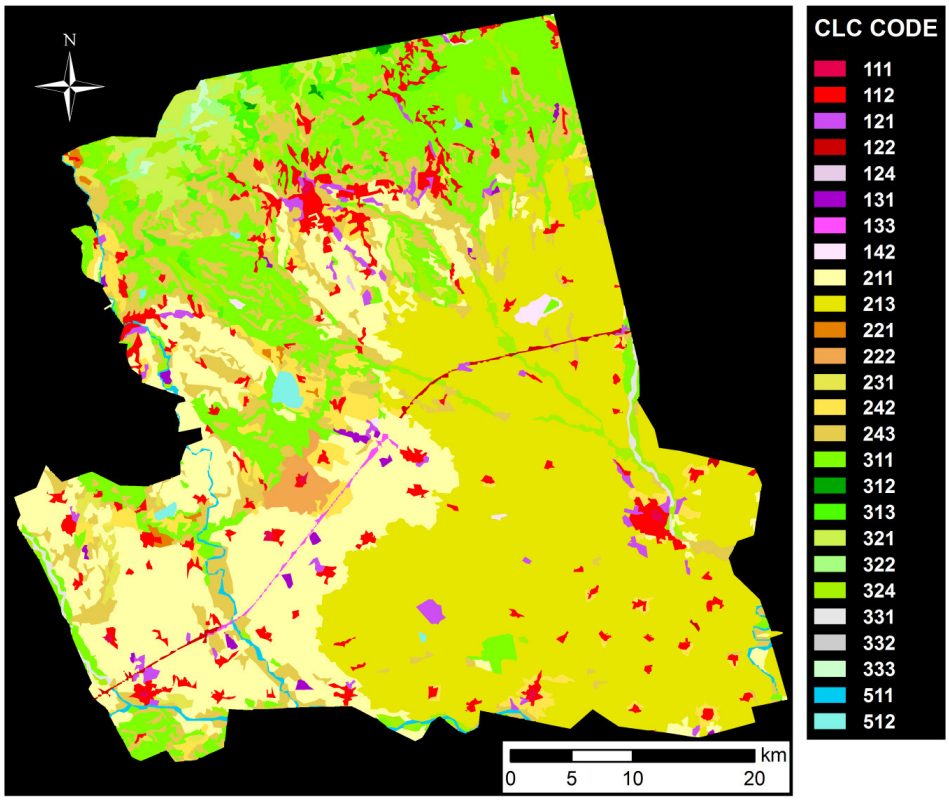

Fig. 35: **CORINE 2006 land cover Ivrea site. (Legend: see Fig. 29).**

a) GlobCover (only) PS-estimation

The visual comparison of the processed (Fig. 32) and estimated PS-density (Fig. 36) based on the values of the GlobCover 2009 graph (Fig. 27) shows that the high PS-density clusters (especially the cities in the SE, N and NW) are clearly identified by the PS-estimation. Also the area of low PS-density (≤ 25 PS/km²) in the southeast of the site shows a good conformity in both PS-density maps.

The figures 37 and 38 show the difference of the estimated and the processed PS-density (cf. ATab. 20, appendix 9). Negative values represent an underestimation (missed hits) while positive values show an overestimation (false-alarm) of the PS-density. Figure 37 confirms visual interpretation of the good conformity of estimation and processed PS-density at the southeastern part of the site. The range of difference of ± 10 PS/km² is with ca. 21.56 % the most frequent one in figure 38 and ca. 40.73 % are within the range of ± 15 PS/km². The southwest of the site is characterized by an overestimation of the PS-density.

Generally this overestimation is more frequent than the underestimation. The estimation is slightly smoothed as the estimated PS-density is equal within the entire land cover class. As opposed to this, the processed PS-density shows more clustering as the PS-targets are mainly concentrated to buildings. Consequently, within the same land cover class there is a slight underestimation at the raster cells containing a high density of buildings, whereas at the other raster cells the PS-density is overestimated. As the latter are more frequent, overestimation dominates the underestimation.

The areas of strong underestimation are located in the city area of the southeast and the north. However, the percentage of difference ≤ -100 PS/km² is very low (5.86 % of the entire site area). As the estimation still recognizes these urban areas as areas with high PS-density, this underestimation is not very relevant for the practical application.

In the northwest of the Ivrea site one can recognize a small area of strong underestimation. This area is covered by sparse vegetation (GlobCover class ‘150’), characterized by a much higher PS-density than the mean of this class from the sites used for the calibration of the relative PS-density. A visual examination of this area in Google Earth™ showed a very high density of rocks, which can function as PS-targets. Furthermore, the area of ca. 15 km² of the class ‘150’ is very small compared to the neighboring sites Domodossola and Varallo, where the area of class ‘150’ sums up to ca. 100 km² in each site. At this small area of the class ‘150’ at the Ivrea site even a small number of PS-targets leads to a higher PS-density.

Despite the generally tendency for overestimation of the PS-density, GlobCover 2009 is relatively well suited for PS-estimation prior to the SAR acquisition of the area of interest. Even with its relatively rough spatial resolution of 300 m, GlobCover achieves an acceptable result.

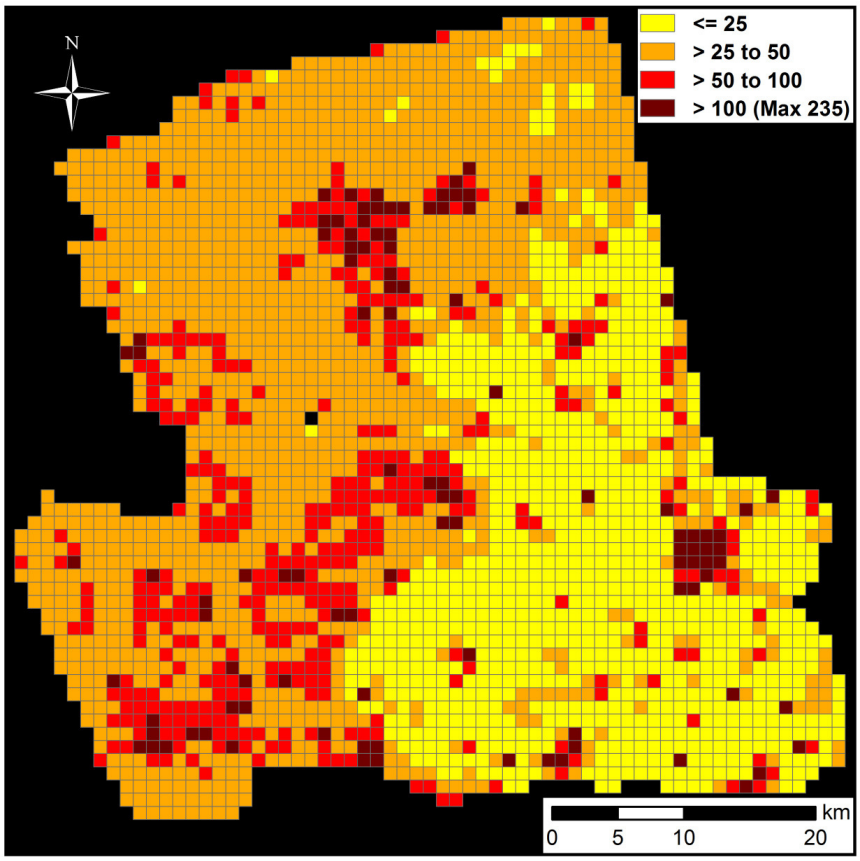

Fig. 36: Estimated PS-density [PS/km²] Ivrea site, GlobCover 2009.

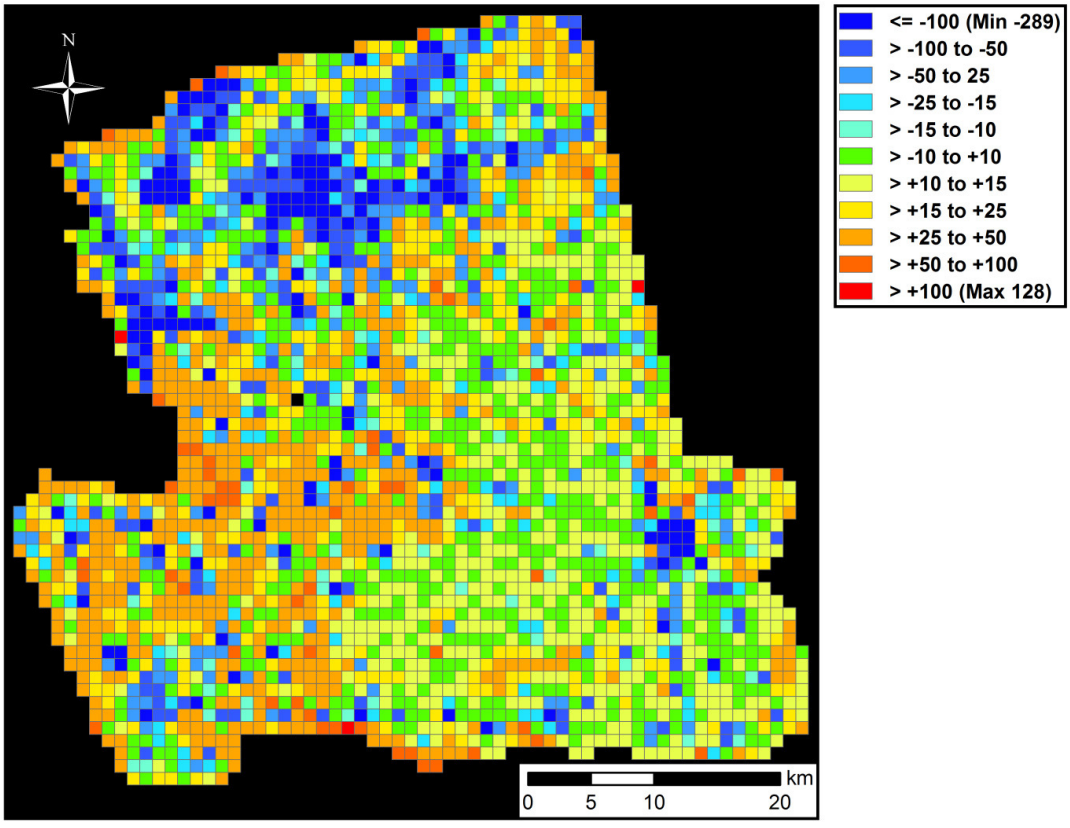

Fig. 37: Difference of estimated and processed PS-density [PS/km²] Ivrea site, GlobCover 2009. Overestimation, false alarm (> 0), underestimation, missed hits (< 0).

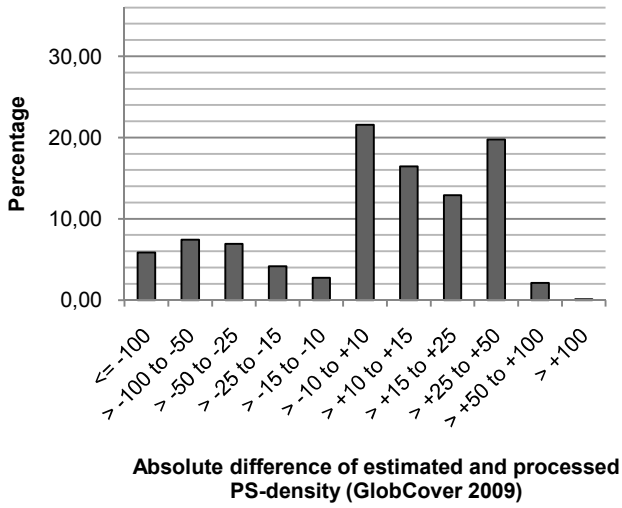

Fig. 38: Percentage of difference of estimated and processed PS-density, Ivrea site GlobCover 2009. Overestimation, false alarm (> 0), underestimation, missed hits (< 0).

b) GlobCover DS&PS-estimation

The comparison of the maximum value of the processed DS&PS-density (554 DS&PS/km²; cf. Fig. 33) and the estimated DS&PS-density (306 DS&PS/km²; cf. Fig. 39) shows that the estimation reaches only ca. 55 % of the processed DS&PS-density (cf. ATab. 31, appendix 9).

The visual comparison of the figures 33 and 39 shows that the clusters of high DS&PS-density (urban areas in the N, SW and SE) and the large area of low DS&PS-density in the southeast are generally recognized by the estimation. However, even in the visual comparison a strong overestimation of the DS&PS-density can be determined. This fact is confirmed by the frequency distribution of the percentage of difference of the estimated and processed DS&PS-density (Fig. 41): The range of difference greater than 15 DS&PS/km² represents more than the half of the site area (ca. 59.68 %), while the range of low difference (±15 DS&PS/km²) is less than 16 % of the area.

The regions of strong underestimation (≤ 100 DS&PS/km²) are located in the centers of densely built up area (in the SE and N) and in the area of sparse vegetation (GlobCover class '150' in the NW; see above). However, this concerns only 8.22 % of the entire site area.

Overall it can be concluded, that the GlobCover land cover dataset cannot be applied very well for the estimation of the DS&PS-density, because of its strong overestimation. Only the trend of the DS&PS-density distribution within the site can be estimated (Fig. 40).

As explained in chapter 3.4, contrary to 'normal' PS, distributed scatterers (DS) do not correspond to one single pixel, but are generated by several neighboring pixels sharing similar reflectivity values (FERRETTI et al. 2011). Therefore, the estimation of DS is quite more complicated than the estimation of PS. As already mentioned above, the estimation is more smoothed and equal within the entire land cover class, while the processed DS&PS are more clustered. Therefore, within the same land cover class there is a slight underestimation at the raster cells containing a high density of DS&PS sources, whereas at the other raster cells the DS&PS-density is overestimated. For the entire site overestimation dominates the underestimation, as the last-mentioned are more frequent.

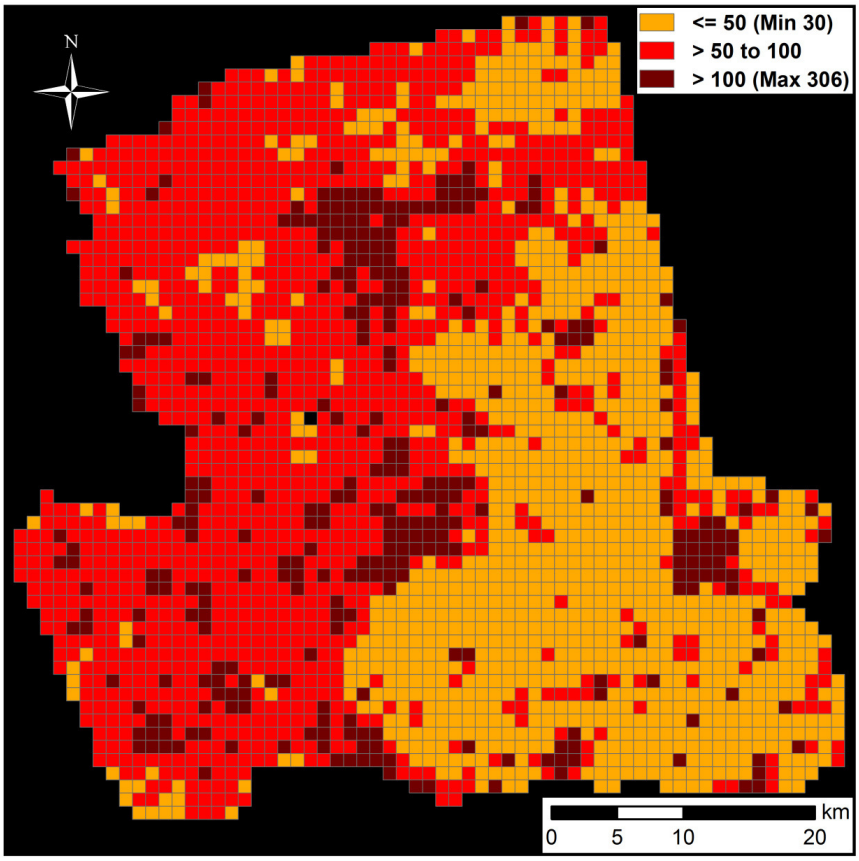

Fig. 39: Estimated DS&PS-density [DS&PS/km²] Ivrea site, GlobCover 2009.

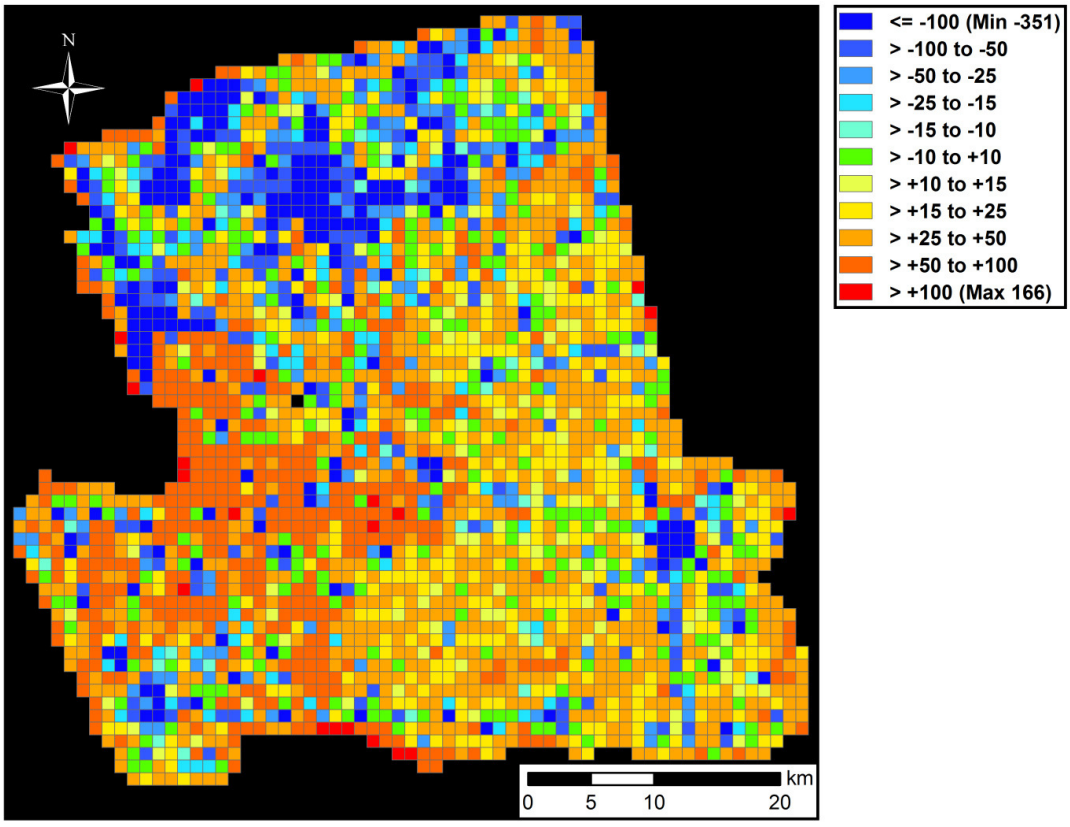

Fig. 40: Difference of estimated and processed DS&PS-density [DS&PS/km²] Ivrea site, GlobCover 2009. Over-estimation, false alarm (> 0), underestimation, missed hits (< 0).

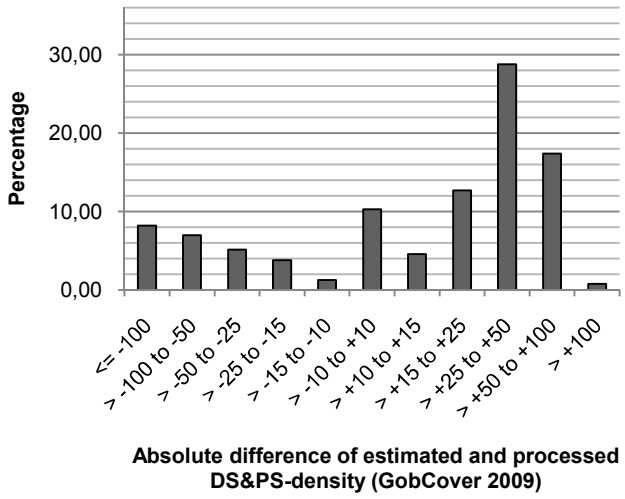

Fig. 41: Percentage of difference of estimated and processed DS&PS-density, Ivrea site GlobCover 2009. Over-estimation, false alarm (> 0), underestimation, missed hits (< 0).

c) CORINE (only) PS-estimation

The visual comparison shows a very good match of processed (Fig. 32) and estimated PS-density (Fig. 42) for the Ivrea site using the CORINE land cover relative PS-density graph (Fig 29; cf. ATab. 47, appendix 9). The maximum value of the estimated PS-density (434 PS/km²) reaches ca. 97.5 % of the processed one (445 PS/km²). The estimation clearly recognizes the clusters of high PS-density (cities in the N, SE and SW). Also the very low PS-density of the southeastern part of the site (CORINE class rice fields) matches very well in estimated and processed PS-density.

As already mentioned at the GlobCover dataset (a)), the estimation is slightly smoothed as the estimated PS-density is equal within the entire land cover class. As opposed to this, the processed PS-density shows more clustering as the PS-targets are mainly concentrated to buildings. Besides the underestimation in the city areas, also in the northwest of the Ivrea site one can recognize a small area of strong underestimation (Fig. 43), which is covered by sparse vegetation (cf. GlobCover, a)).

The visual impression of the good match between the estimated and processed PS-density maps (Figs 29 & 42) is confirmed by the strong concentration of the frequency distribution of the difference between the estimated and the processed PS-density at the interval of ±10 PS/km² (> 35 %; Fig. 44). Therefore, the CORINE data is very well suited for PS-estimation, prior to a SAR recording of the area of interest.

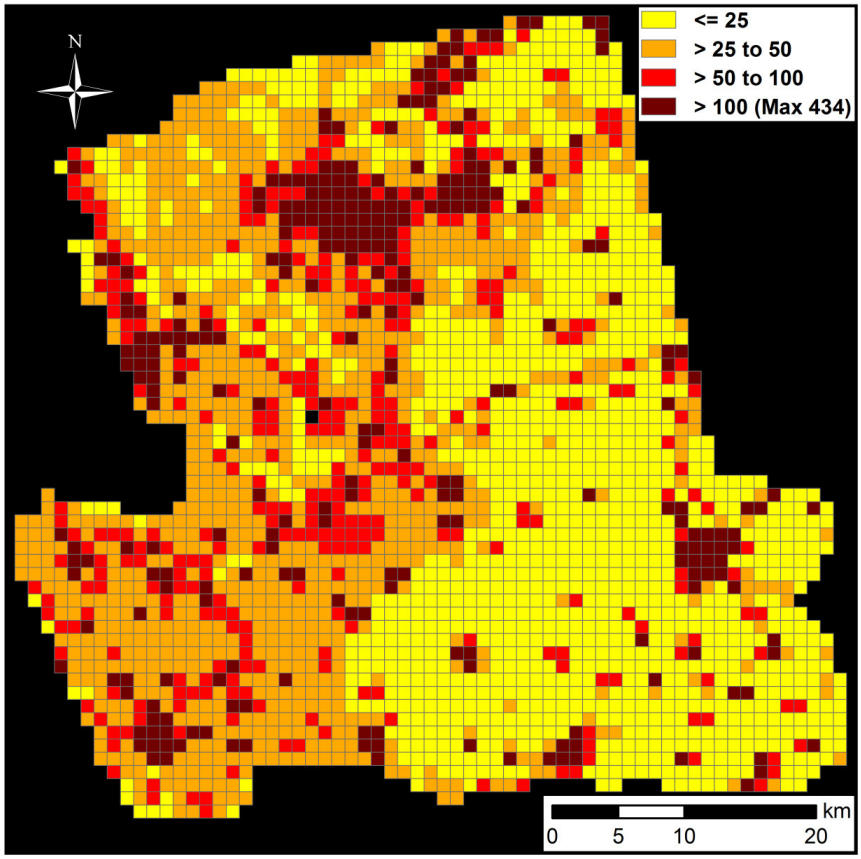

Fig. 42: Estimated PS-density [PS/km²] Ivrea site, CORINE 2006.

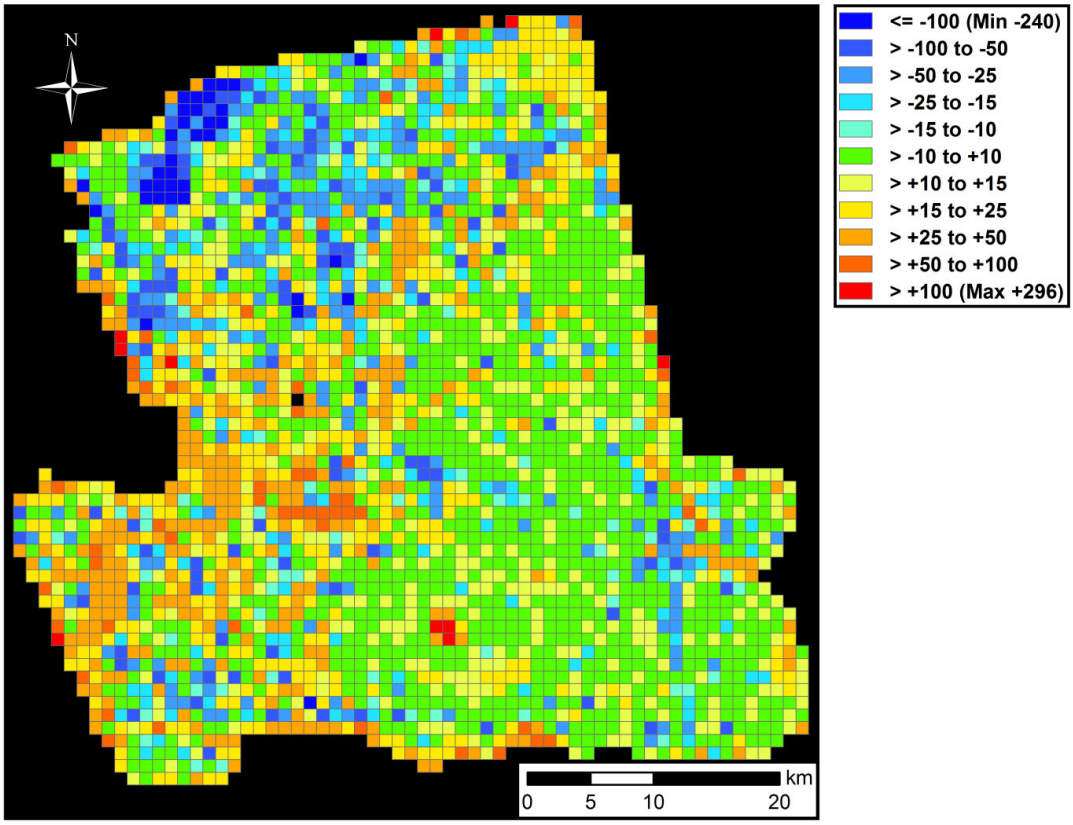

Fig. 43: Difference of estimated and processed PS-density [PS/km²] Ivrea site, CORINE 2006. Overestimation, false alarm (> 0), underestimation, missed hits (< 0).

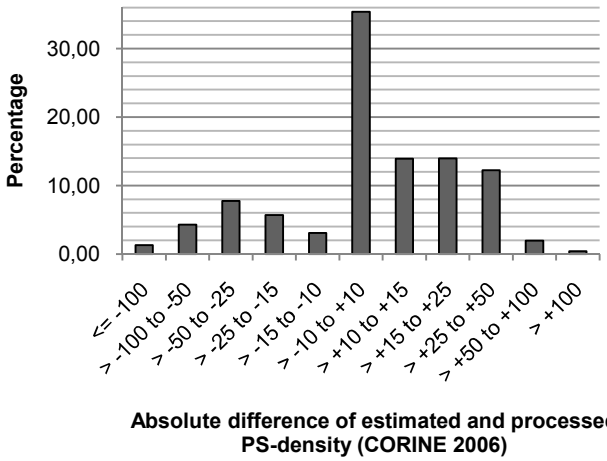

Fig. 44: Percentage of difference of estimated and processed PS-density, Ivrea site CORINE 2006. Overestimation, false alarm (> 0), underestimation, missed hits (< 0).

d) CORINE DS&PS-estimation

The DS&PS-density estimation using CORINE (Fig. 45) reaches ca. 91.5 % of the maximum value of the processed DS&PS-density (Fig. 33). The visual comparison of both DS&PS-density maps shows a relatively good conformity at the clusters of high DS&PS-density (in the N, NW and SE) and the large rice field area of low DS&PS-density values in the south-east. Similarly to 'c) CORINE (only) PS-estimation', underestimation is located at urban areas and in the northwestern corner covered with sparse vegetation (Fig. 46; cf. ATab. 58, appendix 9).

Overall, overestimation of the DS&PS-density dominates, especially in the southwest of the site. The frequency distribution of the percentage of difference between the estimated and processed DS&PS-density (Fig. 47) shows a percentage of ca. 48.10 % for overestimation (difference > + 15 DS&PS/km²), while the areas of low difference (± 15 DS&PS/km²) is only 31.69 % of the site area.

Finally, CORINE is relatively well suited for DS&PS-estimation. However, its relatively high overestimation has to be considered.

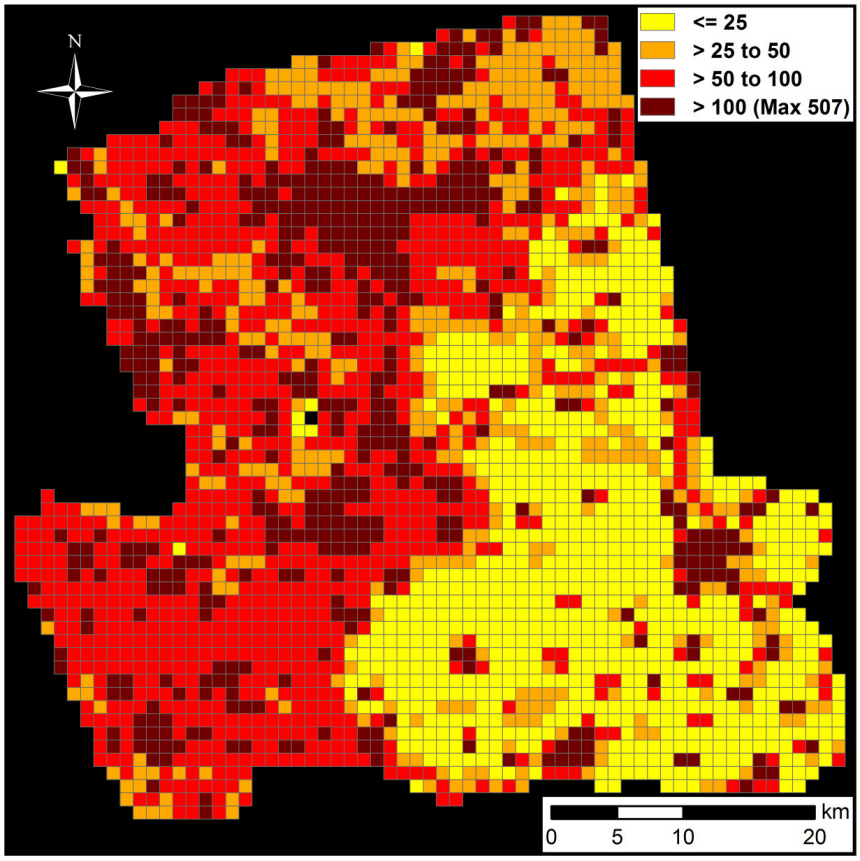

Fig. 45: Estimated DS&PS-density [DS&PS/km²] Ivrea site, CORINE 2006.

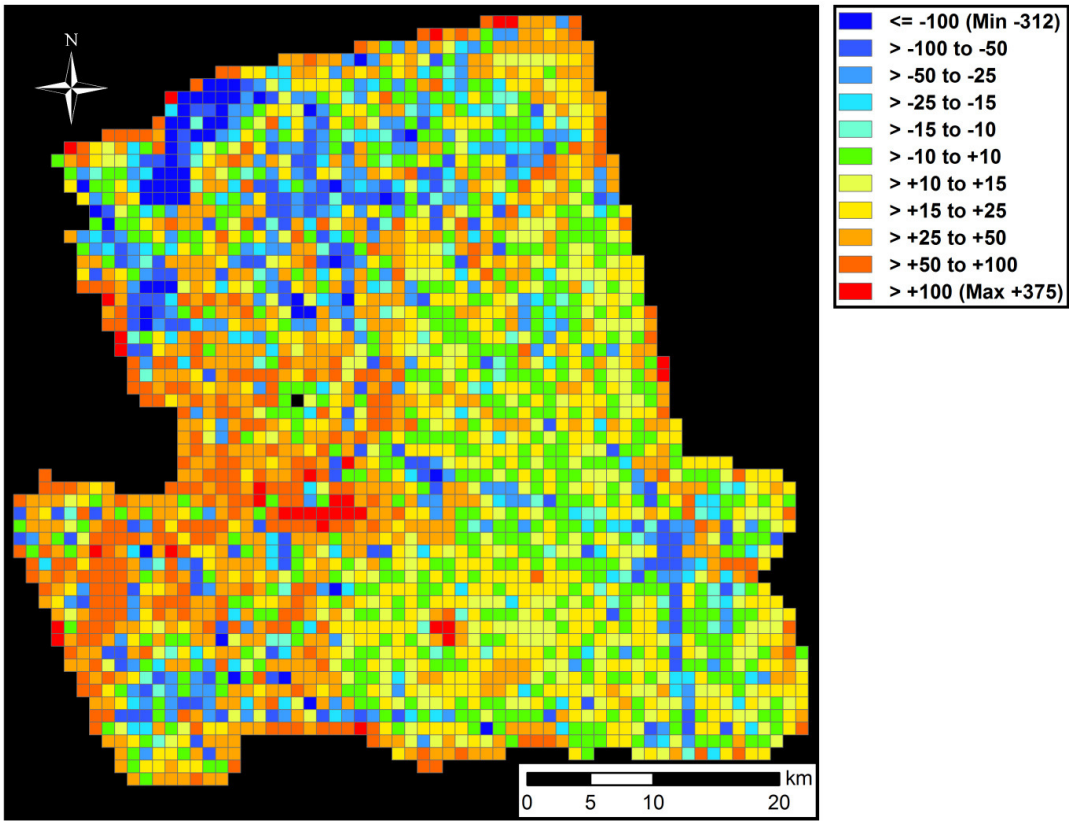

Fig. 46: Difference of estimated and processed DS&PS-density [DS&PS/km²] Ivrea site, CORINE 2006. Over-estimation, false alarm (> 0), underestimation, missed hits (< 0).

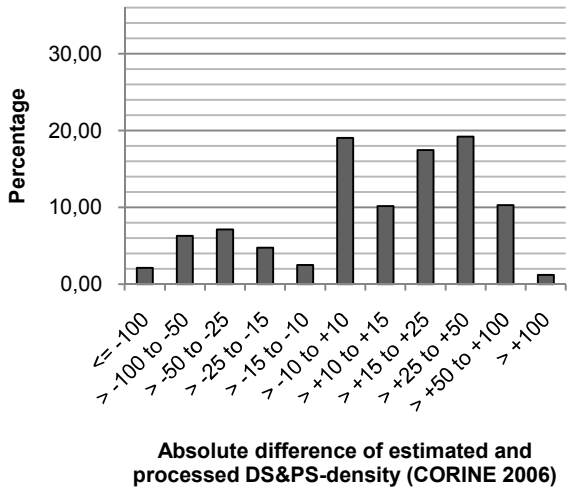

Fig. 47: Percentage of difference of estimated and processed DS&PS-density, Ivrea site CORINE 2006. Overestimation, false alarm (> 0), underestimation, missed hits (< 0).

e) Conclusion of validation

When comparing the validation results of a), b), c) and d) (Figs. 38, 41, 44 & 47), it can clearly be recognized that CORINE achieves the best result (= best fit of estimated and processed PS-density) for PS-estimation. The GlobCover dataset shows the second best result when estimating the PS-density. Generally GlobCover shows a stronger overestimation than the corresponding CORINE graph. Common to both land cover datasets is their stronger overestimation for the DS&PS-density compared with the corresponding PS-density estimation. Due to their different 'nature' (cf. chapter 3.4), the estimation of DS is quite more complicated than the estimation of PS.

When considering their tendency to overestimation, both GlobCover PS-density estimation and CORINE DS&PS-density estimation can be applied relatively well. GlobCover cannot be used for the estimation of absolute values of the DS&PS-density of the site, because of its very high overestimation. At GlobCover only the trend of the DS&PS-density distribution within the area of interest can be estimated.

Due to its higher spatial and thematic resolution the CORINE land cover is better suited for the land cover based PS-estimation method (relative PS-density) than the GlobCover dataset. However, as in some areas only GlobCover is available, it was also considered in this work. The best results can be expected when using the land cover data with the highest spatial and thematic resolution that is available for the site and when its climatic and terrain related conditions are considered.

In future, the statistical power of the relative PS(&DS)-density graphs could be increased by using data of more sites. This is especially meaningful for the estimation of DS&PS, which is based on 'only' nine datasets until now. Moreover, as the better suited CORINE dataset is only available in Europe, for other continents the relative PS(&DS)-density using other higher spatial and thematic resolution land cover data (e.g. Africover, chapter 5.1.3 c) should be applied.

5.2 NDVI based PS-estimation

5.2.1 The normalized difference vegetation index

By using data of optical multispectral (MS) sensors working in the visible and near infrared (NIR) region of the electromagnetic spectrum, one is able to calculate the normalized difference vegetation index (NDVI), being a measure of the site's vegetation density (HILDEBRANDT 1996, LILLESAND & KIEFER 2000:448, GUPTA 2003:572, ALBERTZ & WIGGENHAGEN 2009:284). The figure 48 shows the spectral signatures of water, dry soil and vegetation. The NDVI uses the significant difference of the vegetation signature between the RED (0.6 – 0.7 µm) and NIR (0.7 – 1.1 µm) channel (Eq. 47, HOFFER 1978).

$$NDVI = \frac{NIR - RED}{NIR + RED} \quad (47)$$

The strength of the NDVI is its rationing concept, which makes it independent of the illumination, atmospheric effects, topography, etc. Therefore, it is possible to compare NDVI images acquired at different dates. The scale of the NDVI is from -1 to +1. As water has no reflection in infrared, its NDVI is -1. The NDVI value of bare areas (rock, sand and snow) is less than +0.1. The NDVI increases with denser vegetation (NDVI range +0.1 to +0.7; ALBERTZ & WIGGENHAGEN 2009:284).

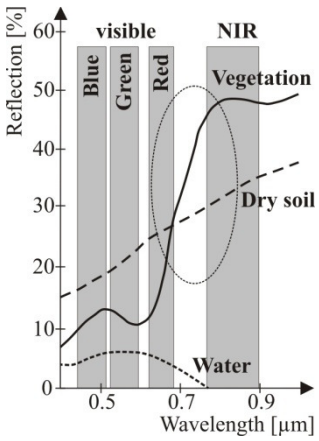

Fig. 48: The spectral signatures of water, dry soil and vegetation in the visible and NIR region of the electromagnetic spectrum (grey boxes: Landsat bands; modified after HILDEBRANDT 1996).

5.2.2 NDVI-PS-percentage method

a) Used datasets and preparation of the data

The NDVI-PS-percentage method enables to estimate for each NDVI value of the area of interest the probability to a find a PS-target, before the area is recorded by radar. This PS-estimation method was exemplary applied at the Aosta Valley site, the Budapest site and the Cairo site. For these sites several free available middle spatial resolution Landsat 7 ETM+ (Enhanced Thematic Mapper Plus) and ASTER (Advanced Spaceborne Thermal Emission and Reflection Radiometer) data from all seasons were chosen. The NDVI based PS-estimation method requires cloud-free optical images. Optical data from about the same acquisition time period as the SAR scenes were chosen (Tab. 1). Landsat and ASTER (orthorectified) data are freely available at: http://glovis.usgs.gov.

Additionally, two high spatial resolution optical images of the Budapest site were available: one KOMPSAT-2 (Korea Multi-Purpose Satellite-2) and one WorldView-2 image. To

achieve very high position accuracy of these images an orthorectification of the ortho-ready provided KOMPSAT-2 and WorldView-2 images using four ground control points was carried out. Two GPS control points from the National GPS Network of Hungary and two control points of the Uniform National Horizontal Network were used (www.geoshop.hu). For the orthorectification a SRTM DEM was used (RABUS et al. 2003). As only for the southern part of the site an X-band SRTM DEM (1 arc second spatial resolution) was available, a mosaic of the higher spatial resolution X-band DEM (in the south) and the lower spatial resolution C-band SRTM DEM (3 arc seconds), covering the northern part was calculated. At the border of these two DEMs, an offset of the height of about 43 m was recognized. This offset is equal to the value of the geoid undulation of 43.5455 m in the area of the Budapest site (central point: 47.5 N / 19.09 E). The geoid undulation is the vertical difference between geoid[7] and the reference ellipsoid[8] (ALBERTZ & WIGGENHAGEN 2009:18) and can be calculated for example at the GeographicLib (http://geographiclib.sourceforge.net/cgi-bin/GeoidEval?) for each location of the Earth. The calculation is based on the Earth Gravitational Model EGM2008, which has been released by the NATIONAL GEOSPATIAL-INTELLIGENCE AGENCY (2010). The value of the geoid undulation was subtracted from the X-band SRTM DEM to correct the offset of the DEM mosaic. Finally, the orthorectification of the WorldView-2 and the KOMPSAT-2 images was executed in the software package ENVI.

b) Description of the NDVI-PS-percentage method

The first step of the NDVI-PS-percentage method is the calculation of the NDVI for each optical remote sensing image according to equation 47. Band 3 (0.63 – 0.69 µm) is the RED channel and band 4 (0.76 – 0.90 µm) is the NIR channel of Landsat (Eq. 48; NASA 2012).

$$NDVI = \frac{NIR - RED}{NIR + RED} = \frac{(LandsatChannel\_4 \; - \; LandsatChannel\_3)}{(LandsatChannel\_4 \; + \; LandsatChannel\_3)} \quad (48)$$

The ASTER band 2 (0.63 – 0.69 µm) represents the RED and the band 3 (0.76 – 0.86 µm) the NIR channel (Eq. 49; NASA 2004).

$$NDVI = \frac{NIR - RED}{NIR + RED} = \frac{(ASTERChannel\_3 \; - \; ASTERChannel\_2)}{(ASTERChannel\_3 \; + \; ASTERChannel\_2)} \quad (49)$$

At KOMPSAT-2 the channel MS4 (0.63 – 0.69 µm) is in the RED and the channel MS3 (0.76 to 0.90 µm) is in the NIR region of the electromagnetic spectrum (Eq. 50; KOREA AEROSPACE RESEARCH INSTITUTE 2008).

$$NDVI = \frac{NIR - RED}{NIR + RED} = \frac{KOMPSATChannel\_MS3 - KOMPSATChannel\_MS4}{KOMPSATChannel\_MS3 + KOMPSATChannel\_MS4} \quad (50)$$

According to the DIGITALGLOBE (no year), the RED channel of WorldView-2 is the red band (0.624 µm – 0.694 µm) and the NIR channel used here the NIR1 band (0.765 – 0.901 µm) (Eq. 51).

$$NDVI = \frac{NIR - RED}{NIR + RED} = \frac{WorldView2\_NIR1 - WorldView2\_red}{WorldView2\_NIR1 + WorldView2\_red} \quad (51)$$

[7] The geoid is an irregular surface of constant gravity potential, which best fits the mean sea level.
[8] The ellipsoid is a mathematically defined surface, which approximates the physical geometry of the Earth with simplified geometry (ALBERTZ & WIGGENHAGEN 2009:18).

Then, the NDVI values and the distribution of the reference PS-data (Tab. 1) were compared. The result of this comparison is the so-called NDVI-PS-percentage. For each single NDVI value the percentage of pixels (of the NDVI raster) containing at least one PS-target is calculated. As the NDVI-PS-percentage is a ratio, it is independent of the absolute number of a certain NDVI value within the area of interest. Appendix 10 shows the implementation of the NDVI-PS-percentage calculation.

The concept of this PS-estimation method is to generate the graph of the NDVI-PS-percentage (see chapter 5.2.3) using geocoded PS-targets of a site where the PS-InSAR processing has already been successfully applied. This site should have a similar climate (and land cover if possible) as the area of interest where a new PS-InSAR processing is planned. Then, the NDVI of the area of interest is calculated. The generated NDVI-PS-percentage graph can be used to estimate for each NDVI value of the area of interest the probability to a find a PS-target, before the area is recorded by radar. It is important to use optical images of the same season for the NDVI calculation at the site (where PS-InSAR has already been applied) and at the area of interest. The optimal case would be that at both areas (the already processed site and the area of interest, where the new PS-InSAR is planned) the same or comparable SAR sensor, PS-detection and processing algorithms are used. However, this is not mandatory for this PS-estimation method. The final result of the NDVI-PS-percentage method is a map of the site showing for each single NDVI pixel the probability to find a PS-target.

5.2.3 Results of the NDVI based PS-estimation method

a) Cairo site – ENVISAT & Landsat

Figure 49a shows for each NDVI value of the Cairo site the percentage of pixels containing at least one PS-target. For the NDVI calculation six Landsat 7 scenes recorded at March and May 2001, May and December 2002 and February and March 2003 were available. Two peaks can be recognized. The first one ranges from NDVI value of ca. -0.2 to 0.0 (for PS-percentage > 5), representing Landsat scenes recorded in summer (March and May). The second peak (NDVI value from 0.0 to +0.16) is derived from the winter scenes (February and December).

The NDVI values of the graphs increase from summer to winter. This can be explained by the desert climate of the Cairo site, where the precipitation and thereby the growing period are limited to the winter season (cf. chapter 2). The higher vegetation density in winter causes an increase of the NDVI. Most PS-targets are surrounded by some vegetation. Therefore, the growing of the vegetation causes an increase of the NDVI value of the raster cell where the PS-target is located.

The NDVI-PS-percentage method is very well suitable at the Cairo site, due to the narrow peaks of figure 49a, which localize the high probability values to very limited NDVI ranges. This effect can be explained by (a) the equal spatial resolution of the sensors used (both ENVISAT ASAR and Landsat 7 have a spatial resolution of ca. 30 m) and (b) wide areas of the site are almost free of vegetation, especially the desert areas.

The graphs of figure 49a can be used to estimate the probability to find a PS-target by calculating the NDVI of the area of interest – prior to its SAR recording. For instance, at a NDVI

value of -0.1 or +0.1 this probability is ca. 25 % when using an optical image of the area of interest acquired in summer or winter, respectively.

b) Budapest site – TerraSAR-X & ASTER

For the Budapest site (Fig. 49c) three ASTER scenes with 0 % cloud cover and of the same time period as the reference SAR data (Tab. 1) were available. The graph of the October scene ranges from NDVI -0.4 to +0.4 (for PS percentage > 5). The May and June graphs (-0.3 to +0.4) match very good. Due to the higher vegetation density in summer (growing season), both graphs show slightly higher NDVI values compared to the October graph.

The graphs of the Budapest site are characterized by two significant differences compared to the graphs of the Cairo site (Fig. 49a): First, the PS-percentage for the Budapest site is very high (up to 65 %). This is due to (a) the very high spatial resolution of the SAR sensor used for the PS-InSAR processing of the Budapest site (TerraSAR-X, SM: ca. 3.3 m spatial resolution) and (b) the domination of urban area within the site, causing a very high number of PS-targets. Second, the graphs of the Budapest site are largely widened, which is caused by the strong differences of the spatial resolution of the optical sensor ASTER (15 m) and the SAR sensor TerraSAR-X (3.3 m). Figure 50 describes the influence of the spatial resolution more in detail.

c) Aosta Valley site – Radarsat-1 & ASTER

The NDVI-PS-percentage of the Aosta Valley site using four ASTER scenes recorded in May 2004, January 2006 and August and September 2009 is shown in figure 49b. The Aosta Valley site is in mountainous area (see chapter 2). This causes strong layover and shadowing complicating PS-InSAR applications (LILLESAND & KIEFER 2000, BARBIERI & LICHTENEGGER 2005, COLESANTI & WASOWSKI 2006). Therefore, layover and shadowing areas were simulated, using the method described in chapter 4.1.2, and then excluded from the succeeding application of the NDVI-PS-percentage method.

The graphs of figure 49b are widely scattered. In spite of the very low PS-percentage values of mostly less than 5 %, two peaks can be distinguished. The first one ranges from NDVI value -0.4 to 0.0 and represents the winter scenes of the mountainous site (January and May). The second peak ranges from NDVI value +0.13 to +0.55 contains the summer scenes of August and September. The NDVI strongly increases from winter to the growing season in summer, because of the increase of the vegetation density.

The wide scattering of the NDVI-PS-percentage graphs is caused by the high vegetation density of large areas of the Aosta Valley. Consequently, it is not possible to apply the NDVI-PS-percentage method in such densely vegetated areas – when using middle spatial resolution optical sensors, such as ASTER (cf. chapter 5.2.3e).

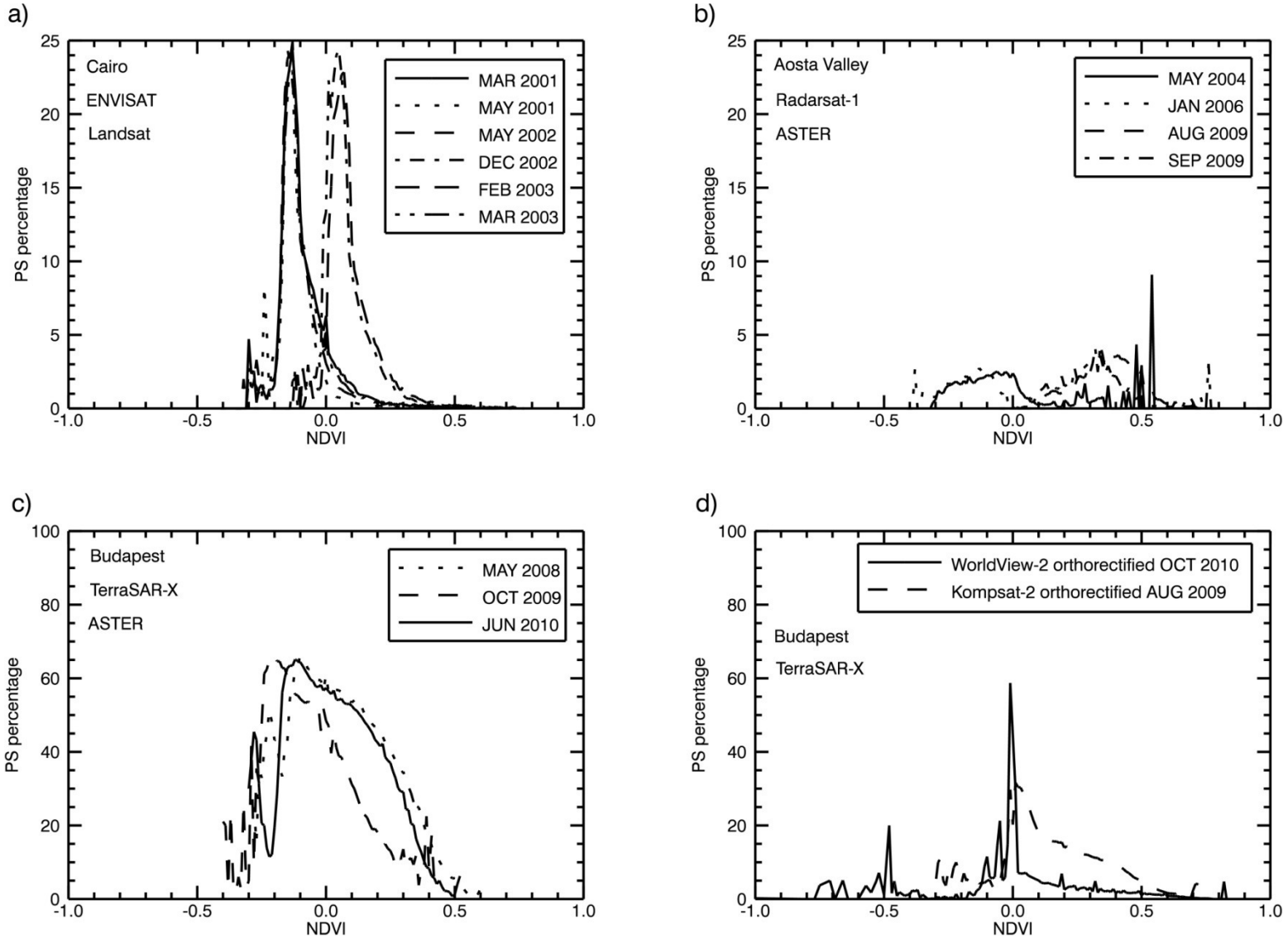

Fig. 49: Percentage of NDVI values with at least one PS-target. Cairo site using ENVISAT ASAR and Landsat 7 (a), Aosta Valley site using Radarsat-1 and ASTER (b), Budapest site using TerraSAR-X and ASTER (c) and Budapest site using TerraSAR-X and orthorectified WorldView-2 and KOMPSAT-2 (d).

d) Budapest site – TerraSAR-X & WorldView-2, KOMPSAT-2

Figure 49d shows the result of the Budapest site for the high spatial resolution optical data of WorldView-2 (October 2010) and KOMPSAT-2 (August 2009). Both graphs show a generally good match. The maximum value is centered at a NDVI value of ca. 0 in each case. The very narrow peak of the WorldView-2 graph reaches a maximum value of ca. 59 % (at NDVI -0.01), while the maximum of the KOMPSAT-2 graph is ca. 31.6 % (at NDVI +0.01). Both graphs are very similar for negative NDVI values, while the KOMPSAT-2 graph shows a slower decrease than the one of WorldView-2 for positive NDVI values. The reason of the slower decrease is (a) the slightly lower spatial resolution of KOMPSAT-2 (4 m MS) in comparison to WorldView-2 (2.4 m MS), causing slightly higher influence of vegetation surrounding a PS-target (for KOMPSAT-2), and (b) the August image of KOMPSAT-2 shows a higher vegetation density than the WorldView-2 scene recorded October. That means, if a PS-target is surrounded by some vegetation, its NDVI value is higher at the KOMPSAT-2 image. Therefore, the KOMPSAT-2 scene shows a higher PS percentage at higher NDVI values.

Figure 49d shows much better results than the middle spatial resolution ASTER data (15 m; Fig. 49c), because of the spatial resolution of KOMPSAT-2 (4 m MS) is almost as high as the spatial resolution of the SAR sensor (TerraSAR-X, SM: ca. 3.3 m) and the spatial resolution of WorldView-2 (2.4 m MS) is even higher than that of the SAR sensor.

e) The influence of the spatial resolution of the sensors

To explain the different behavior of radar and optical sensor and its influence on the NDVI-PS-percentage graphs, figure 50 shows a PS-target represented by one single building, which is surrounded by dense vegetation represented by forest. All the pixels around the illustrated one are covered with dense vegetation. The backscatter of the building dominates the surrounding vegetation in a SAR image of the pixel containing the building and vegetation. Assuming high coherence values in a time series of SAR images, this pixel would function as a PS-candidate. Contrary to this, the reflection and emission of the sunlight from all objects within the pixel is averaged in an optical image. Consequently, the NDVI value of this pixel is almost as high as the NDVI values of the surrounding pixels containing only dense vegetation.

The influence of the surrounding vegetation can be reduced by trimming the pixel area around the PS-targets. This can be realized by using high spatial resolution optical (multispectral) sensors, such as KOMPSAT-2 and WorldView-2 (cf. chapter 5.2.3d). Then, it is possible to apply the NDVI-PS-percentage method even in denser vegetated areas. Although high spatial resolution optical data is very suitable for NDVI-PS-percentage applications, their high charges limit their usage, especially for commercial purposes.

To conclude, the NDVI based PS-estimation method is very well suitable at areas of sparse vegetation when using freely available middle spatial resolution optical sensors such as Landsat and ASTER (cf. chapter 5.2.3a). For world-wide application of this PS-estimation method – also in areas covered with denser vegetation – high spatial resolution optical sensors such as KOMPSAT-2 or WorldView-2 are required (cf. chapter 5.2.3 d).

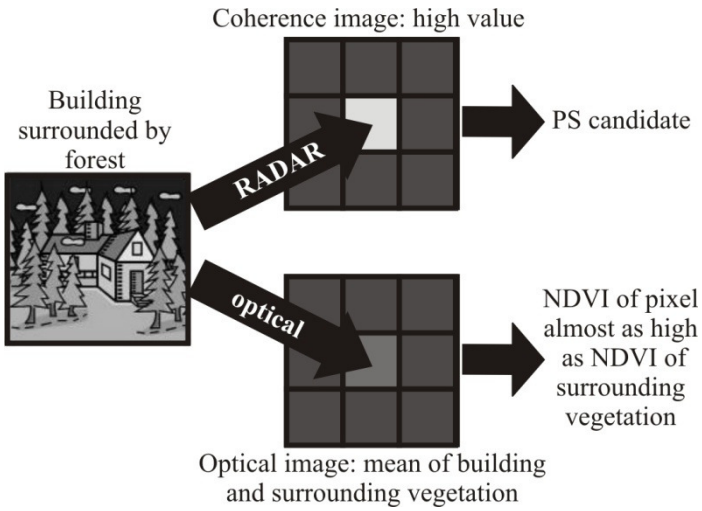

Fig. 50: Different behavior of a ground target in the visible to near infrared (used by optical sensors) and the microwave region of the electromagnetic spectrum (used by radar sensors).

5.3 PS-estimation based on topographic maps and OpenStreetMap data

5.3.1 Topographic maps used

Contrary to the aforementioned PS-estimation methods (chapter 5.1 & 5.2), the one described in this chapter not only enables the determination of the PS-density by using topographic maps (TM) and OpenStreetMap (OSM) data, but also the calculation of the distances between the estimated PS-targets and their distribution within the site – prior to its radar recording. In this work a further development of the groundwork of PLANK (2011) is presented. The PS-estimation method was applied at different types of TMs with different map scales ranging from 1:200,000 to 1:10,000. National and international maps of different formats: paper, scans, digital raster and vector data were used.

For the Cairo site a soviet military map (1:200,000) was available (UNITED STATES OF AMERICA WAR OFFICE 1958). This Russian topographic map uses Gauss Krüger projection based on the Krassowski ellipsoid and the geodetic datum Pulkovo 1942. For a part of the Budapest site a Russian topographic map (1:100,000) was available, too. Additionally, a vectorized topographic map (1:10,000) was acquired. For the Aosta Valley site a Russian topographic map (1:50,000) and the hiking map Courmayeur (1:25,000) were used. For the Bavaria site three types of topographic maps were available: a Russian topographic map (1:200,000), the digital topographic map of Bavaria (1:25,000; Gauss Krüger projection, Bessel-ellipsoid, Potsdam datum) and the so-called Bayern-Map plus. The last one is a vector map based on the digital landscape model and the cadastral map (BAYERISCHES LANDESAMT FÜR VERMESSUNG UND GEOINFORMATION 2012a, b). The aforementioned digital topographic map of Bavaria was also used for the Aschau am Inn (Germany) site. For the North Germany site, the Piedmont sites and the Netherlands site Russian TMs were only available at map scale 1:500,000 or smaller. As the map scale should be 1:200,000 or larger to show enough details for the PS-estimation method, this method could not be applied at these sites. OpenStreetMap data was used for all sites (except of the Cairo site) for the PS-estimation. It is freely available at http://download.geofabrik.de/osm/.

5.3.2 The method of TM and OSM based PS-estimation

5.3.2.1 Theory

Artificial objects are a significant source of PS-targets (FERRETTI et al. 2000a, b, 2001, COLESANTI et al. 2003a, HANSSEN 2005, REFICE et al., 2005, VILARDO et al., 2009). Therefore, in this PS-estimation possible PS-objects such as buildings, larger roads, railroads, etc. are extracted from TM and OSM data. Thereby, it has to be noticed that roads or railroads do not directly work as PS-targets, but PS-objects, such as road signs or overhead line masts, are bound to them. As most topographic maps do not contain natural PS-objects (e.g. single rocks, etc), these natural PS-sources cannot be extracted from the maps.

Depending on the type of the topographic map available for the site, different preparation work is necessary. Vector data, such as the vectorized TM of the Budapest site, the Bayern-Map plus, or the OSM data, can directly be used as input data for the PS-estimation procedure by extracting the useable information such as buildings, roads and railroads. As the roads and railroads are stored as polylines in the OSM data, to each line a buffer zone was calculated. The width of this buffer depends on the type of road or railroad (cf. appendix 11).

Contrary to vector data, raster data needs to be vectorized, which can easily be applied for digital raster data (e.g. the digital TM of Bavaria), where each type of map symbol (e.g. buildings) is classified by a specific color value. However, scanned topographic maps, such as the TM of Courmayeur or the Russian TMs, require time consuming half-automated vectorization. The color values of these maps get slightly distorted during the scanning process. For example, buildings of scanned maps show different color values in neighboring pixels, which makes classification during the vectorization process very difficult. Moreover, as these scanned maps were originally printed on paper, the map objects we are interested in (e.g. buildings, roads and railroads) are overlapped by disturbing map objects, such as labels, grids, contour lines, etc. The elimination of these disturbing map objects requires time consuming manually preparatory work, which limits the suitability of this map type for larger areas.

Figure 51 shows the procedure of the TM and OSM based PS-estimation. In the first step, possible PS-objects are extracted from the topographic maps and OSM data. Then, depending on the spatial resolution of the SAR sensor used the number of possible PS of the area of interest is determined. Afterwards, the PS-density is calculated according to equation 46 (chapter 5.1.2) using the number of estimated PS and the area of the site.

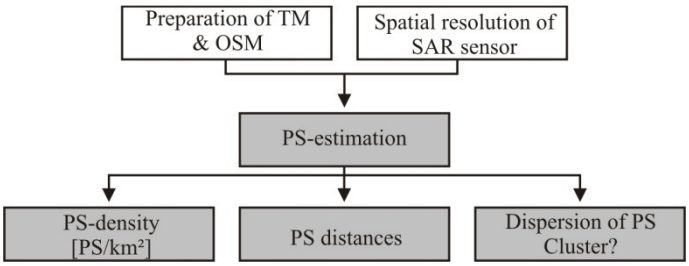

Fig. 51: The procedure of PS-estimation using topographic maps (TM) and OpenStreetMap (OSM) data.

According to ADAM et al. (2011), optimal PS-InSAR processing requires the maximal (horizontal) distance between two PS to be less than 700 m or 1,000 m in an extreme case. However, these values are a rule of thumb and not fixed values. The maximum PS distance for suitable PS-InSAR processing (especially for the phase unwrapping process) strongly depends on the atmospheric influence (cf. chapter 3.4). To be able to evaluate the estimated PS according their distance between each other, the Euclidean distance d_{ij} between each pair of neighboring PS is calculated in the PS-estimation procedure (Eq. 52).

Additionally, to the previously mentioned horizontal distance, also the vertical distance between two neighboring estimated PS is calculated. As radar echoes from PS-targets located at different elevation pass through a different number of atmospheric layers, the duration of the radar pulse is differently delayed. This can be misinterpreted as deformation signal. The influence of the vertical distance on the applicability of PS-InSAR processing strongly depends on the perpendicular baseline $B\perp$ between the two SAR sensors (cf. chapter 3.2). If $B\perp$ equals to zero, the topography of the site (and therefore the vertical distance) has no influence on the interferometric phase. This influence increases with increasing $B\perp$. The influence of the vertical distance between two PS-targets also depends on the climate zone of the site and on the season and daytime when the SAR data was recorded. For example in Central Europe, the atmosphere is more turbulent in the summer season than in winter. Therefore, in the worst case in an interferogram generated by a summer and a winter scene a vertical difference between two PS-targets of 100 m can cause a signal, which can be falsely interpreted as defor-

mation in the range of millimeters. As the turbulence in the atmosphere increases throughout the day due to increasing temperature caused by the solar radiation, the best recording time for SAR images is in the morning. However, this is not always possible, as the recording time is predetermined by the orbit of the satellite (MINET 2012). As the influence of the vertical distance on the applicability of PS-InSAR strongly depends on the individual situation for each site (clime zone, recording date and time and $B\perp$), in this work the calculation of the vertical distance is described (cf. appendix 12), but it is not classified like the horizontal distance (see above). Furthermore, one has to notice that the influence of the horizontal distance between the estimated PS on the applicability of PS-InSAR processing is much stronger than that of the vertical distance.

Next, the point pattern analysis (PPA) method nearest neighbor analysis (NNA) is used to analyze the distribution of the estimated PS. The NNA statistically compares an empirical point pattern (in our case the estimated PS-points) with a theoretical point pattern of a random distribution (CHEN, M.D. & GETIS 1998). First, the Euclidean distance d_{ij} for each empirical point i with the coordinates x_i/y_i to the nearest point j (x_j/y_j) is calculated (VASILIEV 1996; Eq. 52).

$$d_{ij} = \sqrt{\left(x_i - x_j\right)^2 + \left(y_i - y_j\right)^2} \quad (52)$$

Then, d_{ij} is arithmetically averaged over the number of estimated PS-points M (Eq. 53).

$$d_{averaged} = \frac{1}{M}\sum_{i=1}^{M} d_{ij} \quad (53)$$

Then, $r_{averaged}$, the arithmetically averaged distance of the random point pattern, is calculated with A representing the site area (Eq. 54).

$$r_{averaged} = \frac{1}{2\sqrt{\frac{M}{A}}} \quad (54)$$

Next, both the distribution of the empirical points (PS) and the distribution of the random point pattern are compared (Eq. 55).

$$Q = \frac{d_{averaged}}{r_{averaged}} = 2\frac{1}{M}\sum_{i=1}^{M} d_{ij} \cdot \sqrt{\frac{M}{A}} \quad (55)$$

If $Q = 1$, the empirical point pattern corresponds to a random distribution, as the arithmetically averaged distances of both point patterns are equal. $Q < 1$ indicates a clustered pattern of the empirical points, whereas $Q > 1$ is equal to a regular pattern. At $Q = 0$ all points are clustered to the same location. Parameter A has a big influence on the result of the NNA. Therefore, A is set to the area of the site.

5.3.2.2 The procedure of PS-estimation using TM and OSM data

This chapter explains the previously theoretically described (chapter 5.3.2.1) PS-estimation, which was implemented in ArcGIS®, step by step at a section of the Aosta Valley site. (For description of the technical implementation, see appendix 12). Figure 52a shows the topo-

graphic map of the city of Courmayeur (1:25,000). Bright green areas represent forest, white areas grassland and the buildings are mapped with a brown color. Then, possible PS-objects (e.g. buildings, railroads, etc. – red areas of figure 52b) are extracted from the topographic map and the OSM data. Next, a raster with cell size equal to the spatial resolution of the used SAR sensor (in this case 27 m; Radarsat-1 S3; see Tab. 1) is laid over the entire site (Fig. 52c). Then, the estimated PS are determined by selecting all raster cells that intersect with at least one possible PS-object (e.g. a building; Fig. 52d). In the next step, the Euclidean distance between the estimated PS is calculated according to equation 52 and classified regarding to the usability for PS-InSAR processing as described in chapter 5.3.2.1; Fig. 52e). As this figure only shows a small section of the site, only Euclidean distances less than 700 m are shown. Additionally to the horizontal Euclidean distance also the relative vertical distance to the nearest neighbor is calculated. The last step of the PS-estimation procedure based on TM and OSM data is the execution of the NNA (see chapter 5.3.2.1) to analyze the distribution of the estimated PS.

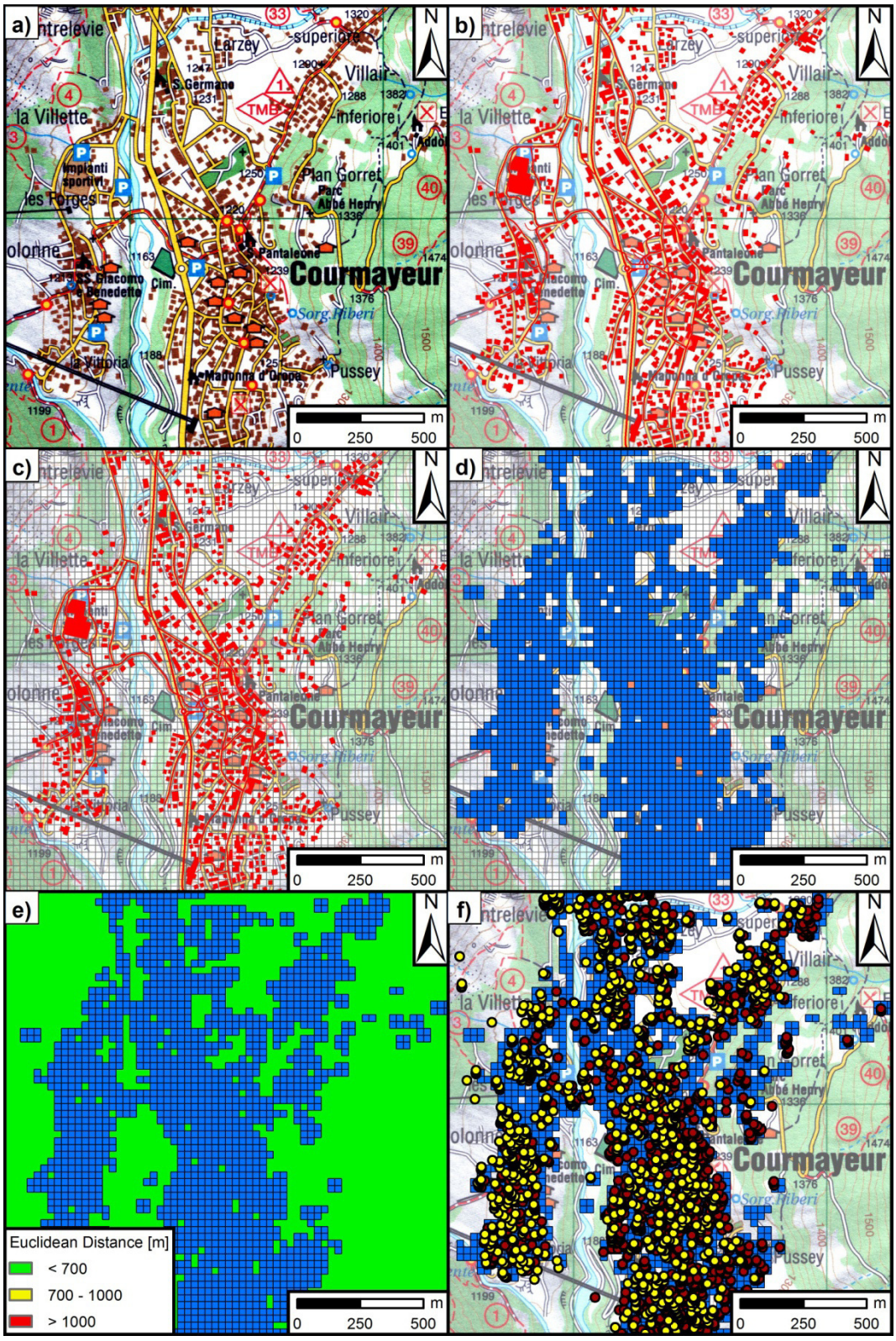

Fig. 52: **Original topographic map (a). Result of TM and OSM preparation (b). Raster over site (c). Raster cells selected: estimated PS (d). Euclidean distance between estimated PS (e). Validation of PS-estimation with real PS-targets (ascending: yellow; descending: red) (f).**

5.3.3 Results of the TM and OSM based PS-estimation

The PS-estimation procedure described in chapter 5.3.2 was executed twice for all aforementioned sites. First, it was executed by only using the topographic map (possible PS-objects: only buildings) and then by using both the TM and OSM data (additional consideration of roads and railroads). This twofold execution of the PS-estimation procedure was done to examine the influence of the additional use of OSM data on the quality of the PS-estimation.

As an example for all sites the results of the Bavaria site are shown in figure 53. The figure 53a shows the results of the PS-estimation by only using the topographic map of Bavaria (map scale 1:25,000) for extracting possible PS-objects. In the figure 53b the topographic map and the OSM data are used for this extraction. The estimated PS in figure 53a are restricted to settlement areas, causing more and larger areas which exceed the suitable-threshold of the Euclidean distance of 700 m between two PS. The estimated PS-density for the first case (only TM) is ca. 108 PS/km² (Eq. 46, chapter 5.1.2).

This PS-density increases by about 62 % (up to ca. 176 PS/km²) when both the topographic map and OpenStreetMap data are used for extraction of the possible PS-objects (Fig. 53b). As additional roads and railroads are considered as possible PS-objects when using OSM data, also the number and areas exceeding the maximal PS distance decrease. These areas are now mainly restricted to large water bodies (e.g. the Ammersee and Starnberger See southwest of Munich).

The results of the NNA for the Bavaria site show Q values less than 1, which indicates clustering of the estimated PS (cf. chapter 5.3.2.1) for both cases (only topographic map: $Q = 0.64$ and TM & OSM data: $Q = 0.80$). The NNA confirms the visual interpretation of figure 53: the estimated PS show strong clustering – especially in the areas of the cities Augsburg and Munich. As in the first case (only TM) the estimated PS are constricted to buildings, its Q value shows stronger clustering than for case two (TM & OSM): $Q_{TM} < Q_{TM\&OSM}$.

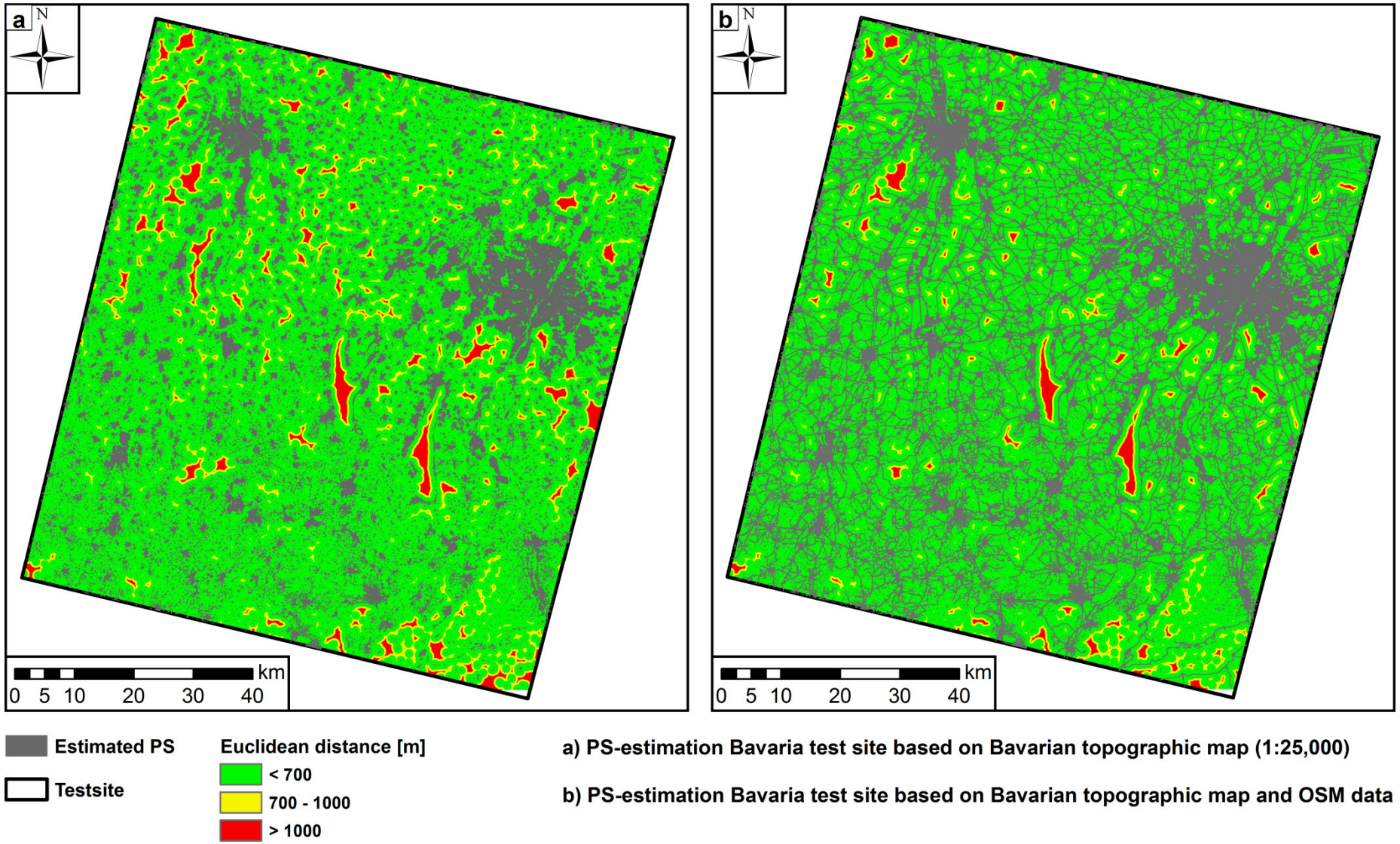

Fig. 53: **PS-estimation of the Bavaria site based on Bavarian TM (1:25,000). Only using the TM (a). Using both TM & OSM data (b). The largest PS-densities can be found at the cities Augsburg (NW) and Munich (NE). The lakes Ammersee and Starnberger See can clearly be recognized (red areas SW from Munich, no PS on water bodies).**

5.3.4 Validation of the results with real PS-data

The results of the PS-estimation were validated using real processed PS-datasets (Fig. 52f, Tab. 1). The validation addresses two questions concerning the PS-estimation results:

1) What percentage of the real PS is detected by the estimated PS?
2) How great is the probability of an estimated PS being a real PS?

The first question determines the quality of the PS-estimation, the percentage of the real PS detected by the assumed possible PS-objects (buildings etc.). The result of the second question, the probability of an estimated PS being a real PS, should be used at new sites where no SAR data is yet available.

Figure 54 shows the results of the first validation question for all sites. It can be recognized that the percentage of the real PS detected by the estimation is higher for all sites when additionally considering OSM data. This is due to the higher number of possible PS-objects that are considered in this case.

As already mentioned in chapter 5.3.1, due to the type of topographic map natural sources for PS-objects, such as single rocks, could not be considered in the PS-estimation procedure, as these objects are not mapped in the TM. This concerns also the Cairo site, where a section of it is dominated by rocky and stony desert, which is characterized by very good properties to form PS-targets (long term high coherence values; cf. chapters 2 & 5.1.3). However, the single rocks of the desert are not explicitly mapped in the Russian map of the Cairo site. Consequently, these areas could not be considered as possible PS-objects in the estimation. To eliminate the influence of the desert areas, a sub site without these areas was created. The percentage of real PS detected by the estimation is much higher for this sub site as the possible PS-objects are now mainly restricted to buildings and roads.

The relationship of the map scale and the probability of an estimated PS being a real PS is shown in figure 55. It is important to notice that not each building (or road sign, overhead line mast, etc.) always works as a PS-target in reality. Depending on the orbit (ascending/descending), incidence angle and spatial resolution of the satellite, the geometry, orientation and construction material of the building, etc., a building (or road sign, overhead line mast, etc.) could work as PS-target or not.

As ‘with OSM’ considers more possible PS-objects in the PS-estimation than ‘without OSM’, also the probability for overestimation increases. This is represented by the lower values in figure 55.

Generally the probability value increases with increasing map scale (Fig. 55). The map scale 1:10,000 (Budapest site) is an outlier due to the very specific land cover of this site. As the part of the Budapest site where this vectorized TM was available is a densely build-up area, almost each pixel within this area was estimated as a PS. This led to a strong overestimation of the PS and consequently to a lower probability value in figure 55. For larger sites with more variable types of land cover classes (not only densely build-up area), one could generally estimate higher probability values for such a large map scale.

The map scale 1:25,000 shows a very strong variance. The probability values of the Bavaria site are much lower than those of the Aosta valley site due to the more ‘imprecise’ geocoding

of the real (processed) PS-targets of the Bavaria site, which is caused by (a) using data from the ‘old’ ERS satellites with lower orbit accuracy and (b) mainly by using a ‘low’ spatial resolution DEM (SRTM C-band) for geocoding of the PS-targets. This ‘imprecise’ geocoding of the real PS distorted the results of the validation. The probability for an estimated PS being a real PS was estimated too low. For such large map scales one can estimate a probability value for the Bavaria site being as almost high as for the Aosta valley site.

The lowest value at the map scale 1:25,000, which belongs to the Aschau am Inn site, is caused by the very high spatial resolution of the radar sensor (TerraSAR-X, SM, ca. 3.3 m spatial resolution) used for the data acquisition. Due to this high spatial resolution very small (3.3 m x 3.3 m) raster cells representing the possible PS-targets were estimated in the PS-estimation method. Therefore, even very small geocoding inaccuracies (greater than 3.3 m), caused by the ‘low’ spatial resolution of the DEM, distort the validation of the PS-estimation. That means a geocoding error greater than the size of one raster cell can lead to a falsely underestimation of the validation.

The dotted lines of figure 55 show the ideal case of the probability values. Only the results of sites with relatively high geocoding accuracy of the PS-targets and no high spatial resolution SAR data (e.g. no TerraSAR-X data) are considered, reducing the values to the sites Aosta Valley and Cairo.

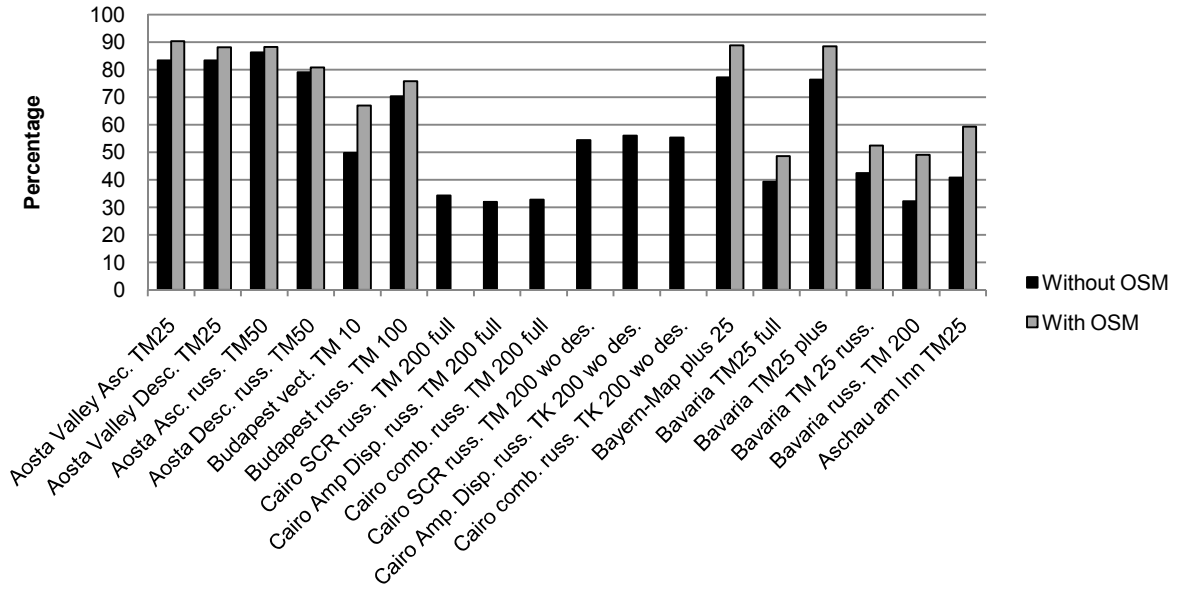

Fig. 54: **Percentage of real PS detected by estimated PS. Results without (black) and with (grey) additional consideration of OSM data (not available for the Cairo site). Aosta Valley site (Asc. = Ascending, Desc. = Descending orbit; TM25: TM of Courmayeur; russ. TM: Russian TM), Budapest site (vect. TM = vectorized TM), Cairo site (full = entire site; wo des. = site without desert), Bavaria site (full = entire site; russ. = sub site Russian TM; plus = sub site Bayern-Map plus).**

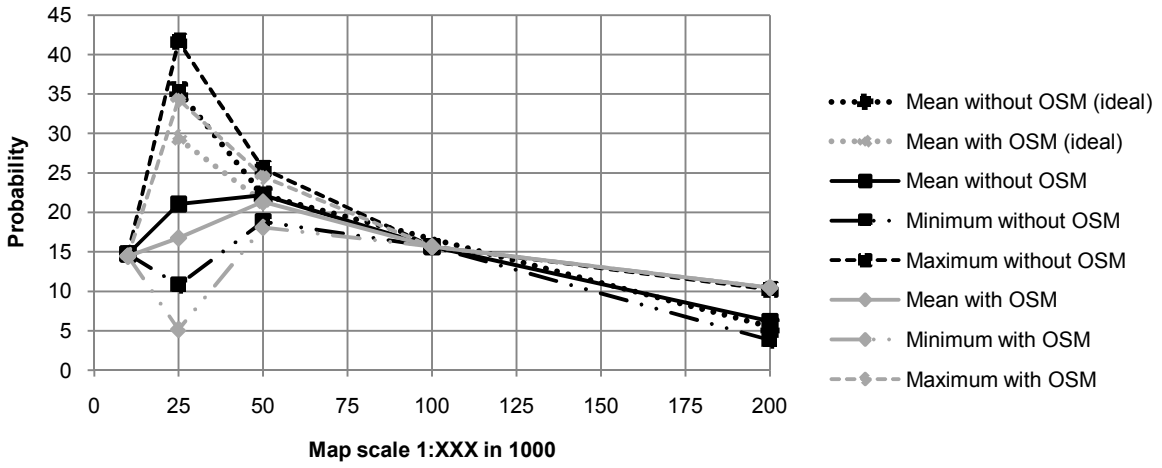

Fig. 55: **Influence of the map scale (in 1:XXX; e.g. '25' = 1:25,000) on the probability of an estimated PS being a PS in reality. The probability increases with increasing map scale (the vectorized TM of the Budapest site (1:10,000) is an outlier, see description in the text). The black lines show the results for 'without considering OSM', the grey lines 'with considering OSM'. The continuous line is the mean value of all sites in each case. The dashed-dotted line is the minimum and the short-dashed line the maximum value in each case. At the scales 1:10,000 and 1:100,000 (Budapest site) mean and extremes have the same values, because there is only one measured value. The dotted lines show the ideal case (see description in the text) of the mean value 'without considering OSM' and of the mean value 'with considering OSM', respectively.**

5.4 Conclusion of the second topic

Reliable PS-InSAR processing requires a stack of at least 15 to 50 SAR images, which makes its processing very time-consuming and costly. For a successful PS-InSAR application a sufficiently high number of PS within the site is needed. An estimation of these PS prior to the processing of several SAR images is very complicated. Therefore, the second topic of this work presented three new developed methods for estimating PS, prior to the radar recording of the site. Figure 56 shows a decision diagram to summarize the prerequisites, applicability and limitations of these PS-estimation procedures. The first method (cf. chapter 5.1) uses freely available land cover data (GlobCover and CORINE). This PS-estimation method can be applied, if an estimation or information about the absolute PS-density in the reference class 'urban area' of a site recorded by the same or comparable SAR sensor and processed by the same or comparable PS-processing method, as planned for the area of interest, is available. This PS-estimation method can be applied worldwide, if one considers the climatic and terrain related properties of the site (cf. chapter 5.1.3). The land cover based PS-estimation procedure is a very well suited and fast tool to get an overview of the expected PS-density of large areas. For instance, the PS-density for the entire European continent could be estimated for a given SAR sensor and PS processing method – when using CORINE land cover data.

The validation with real PS-data showed that CORINE land cover data can be applied very well for estimating the PS-density. For CORINE the difference of the estimated and processed PS-density is very low (chapter 5.1.4c). For instance, the majority (over 52 %) of the site area show differences of only ±15 PS/km² between the estimated and processed PS-density, from which over 35 % of the site area show even a difference of only ±10 PS/km². GlobCover is not as suitable due to its lower spatial resolution. The validation of the PS-estimation using GlobCover land cover data showed that the percentage of areas of low difference between estimated and processed PS-density (±15 PS/km²) is ca. 41 % (chapter 5.1.4a). Consequently, CORINE is preferred for European sites.

The second PS-estimation method uses the NDVI calculated from optical satellite data (cf. chapter 5.2). The procedure determines for each single NDVI value the percentage of pixels containing at least one PS-target. This method can be applied if (a) geocoded PS-targets of a site with similar climate as the area of interest or (b) a NDVI-PS-percentage graph of such a site are available (cf. chapter 5.2.3). NDVI-PS-percentage graphs, which show a strong narrow peak limited to a small NDVI value range, are very well suited for PS-estimation. It could be shown, that this procedure is very well suited in sites dominated by sparsely vegetated areas (e.g. the Cairo site) when using freely available middle spatial resolution optical sensors, such as Landsat and ASTER. If high spatial resolution optical sensors (e.g. WorldView-2 and KOMPSAT-2) are available, this PS-estimation method can be applied worldwide – even in areas with denser vegetation. As final result of the NDVI based PS-estimation method, one gets a map of the area of interest showing for each single NDVI pixel the probability to find a PS-target.

The third PS-estimation method (cf. chapter 5.3) not only estimates the PS-density of the area of interest, but also calculates and analyzes the distances between the estimated PS and their distribution within the site. This PS-estimation procedure is based on freely available and low-cost topographic maps (TM) and OpenStreetMap (OSM) data. Prerequisite for applica-

tion of this method is a topographic map with a map scale greater or equal than 1:200,000. Contrary to the aforementioned PS-estimation methods no results of PS-InSAR processing of another site are required for applying this procedure. Although this method is the most work-intensive one, it is the most site specific one. Consequently, this PS-estimation procedure is best suited for smaller sites – e.g. for monitoring landslides.

The method was validated using processed PS-data (results of real SAR data). The investigation of the first validation question 'What percentage of the processed PS is detected by the estimated PS?' showed that the additional use of OSM data increases this percentage value, as in the case of TM & OSM data more possible PS-objects are considered in the estimation (Fig. 54). The value of the percentage of processed PS detected by the estimated PS depends on the map scale of the topographic map used. For instance, at the Aosta Valley site this percentage is up to ca. 83 % based on a TM of map scale 1:25,000, while at the Cairo site (map scale 1:200,000) this percentage is only between 33 % and 56 %.

The second validation question is: 'How great is the probability of an estimated PS being a real (processed) PS?'. It is important to notice that not each building (or overhead line mast, etc.) always works as a PS-target in reality. Depending on the imaging geometry (orbit, incidence angle) and the spatial resolution of the satellite and the geometry, orientation and material of the ground target, a building could work as a PS or not. The probability of an estimated PS being a PS in reality strongly increases with increasing map scale, as the TMs are more detailed at a larger map scale. At a map scale of 1:200,000 this probability value is very low (ca. 5.5 % ±2 %). For a map scale of 1:50,000 it increases to about 22.1 % (±3.4 %) and for a map scale of 1:25,000 to about 35.4 % (±6.3 %) (ideal case in Fig. 55). These probability values can be used at new sites where SAR data is not yet available.

A general answer to the question 'When use which PS-estimation method?' is: If – in the ideal case – the prerequisites of all three PS-estimation methods are fulfilled, all three procedures should be applied, starting with the one based on land cover data to get a fast overview of the expected PS-density of the area of interest – even for large areas. Then, the NDVI-PS-percentage method should be applied to get information about the probability to find a PS-target at a certain pixel, based on its NDVI value. As the accuracy of this PS-estimation method is at the level of the spatial resolution of the optical data used, it is more detailed than the first method based on land cover data. The last step would be the application of the third PS-estimation method, which is based on topographic maps and OpenStreetMap data, to get the most site specific information about the expected PS-targets, including (a) their density, (b) the distances between each other and the analysis of it and (c) the analysis of their distribution within the area of interest. As, due to the map content, the TM and OSM based PS-estimation method only considers artificial PS-objects (e.g. buildings, road signs, overhead line masts, etc.), the other two PS-estimation methods based on land cover data and the NDVI, respectively, should also be applied, to get additional information on natural PS-targets.

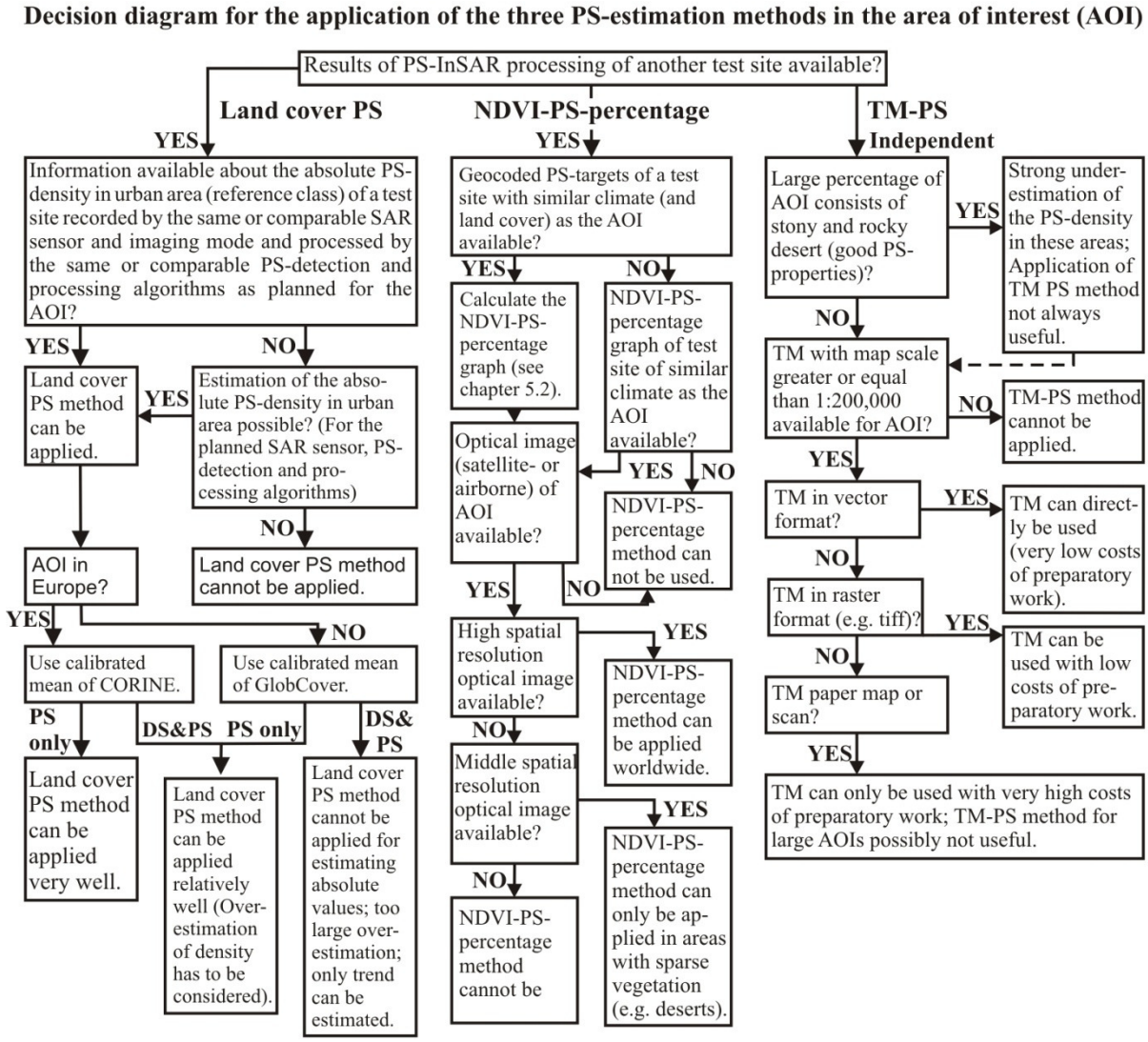

Fig. 56: Decision diagram for the application of the three PS-estimation methods in the area of interest (AOI).

6. Determination of the minimum number of SAR images required for PS-detection

The third topic of this work deals with a subject that is – compared to the second topic (chapter 5) – one step further towards PS-InSAR processing. As already mentioned in chapter 3.4, high quality PS-InSAR processing requires a stack containing at least 15 to 50 SAR images (FERRETTI et al. 2000b, COLESANTI et al. 2003a, HANSSEN 2005, CROSETTO et al. 2010, WASOWSKI et al. 2012), which is a very critical cost factor when applying this method. It is difficult to estimate the applicability of the PS-InSAR technique at a certain site prior to the processing of several SAR images (COLESANTI et al. 2003b, COLESANTI & WASOWSKI 2006, CASCINI et al. 2009). The most interesting areas for this research are rural areas, as in such areas the PS-density is not always high enough for a successful PS-InSAR processing.

Here, the minimum numbers of SAR images required for PS-detection is examined. That means, this topic deals with the number of SAR scenes needed for detection of PS-targets (PS candidates) to test whether the number of PS-targets of a certain site is high enough for a subsequent PS-InSAR processing, which of course then requires a higher number of SAR images (see above).

As a reference PS-detection was applied to a stack of 81 co-registered ERS scenes (see chapter 2c for the description of the site). Then, the number of SAR scenes of the stack was halved and again the PS-detection was applied optimized for a certain false alarm rate, which was set constant in the succeeding steps of the procedure (constant false alarm rate, CFAR). Afterwards, this procedure of halving the number of SAR images and PS-detection using a CFAR was continued until the number of SAR images of the stack was reduced to only one image. Additionally, a suitability criterion was used to guarantee that the number of correctly detected PS is at least as high as the one of falsely detected PS.

The goal is to use the results of this topic to order the minimum number of SAR scenes to test the applicability of the PS-InSAR technique – prior to the ordering of the entire stack of SAR images required for PS-InSAR processing.

6.1 Detection theory

In chapter 3.4 the two main techniques for PS-detection, amplitude dispersion index D_a and SCR, are described. In this topic, the PS-detection by continuously reducing the number of SAR images – even to only one image – is studied. Therefore, only the second PS-detection concept thresholding on the SCR can be applied, as this method compares the intensity of the pixel with its spatial neighborhood and not only in time as the concept of the thresholding on the amplitude dispersion index. In this work amplitude data was used – not the complex SAR data, as the phase signal contains no useful information when using only one SAR image.

This chapter describes the theory for PS-detection using the concepts of detection theory (BARKAT 1991, MACMILLAN & CREELMAN 2005). When deciding whether a pixel of a SAR image is a PS-target or not, the null hypothesis H_0 is that the pixel is no PS and belongs to the clutter. The alternate hypothesis H_1 determines the pixel as PS-target. There are four possibilities when applying PS-detection:

I) Deciding for H_0 when H_0 is true → correct rejection → pixel is correctly not selected as PS

II) Deciding for H_0 when H_1 is true → missed hit → pixel is falsely not selected as PS

III) Deciding for H_1 when H_0 is true → false alarm → pixel is falsely selected as PS

IV) Deciding for H_1 when H_1 is true → correct detection (hit) → pixel is correctly selected as PS

P_0 being the probability of H_0 and P_1 being the probability of H_1 and having a binary hypothesis testing problem, it follows $P_0 + P_1 = 1$.

Being $f_{X|H_j}(x|H_j)$ the conditional density functions of $P(Decide\ H_i|H_j)$, with $i, j = 0$ or 1, the probabilities of missed hit P_M, correct detection P_D and false alarm P_F are as follows (Eqs. 56 to 58).

$$P_M = \int_{-\infty}^{\gamma} f_{X|H_1}(x|H_1)dx \quad (56)$$

$$P_D = \int_{\gamma}^{+\infty} f_{X|H_1}(x|H_1)dx \quad (57)$$

$$P_F = \int_{\gamma}^{+\infty} f_{X|H_0}(x|H_0)dx \quad (58)$$

With X being a random variable and γ the threshold at which a pixel is detected as a PS (value of SCR).

Since it is not possible to assign cost values for the four decision options (I to IV) and a priori probability values of P_0 and P_1 are not known, P_F is fixed to some value w while P_D is maximized (CFAR, Neyman-Pearson test; BARKAT 1991).

In the literature, the CFAR method is mainly used for automatic target detection in SAR images (using one SAR image and a stack of images), especially for ship detection (CRISP 2004, LÒPEZ-ESTRADA et al. 2004). In this technique, for each pixel of the SAR image the mean μ and the standard deviation σ of the clutter around the pixel are determined. Then, the optimal threshold γ for each pixel is calculated by using μ and σ and a certain probabilistic model describing the distribution of the clutter. In this way, the false alarm rate can be made constant at each pixel (CFAR). According to LÒPEZ-ESTRADA et al. (2004) and MARINO & HUGHES (2011), the most used probabilistic models are the Weibull, Rayleigh, K and Gaussian distributions. The K-distribution (and the Gaussian for calm sea) are usually used for ship detection applications (sea as clutter), while the Weibull distribution and its special form, the Rayleigh distribution, are mainly used for detection of stationary man-made objects (such as PS; WANG et al. 1994).

In this work the term CFAR is used in another way. The goal is to determine the minimum number of SAR images required for suitable PS-detection. This was achieved by applying an entirely experimental approach (see chapter 6.2.1). No probabilistic model was used to estimate the distribution of the clutter. Instead of this, the threshold γ was optimized for each number N of used images to receive a certain false alarm rate, which was set constant for the

entire experiment (CFAR). This CFAR can be called 'global' CFAR, as this value is used for the entire SAR image.

6.2 Constant False Alarm Rate – CFAR

6.2.1 CFAR experiment methodology

As described above, PS-detection was applied using a stack of 81 co-registered ERS scenes. In the first step, the intensity of all 81 SAR images was calculated by squaring the amplitude. Then, following multi-looks were generated by calculating the mean over time for each single pixel of the SAR images (Fig. 57, temporal averaging, BARBIERI & LICHTENEGGER 2005): one 81-look image, two 40-look images, five 16-look images, ten 8-look images, twenty 4-look images, forty 2-look images and the original (1 look) SAR data. The images were sorted by the acquisition time.

As a reference PS-detection was applied at the 81-look SAR image. The SCR was calculated according to equation 17 (cf. chapter 3.4) by using a 5 times 5 pixel matrix for the clutter and considering only the main lobe (1 pixel) for the signal. To guarantee that image regions with high intensity values (e.g. urban areas or layover areas) do not cause too strong clustering of the PS, a pixel with a SCR value above a certain threshold γ is only selected as a PS-target, if it is also the maximum value in a 5 times 5 pixel neighborhood (LAMBERS & KOLBS 2008), which ensures that the distance between two PS is at least three pixels (two pixels buffer zone in between).

For the reference PS-detection, based on the 81-look SAR image, all pixels above a SCR threshold of $\gamma = 1.5$ were chosen as PS-targets. In the next step, the number of SAR scenes of the stack was halved to 40-looks and again the algorithm described above was applied. As described in chapter 6.1, the SCR threshold γ was increased to receive for the two 40-look SAR images a certain false alarm rate, which was fixed to 5.000 E-04 for the entire procedure (CFAR). As two 40-look images were calculated (image 1 to image 40 and image 41 to image 80), this procedure was executed twice. The procedure of halving the number of SAR images (number of used images N) and PS-detection by optimizing (increasing) γ to receive a CFAR was continued until the number of SAR images of the stack was reduced to only one image. It was executed five times for the 16-look image, ten times for the 8-look image, twenty times for the 4-look image, etc. (see above).

6.2.2 CFAR experiment – results and discussion

Figure 57 shows the reduction of the speckle[9] effect by temporal averaging. PS-detection by applying the SCR method is very well suited, if there is a large number of SAR images available (e.g. the reference 81-look intensity image), as the influence of the speckle effect is then strongly reduced. However, when reducing the number of images down to only one (ML01 in Fig. 57), the influence of speckle increased. Consequently, more pixels showed high intensity

[9] The speckle effect is a noise-like characteristic, which occurs at coherent systems such as SAR. Speckle is a random structure of pixels and is caused by the interference of electromagnetic waves scattered from objects on the ground. The different backscatter of all ground objects within one pixel is coherently added up to one value. This sum can be either high (constructive interference) or low (destructive interference). This interference determines the brightness of each image pixel and causes the 'salt and pepper' like structure of a SAR image. Speckle can be reduced by multilooking (filtering in time or space; ALBERTZ & WIGGENHAGEN 2009:307).

values over a short time period, resulting in a falsely high SCR value and a higher false alarm rate.

The visual interpretation of figure 57 shows a noticeable reduction of the speckle effect by temporal averaging for $N = 4$ and a significant decrease of this effect for $N = 8$.

To show the influence of the speckle effect's increase caused by the reducing of N on the SCR more detailed, the histogram of all SCR images was calculated (Fig. 58). The SCR of the 81-look image showed the strongest centering on its mean value μ (low standard deviation σ). When reducing N, the frequency value at μ is reduced while σ increases. The integral of the SCR histograms remains constant for all values of N. As the graphs get wider (σ increases) with decreasing of N, γ had to be increased to preserve CFAR (constant integral for SCR values greater than γ).

Figure 59 confirms the visual interpretation of figure 58: σ of the SCR images decreases with increasing N. The strongest decrease of σ can be recognized for $N < 4$ looks. For $N > 4$ and especially for $N > 8$ looks the decrease σ is relatively small. That means the strongest reduction of the speckle effect appears within the first 8 looks (see also figure 57 for visual comparison). For $N > 8$, there is only less improvement in the reduction of the speckle.

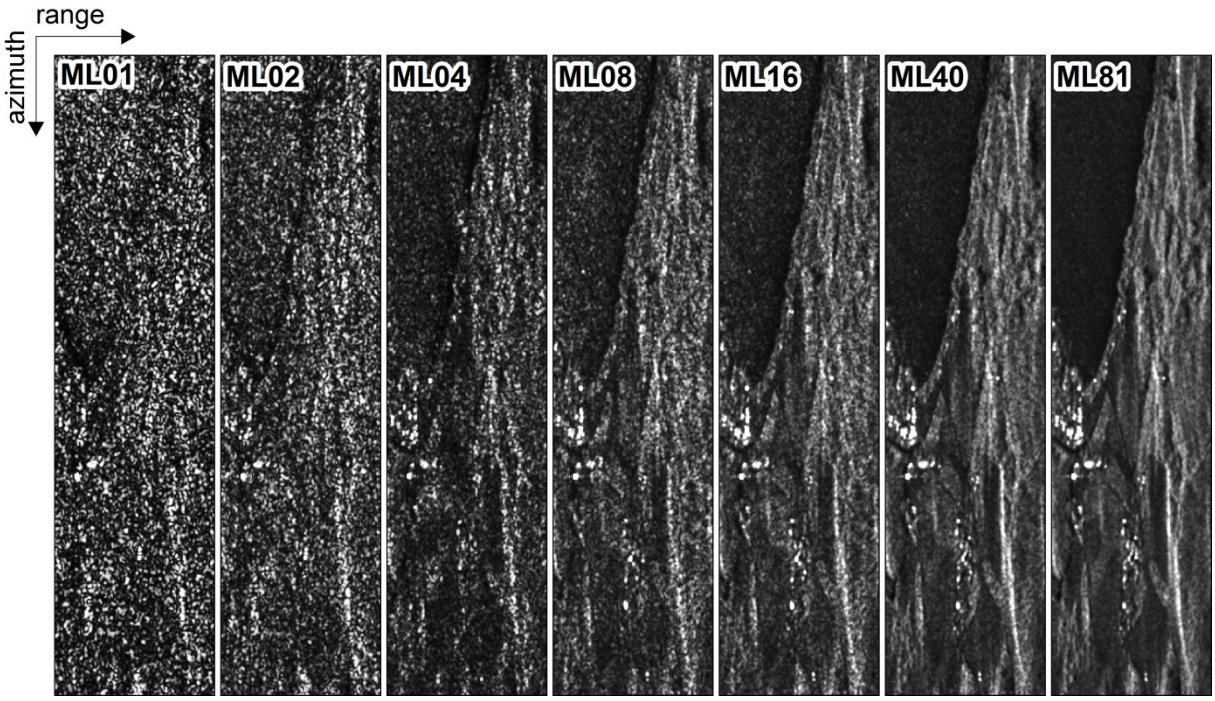

Fig. 57: **Intensity ERS SAR image of a detail of the test area. The upper left parts of the images show the lake Wörthsee. The 1-look image (ML01) shows high influence of the speckle effect. One can clearly see the speckle reduction by temporal averaging up to the best result for the 81-look image (ML81).**

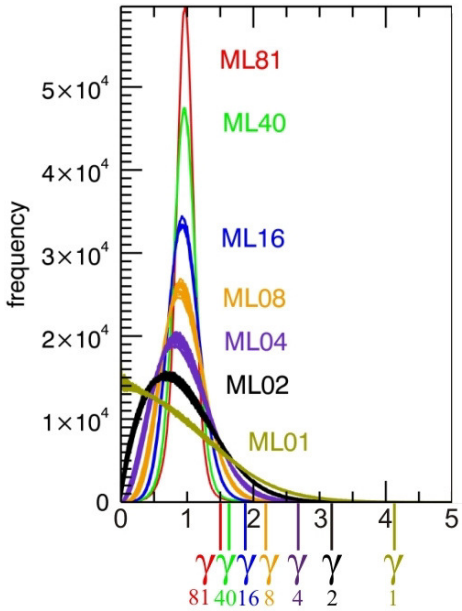

Fig. 58: **Histogram of the SCR images from 81-looks (ML81) to 1-look (ML01). One can clearly see the widening of the graphs (= increase of σ) when reducing N. The colored lines on the x-axis show the positions of the mean of the SCR threshold γ for the different numbers of N to preserve CFAR.**

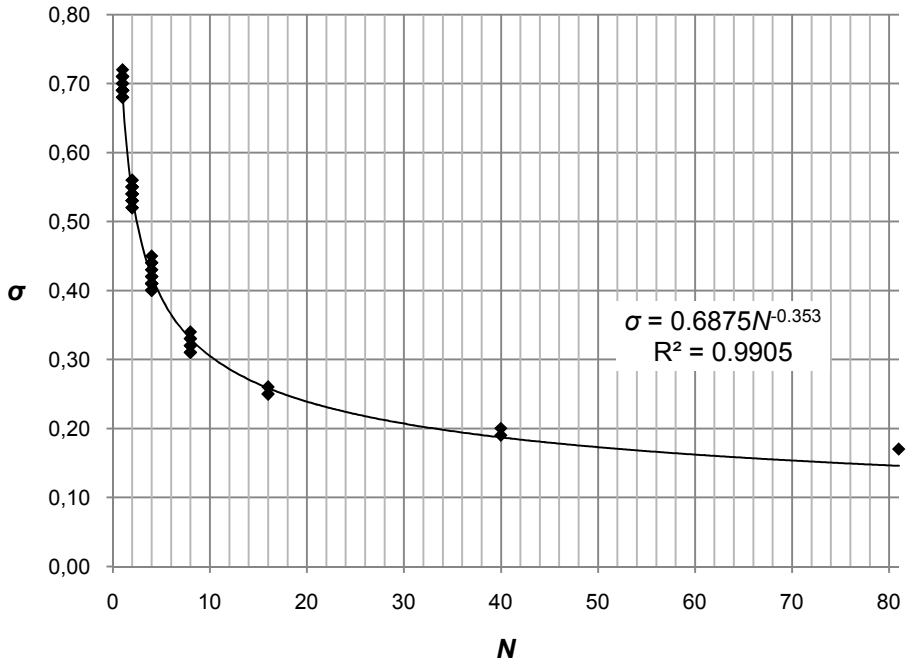

Fig. 59: **σ of the SCR image decreases with increasing N.**

$\Delta\gamma_i$ be the increment from the SCR threshold γ_{81} of the reference PS-detection to the SCR threshold γ_i to fulfill CFAR for a certain number of N, with i = 1, 2, 4, 8, 16, 40 (Eq. 59).

$$\Delta\gamma_i = \gamma_i - \gamma_{81} \quad (59)$$

Figure 60 shows a strong linear relationship between $\Delta\gamma$ and μ. The trend line of figure 60 (Eq. 60) has a high coefficient of determination R^2 of 0.9722 (R^2 = 1 means a total conformity of the data values and the trend line).

$$\Delta\gamma = -42.053\mu + 41.448 \quad (60)$$

After the computation of the optimal value of γ to preserve CFAR for the two 40-look and the five 16-look images, the precursor of equation 60 was calculated the first time. This equation and the transformation of equation 59 were used in the experiment to estimate γ of each SCR image for $N = 8$ prior to its detailed computation (with γ_{81} equal to 1.5, see above; Eq. 61). As for each single SCR image for each number of N several courses of the experiment were required to 'find' the optimal value of γ to preserve CFAR, this a priori estimation of γ enabled to reduce the number of optimization tests for each SCR image.

$$\gamma_i = -42.053\mu_i + 42.948 \quad (61)$$

In the next step, a precursor of equation 61 was optimized using the additional results of the computation of γ for $N = 8$. This procedure was continued until γ was determined for all images of $N = 4$, $N = 2$ and $N = 1$, while continuously optimizing equation 61 and figure 60 to the final version shown here.

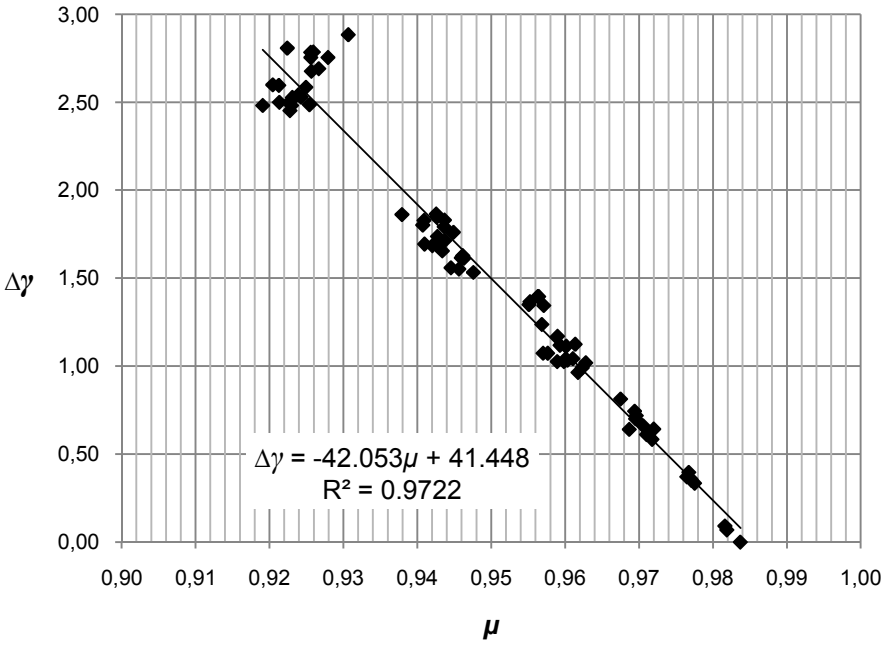

Fig. 60: Relationship between $\Delta\gamma$ and μ. The seven clusters show the different numbers of N: from the lower right ($N = 81$) to the upper left ($N = 1$).

Also the parameters $\Delta\gamma$ and σ show a strong linear relationship (Fig. 61, Eq. 62). The increase of σ with decreasing N (see Fig. 59) reflects the increase of the speckle effect when reducing N (see Fig. 57). Therefore, γ (and $\Delta\gamma$) has to be increased to preserve CFAR.

$$\Delta\gamma = 5.1358\sigma - 0.9931 \quad (62)$$

Similarly to equation 61 and figure 60 (see above), equation 63 and figure 61 were optimized step by step while continuously decreasing N. As R^2 (= 0.9913) of the trend line of figure 61 (Eq. 62) is even higher than R^2 of figure 60, the image parameter σ is slightly better suited for the estimation of γ than the parameter μ.

$$\gamma_i = 5.1358\sigma_i + 0.5069 \quad (63)$$

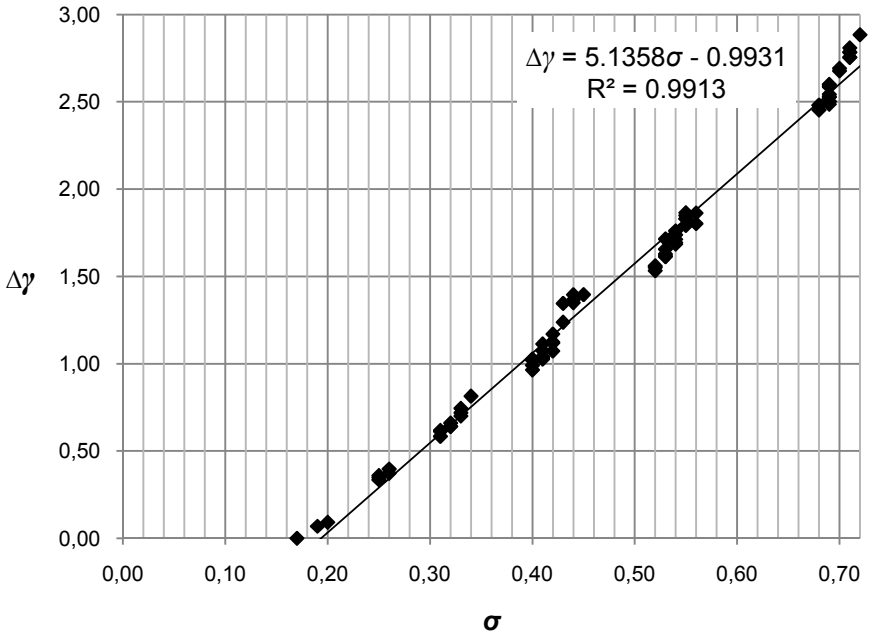

Fig. 61: Relationship between $\Delta\gamma$ and σ. The seven clusters show the different numbers of N: from the lower left ($N = 81$) to the upper right ($N = 1$).

Next, the behavior of the hit rate D (correctly detected PS-targets) was investigated. As explained above, when reducing N, γ has to be increased to preserve CFAR. Consequently, P_M increases while P_D decreases. The hit rate of the reference PS is equal to 1 (= 100 %). With decreasing N, the hit rate decreases down to ca. 0.02 for $N = 1$ (Fig. 62). At $N = 8$ ca. 32 % of the final hit rate of the 81-look image is received. For $N > 8$ the gradient of the increase of the hit rate flattens out (logarithmic-function). At high values for N there is only a small increase of the hit rate.

The horizontal line in figure 62 marks the suitability boundary. At this boundary, the absolute number of correctly detected PS is equal to the number of falsely detected PS. As a CFAR of $^1/_{2000}$ (= 5E-04) was used in the experiment and the site contains 2034095 pixels, 1017 PS are falsely detected in each instance of the experiment ($^{2034095}/_{2000} = 1017$), which is equal to a hit rate of ca. 0.325 ($^{1017}/_{3134}$; with 3134 PS detected at the reference 81 look SAR image). Below the suitability boundary the number of falsely detected PS is higher than the one of correctly detected. For the chosen value of the CFAR (see above), the suitability boundary cuts the trend line of the hit rate at ca. $N = 8$. Therefore, for the chosen CFAR (5E-04), at least 8 SAR images are required to guarantee that more correctly than falsely detected PS are hit.

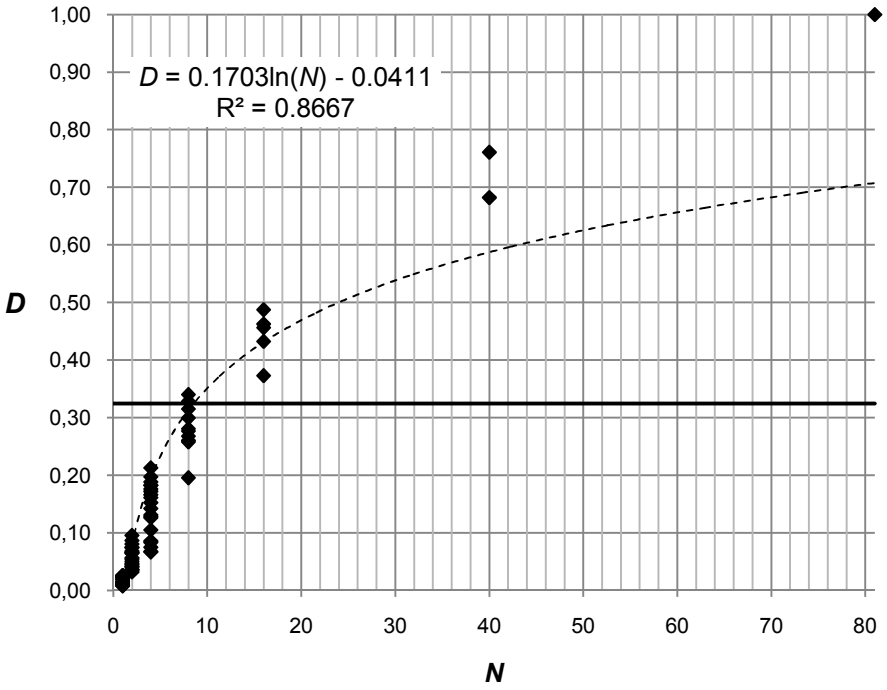

Fig. 62: The hit rate *D* decreases with decreasing of *N*. The horizontal line marks the suitability boundary, at which the number of correctly and falsely PS is equal.

As the influence of the speckle effect increases with decreasing N (see Fig. 57), also σ increases with decreasing N (see Fig. 59). Consequently, as D decreases with decreasing N (Fig. 62), an increase of σ is related to the decrease of D (Fig. 63). As the increase of the speckle effect's influence is more related to σ, D shows a much stronger relationship to σ, than to N (higher value of R^2 at the trend line of figure 63 than at the one of figure 62).

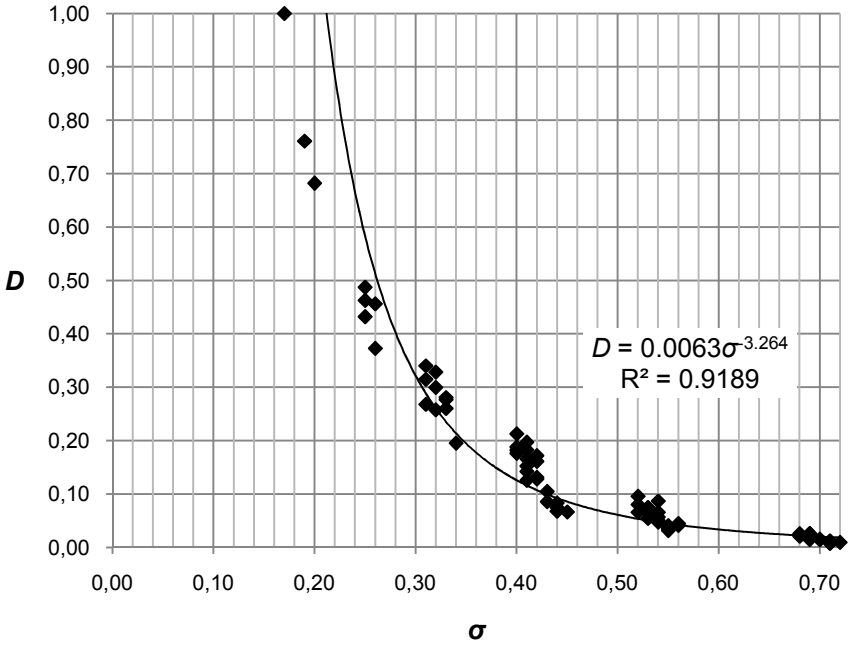

Fig. 63: The hit rate *D* decreases with increasing of *σ*. The seven clusters show the different numbers of *N*: from the upper left (*N* = 81) to the lower right (*N* = 1).

As described above, the significant changes in the graphs of the figures 57, 59 and 62 can be noticed at the interval $4 < N < 8$. The significant flattening of the graphs begins at about $N > 8$. That means for $N > 8$ no significant effect for reducing σ by increasing N was achieved (Fig. 59). The speckle effect is mostly reduced within the first 4 to 8 looks (Fig. 57). When additionally considering the suitability boundary of figure 62 – number of correctly detected PS should be at least as high as the one of falsely detected PS –, it can be concluded that at least 8 SAR images are required for PS-detection with usable results.

σ, which is related to the speckle effect, is well reduced at this value of N. The speckle effect is the most influencing factor when applying PS-detection based on the SCR method, especially when using a small number of SAR images.

6.3 Receiver Operating Characteristic – ROC

6.3.1 ROC experiment methodology

In the next step, the CFAR method described in chapter 6.2.1 was extended as follows to get more generally valid results. Contrary to the first experiment (CFAR, chapter 6.2), this second experiment was applied for different false alarm rates (rate of falsely detected PS) F. For all generated multi-looks the hit rate D (rate of correctly detected PS) and F were determined for different values of SCR thresholds γ. The experiment was applied for $0 \leq F \leq$ 5E-04 (value of CFAR of the first experiment) for N equal to 40, 16, 8 and 4 (for smaller numbers of N (2 and 1) this experiment was not sensible as at this number of N the number of falsely detected PS strongly overtakes the one of correctly detected PS).

To evaluate the results, suitability boundaries were set: The number of correctly detected PS should be at least k times the number of falsely detected PS (Eq. 64).

$$D \cdot PS_{81} \geq k \cdot F \cdot Pixel \quad (64)$$

With: PS_{81} = number of PS at reference 81 look SAR image (3134 PS); $Pixel$ = number of all pixels within the site (2034095). From equation 64 it follows (Eq. 65).

$$D \geq k \frac{F \cdot Pixel}{PS_{81}} \approx 649.41 \cdot k \cdot F \quad (65)$$

k equal to 1 marks the lowest suitability boundary: the number of correctly detected PS should be at least equal to the one of falsely detected PS (cf. also Fig. 62). In the experiment the suitability boundaries of k = 1, 1.5 and 2 were used.

6.3.2 ROC experiment – results and discussion

Figure 64 shows the results of the experiment described in chapter 6.3.1. The hit rate D and false alarm rate F are plotted in a so-called Receiver Operating Characteristic (ROC) plot (BARKAT 1991:150). Altogether 223 tests were applied. For N = 40 all data points are above the suitability boundaries. That means, at N = 40 the number of correctly detected PS strongly exceeds the one of falsely detected PS. At N = 16 all data points are above the lowest suitability boundary (k = 1). Consequently, 16 SAR images are enough to guarantee that the number of correctly detected PS is at least as high as the one of falsely detected PS. At N = 8 it strongly depends on the value of k, whether a data point is in the suitable region of the graph or not. For N = 4 the majority of the tests are below the suitability boundaries.

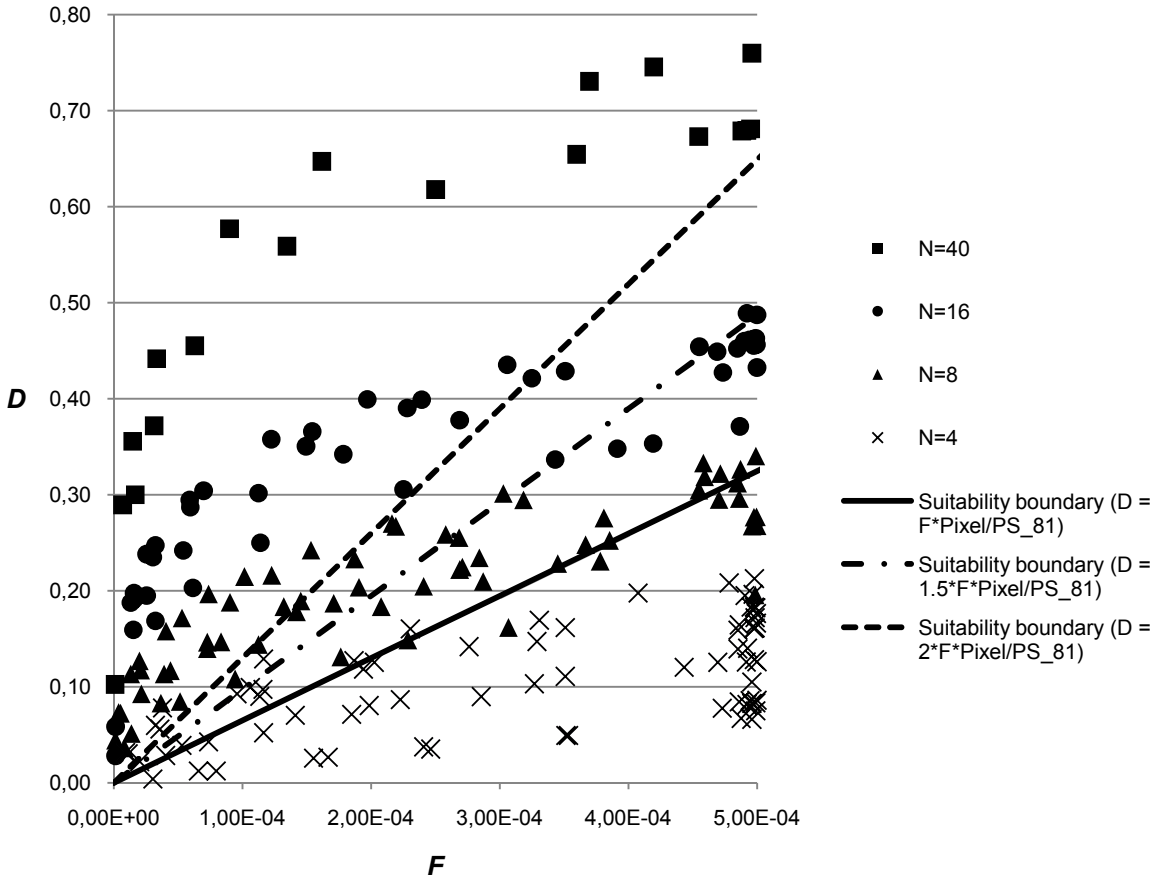

Fig. 64: ROC experiment. Hit rate *D* and false alarm rate *F* for different values of *γ*. The black lines mark the suitability boundaries for *k* = 1, 1.5 and 2.

To quantify the results of figure 64, for each value of *k* the percentage of data points below the suitability boundary was calculated (for each value of *N*, Fig. 65). As already described above, for *N* = 40 all data points are above the suitability boundaries (Fig. 64) and get therefore the value 0 in figure 65. The same also applies for *N* = 16 for the lower limit suitability boundary of *k* = 1. At this value of *k* ca. 14.1 % of the 8-look and 81.9 % of the 4-look data points are below the suitability boundary. At *k* = 2 ca. 37.5 % of the 16-look data points are below the suitability boundary. *N* = 8 already crosses the 50-percentage line, which marks that the majority of the data points is below the suitability boundary. The results for *k* = 1.5 are more close to *k* = 2 than to *k* = 1. At *k* = 1.5 ca. 39.4 % of the 8-look data points are below the suitability boundary.

Altogether, figure 65 clearly shows that the data points for *N* = 8 are close to the important 50-percentage boundary. This is especially true for *k* = 1.5 and *k* = 2. For the lowest suitability boundary of *k* = 1 one can estimate the cross of the 50-percentage line at ca. *N* = 6. However, as *k* = 1 is the lowest suitability boundary and *k* = 1.5 or *k* = 2, respectively, are stricter suitability boundaries, one should use *N* = 8 as the minimum number of SAR images to enable suitable pre-estimation of the expectable number of PS prior to ordering the entire stack of SAR images.

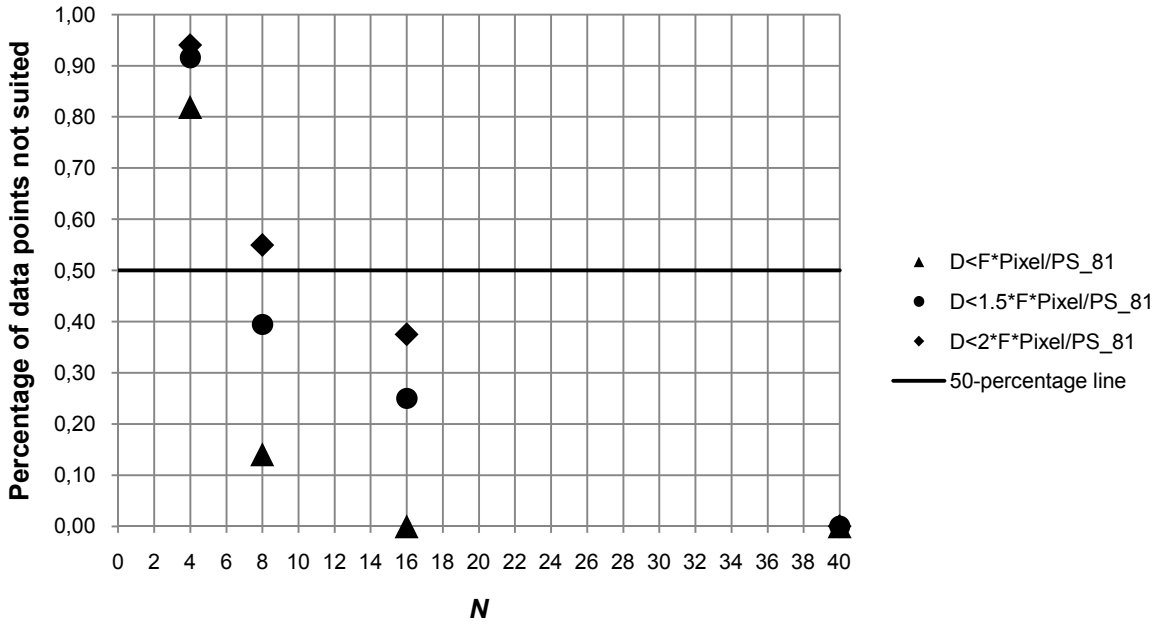

Fig. 65: Percentage of data points below the suitability boundary (cf. Fig. 64). For $N = 8$ the data values are near the important 50-percentage line (especially for $k = 1.5$ and $k = 2$).

6.4 Conclusion of the third topic

The third topic of this work showed the effects on PS-detection of continuously reducing the number of SAR images in the stack. After a theoretical derivation of the concept of detection theory, two experiments with ERS data were executed. To achieve a significant reduction of the speckle effect to guarantee usable results of PS-detection, the undertaken CFAR experiment (chapter 6.2) showed that at least 4, but preferable 8 SAR images are required. However, to ensure that the number of correctly detected PS is at least as high as the one of falsely detected PS, 8 SAR images should be used (cf. chapter 6.3). Therefore, this small number of SAR images enables one to test whether the number of PS-targets of a certain site is high enough for a subsequent PS-InSAR processing, which of course then requires a higher number of SAR images.

In the experiments it could be determined that at small number of 4 or less SAR images water surfaces show a high rate of falsely detected PS. However, as the final result is that at least 8 SAR images should be used to achieve a meaningful PS-detection, the influence of water surfaces is very low at this number of images. Therefore, it can be concluded, that the results are also valid for other sites, especially for those of similar climate and rural area land cover (cf. chapter 2c). At urban area, the number of PS is significantly higher.

In the experiments ERS SAR data were used. Therefore, first of all it could be concluded that the results are valid for SAR sensors of about the same spatial resolution (e.g. ENVISAT ASAR, Imaging Mode). At high resolution SAR sensors, such as TerraSAR-X, the number of PS-targets strongly increases. Until now, it is very difficult to say, whether the results are also perfectly valid for high spatial resolution SAR sensors. Such experiments may be ideas for future work. However, it can be expected that the number of SAR images required for a useful PS-detection is very close to 8 SAR images also for such high spatial resolution sensors, assuming a comparable relationship of correctly and falsely detected PS as in the experiment.

7. Conclusion

7.1 Summary and discussion of the thesis

D-InSAR and PS-InSAR are powerful methods for deformation monitoring of the Earth's crust. However, topography related effects, such as shadowing (no radar responses) or layover (overlap of radar echoes from different ground positions), and high vegetation density of the area of the site complicate the application of these SAR interferometry methods. Reliable PS-InSAR can only be applied, if there is a sufficiently high number of PS within the site. But an estimation of these PS prior the processing of several SAR images is very complicated. Therefore, the overall topic of this thesis is the development of pre-processing methods to enable objective suitability evaluation of D-InSAR and PS-InSAR to monitor a certain site – prior to its radar recording. The thesis is divided into three major topics. To answer the key question of topic one 'Can D-InSAR be applied for monitoring a certain landslide?' (cf. chapter 1.2), three pre-processing GIS-based procedures were developed: prediction of layover and shadow areas (chapter 4.1), the calculation of the measurable percentage of movement (chapter 4.2) and the classification of the land cover regarding its influence on the applicability of D-InSAR (chapter 4.3). Finally, the results of these three methods were combined to enable the evaluation of the applicability of D-InSAR for each single landslide within the area of interest prior to radar recording.

The developed procedures were validated with real SAR data. When using a low spatial resolution DEM (80 m), the simulation showed a generally good match with the processed layover / shadow, which is based on a higher resolution DEM (mosaic of 21 m and 62 m spatial resolution, respectively). Although only about 58 % of the processed layover / shadow areas were detected by the simulation, it provides useable results on regional scale, as all main parts of the processed layover / shadow areas were correctly recognized (cf. chapter 4.1.3.1). More detailed analysis requires higher quality DEMs. A second simulation based on a high resolution laserscan DEM (10 m) detected about 88 % of the processed layover / shadow areas (cf. chapter 4.1.3.2). However, it is important to notice that the processed layover / shadow are also the result of a model and not absolutely the 'real' layover / shadow. Depending on the spatial resolution of the DEM used, the simulation shows even better results (more details) than the processed layover / shadow.

To decide, which imaging parameters (incidence angle and orbit) and SAR sensor (especially regarding the wavelength it is using) will provide the best results for monitoring a certain land slide, an iterated analysis of the developed procedures should be applied for different SAR acquisition geometries. This concerns especially the prediction of layover and shadow areas (chapter 4.1) and the calculation of the measurable percentage of movement (chapter 4.2), as the classification of the land cover's influence on the applicability of D-InSAR has already been executed for entire Europe, based on CORINE 2006 land cover data (cf. chapter 4.3).

Before deciding whether to use D-InSAR or not, other factors such as the spatial resolution of the SAR sensor, data availability (repeat cycle) and atmospheric disturbances, need to be considered. The usage of the freely available SRTM DEMs gives an overview on the applicabili-

ty of D-InSAR for large areas (e.g. an entire footprint), whereas detailed analysis (e.g. examination of corner reflector positions on a landslide) requires DEMs of higher spatial resolution.

Topic 2 of this dissertation dealt with the following key question: 'Can the PS-density of a site be estimated prior to its radar recording?' (cf. chapter 1.2). Successful PS-InSAR processing requires a sufficiently high number of PS within the area of interest. As it is very difficult to estimate these PS prior to the processing of several SAR images, the answer to this key question was the development of three new pre-processing methods for estimating PS. The prerequisites, applicability and limitations of these PS-estimation procedures are presented in a decision diagram (Fig. 56).

The first method uses freely available land cover data (GlobCover and CORINE). This PS-estimation method is a very suitable, worldwide applicable and fast tool to get an overview of the expected PS-density of large areas. The validation with real PS-data showed a very good applicability of this PS-estimation method when using higher spatial resolution land cover data, such as CORINE. For this land cover dataset the difference of the estimated and processed PS-density is very low, the majority (over 52 %) of the site area show differences of only ±15 PS/km², from which over 35 % are within ±10 PS/km² (chapter 5.1.4c). Low spatial resolution land cover data (e.g. GlobCover) is less suitable. The validation of the PS-estimation using GlobCover land cover data showed that the percentage of areas of low difference between estimated and processed PS-density (±15 PS/km²) is ca. 41 % (chapter 5.1.4a). However, also this low spatial resolution land cover data enables an overview of the to be expected PS-density of a certain site. As in many areas of the world only this lower spatial resolution land cover data (GlobCover) is available, it was also considered in this thesis.

Prerequisite of this PS-estimation is estimation or information about the absolute PS-density in the reference class urban area of a site recorded by the same or comparable SAR sensor and processed by the same or comparable PS-processing method, as planned for the area of interest (cf. chapter 5.1).

The second PS-estimation method uses optical remote sensing data of the site, more precisely the NDVI calculated from these datasets (cf. chapter 5.2). The result of this procedure is a map of the area of interest showing for each single NDVI pixel the probability to find a PS-target. This is achieved by comparing the distribution of real (processed) PS-targets of a site with the NDVI value. As the accuracy of the NDVI based PS-estimation method is at the level of the spatial resolution of the optical data used, it is more detailed than the first method based on land cover data. The NDVI based PS-estimation procedure can be applied if (a) geocoded PS-targets of a site with similar climate as the area of interest or (b) a NDVI-PS-percentage graph of such a site are available. This work showed, that the NDVI based PS-estimation procedure is very good suited at regions dominated by sparsely vegetated areas – when using freely available middle spatial resolution optical sensors, such as Landsat and ASTER. For application of this method in areas covered by denser vegetation, high spatial resolution optical sensors (e.g. WorldView-2 and KOMPSAT-2) are required. If this is fulfilled, it is possible to apply this PS-estimation method worldwide.

A great advantage of the third PS-estimation method, which is based on freely available and low-cost topographic maps (TM) and OpenStreetMap (OSM) data, is that it not only estimates

the PS-density of the area of interest, but also calculates and analyzes the distances between the estimated PS and their distribution within the site (cf. chapter 5.3). This PS-estimation method is the most site specific one and is most suited for application at smaller sites (e.g. monitoring of a certain landslide), as it is the most work-intensive procedure. The only prerequisite of this PS-estimation procedure is a topographic map of the site with map scale 1:200,000 or greater. Another advantage of this method is that – contrary to the aforementioned PS-estimation procedures – no information about a PS-InSAR processing of another site is required for its application.

The validation of the third PS-estimation method using processed PS-data (results of real SAR data) investigated two validation questions (chapter 5.3.4). The first one 'What percentage of the processed PS is detected by the estimated PS?' showed that this percentage value depends on the map scale of the topographic map used. For instance, using a large scale map (e.g. 1:25,000 at the Aosta Valley site) this percentage is up to ca. 83 %, while at a small map scale (e.g. 1:200,000 at the Cairo site) this percentage is only between 33 % and 56 %.

The second validation question investigated the probability of an estimated PS being a real (processed) PS. It is important to notice that not each building (or overhead line mast, etc.) always works as a PS-target in reality. Depending on the imaging geometry (orbit, incidence angle) and the spatial resolution of the SAR sensor and the orientation, geometry and material of the ground target, a building could work as a PS or not. The probability of an estimated PS being a PS in reality strongly increases with increasing map scale, as the TMs are more detailed at a larger map scale. At a map scale of 1:200,000 this probability value is very low (ca. 5.5 %). For a map scale of 1:50,000 it increases to about 22.1 % and for a map scale of 1:25,000 to about 35.4 % (Fig. 55). The calculated probability values can be used at new sites where SAR data is not yet available.

Assuming the prerequisites of all three PS-estimation methods are fulfilled (which is the ideal case), at first the land cover based PS-estimation procedure should be applied to get a quick overview of the expected PS-density of the area of interest. The second step should be the application of the NDVI based method to get information about the probability to find a PS-target at a certain NDVI pixel. Finally, the PS-estimation procedure based on topographic maps and OpenStreetMap data enables to get the most site specific information about the expected PS-targets, including (a) their density, (b) the distances between each other and the analysis of it and (c) the analysis of their distribution within the area of interest. However, due to the map content, the TM and OSM based PS-estimation method only considers artificial PS-objects (e.g. buildings, road signs, overhead line masts, etc.). Therefore, also the other two PS-estimation methods based on land cover data and the NDVI, respectively, should be applied, to get additional information on natural PS-targets within the area of interest.

The sites used for the second topic of this work were predetermined by the PS-datasets that were available. These sites are located at different climatic zones, the SAR data was recorded by different SAR sensors and the PS-InSAR processing was done with different PS detection and processing algorithms (from different institutions and companies). At the beginning of the work all these differences between the sites made the development of the PS-estimation procedures difficult. However, as with all these different SAR data and PS-targets datasets a cross-section of the most used SAR sensors (ERS-1 & 2, ENVISAT, Radarsat-1 and Terra-

SAR-X) and PS-InSAR processing results of the leading institutions and companies in this field (e.g. DLR, T.R.E., TU Delft and Astrium Infoterra) were available, it was possible to develop PS-estimation procedures with wide usability.

The third topic of this work is one step further towards PS-InSAR processing compared to the second topic. For high quality PS-InSAR processing a stack containing at least 15 to 50 SAR images is required (cf. chapter 3.4). Consequently, the idea of the third topic is to use a small number of SAR images to test whether the number of PS-targets of a certain site is high enough for a subsequent PS-InSAR processing, which of course then requires a higher number of SAR images. Therefore, this topic answered the following key question 'How many SAR images are required for a meaningful PS-detection?' by continuously reducing the number of SAR images in the stack.

The first part of topic three covered the theoretical derivation of the concept of detection theory. Then, two experiments with ERS data were executed. It could be shown that at least 4, but preferable 8 SAR images are required to achieve a significant reduction of the speckle effect to allow usable results of PS-detection. However, to ensure that the number of correctly detected PS is at least as high as the one of falsely detected PS, 8 SAR images should be used (cf. chapter 6.3). With ca. 8 SAR images it is possible to evaluate, whether the PS-density of a certain site is high enough, prior to ordering a larger stack of SAR images required for the succeeding PS-InSAR processing (see above).

This dissertation showed seven methods for the suitability evaluation of the applicability of the D-InSAR and PS-InSAR method for deformation monitoring, prior to the SAR recording of the area of interest (topic one and two), or based on a small number of SAR images (topic three), respectively. These methods do not replace high functionally SAR processing software. They are intended as a first step evaluation to test where the application of these SAR interferometry techniques is promising. These procedures can be used for a wide area feasibility assessment, which is very interesting for geological surveys and the companies executing the InSAR processing for them.

7.2 Outlook

First of all, a web processing service (WebGIS) of the pre-survey suitability evaluation methods developed in topic one (cf. chapter 4) would enable its application to a wider user community. This mainly concerns the simulation of layover and shadowing areas (cf. chapter 4.1) and the calculation of the measurable percentage of a possible movement on the ground (e.g. a landslide; cf. chapter 4.2), as the classification of the land cover's influence on the applicability of D-InSAR can be applied for each kind of land cover data. Chapter 4.3.3 showed its application on the CORINE 2006 for entire Europe.

Also for the PS-estimation methods, especially for the one based on topographic maps and OpenStreetMap data (cf. chapter 5.3), such a web processing service might be helpful for its application.

Moreover, in future, the statistical power of the relative PS(&DS)-density graphs of the land cover based PS-estimation method (chapter 5.1) could be increased by using data of more sites. This is especially meaningful for the estimation of DS&PS, which is based on 'only'

nine datasets until now (cf. chapter 5.1). Furthermore, as the better suited CORINE dataset is only available in Europe, for other continents the relative PS(&DS)-density using other higher spatial and thematic resolution land cover data (e.g. Africover, cf. chapter 5.1.3 c) should be applied.

For the OpenStreetMap data used in the third PS-estimation method (cf. chapter 5.3), an increase of the data density is expected in future. When the coverage rate of the OSM data, especially of buildings, reaches the level of topographic maps, a PS-estimation based on free available vector data, which requires very low preparatory work, would be possible.

To test, whether the results of the third topic – the determination of the minimum number of SAR images required for a meaningful PS-detection – are also valid for high spatial resolution SAR sensors, such as TerraSAR-X, an idea for future work may be the application of the experiments of this topic also with data of such high spatial resolution sensors.

8. References

ADAM, N., KAMPES, B.M. & EINEDER, M. (2005): Development of a scientific permanent scatterer system: modifications from mixed ERS/Envisat time series. - Proc. of the 2004 Envisat & ERS Symposium, Salzburg, ESA SP-572.

ADAM, N., GONZALEZ, F.R., PARIZZI, A. & LIEBHART, W. (2011): Wide area persistent scatterer interferometry. - Proc. of IGARSS 2011, Vancouver, Canada, 1481-1484.

AHMED, R., SIQUEIRA, P., HENSLEY, S., CHAPMAN, B. & BERGEN, K. (2011): A survey of temporal decorrelation from spaceborne L-Band repeat-pass InSAR. - Remote Sensing of Environment, **115**, 2887-2896.

ALBERTZ, J. & WIGGENHAGEN, M. (2009): Guide for Photogrammetry and Remote Sensing. - 334 pp., 5th ed., Paderborn (Wichmann).

ARCGIS DESKTOP HELP 9.3 (2009): Cell size and resampling in analysis. - <http://webhelp.esri.com/arcgisdesktop/9.3/index.cfm?TopicName=Cell%20size%20and%22resampling%20in%20analysis>. (as of: 2009-04-29) (access: 2010-06-11).

AUER, S., GERNHARDT, S. & BAMLER, R. (2011): Investigations on the Nature of Persistent Scatterers Based on Simulation Models. - In: STILLA, U., GAMBA, P., JUERGENS, C. & MAKTAV, D. (Eds.): JURSE 2011 - Joint Urban Remote Sensing Event, Munich, Germany, 61-64.

BAMLER, R. & HARTL, P. (1998): Synthetic aperture radar interferometry. - Inverse Problems, **14**, 1-54.

BARBIERI, M. & LICHTENEGGER, J. (2005): Introduction to SAR for Geology. - In: FLETCHER, K. (Ed.): Spaceborne radar applications in Geology. ESA TM-17, Noordwijk (ESA Publications Division, European Space Agency), 1-54.

BARKAT, M. (1991): Signal Detection and Estimation. - 434 pp., Boston (Artech House).

BARTUSCH, M., HAINSEK, I., JANOTH, J., MARSCHNER, C., MILLER, D., MOREIRA, A., SPARWASSER, N. & ZINK, M. (2009): TanDEM-X. Die Erde in drei Dimensionen. - 24pp., Köln (Deutsches Zentrum für Luft- und Raumfahrt).

BAYERISCHES LANDESAMT FÜR VERMESSUNG UND GEOINFORMATION (2012a): Digitale Topographische Karte 1:25.000 - DTK25. - <http://www.vermessung.bayern.de/geobasis_lvg/dtk/DTK25.html>. (as of: 2012) (access: 2012-05-17).

BAYERISCHES LANDESAMT FÜR VERMESSUNG UND GEOINFORMATION (2012 b): Bayern-Map plus. - <http://www.vermessung.bayern.de/geobasis_lvg/BayernMapplus.html>. (as of: 2012) (access: 2012-05-17).

BONTEMPS, S., DEFOURNY, P., VAN BOGAERT, E., ARINO, O., KALOGIROU, V. & PEREZ, J. R. (2011): GLOBCOVER 2009 - Products Description and Validation Report. - 53 pp., ESA & Université catholique de Louvain.

BORGEAUD, M. & WEGMÜLLER, U. (1997): On the Use of ERS SAR Interferometry for the Retrieval of Geo- and Bio-Physical Information. - Proc. of Fringe 1996, Zürich, Switzerland, ESA SP-406, Noordwijk (ESA Communications) (CD-ROM).

BOVENGA, F., NUTRICATO, R., REFICE, A. & WASOWSKI, J. (2006): Application of multitemporal differential interferometry to slope instability detection in urban/peri-urban areas. - Engineering Geology, **88**, 218-239.

BOVENGA, F., WASOWSKI, J., NITTI, D.O., NUTRICATO, R. & CHIARADIA, M.T. (2012): Using COSMO/SKYMed X-band and ENVISAT C-band SAR interferometry for landslides analysis. - Remote Sensing of Environment, **119**, 272-285.

BRUNSDEN, D., DIKAU, R., IBSEN, M.-L. & SCHROTT, L. (1996): Landslide Recognition - Identification, Movement and Causes. - 251 pp., Chichester (John Wiley & Sons).

CARNEC, C. & DELACOURT, C. (2000): Three years of mining subsidence monitored by SAR interferometry, near Gardanne, France. - Journal of Applied Geophysics, **43**, 43-54.

CARTUS, O., SANTORO, M., SCHMULLIUS, C. & LI, Z. (2011): Large area forest stem volume mapping in the boreal zone using synergy of ERS-1/2 tandem coherence and MODIS vegetation continuous fields. - Remote Sensing of Environment, **115**, 931-943.

CASCINI, L., PEDUTO, D., FORNARO, G., LANARI, R., ZENI, G. & GUZZETTI, F. (2009): Spaceborne Radar Interferometry for Landslide Monitoring. - Proc. of the 1st Italian workshop on landslides, Naples, Italy, 138-144.

CATANI, F., FARINA, P., MORETTI, S., NICO, G. & STROZZI, T. (2005): On the application of SAR interferometry to geomorphological studies: estimation of landform attributes and mass movements. - Geomorphology, **66**, 119-131.

CHATTERJEE, R.S., FRUNEAU, B., RUDANT, J.P., ROY, P.S., FRISON, P.-L., LAKHERA, R.C., DADHWAL, V.K. & SAHA, R. (2003): Subsidence of Kolkata (Calcutta) City, India during the 1990s as observed from space by Differential Synthetic Aperture Radar Interferometry (D-InSAR) technique. - Remote Sensing of Environment, **102**, 176-185.

CHEN, M.D. & GETIS, A. (1998): Point Pattern Analysis. - <http://www.nku.edu/~longa/geomed/ppa/doc/html/ppa.html.>. (as of: 1998-05-12) (access: 2012-04-20).

CHEN, Y., ZHANG, G., DING, X. & LI, Z. (2002): Monitoring Earth Surface Deformation with InSAR Technology: Principle and Some critical Issues. - Journal of Geospatial Engineering, **2**, 3-21.

CIGNA, F., OSMANOĞLU, B., CABRAL-CANO, E., DIXON, T.H., ÁVILA-OLIVERA, J.A., GARDUÑO-MONROY, V.H., DEMETS, C. & WDOWINSKI, S. (2012): Monitoring land subsidence and its induced geological hazard with Synthetic Aperture Radar Interferometry: A case study in Morelia, Mexico. - Remote Sensing of Environment, **117**, 146-161.

COLESANTI, C., FERRETTI, A., NOVALI, F., PRATI, C. & ROCCA, F. (2003a): SAR Monitoring of Progressive and Seasonal Ground Deformation Using the Permanent Scatterers Technique. - IEEE Transactions on Geoscience and Remote Sensing, **41**, 1685-1701.

COLESANTI, C., FERRETTI, A., PRATI, C. & ROCCA, F. (2003b): Monitoring landslides and tectonic motions with the Permanent Scatterers Technique. - Engineering Geology, **68**, 3-14.

COLESANTI, C. & WASOWSKI, J. (2006): Investigation landslides with space-borne Synthetic Aperture Radar (SAR) interferometry. - Engineering Geology, **88**, 173-199.

CORSINI, A., FARINA, P., ANTONELLO, G., BARBIERI, M., CASAGLI, N., COREN, F., GUERRI, L., RONCHETTI, F., STERZAI, P. & TARCHI, D. (2006): Space-borne and ground-based SAR interferometry as tools for landslide hazard management in civil protection. - International Journal of Remote Sensing, **27**, 2351-2369.

CRISP, D.J. (2004): The State-of-the-Art in Ship Detection in Synthetic Aperture Radar Imagery. - 115 pp., Department of Defence, Edinburgh, Australia (Intelligence, Surveillance and Reconnaissance Division, Information Sciences Laboratory).

CROSETTO, M., MONSERRAT, O., IGLESIAS, R. & CRIPPA, B. (2010): Persistent Scatterer Interferometry: potential, limits and initial C- and X-band comparison. - Photogrammetric Engineering & Remote Sensing, **76**, 1061-1069.

CRUDEN, D.M . & VARNES, D.J. (1996): Landslide Types and Processes. – In: TURNER, A.K. & SCHUSTER, R.L. (Eds.): Landslides – Investigation and mitigation. Special Report 247, Transportation Research Board, National Research Council, Washington D. C. (National Academy Press), 36-75.

DAITO, K., FERRETTI, A., KUZUOKA, S., NOVALI, F., PANZERI, P. & ROCCA, F. (2004): L-band PS analysis: JERS-1 results and TerraSAR–L predictions. - Proc. of Fringe 2003, Frascati, Italy, ESA SP-550, Noordwijk (ESA Communications) (CD-ROM).

DEBELLA-GILO, M. & KÄÄB, A. (2011): Sub-pixel precision image matching for measuring surface displacements on mass movements using normalized cross-correlation. - Remote Sensing of Environment, **115**, 130-142.

DIGITALGLOBE (no year): DigitalGlobe Core Imagery Products Guide. - 40 pp., DigitalGlobe.

EINEDER, M. (2003): Efficient Simulation of SAR Interferograms of Large Areas and of Rugged Terrain. - IEEE Transactions on Geoscience and Remote Sensing, **41**, 1415-1427.

FERRETTI, A., PRATI, C. & ROCCA, F. (1999): Permanent scatterers in SAR interferometry. - Proc. of IGARSS 1999, Hamburg, Germany, 1528-1530.

FERRETTI, A., PRATI, C. & ROCCA F. (2000a): Analysis of Permanent Scatterers in SAR Interferometry. - Proc. of IGARSS 2000, Honolulu, Hawaii, 761-763.

FERRETTI, A., PRATI, C. & ROCCA F. (2000b): Nonlinear Subsidence Rate Estimation Using Permanent Scatterers in Differential SAR Interferometry. - IEEE Transactions on Geoscience and Remote Sensing, **38**, 2202-2212.

FERRETTI, A., PRATI, C. & ROCCA, F. (2001): Permanent Scatterers in SAR Interferometry. - IEEE Transactions on Geoscience and Remote Sensing, **39**, 8-20.

FERRETTI, A., PERISSIN, D., PRATI, C. & ROCCA, F. (2005): On the physical nature of SAR Permanent Scatterers. - Proc. of the 2005 URSI Commission F Symposium on Microwave Remote Sensing of the Earth, Oceans, Ice, and Atmosphere, Ispra, Italy.

FERRETTI, A., MASSONNET, D., MONTI-GUARNIERI, A., PRATI, C. & ROCCA, F. (2007): Guidelines for SAR Interferometry - Processing and Interpretation. - In: FLETCHER, K. (Ed.): InSAR Principles. 255 pp., ESA TM-19. Noordwijk (ESA Publications Division).

FERRETTI, A. FUMAGALLI, A., NOVALI, F., PRATI, C., ROCCA, F. & RUCCI A. (2011): A New Algorithm for Processing Interferometric Data-Stacks: SqueeSAR. - IEEE Transactions on Geoscience and Remote Sensing, **49**, 3460-3470.

FRANCESCHETTI, G. & LANARI, R. (1999): Synthetic aperture radar processing. - 307 pp., Boca Raton (CRC Press).

FREEMAN, A. (1992): SAR Calibration: An overview. - IEEE Transactions on Geoscience and Remote Sensing, **30**, 1107-1120.

FROESE, C.R., PONCOS, V., SKIRROW, R., MANSOUR, M. & MARTIN, D. (2008): Characterizing complex deep seated landslide deformation using corner reflector InSAR (CR-InSAR): Little Smoky Landslide, Alberta. - In: LOCAT, J., PERRET, D., TURMEL, D., DEMERS, D. & LEROUEIL, S. (Eds): Proc. of the 4th Canadian Conference on Geohazards: From Causes to Management. Laval, Québec (Presse de l'Université Laval), 287-294.

FRUNEAU, B., ACHACHE, J. & DELACOURT, C. (1996): Observation and modelling of the Saint-Etienne-de-Tinée landslide using SAR interferometry. - Tectonophysics, **265**, 181-190.

GABRIEL, A.K., GOLDSTEIN, R.M. & ZEBKER, H.A. (1989): Mapping Small Elevation Changes Over Large Areas: Differential Radar Interferometry. - Journal of Geophysical Research, **94**, 9183-9191.

GEUDTNER, D. (1995): Die interferometrische Verarbeitung von SAR-Daten des ERS-1. - 141 pp., Forschungsbericht 1995-28, Köln (Deutsches Zentrum für Luft- und Raumfahrt).

GUPTA, R.P. (2003): Remote Sensing Geology. - 655 pp., Heidelberg (Springer).

HANSSEN, R.F. (2005): Satellite radar interferometry for deformation monitoring: a priori assessment of feasibility and accuracy. - International Journal of Applied Earth Observation and Geoinformation, **6**, 253-260.

HEIN, A. (1998): Verarbeitung von SAR-Daten unter besonderer Berücksichtigung interferometrischer Anwendungen. - 227 pp., Dissertation, Universität Gesamthochschule Siegen.

HELENO, S.I.N., OLIVEIRA, L.G.S., HENRIQUES, M.J., FALCÃO, A.P., LIMA, J.N.P., COOKSLEY, G., FERRETTI, A., FONSECA, A.M., LOBO-FERREIRA, J.P. & FONSECA, J.F.B.D. (2011): Persistent Scatterers Interferometry detects and measures ground subsidence in Lisbon. - Remote Sensing of Environment, **115**, 2152-2167.

HILDEBRANDT G. (1996): Fernerkundung und Luftbildvermessung - Für Forstwirtschaft, Vegetationskartierung und Landschaftsökologie. - 676 pp., Reinheim (Wichmann).

HOFFER, R.M. (1978): Biological and Physical Considerations in applying Computer-Aided Analysis Techniques to Remote Sensor Data. – In: SWAIN, P.H. & DAVIS, S.M. (Eds.): Remote Sensing: The Quantitative Approach, New York (McGraw-Hill), 227-289.

HUNG, W.-C., HWANG, C., CHEN, Y.-A., CHANG, C.-P., YEN, J.-Y., HOOPER, A. & YANG, C.-Y. (2011): Surface deformation from persistent scatterers SAR interferometry and fusion with levelling data: A case study over the Choushui River Alluvial Fan, Taiwan. - Remote Sensing of Environment, **115**, 957-967.

KAMPES, B.M. (2006): Radar interferometry – Persistent Scatterer Technique. - 211 pp., Dordrecht (Springer).

KEIL, M., BOCK, M., ESCH, T., METZ, A., NIELAND, A. & PFITZNER, A. (2010): CORINE Land Cover Aktualisierung 2006 für Deutschland. - 67 pp., Umweltforschungsplan des Bundesministeriums für Umwelt, Naturschutz und Reaktorsicherheit, Oberpfaffenhofen (Deutsches Zentrum für Luft- und Raumfahrt).

KETELAAR, V.B.H. (2009): Satellite Radar Interferometry – Subsidence Monitoring Techniques. - 243 pp., New York (Springer).

KIRCHNER, M. (2005): Analyse flächenhafter Senkungserscheinungen in sedimentären Gebieten mit den neuen Techniken der Radarfernerkundung. - 129 pp., Forschungsbericht DLR, 2005-01. Köln (Deutsches Zentrum für Luft- und Raumfahrt).

KOREA AEROSPACE RESEARCH INSTITUTE (2008): KOMPSAT-2 Image data Manual. - 42 pp., Version 1.1, Satellite Information Research Institute, Korea Aerospace Research Institute.

LAMBERS, M. & KOLB, A. (2008): Automatic point target detection for interactive visual analysis of SAR images. - Proc. of IGARSS 2008, Boston, Massachusetts, U.S.A., 903-906.

LAUKNES, T.R., PIYUSH SHANKER, A., DEHLS, J.F., ZEBKER, H.A., HENDERSON, I.H.C. & LARSEN, Y. (2010): Detailed rockslide mapping in northern Norway with small baseline and persistent scatterer interferometric SAR time series methods. - Remote Sensing of Environment, **114**, 2097-2109.

LILLESAND, T.M. & KIEFER, R.W. (2000): Remote Sensing and Image Interpretation. - 724 pp., 4th ed., New York (John Wiley & Sons).

LÒPEZ-ESTRADA, S., CUMPLIDO-PARRA, R. & TORRES-HUITZIL, C. (2004): A Hybrid Approach for Target Detection Using CFAR Algorithm and Image Processing. - Proc. of the Fifth Mexican International Conference in Computer Science, ENC 2004, Colima, Mexico, 108-115.

LÖFFLER, E., HONECKER, U. & STABEL, E. (2005): Geographie und Fernerkundung. Eine Einführung in die geographische Interpretation von Luftbildern und modernen Fernerkundungsdaten. - 275 pp., Berlin (Borntraeger).

LU, Z. (2007): InSAR Imaging of Volcanic Deformation over Cloud-prone Areas – Aleutian Islands. - Photogrammetric Engineering & Remote Sensing, **73**, 245–257.

MACMILLAN, N.A. & CREELMAN, C.D. (2005): Detection theory – A User's Guide. - 492 pp., New York (Lawrence Erlbaum Associates).

MANZO, M., RICCIARDI, G.P., CASU, F., VENTURA, G., ZENI, G., BORGSTRÖM, S., BERARDINO, P., DEL GAUDIO, C. & LANARI, R. (2006): Surface deformation analysis in the Ischia Island (Italy) based on spaceborne radar interferometry. - Journal of Volcanology and Geothermal Research, **151**, 399-416.

MARINO, G. & HUGHES, E.J. (2011): A Novel Mathematical Approach for the Problem of CFAR Clutter Model Approximation. - Proc. of Microwave, Radar and Remote Sensing Symposium 2011, Kiev, Ukraine, 332-335.

MASSIRONI, M., ZAMPIERI, D., BIANCHI, M., SCHIAVO, A. & FRANCESCHINI, A. (2009): Use of PSInSAR™ data to infer active tectonics: Clues on the differential uplift across the Giudicarie belt (Central-Eastern Alps, Italy). - Tectonophysics, **476**, 297-303.

MASSONNET, D., ROSSI, M., CARMONA, C., ADRAGNA, F., PEITZER, G., FEIGL, K. & RABAUTE, T. (1993): The displacement field of the Landers earthquake mapped by radar interferometry. - Nature, **364**, 138-142.

MASSONNET, D. & FEIGL, K.L. (1998): Radar interferometry and its application to changes in the earth's surface. - Reviews of Geophysics, **36**, 441-500.

METTERNICHT, G., HURNI, L. & GOGU, R. (2005): Remote sensing of landslides: An analysis of the potential contribution to geo-spatial systems for hazard assessment in mountainous environments. - Remote Sensing of Environment, **98**, 284-303.

MEYER, B. ARMIJO, R., MASSEY, C.I., DE CHABLIER, J.B., DELACOURT, C., RÜGG, J.C., ACHACHE, J. & PAPATASTASSIOU, D. (1998): Results from combining tectonic observations and SAR interferometry for the 1995 Greneva Earthquake: A summary. - Journal of Geodynamics, **26**, 255-259.

MINET, C. (2012): Private Communication (2012-05-24).

MÜLLENHOFF (2004): Rekonstruktion von Gewässerstrukturen im Oderbruch bei Manschnow durch multifrequente und multipolarimetrische Radarfernerkundungs- und GIS-Analyse. - 171 pp., Dissertation, Westfälische Wilhems-Universität.

NASA (2004): ASTER. - <http://asterweb.jpl.nasa.gov>. (as of: 2004-09-07) (access: 2012-05-15).

NASA (2012): Landsat 7. - <http://landsat.gsfc.nasa.gov/>. (as of: 2012-05-09) (access: 2012-05-15).

NATIONAL GEOSPATIAL-INTELLIGENCE AGENCY (2010): Earth Gravitation Model 2008 (EGM2008). - <http://earth-info.nga.mil/GandG/wgs84/gravitymod/egm2008/>. (as of: 2010-09-20) (access: 2012-04-29).

OPENSTREETMAP WIKI (2008): Road types. - <http://wiki.openstreetmap.org/wiki/User:Gyrbo/Road_types>. (as of: 2008-02-18) (access: 2011-10-04).

OPENSTREETMAP WIKI (2011): Railway. - <http://wiki.openstreetmap.org/wiki/DE:Key:railway>. (as of: 2011-04-22) (access: 2011-10-04).

PEEL, M.C., FINLAYSON, B.L. & MCMAHON, T.A. (2007): Updated world map of the Köppen-Geiger climate classification. - Hydrology and Earth System Sciences, **11**, 1633-1644.

PERISSIN, D., PRATI, C. & FERRETTI, A. (2006): Spaceborne SAR anatomy of a city. - Proc. of Fringe 2005, Frascati, Italy, ESA SP-610, Noordwijk (ESA Communications) (CD-ROM).

PLANK, S. (2009): GIS-based suitability evaluation of the Differential Radar Interferometry method (D-InSAR) for detection and deformation monitoring of landslides. - 142 pp., unpublished diploma thesis, Technische Universität München.

PLANK, S. (2011): Abschätzung von Persistent Scatterers mit digitalen topographischen Karten und OpenStreetMap Daten. - 107 pp., unpublished master thesis, Paris Lodron-Universität Salzburg.

PLANK, S., SINGER, J. MINET, C. & THURO, K. (2012): Pre-survey suitability evaluation of the differential synthetic aperture radar interferometry method for landslide monitoring. - doi: 10.1080/01431161.2012.693646, International Journal of Remote Sensing, **33**, 6623-6637.

PLANK, S., SINGER, J. & THURO, K. (in review): Persistent scatterers (PS-InSAR) estimation prior to radar acquisition using NDVI and open access land cover and topographical data. - ISPRS Journal of Photogrammetry and Remote Sensing.

RABUS, B., EINEDER, M., ROTH, A. & BAMLER, R. (2003): The shuttle radar topography mission – a new class of digital elevation models acquired by spaceborne radar. - ISPRS Journal of Photogrammetry and Remote Sensing, **57**, 241-261.

RAGGAM, H. & GUTJAHR, K. (2005): Generation of Layover/Shadow Mask (GIM Product) in EGEO Software. - In: Technical Note. 37 pp., Graz (Johanneum Research).

RAUCOULES, D., RISTORI, B., DE MICHELE, M. & BRIOLE, P. (2010): Surface displacement of the Mw 7 Machaze earthquake (Mozambique): Complementary use of multiband InSAR and radar amplitude image correlation with elastic modelling. - Remote Sensing of Environment, **114**, 2211-2218.

REFICE, A., BOVENGA, F., NUTRICATO, R., CHIARADI, M.T. & WASOWSKI J. (2005): Land-cover classification-based Persistent Scatterers identification for peri-urban applications. - Proc. of IGARSS 2005, Seoul, Korea, 2668-2671.

ROSEN, P.A., HENSLEY, S., JOUGHIN, I.R., LI, F.K, MADSEN, S.N, RODRIGUEZ, E. & GOLDSTEIN, R.M. (2000): Synthetic aperture radar interferometry. - Proc. of the IEEE, **88**, 333-382.

ROSIN, P.L. & HERVÁS, J. (2005): Remote sensing image thresholding methods for determining landslide activity. - International Journal of Remote Sensing, **26**, 1075-1092.

ROTT, H. & NAGLER, T. (2006): The contribution of radar interferometry to the assessment of landslide hazards. - Advances in Space Research, **37**, 710-719.

SCHWÄBISCH, M. (1995): Die SAR-Interferometrie zur Erzeugung digitaler Geländemodelle. - 125 pp., Forschungsbericht 1995-25, Köln (Deutsches Zentrum für Luft- und Raumfahrt).

SÖRGEL, U. (2006): Stand der Technik und Trends der Radarfernerkundung. - Wissenschaftliche Arbeiten der Fachrichtung Geodäsie und Geoinformatik der Leibniz Universität Hannover, **263**, 295-302.

SQUARZONI, C., DELACOURT, C. & ALLEMAND, P. (2003): Nine years of spatial and temporal evolution of the La Valette landslide observed by SAR interferometry. - Engineering Geology, **68**, 53-66.

STROZZI, T., DAMMERT, P.B.G., WEGMÜLLER, U., MARTINEZ, J.-M., ASKNE, J.I.H., BEAUDOIN, A. & HALLIKAINEN, M.T. (2000): Landuse Mapping with ERS SAR Interferometry. - IEEE Transactions on Geoscience and Remote Sensing, **38**, 766-774.

SUNDAL, A.V., SHEPHERD, A., GOURMELEN, N. & PARK, J. (2012): Ice velocity observations at Greenland's Jacobshavn Glacier using ERS-2 3-Day Repeat Campaign data. - Proc. of Fringe 2011, Frascati, Italy, ESA SP-697, Noordwijk (ESA Communications) (CD-ROM).

THIEL, C.J., THIEL, C. & SCHMULLIUS, C.C. (2009): Operational Large-Area Forest Monitoring in Siberia Using ALOS PALSAR Summer Intensities and Winter Coherence. - IEEE Transactions on Geoscience and Remote Sensing, **47**, 3993-4000.

UNITED STATES OF AMERICA WAR OFFICE (1958): Soviet topographic map symbols. - Department of the army technical manual, TM 30-548, Washington (U.S. Government printing office).

VASILIEV, I.R. (1996): Visualization and Spatial Autocorrelation. - In: ARLINGHAUS, S.L. (Ed.): Practical Handbook of Spatial Statistics. Boca Raton (CRC Press), 17-30.

VILARDO, G., VENTURA, G., TERRANOVA, C., MATANO, F. & NARDÒ, S. (2009): Ground deformation due to tectonic, hydrothermal, gravity, hydrogeological, and anthropic processes in the Campania Region (Southern Italy) from Permanent Scatterers Synthetic Aperture Radar Interferometry. - Remote Sensing of Environment, **113**, 197-212.

WANG, Y., CHELLAPPA, R. & ZHENG Q. (1994): Detection of Point Targets in High Resolution Synthetic Aperture Radar Images. - Proc. of ICASSP 1994, Adelaide, Australia, 9-12.

WASOWSKI, J., BOVENGA, F., NITTI, D.O. & NUTRICATO, R. (2012): Investigating landslides with Persistent Scatterers Interferometry (PSI): Current Issues and challenges. - In: EBERHARDT, E., FROESE, C., TURNER, A.K. & LEROUEIL, S. (Eds): Landslides and Engineered Slopes, Protecting Society through Improved Understanding. London (Taylor & Francis Group), 1295-1301.

WEGMÜLLER, U. & WERNER, C.L. (1995): SAR Interferometric Signatures of Forest. - IEEE Transactions on Geoscience and Remote Sensing, **33**, 1153-1161.

WIKIPEDIA (2011a): Richtlinie für die Anlage von Straßen - Querschnitt. <http://de.wikipedia.org/wiki/Richtlinie_f%C3%BCr_die_Anlage_von_Stra%C3%9Fen_%E2%80%93_Querschnitt>. (as of: 2011-04-26) (access: 2011-10-04).

WIKIPEDIA (2011b): Liste der Spurweiten. <http://de.wikipedia.org/wiki/Liste_der_Spurweiten>. (as of: 2011-09-14) (access: 2011-10-04).

WORAWATTANAMATEEKUL, J. (2006): The Application of Advanced Interferometric Radar Analysis for Monitoring Ground Subsidence: A Case Study in Bangkok. - 171 pp., Dissertation, Technische Universität München.

WU, X. (1998): Anwendungen der Satellitengestützten-Radarinterferometrie zur Bestimmung von Topographie und Geschwindigkeitsfeldern. - 103 pp., Deutsche Geodätische Kommission, Heft Nr. 499, Reihe C Dissertationen, München (Beck).

ZEBKER, H.A. & VILLASENOR, J. (1992): Decorrelation in Interferometric Radar Echoes. - IEEE Transactions on Geoscience and Remote Sensing, **30**, 950-959.

ZHOU, X, CHANG, N.B & LI, S. (2009): Applications of SAR Interferometry in Earth and Environmental Science Research. - Sensors, **9**, 1876-1912.

Appendix

Appendix 1: Maps of the sites

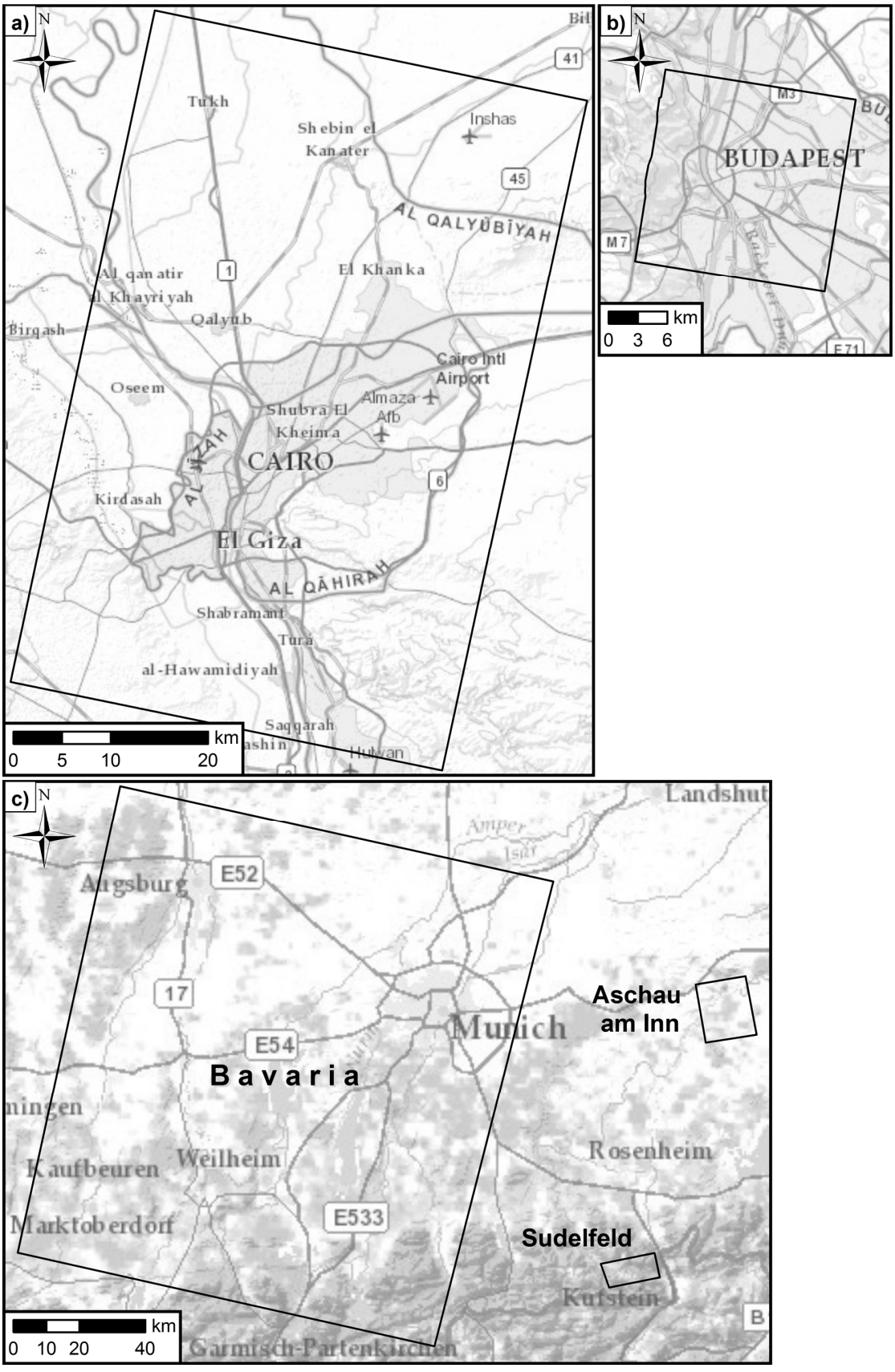

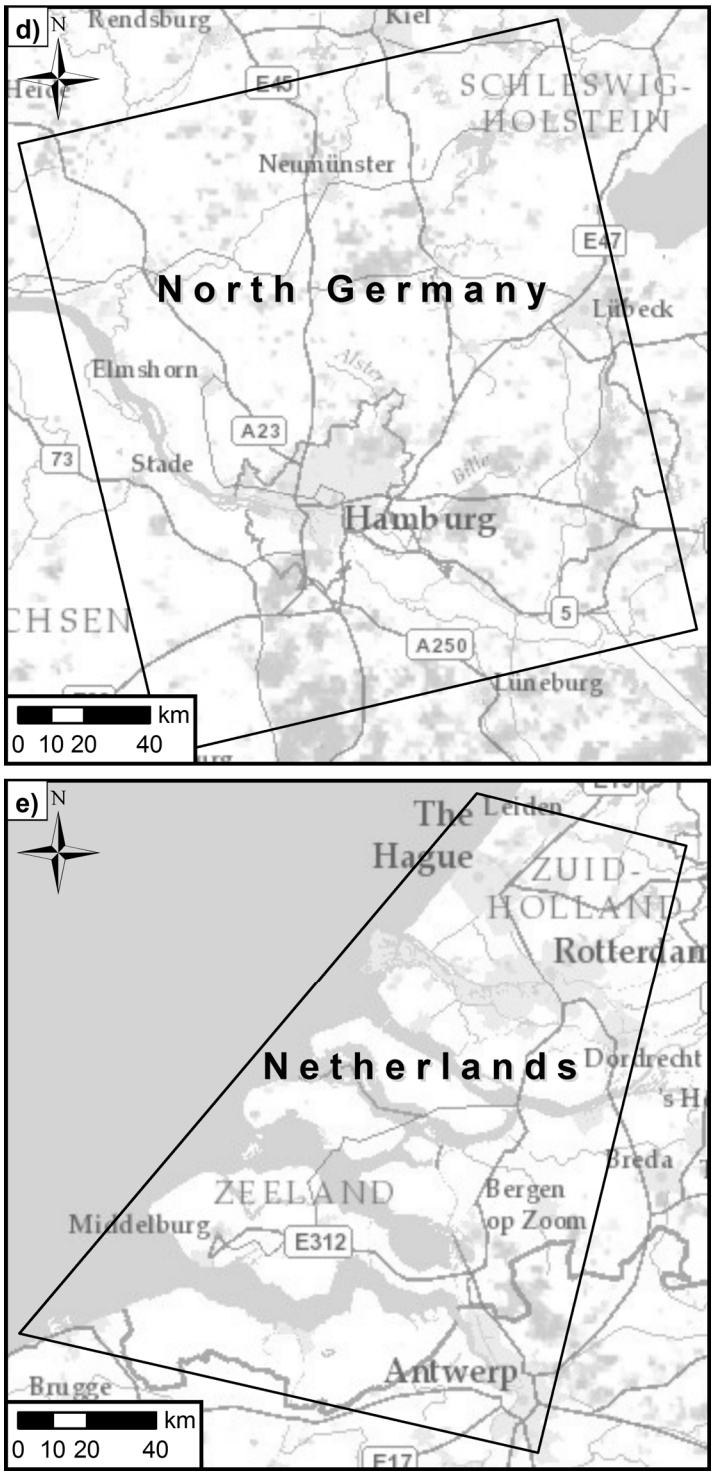
d)
N
Rendsburg
Kiel
E45
SCHLESWIG-
HOLSTEIN
Neumünster
E47
North Germany
Lübeck
Elmshorn
A23
73
Stade
Hamburg
5
A250
Lüneburg
km
0 10 20 40
e)
N
The
Hague
Leiden
ZUID-
HOLLAND
Rotterdam
Netherlands
Dordrecht
Breda
ZEELAND
Bergen
op Zoom
Middelburg
E312
Antwerp
Brugge
km
0 10 20 40
E17

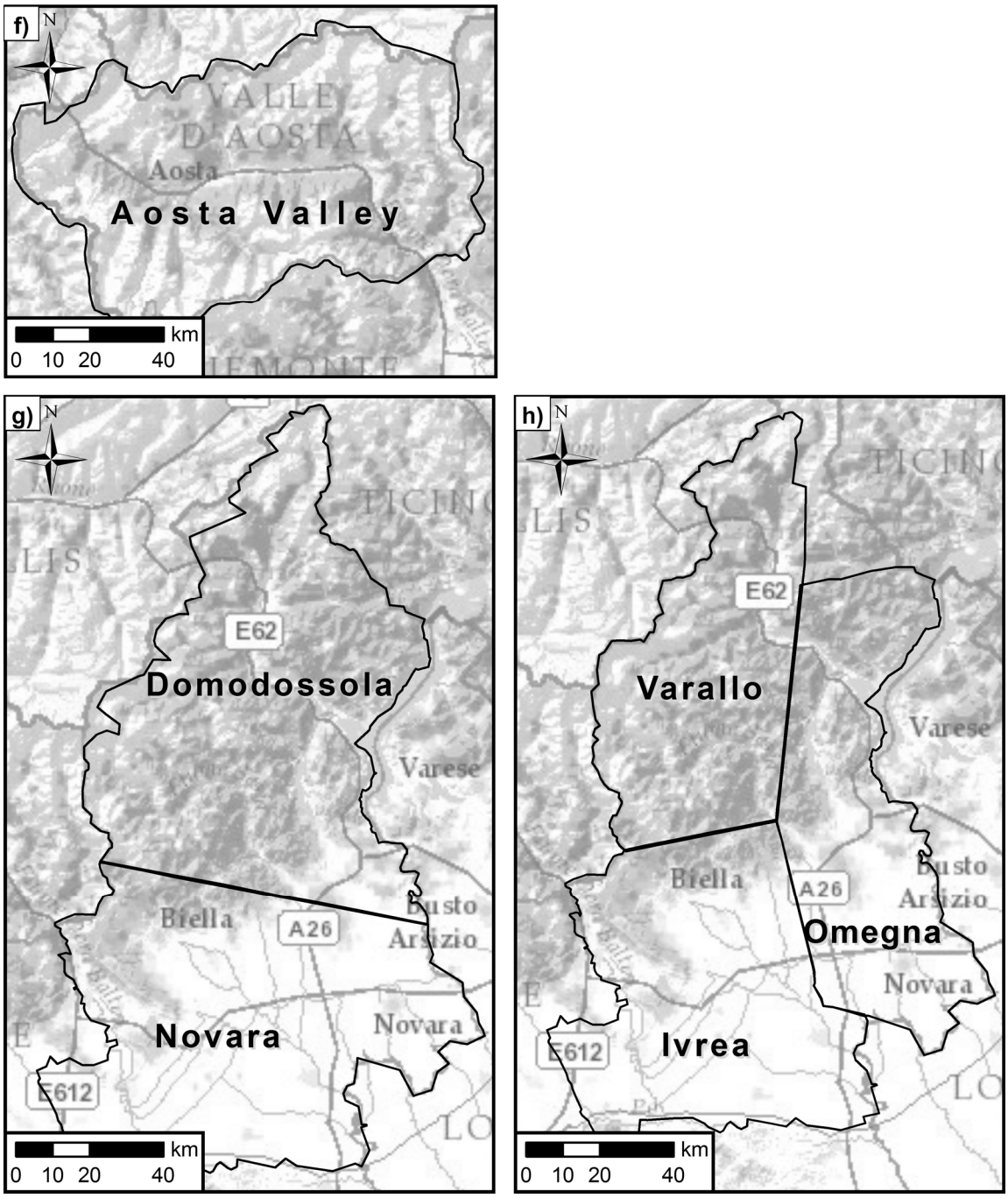

AFig. 1: Maps of the sites: Cairo (a), Budapest (b), Bavaria, Aschau am Inn, Sudelfeld (c), North Germany (d), Netherlands (e), Aosta Valley (f), Piedmont descending: Domodossola and Novara (g), Piedmont ascending: Varallo, Omegna and Ivrea (h). See also Fig. 2. © Background map ESRI.

Appendix 2: Programming code for rotation angle and footprint length

VBA code for calculating the rotation angle ε and the length of the footprint l.

```
Const Pi = 3.14159265358979
Private Sub cmdCalculate_Click()
If txtX1 = txtX2 Then
    txttau = 0
Else
    txttau = Atn((Abs(txtY2 - txtY1)) / (Abs(txtX2 - txtX1))) * (180 / Pi)
End If
End Sub
Private Sub cmdLength_Click()
txtLength = Sqr(((txtX2 - txtX1) ^ 2) + ((txtY2 - txtY1) ^ 2))
End Sub
```

Appendix 3: Programming code for optimal moving distance

Python Code optimal moving distance.

```
import math, sys, os
r = input("Input Cellsize of Raster: ")
h = input("Input maximum difference of height: ")
inci = input("Input incidence angle: ")
if (inci >= 90.0-inci):                    #if and else because of
                                           #layover and shadowing
    m = h*(math.tan(inci*(math.pi/180.0))) #the optimal moving distance has
                                           #to be calculated for the
#greatest angle inci or (90.0 - inci)
else:
    m = h*(math.tan((90.0-inci)*(math.pi/180.0)))

m_int=int(m)
while m_int%r != 0:
    m_int = m_int + 1
print """%f meter is the optimal moving distance
```

Appendix 4: Programming code for split lines

VBA code for the split lines.

```
If [FID] = 0 Or [FID] = 2 Then
    b = 100
ElseIf [FID] = 1 Or [FID] = 3 Then
    b = 12000 'Insert here the optimal Move-Distance
End If
BufferDist = b
```

Appendix 5: Programming code for the individual incidence angle

VBA code for calculation of the individual incidence angle of each observer point.

```
Select Case [Pass]
Case 1
     Ascangle = [inci_near] + ((([inci_far] - [inci_near])/
[LengthL])*([Point_X] - [X_Pivot]))
     If (Ascangle < [inci_near]) Then
          inci = [inci_near]
     ElseIf (Ascangle > [inci_far]) Then
```

```
          inci = [inci_far]
     Else
          inci = Ascangle
     End If
Case 2
     Descangle = [inci_far] - ((([inci_far] - [inci_near])/
[LengthL])*([Point_X] - [X_Pivot]))
     If (Descangle < [inci_near]) Then
          inci = [inci_near]
     ElseIf (Descangle > [inci_far]) Then
          inci = [inci_far]
     Else
          inci = Descangle
     End If
End Select
```

Appendix 6: Programming code for observer height and visual field

VBA codes for the calculation of the height (*OFFSETA*), the vertical (*VERT1 & 2*) and the horizontal (*AZIMUTH1 & 2*) visual field of each observer.

- Height:

Layover:

```
Offseta = [movedist]*(Tan([inci_angle]*(3.1415926535897931/180.0)))
```

Shadow:

```
Offseta = [movedist]/(Tan([inci_angle]*(3.1415926535897931/180.0)))
```

- VERT1

Layover:

```
vert1 = (-1.0)*(Atn(([movedist]*Tan([inci_angle]*
(3.1415926535897931/180.0)))/([movedist]+([cellsize]/2))))*(180.0/3.1415926
535897931)
```

Shadow:

```
vert1 = (-1.0)*(90.0-(Atn((([movedist]+([cellsize]/2))*Tan( [in-
ci_angle]*(3.1415926535897931/180.0)))/[movedist])*(180.0/3.141592653589793
1)))
```

- VERT2

Layover:

```
vert2 = (-1.0)*(Atn(([movedist]*Tan([inci_angle]*
(3.1415926535897931/180.0)))/([movedist]-
([cellsize]/2))))*(180.0/3.1415926535897931)
```

Shadow:

```
vert2 = (-1.0)*(90.0 - (Atn((([movedist]-
([cellsize]/2))*Tan([inci_angle]*(3.1415926535897931/180.0)))/[movedist])*
(180.0/3.1415926535897931)))
```

- AZIMUTH1

Layover:

```
Select Case [Pass]
Case 2
     azimuth1 = 90.0-(Atn([cellsize]/(2*[movedist]))*(180.0/
3.1415926535897931))
Case 1
     azimuth1 = 270.0-
(Atn([cellsize]/(2*[movedist]))*(180.0/3.1415926535897931))
End Select
```

Shadow:

```
Select Case [Pass]
Case 1
     azimuth1 = 90.0-(Atn([cellsize]/(2*[movedist]))*(180.0/
3.1415926535897931))
Case 2
     azimuth1 = 270.0-
(Atn([cellsize]/(2*[movedist]))*(180.0/3.1415926535897931))
End Select
```

- AZIMUTH2

Layover:

```
Select Case [Pass]
Case 2
     azimuth2 = 90.0+(Atn([cellsize]/(2*[movedist]))*(180.0/
3.1415926535897931))
Case 1
     azimuth2 =
270.0+(Atn([cellsize]/(2*[movedist]))*(180.0/3.1415926535897931))
End Select
```

Shadow:

```
Select Case [Pass]
Case 1
     azimuth2 = 90.0+(Atn([cellsize]/(2*[movedist]))*(180.0/
3.1415926535897931))
Case 2
     azimuth2 =
270.0+(Atn([cellsize]/(2*[movedist]))*(180.0/3.1415926535897931))
End Select
```

Appendix 7: Application of the land cover classification

ATab. 1: Application of the classification of the main types of land cover regarding the applicability of D-InSAR on the CORINE 2006 land cover data ('1' = 'very well' to '6' = 'not at all suitable')

CORINE 2006 Class	X-band	C-band	L-band	Corresponding main type of land cover class (Tab. 4)
Continuous urban fabric	1	1	1	Continuous urban area
Port areas				
Industrial or commercial units				
Road and rail networks and associated land	1	1	2	Discontinuous urban area and infrastructural work
Discontinuous urban fabric				
Airports				
Glaciers and perpetual snow	6	6	6	Glaciers and perpetual snow
Mineral extraction sites	6	6	6	Fast changing areas
Dump sites				
Construction sites				
Burnt areas				
Green urban areas	5	4	3	Mixture of 'forest' and 'pastures'.
Principally farmland with significant natural vegetation				
Vineyards				
Fruit trees and berry plantations				
Sclerophyllous vegetation				
Transitional woodland-shrub				
Moors and heathland				
Peat bogs				
Sport and leisure facilities	3	2	2	Alluvium
Beaches, dunes, sands				
Sparsely vegetated areas				
Non-irrigated arable land	6	6	6	Farmland
Annual crops associated with permanent crops				
Complex cultivation patterns				
Rice fields				
Permanently irrigated land				
Bare rocks	2	1	1	Rocks
Pastures	4	3	2	Meadows and pastures
Natural grasslands				
Salt marshes				
Inland marshes				
Salines	6	6	6	Permanently or at least periodically covered by water.
Intertidal flats				
Water courses				
Water bodies				
Coastal lagoons				
Estuaries				
Sea and ocean				
Broad-leaved forest	6	5	3	Forest
Coniferous forest				
Mixed forest				
Olive groves				
Agro-forestry areas				

Appendix 8: Implementation of the land cover based PS-estimation method

This appendix briefly describes the ArcGIS® model and SQL codes developed for the calculation of the absolute and relative PS(DS)-density calculation.

Both the land cover data and the geocoded PS-targets have to be in vector format (shapefile) and transformed into UTM projection of the corresponding UTM zone. If the land cover data is originally in raster format (e.g. tiff), the tool *Raster to Polygon* (based on *value*) can be used for the transformation to shapefile. In the next step, the developed ArcGIS® model 'LandCover Shapefile PS Relation' is executed. This model *clips* the land cover shapefile to the site area and calculates the area of each single land cover polygon. Next, *Identiy* is used to assign to each PS-target the code (GRIDCODE) and area of the land cover polygon at which it is located. Finally, the land cover and updated geocoded PS-targets are saved as feature class in a personal geodatabase (*.mdb).

The aforementioned geodatabase is opened in e.g. Microsoft® Access® and following SQL queries are applied:

- Calculation of the total area (in km²) of each land cover class within the site:

```
SELECT gridcode AS "Land Cover Type", SUM(f_area)/10^6 AS "Area (km^2)"
FROM GlobCov_UTM36N_Clip_Area_aggr
GROUP BY gridcode;
```

- Frequency (number) of geocoded PS-targets within each land cover class:

```
SELECT gridcode AS ["Land Cover Type"], COUNT(*) AS ["Frequency"]
FROM pt_sp_cairo_GlobCover_2009_aggr
GROUP BY gridcode;
```

- Inner join of the two SQL queries explained above to calculate the PS(DS)-density (per km², rounded to 2 decimal places):

```
SELECT f.["Land Cover Type"], f.["Frequency"], ROUND(l.["Area (km^2)"], 2)
AS "Areakm2", ROUND(f.["Frequency"]/l.["Area (km^2)"], 2) AS ["PS-targets
per km2"]
FROM Frequency AS f INNER JOIN LandCoverType_AreaSum AS l ON f.["Land Cover
Type"] = l.["Land Cover Type"];
```

Finally, the absolute PS(DS)-density value of each land cover class is divided by the PS(DS)-density value of the corresponding reference class ('urban area') to determine the relative PS(DS)-density of each class.

Appendix 9: Absolute and relative PS(DS)-density of all sites

At all sites water bodies were omitted in the tables described below. Water can not contain any PS-targets. However, due to the rough spatial resolution (especially of GlobCover – 300 m), a few PS-targets were falsely assigned to water bodies. These PS-targets are mainly caused by buildings near the waterfront, or by bridges. Rows that are written *italic* are not considered in the succeeding calculation of the relative PS(DS)-density. In the following each exclusion is briefly explained.

I. GlobCover 2009

I.I 'normal' PS

I.I.I Cairo site – GlobCover 2009

The class '14' (Rainfed croplands) is excluded from the succeeding calculations, as this land cover class has a very small area within the Cairo site. At such a small area very small changes of the number of PS-targets cause strong changes in the PS-density. In the case of the Cairo site the PS-density is strongly overestimated in class '14'.

ATab. 2: Absolute & relative PS-density Cairo site for thresholding on the SCR

Class	Frequency	Area [km²]	PS-targets per km²	LCCS GlobCover global legend	relative PS-density based on '190'
11	3983	955.86	4.17	Post-flooding or irrigated croplands	0.05
14	*19*	*0.44*	*42.72*	*Rainfed croplands*	*0.51*
20	1004	30.67	32.74	Mosaic Cropland (50-70%) / Vegetation (grassland, shrubland, forest) (20-50%)	0.39
30	239	8.69	27.5	Mosaic Vegetation (grassland, shrubland, forest) (50-70%) / Cropland (20-50%)	0.33
130	1232	36.66	33.61	Closed to open (>15%) shrubland (<5m)	0.40
150	565	12.21	46.28	Sparse (>15%) vegetation (woody vegetation, shrubs, grassland)	0.55
190	38953	465.12	83.75	Artificial surfaces and associated areas (urban areas >50%)	1.00
200	73301	852.28	86.01	Bare areas	1.03

ATab. 3: Absolute & relative PS-density Cairo site for thresholding on the D_a

Class	Frequency	Area [km²]	PS-targets per km²	LCCS GlobCover global legend	relative PS-density based on 190
11	4362	955.86	4.56	Post-flooding or irrigated croplands	0.04
14	*16*	*0.44*	*35.97*	*Rainfed croplands*	*0.30*
20	1355	30.67	44.18	Mosaic Cropland (50-70%) / Vegetation (grassland, shrubland, forest) (20-50%)	0.36
30	297	8.69	34.18	Mosaic Vegetation (grassland, shrubland, forest) (50-70%) / Cropland (20-50%)	0.28
130	1593	36.66	43.46	Closed to open (>15%) shrubland (<5m)	0.36
150	856	12.21	70.12	Sparse (>15%) vegetation (woody vegetation, shrubs, grassland)	0.58
190	56631	465.12	121.75	Artificial surfaces and associated areas (urban areas >50%)	1.00
200	261712	852.28	307.07	Bare areas	2.52

ATab. 4: Absolute & relative PS-density Cairo site for combination of thresholding on the SCR and thresholding on the D_a

Class	Frequency	Area [km²]	PS-targets per km²	LCCS GlobCover global legend	relative PS-density based on 190
11	7607	955.86	7.96	Post-flooding or irrigated croplands	0.04
14	*34*	*0.44*	*76.45*	*Rainfed croplands*	*0.39*
20	2231	30.67	72.75	Mosaic Cropland (50-70%) / Vegetation (grassland, shrubland, forest) (20-50%)	0.37
30	499	8.69	57.42	Mosaic Vegetation (grassland, shrubland, forest) (50-70%) / Cropland (20-50%)	0.29
130	2663	36.66	72.65	Closed to open (>15%) shrubland (<5m)	0.37
150	1327	12.21	108.7	Sparse (>15%) vegetation (woody vegetation, shrubs, grassland)	0.56
190	91057	465.12	195.77	Artificial surfaces and associated areas (urban areas >50%)	1.00
200	322279	852.28	378.14	Bare areas	1.93

I.I.II Aosta Valley site – GlobCover 2009

The datasets of Aosta Valley east (ascending & descending) cannot be considered in the succeeding calculations, as at these sites the area of reference class '190' (urban area) is very small. As already mentioned above, at such a small area even small changes in the number of PS-targets can cause strong variations of the PS-density. As the area of the reference class is too small, the entire dataset of Aosta Valley east cannot be considered (valid for GlobCover 2009).

ATab. 5: Absolute & relative PS-density site Aosta Valley ascending east

Class	Frequency	Area [km²]	PS-targets per km²	LCCS GlobCover global legend	relative PS-density based on '190'
14	*19146*	*183.61*	*104.28*	*Rainfed croplands*	*0.58*
20	*27850*	*374.44*	*74.38*	*Mosaic Cropland (50-70%) / Vegetation (grassland, shrubland, forest) (20-50%)*	*0.41*
30	*14556*	*203.14*	*71.65*	*Mosaic Vegetation (grassland, shrubland, forest) (50-70%) / Cropland (20-50%)*	*0.40*
50	*7836*	*127.07*	*61.66*	*Closed (>40%) broadleaved deciduous forest (>5m)*	*0.34*
70	*5995*	*152.32*	*39.36*	*Closed (>40%) needleleaved evergreen forest (>5m)*	*0.22*
90	*648*	*20.95*	*30.94*	*Open (15-40%) needleleaved deciduous or evergreen forest*	*0.17*
100	*3427*	*69.24*	*49.49*	*Closed to open (>15%) mixed broadleaved and needleleaved*	*0.27*
110	*199*	*1.67*	*119.15*	*Mosaic forest or shrubland (50-70%) / grassland (20-50%)*	*0.66*
120	*4852*	*52.57*	*92.3*	*Mosaic grassland (50-70%) / forest or shrubland (20-50%)*	*0.51*
140	*3266*	*29.02*	*112.54*	*Closed to open (>15%) herbaceous vegetation (grassland, savannas or lichens/mosses)*	*0.62*
150	*8706*	*149.64*	*58.18*	*Sparse (<15%) vegetation (woody vegetation, shrubs, grassland)*	*0.32*
190	*684*	*3.77*	*181.31*	*Artificial surfaces and associated areas (urban areas >50%)*	*1.00*
200	*3735*	*86.19*	*43.34*	*Bare areas*	*0.24*
220	*711*	*61.35*	*11.59*	*Permanent snow and ice*	*0.06*

ATab. 6: Absolute & relative PS-density site Aosta Valley descending east

Class	Frequency	Area [km²]	PS-targets per km²	LCCS GlobCover global legend	relative PS-density based on '190'
14	*18367*	*183.61*	*100.03*	*Rainfed croplands*	*0.46*
20	*29840*	*374.44*	*79.69*	*Mosaic Cropland (50-70%) / Vegetation (grassland, shrubland, forest) (20-50%)*	*0.37*
30	*12127*	*203.14*	*59.7*	*Mosaic Vegetation (grassland, shrubland, forest) (50-70%) / Cropland (20-50%)*	*0.28*
50	*8688*	*127.07*	*68.37*	*Closed (>40%) broadleaved deciduous forest (>5m)*	*0.32*
70	*7765*	*152.32*	*50.98*	*Closed (>40%) needleleaved evergreen forest (>5m)*	*0.24*
90	*1054*	*20.95*	*50.32*	*Open (15-40%) needleleaved deciduous or evergreen forest*	*0.23*
100	*3334*	*69.24*	*48.15*	*Closed to open (>15%) mixed broadleaved and needleleaved*	*0.22*
110	*94*	*1.67*	*56.28*	*Mosaic forest or shrubland (50-70%) / grassland (20-50%)*	*0.26*
120	*3736*	*52.57*	*71.07*	*Mosaic grassland (50-70%) / forest or shrubland (20-50%)*	*0.33*
140	*1797*	*29.02*	*61.92*	*Closed to open (>15%) herbaceous vegetation (grassland, savannas or lichens/mosses)*	*0.29*
150	*9257*	*149.64*	*61.86*	*Sparse (<15%) vegetation (woody vegetation, shrubs, grassland)*	*0.29*
190	*812*	*3.77*	*215.24*	*Artificial surfaces and associated areas (urban areas >50%)*	*1.00*
200	*3051*	*86.19*	*35.4*	*Bare areas*	*0.16*
220	*338*	*61.35*	*5.51*	*Permanent snow and ice*	*0.03*

ATab. 7: Absolute & relative PS-density site Aosta Valley ascending west

Class	Frequency	Area [km²]	PS-targets per km²	LCCS GlobCover global legend	relative PS-density based on '190'
14	20898	212.73	98.24	Rainfed croplands	0.21
20	27102	481.21	56.32	Mosaic Cropland (50-70%) / Vegetation (grassland, shrubland, forest) (20-50%)	0.12
30	16498	215.45	76.57	Mosaic Vegetation (grassland, shrubland, forest) (50-70%) / Cropland (20-50%)	0.17
50	7010	124.25	56.42	Closed (>40%) broadleaved deciduous forest (>5m)	0.12
70	4082	204.22	19.99	Closed (>40%) needleleaved evergreen forest (>5m)	0.04
90	106	11.52	9.2	Open (15-40%) needleleaved deciduous or evergreen forest	0.02
100	3103	62.22	49.87	Closed to open (>15%) mixed broadleaved and needleleaved	0.11
110	189	1.84	102.97	Mosaic forest or shrubland (50-70%) / grassland (20-50%)	0.22
120	4990	37.1	134.52	Mosaic grassland (50-70%) / forest or shrubland (20-50%)	0.29
140	1996	15.37	129.85	Closed to open (>15%) herbaceous vegetation (grassland, savannas or lichens/mosses)	0.28
150	10161	199.28	50.99	Sparse (<15%) vegetation (woody vegetation, shrubs, grassland)	0.11
190	5054	10.99	459.72	Artificial surfaces and associated areas (urban areas >50%)	1.00
200	7117	195.99	36.31	Bare areas	0.08
220	543	43.28	12.55	Permanent snow and ice	0.03

ATab. 8: Absolute & relative PS-density site Aosta Valley descending west

Class	Frequency	Area [km²]	PS-targets per km²	LCCS GlobCover global legend	relative PS-density based on '190'
14	14974	233.52	64.12	Rainfed croplands	0.15
20	25180	512.77	49.11	Mosaic Cropland (50-70%) / Vegetation (grassland, shrubland, forest) (20-50%)	0.12
30	11029	240.57	45.84	Mosaic Vegetation (grassland, shrubland, forest) (50-70%) / Cropland (20-50%)	0.11
50	6500	126.82	51.25	Closed (>40%) broadleaved deciduous forest (>5m)	0.12
70	5687	207.69	27.38	Closed (>40%) needleleaved evergreen forest (>5m)	0.07
90	214	11.61	18.44	Open (15-40%) needleleaved deciduous or evergreen forest	0.04
100	2914	62.37	46.72	Closed to open (>15%) mixed broadleaved and needleleaved	0.11
110	109	1.84	59.39	Mosaic forest or shrubland (50-70%) / grassland (20-50%)	0.14
120	4055	37.1	109.31	Mosaic grassland (50-70%) / forest or shrubland (20-50%)	0.26
140	1622	16.18	100.23	Closed to open (>15%) herbaceous vegetation (grassland, savannas or lichens/mosses)	0.24
150	8506	219.37	38.77	Sparse (<15%) vegetation (woody vegetation, shrubs, grassland)	0.09
190	4929	11.72	420.56	Artificial surfaces and associated areas (urban areas >50%)	1.00
200	4138	214.74	19.27	Bare areas	0.05
220	349	46.72	7.47	Permanent snow and ice	0.02

ATab. 9: Absolute & relative PS-density site Aosta Valley ascending west, layover and shadow areas excluded

Class	Frequency	Area [km²]	PS-targets per km²	LCCS GlobCover global legend	relative PS-density based on '190'
14	10319	51.03	202.21	Rainfed croplands	0.22
20	13678	140.07	97.65	Mosaic Cropland (50-70%) / Vegetation (grassland, shrubland, forest) (20-50%)	0.10
30	6941	46.88	148.05	Mosaic Vegetation (grassland, shrubland, forest) (50-70%) / Cropland (20-50%)	0.16
50	3310	35.55	93.12	Closed (>40%) broadleaved deciduous forest (>5m)	0.10
70	2699	93.75	28.79	Closed (>40%) needleleaved evergreen forest (>5m)	0.03
90	30	2.99	10.03	Open (15-40%) needleleaved deciduous or evergreen forest	0.01
100	1878	28.12	66.8	Closed to open (>15%) mixed broadleaved and needleleaved	0.07
120	1560	11.32	137.79	Mosaic grassland (50-70%) / forest or shrubland (20-50%)	0.15
140	751	3.92	191.65	Closed to open (>15%) herbaceous vegetation (grassland, savannas or lichens/mosses)	0.20
150	3461	46.94	73.74	Sparse (<15%) vegetation (woody vegetation, shrubs, grassland)	0.08
190	4925	5.26	935.93	Artificial surfaces and associated areas (urban areas >50%)	1.00
200	1903	30.92	61.54	Bare areas	0.07
220	1	0.21	4.83	Permanent snow and ice	0.01

I.I.III Budapest site – GlobCover 2009

ATab. 10: Absolute & relative PS-density Budapest site

Class	Frequency	Area [km²]	PS-targets per km²	LCCS GlobCover global legend	relative PS-density based on '190'
14	23115	8.87	2606.5	Rainfed croplands	0.26
20	20042	7.86	2550.4	Mosaic Cropland (50-70%) / Vegetation (grassland, shrubland, forest) (20-50%)	0.25
30	14470	5.21	2778.7	Mosaic Vegetation (grassland, shrubland, forest) (50-70%) / Cropland (20-50%)	0.27
50	2346	2.11	1111.8	Closed (>40%) broadleaved deciduous forest (>5m)	0.11
150	2016	0.39	5198.4	Sparse (>15%) vegetation (woody vegetation, shrubs, grassland)	0.51
190	1528843	150.31	10171.	Artificial surfaces and associated areas (urban areas >50%)	1.00
200	2960	0.38	7701.9	Bare areas	0.76

I.I.IV Bavaria site – GlobCover 2009

The values of the classes '180' and '200' are not considered, due to their small area.

ATab. 11: Absolute & relative PS-density Bavaria site

Class	Frequency	Area [km²]	PS-targets per km²	LCCS GlobCover global legend	relative PS-density based on '190'
14	57459	1334.7	43.05	Rainfed croplands	0.16
20	54173	854.55	63.39	Mosaic Cropland (50-70%) / Vegetation (grassland, shrubland, forest) (20-50%)	0.24
30	36394	750.33	48.5	Mosaic Vegetation (grassland, shrubland, forest) (50-70%) / Cropland (20-50%)	0.18
50	55653	1642.4	33.88	Closed (>40%) broadleaved deciduous forest (>5m)	0.13
70	11636	389.55	29.87	Closed (>40%) needleleaved evergreen forest (>5m)	0.11
90	870	30.36	28.65	Open (15-40%) needleleaved deciduous or evergreen forest	0.11
100	20646	907.15	22.76	Closed to open (>15%) mixed broadleaved and needleleaved	0.09
110	32331	791.78	40.83	Mosaic forest or shrubland (50-70%) / grassland (20-50%)	0.15
120	30399	760.01	40.00	Mosaic grassland (50-70%) / forest or shrubland (20-50%)	0.15
140	26518	655.73	40.44	Closed to open (>15%) herbaceous vegetation (grassland, savannas or lichens/mosses)	0.15
150	1795	11.41	157.29	Sparse (<15%) vegetation	0.59
180	*30*	*0.2*	*148.22*	*Closed to open (>15%) grassland or woody vegetation on regularly flooded or water-logged soil - Fresh, brackish or saline*	*0.55*
190	73546	274.76	267.68	Artificial surfaces and associated areas (urban areas >50%)	1.00
200	*748*	*4.04*	*185.05*	*Bare areas*	*0.69*

I.I.V North Germany site – GlobCover 2009

The values of the classes '180' and '200' are not considered, due to their small area. The class '90' shows a very high PS-density. Visual comparison with optical data (Google Earth™) showed that this land cover class is located at very narrow zones of 200 to 300 m width surrounding urban area. The area of class '90' is characterized by a high density of buildings, but, due to the relatively high number of trees and the rough spatial resolution of GlobCover (300 m), this area was falsely classified as 'mixed forest' and not as 'urban area'. Therefore,

the high PS-density of this class is an outlier, which is not considered in the succeeding calculations.

ATab. 12: Absolute & relative PS-density North Germany site

Class	Frequency	Area [km²]	PS-targets per km²	LCCS GlobCover global legend	relative PS-density based on '190'
14	15079	1509.3	9.99	Rainfed croplands	0.07
20	22189	1436.1	15.45	Mosaic Cropland (50-70%) / Vegetation (grassland, shrubland, forest) (20-50%)	0.11
30	22611	1800.4	12.56	Mosaic Vegetation (grassland, shrubland, forest) (50-70%) / Cropland (20-50%)	0.09
50	27856	1989.8	14.00	Closed (>40%) broadleaved deciduous forest (>5m)	0.10
70	1373	130.41	10.53	Closed (>40%) needleleaved evergreen forest (>5m)	0.08
90	*5563*	*59.61*	*93.33*	*Open (15-40%) needleleaved deciduous or evergreen forest*	*0.66*
100	4832	522.19	9.25	Closed to open (>15%) mixed broadleaved and needleleaved	0.07
110	279	172.15	1.62	Mosaic forest or shrubland (50-70%) / grassland (20-50%)	0.01
120	13943	1916.8	7.27	Mosaic grassland (50-70%) / forest or shrubland (20-50%)	0.05
140	4151	868.66	4.78	Closed to open (>15%) herbaceous vegetation (grassland, savannas or lichens/mosses)	0.03
150	626	7.56	82.8	Sparse (>15%) vegetation (woody vegetation, shrubs, grassland)	0.59
180	*3*	*2.1*	*1.43*	*Closed to open (>15%) grassland or woody vegetation on regularly flooded or waterlogged soil - Fresh, brackish or saline wa-*	*0.01*
190	60517	431.16	140.36	Artificial surfaces and associated areas (urban areas >50%)	1.00
200	205	3.88	52.81	Bare areas	0.38

I.I.VI Aschau am Inn site – GlobCover 2009

Similarly to the sites Aosta Valley east (ascending & descending), this site cannot be considered (in the case of GlobCover 2009) because of its very small area of the reference class '190' (urban area), which distort the relative PS-density calculations.

ATab. 13: Absolute & relative PS-density Aschau am Inn site

Class	Frequency	Area [km²]	PS-targets per km²	LCCS GlobCover global legend	relative PS-density based on '190'
14	*9090*	*13.86*	*655.87*	*Rainfed croplands*	*1.09*
20	*4395*	*10.41*	*422.19*	*Mosaic Cropland (50-70%) / Vegetation (grassland, shrubland, forest) (20-50%)*	*0.70*
30	*5454*	*18.28*	*298.32*	*Mosaic Vegetation (grassland, shrubland, forest) (50-70%) / Cropland (20-50%)*	*0.50*
50	*7532*	*35.32*	*213.24*	*Closed (>40%) broadleaved deciduous forest (>5m)*	*0.35*
70	*6*	*2.27*	*2.64*	*Closed (>40%) needleleaved evergreen forest (>5m)*	*0.00*
100	*323*	*5.1*	*63.35*	*Closed to open (>15%) mixed broadleaved and needleleaved*	*0.11*
110	*368*	*2.59*	*142.28*	*Mosaic forest or shrubland (50-70%) / grassland (20-50%)*	*0.24*
120	*4856*	*18.79*	*258.44*	*Mosaic grassland (50-70%) / forest or shrubland (20-50%)*	*0.43*
140	*3628*	*13.31*	*272.56*	*Closed to open (>15%) herbaceous vegetation (grassland, savannas or lichens/mosses)*	*0.45*
190	*208*	*0.35*	*601.44*	*Artificial surfaces and associated areas (urban areas >50%)*	*1.00*

I.I.VII Netherlands site – GlobCover 2009

Class '180' is not considered, due to its small area.

ATab. 14: Absolute & relative PS-density Netherlands site

Class	Frequency	Area [km²]	PS-targets per km²	LCCS GlobCover global legend	relative PS-density based on '190'
14	6723	1429.6	4.7	Rainfed croplands	0.15
20	7305	1421.9	5.14	Mosaic Cropland (50-70%) / Vegetation (grassland, shrubland, forest) (20-50%)	0.17
30	3443	689.72	4.99	Mosaic Vegetation (grassland, shrubland, forest) (50-70%) / Cropland (20-50%)	0.16
50	2133	371.05	5.75	Closed (>40%) broadleaved deciduous forest (>5m)	0.19
70	261	43.48	6.00	Closed (>40%) needleleaved evergreen forest (>5m)	0.19
90	103	14.49	7.11	Open (15-40%) needleleaved deciduous or evergreen forest	0.23
100	410	108.86	3.77	Closed to open (>15%) mixed broadleaved and needleleaved	0.12
110	10	15.92	0.63	Mosaic forest or shrubland (50-70%) / grassland (20-50%)	0.02
120	1008	303.56	3.32	Mosaic grassland (50-70%) / forest or shrubland (20-50%)	0.11
140	395	152.89	2.58	Closed to open (>15%) herbaceous vegetation (grassland, savannas or lichens/mosses)	0.08
150	882	50.04	17.63	Sparse (>15%) vegetation (woody vegetation, shrubs, grassland)	0.57
180	*10*	*4.97*	*2.01*	*Closed to open (>15%) grassland or woody vegetation on regularly flooded or waterlogged soil - Fresh, brackish or saline*	*0.07*
190	24623	799.42	30.8	Artificial surfaces and associated areas (urban areas >50%)	1.00
200	589	20.83	28.28	Bare areas	0.92

I.I.VIII Piedmont sites – GlobCover 2009

At the Domodossola site the values of the class '130' are not considered, due to its very small area.

ATab. 15: Absolute & relative PS-density Domodossola (Piedmont) site

Class	Frequency	Area [km²]	PS-targets per km²	LCCS GlobCover global legend	relative PS-density based on '190'
14	19594	343.01	57.12	Rainfed croplands	0.22
20	25497	740.85	34.42	Mosaic Cropland (50-70%) / Vegetation (grassland, shrubland, forest) (20-50%)	0.13
30	13444	387.18	34.72	Mosaic Vegetation (grassland, shrubland, forest) (50-70%) / Cropland (20-50%)	0.13
50	14383	849.41	16.93	Closed (>40%) broadleaved deciduous forest (>5m)	0.07
70	2542	224.68	11.31	Closed (>40%) needleleaved evergreen forest (>5m)	0.04
90	652	47.71	13.67	Open (15-40%) needleleaved deciduous or evergreen forest	0.05
100	2268	208.96	10.85	Closed to open (>15%) mixed broadleaved and needleleaved	0.04
110	66	12.05	5.48	Mosaic forest or shrubland (50-70%) / grassland (20-50%)	0.02
120	7916	421.95	18.76	Mosaic grassland (50-70%) / forest or shrubland (20-50%)	0.07
130	*2*	*0.03*	*59.34*	*Closed to open (>15%) (broadleaved or needleleaved, evergreen of deciduous) shrubland (<5m)*	*0.23*
140	2014	164.98	12.21	Closed to open (>15%) herbaceous vegetation (grassland, savannas or lichens/mosses)	0.05
150	3538	108.79	32.52	Sparse (>15%) vegetation	0.13
190	5962	23.16	257.39	Artificial surfaces and associated areas (urban areas >50%)	1.00
200	196	22.84	8.58	Bare areas	0.03

220	37	3,64	10.17	Permanent snow and ice	0.04

At the Novara site the class '110' was not considered, due to its small area and the following very strong overestimation of the PS-density.

ATab. 16: Absolute & relative PS-density Novara (Piedmont) site

Class	Frequency	Area [km²]	PS-targets per km²	LCCS GlobCover global legend	relative PS-density based on '190'
11	20236	1359.9	14.88	Post-flooding or irrigated croplands	0.06
14	16127	345.63	46.66	Rainfed croplands	0.19
20	31349	550.93	56.9	Mosaic Cropland (50-70%) / Vegetation (grassland, shrubland, forest) (20-50%)	0.23
30	14605	193.56	75.45	Mosaic Vegetation (grassland, shrubland, forest) (50-70%) / Cropland (20-50%)	0.31
50	13371	584.93	22.86	Closed (>40%) broadleaved deciduous forest (>5m)	0.09
70	284	13.23	21.46	Closed (>40%) needleleaved evergreen forest (>5m)	0.09
90	87	5.52	15.75	Open (15-40%) needleleaved deciduous or evergreen forest	0.06
100	92	7.34	12.53	Closed to open (>15%) mixed broadleaved and needleleaved	0.05
110	*843*	*4.63*	*182.26*	*Mosaic forest or shrubland (50-70%) / grassland (20-50%)*	*0.74*
120	5130	142.43	36.02	Mosaic grassland (50-70%) / forest or shrubland (20-50%)	0.15
130	2420	19.99	121.06	Closed to open (>15%) (broadleaved or needleleaved, evergreen of deciduous) shrubland (<5m)	0.49
140	886	30.42	29.13	Closed to open (>15%) herbaceous vegetation (grassland, savannas or lichens/mosses)	0.12
150	1548	15.8	97.97	Sparse (<15%) vegetation	0.40
190	36020	146.33	246.16	Artificial surfaces and associated areas (urban areas >50%)	1.00

The classes '150' and '200' are not considered in the Omegna site, because of their small area and following strong overestimation.

ATab. 17: Absolute & relative PS-density Omegna (Piedmont) site

Class	Frequency	Area [km²]	PS-targets per km²	LCCS GlobCover global legend	relative PS-density based on '190'
11	12001	461.21	26.02	Post-flooding or irrigated croplands	0.11
14	16063	210.57	76.28	Rainfed croplands	0.32
20	20862	251.13	83.07	Mosaic Cropland (50-70%) / Vegetation (grassland, shrubland, forest) (20-50%)	0.35
30	8793	151.2	58.15	Mosaic Vegetation (grassland, shrubland, forest) (50-70%) / Cropland (20-50%)	0.25
50	11923	526.65	22.64	Closed (>40%) broadleaved deciduous forest (>5m)	0.10
70	2399	52.68	45.54	Closed (>40%) needleleaved evergreen forest (>5m)	0.19
90	355	15.98	22.21	Open (15-40%) needleleaved deciduous or evergreen forest	0.09
100	1452	74.99	19.36	Closed to open (>15%) mixed broadleaved and needleleaved	0.08
110	283	5.06	55.98	Mosaic forest or shrubland (50-70%) / grassland (20-50%)	0.24
120	4209	171.16	24.59	Mosaic grassland (50-70%) / forest or shrubland (20-50%)	0.10
130	909	8.84	102.87	Closed to open (>15%) (broadleaved or needleleaved, evergreen of deciduous) shrubland (<5m)	0.44
140	369	31.27	11.8	Closed to open (>15%) herbaceous vegetation (grassland, savannas or lichens/mosses)	0.05

150	*1941*	*7.47*	*259.95*	*Sparse (<15%) vegetation*	*1.10*
190	17266	73.21	235.85	Artificial surfaces and associated areas (urban areas >50%)	1.00
200	*9*	*0.13*	*67.42*	*Bare areas*	*0.29*

ATab. 18: Absolute & relative PS-density Varallo (Piedmont) site

Class	Frequency	Area [km²]	PS-targets per km²	LCCS GlobCover global legend	relative PS-density based on '190'
14	11842	180.78	65.51	Rainfed croplands	0.28
20	22832	507.11	45.02	Mosaic Cropland (50-70%) / Vegetation (grassland, shrubland, forest) (20-50%)	0.20
30	10759	237.55	45.29	Mosaic Vegetation (grassland, shrubland, forest) (50-70%) / Cropland (20-50%)	0.20
50	9253	366.9	25.22	Closed (>40%) broadleaved deciduous forest (>5m)	0.11
70	1210	137.11	8.83	Closed (>40%) needleleaved evergreen forest (>5m)	0.04
90	369	26.13	14.12	Open (15-40%) needleleaved deciduous or evergreen forest	0.06
100	1163	110.4	10.53	Closed to open (>15%) mixed broadleaved and needleleaved	0.05
110	70	7.5	9.33	Mosaic forest or shrubland (50-70%) / grassland (20-50%)	0.04
120	5811	233.53	24.88	Mosaic grassland (50-70%) / forest or shrubland (20-50%)	0.11
140	5641	125.74	44.86	Closed to open (>15%) herbaceous vegetation (grassland, savannas or lichens/mosses)	0.19
150	5571	98.5	56.56	Sparse (<15%) vegetation	0.25
190	1640	7.11	230.8	Artificial surfaces and associated areas (urban areas >50%)	1.00
200	1616	42.07	38.42	Bare areas	0.17
220	887	18.08	49.06	Permanent snow and ice	0.21

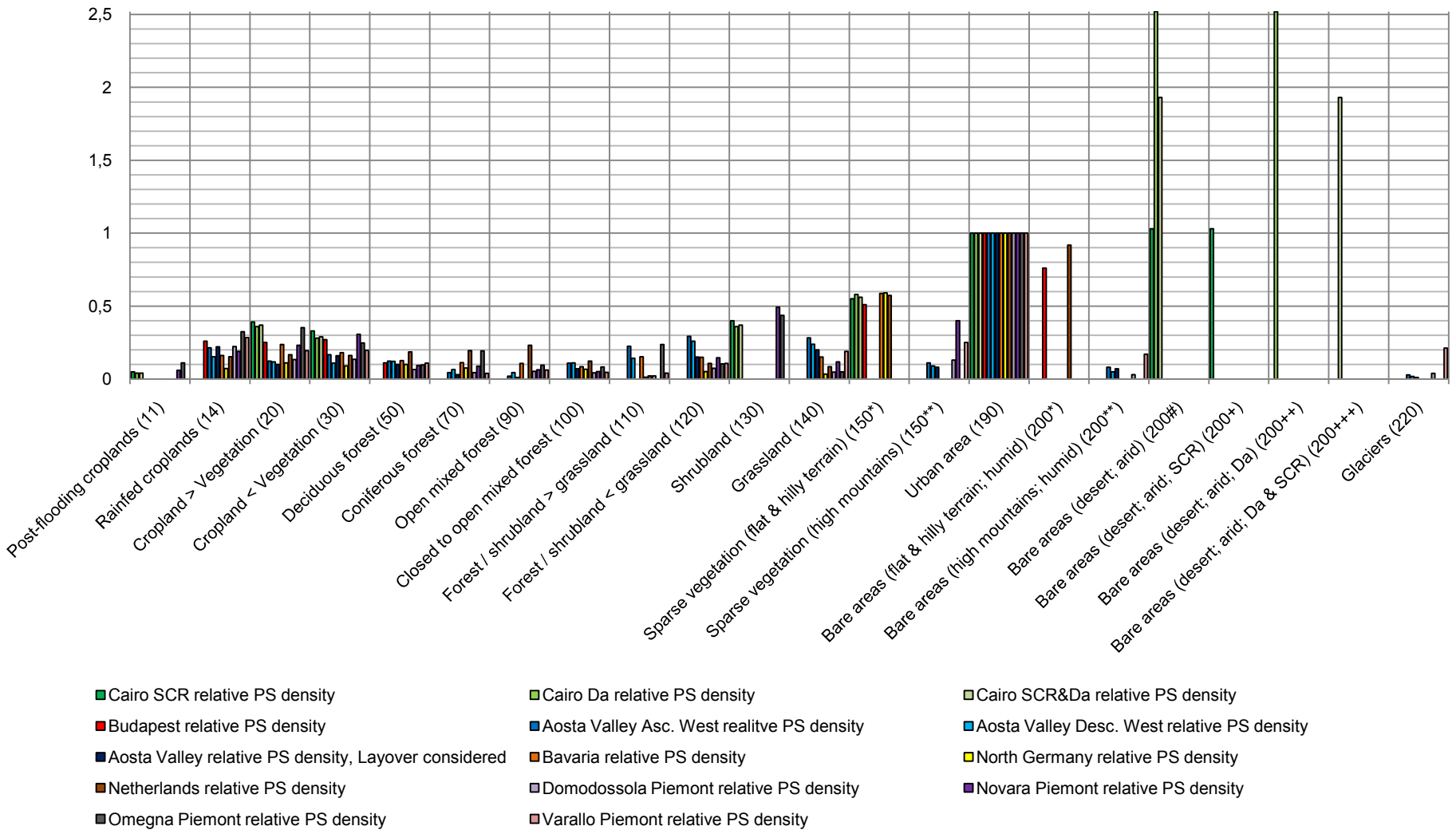

AFig. 2: GlobCover 2009 relative PS-density. The numbers show the ID of the GlobCover land cover classification.

I.I.IX Arithmetic mean and validation of relative PS-density – GlobCover 2009

ATab. 19: Arithmetic mean of relative PS-density of all suitable GlobCover sites (calculated using the data from ATab. 2 to 18, excluding the ATab. 5, 6 and 13)

Updated GlobCover 2009 land cover (class)	Arithmetic mean of relative PS-density	Minimum of relative PS-density	Maximum of relative PS-density
Post-flooding croplands (11)	0.06	0.04	0.11
Rainfed croplands (14)	0.20	0.07	0.32
Cropland > Vegetation (20)	0.22	0.10	0.39
Cropland < Vegetation (30)	0.21	0.09	0.33
Deciduous forest (50)	0.11	0.07	0.19
Coniferous forest (70)	0.09	0.03	0.19
Open mixed forest (90)	0.08	0.01	0.23
Closed to open mixed forest (100)	0.08	0.04	0.12
Forest / shrubland > grassland (110)	0.11	0.01	0.24
Forest / shrubland < grassland (120)	0.14	0.05	0.29
Shrubland (130)	0.41	0.36	0.49
Grassland (140)	0.14	0.03	0.28
Sparse vegetation (flat & hilly terrain) (150*)	0.56	0.51	0.59
Sparse vegetation (high mountains) (150**)	0.18	0.08	0.40
Urban area (190)	1.00	1.00	1.00
Bare areas (flat & hilly terrain; humid) (200*)	0.84	0.76	0.92
Bare areas (high mountains; humid) (200**)	0.08	0.03	0.17
Bare areas (desert; arid) (200#)	1.83	1.03	2.52
Bare areas (desert; arid; SCR) (200+)	1.03	1.03	1.03
Bare areas (desert; arid; Da) (200++)	2.52	2.52	2.52
Bare areas (desert; arid; Da & SCR) (200+++)	1.93	1.93	1.93
Glaciers (220)	0.06	0.01	0.21

ATab. 20 shows the result of the validation of the relative PS-density method using GlobCover 2009. Both the processed and estimated PS-density as well as their difference are shown. Great differences are written in *italics*. Due to its small area, the processed PS-density of class '110' is too high. Also class '150**' shows a very high processed PS-density compared with all other sites. Consequently, at these classes there is a large difference between the estimated and processed PS-density. However, as the area of these classes is only a very small part of the entire site area, the influence on the quality of the overall PS-estimation is not very high (cf. chapter 5.1.4.2 a).

ATab. 20: Validation of relative PS-density method at Ivrea (Piedmont) site: Multiplication of the mean values from ATab. 19 and the absolute PS-density of the reference class from the Omegna site (ATab. 17)

Updated GlobCover 2009 land cover (class)	Frequency	Area [km²]	Processed PS-targets per km²	Estimated PS-targets per km²	Difference of estimated and processed PS-density
Post-flooding croplands (11)	11683	891.71	13.1	14.19	1.09
Rainfed croplands (14)	15288	266.17	57.44	48.23	-9.21
Cropland > Vegetation (20)	28023	432.82	64.75	52.82	-11.93
Cropland < Vegetation (30)	13320	166.43	80.03	49.23	-30.8
Deciduous forest (50)	14176	498.39	28.44	26.40	-2.04

Coniferous forest (70)	92	8.06	11.42	20.81	9.39
Open mixed forest (90)	130	8.18	15.9	17.93	2.03
Closed to open mixed forest (100)	115	7.61	15.12	18.48	3.36
Forest / shrubland > grassland (110)	*669*	*3.85*	*173.86*	*25.02*	*-148.84*
Forest / shrubland < grassland (120)	5378	132.02	40.73	34.03	-6.7
Shrubland (130)	1466	11.33	129.37	97.07	-32.3
Grassland (140)	1848	30.00	61.61	32.91	-28.7
*Sparse vegetation (high mountains) (150**)*	*1598*	*10.46*	*152.81*	*41.70*	*-111.11*
Urban area (190)	21651	88.61	244.33	235.85	-8.48

I.II DS&PS

For the explanation of the excluded classes (*italic*) the reader is referred to the corresponding table in chapter I.I (only PS).

I.II.I Aosta Valley site – GlobCover 2009

ATab. 21: Absolute & relative DS&PS-density site Aosta Valley ascending east

Class	Frequency	Area [km²]	DS&PS -targets per km²	LCCS GlobCover global legend	relative DS&PS-density based on '190'
14	*69711*	*183.61*	*379.67*	*Rainfed croplands*	*1.16*
20	*100629*	*374.44*	*268.75*	*Mosaic Cropland (50-70%) / Vegetation (grassland, shrubland, forest) (20-50%)*	*0.82*
30	*55362*	*203.14*	*272.53*	*Mosaic Vegetation (grassland, shrubland, forest) (50-70%) / Cropland (20-50%)*	*0.83*
50	*21853*	*127.07*	*171.97*	*Closed (>40%) broadleaved deciduous forest (>5m)*	*0.52*
70	*19974*	*152.32*	*131.13*	*Closed (>40%) needleleaved evergreen forest (>5m)*	*0.40*
90	*2580*	*20.95*	*123.17*	*Open (15-40%) needleleaved deciduous or evergreen forest*	*0.38*
100	*9073*	*69.24*	*131.03*	*Closed to open (>15%) mixed broadleaved and needleleaved*	*0.40*
110	*357*	*1.67*	*213.76*	*Mosaic forest or shrubland (50-70%) / grassland (20-50%)*	*0.65*
120	*10753*	*52.57*	*204.56*	*Mosaic grassland (50-70%) / forest or shrubland (20-50%)*	*0.62*
140	*9378*	*29.02*	*323.14*	*Closed to open (>15%) herbaceous vegetation (grassland, savannas or lichens/mosses)*	*0.98*
150	*37960*	*149.64*	*253.68*	*Sparse (>15%) vegetation (woody vegetation, shrubs, grassland)*	*0.77*
190	*1239*	*3.77*	*328.43*	*Artificial surfaces and associated areas (urban areas >50%)*	*1.00*
200	*15673*	*86.19*	*181.85*	*Bare areas*	*0.55*
220	*1903*	*61.35*	*31.02*	*Permanent snow and ice*	*0.09*

ATab. 22: Absolute & relative DS&PS-density site Aosta Valley descending east

Class	Frequency	Area [km²]	DS&PS -targets per km²	LCCS GlobCover global legend	relative DS&PS-density based on '190'
14	*64348*	*183.61*	*350.46*	*Rainfed croplands*	*0.64*
20	*105831*	*374.44*	*282.64*	*Mosaic Cropland (50-70%) / Vegetation (grassland, shrubland, forest) (20-50%)*	*0.52*
30	*47575*	*203.14*	*234.2*	*Mosaic Vegetation (grassland, shrubland, forest) (50-70%) / Cropland (20-50%)*	*0.43*
50	*22497*	*127.07*	*177.04*	*Closed (>40%) broadleaved deciduous forest (>5m)*	*0.32*
70	*24967*	*152.32*	*163.91*	*Closed (>40%) needleleaved evergreen forest (>5m)*	*0.30*
90	*3480*	*20.95*	*166.14*	*Open (15-40%) needleleaved deciduous or evergreen forest*	*0.30*
100	*8283*	*69.24*	*119.62*	*Closed to open (>15%) mixed broadleaved and needleleaved*	*0.22*
110	*228*	*1.67*	*136.52*	*Mosaic forest or shrubland (50-70%) / grassland (20-50%)*	*0.25*

120	*8634*	*52.57*	*164.25*	*Mosaic grassland (50-70%) / forest or shrubland (20-50%)*	*0.30*
140	*5252*	*29.02*	*180.97*	*Closed to open (>15%) herbaceous vegetation (grassland, savannas or lichens/mosses)*	*0.33*
150	*44052*	*149.64*	*294.39*	*Sparse (<15%) vegetation (woody vegetation, shrubs, grassland)*	*0.54*
190	*2058*	*3.77*	*545.53*	*Artificial surfaces and associated areas (urban areas >50%)*	*1.00*
200	*15483*	*86.19*	*179.64*	*Bare areas*	*0.33*
220	*1564*	*61.35*	*25.49*	*Permanent snow and ice*	*0.05*

ATab. 23: Absolute & relative DS&PS-density site Aosta Valley ascending west

Class	Frequency	Area [km²]	DS&PS -targets per km²	LCCS GlobCover global legend	relative DS&PS-density based on '190'
14	71049	212.73	333.98	Rainfed croplands	0.54
20	101205	481.21	210.32	Mosaic Cropland (50-70%) / Vegetation (grassland, shrubland, forest) (20-50%)	0.34
30	61000	215.45	283.13	Mosaic Vegetation (grassland, shrubland, forest) (50-70%) / Cropland (20-50%)	0.45
50	19483	124.25	156.81	Closed (>40%) broadleaved deciduous forest (>5m)	0.25
70	15567	204.22	76.23	Closed (>40%) needleleaved evergreen forest (>5m)	0.12
90	567	11.52	49.21	Open (15-40%) needleleaved deciduous or evergreen forest	0.08
100	6544	62.22	105.18	Closed to open (>15%) mixed broadleaved and needleleaved	0.17
110	250	1.84	136.21	Mosaic forest or shrubland (50-70%) / grassland (20-50%)	0.22
120	9412	37.1	253.72	Mosaic grassland (50-70%) / forest or shrubland (20-50%)	0.41
140	4218	15.37	274.4	Closed to open (>15%) herbaceous vegetation (grassland, savannas or lichens/mosses)	0.44
150	39541	199.28	198.42	Sparse (<15%) vegetation (woody vegetation, shrubs, grassland)	0.32
190	6860	10.99	624.00	Artificial surfaces and associated areas (urban areas >50%)	1.00
200	25533	195.99	130.28	Bare areas	0.21
220	1792	43.28	41.4	Permanent snow and ice	0.07

ATab. 24: Absolute & relative DS&PS-density site Aosta Valley descending west

Class	Frequency	Area [km²]	DS&PS -targets per km²	LCCS GlobCover global legend	relative DS&PS-density based on '190'
14	46593	233.52	199.53	Rainfed croplands	0.30
20	92301	512.77	180.00	Mosaic Cropland (50-70%) / Vegetation (grassland, shrubland, forest) (20-50%)	0.27
30	41234	240.57	171.4	Mosaic Vegetation (grassland, shrubland, forest) (50-70%) / Cropland (20-50%)	0.26
50	17631	126.82	139.03	Closed (>40%) broadleaved deciduous forest (>5m)	0.21
70	19864	207.69	95.64	Closed (>40%) needleleaved evergreen forest (>5m)	0.14
90	999	11.61	86.06	Open (15-40%) needleleaved deciduous or evergreen forest	0.13
100	6048	62.37	96.96	Closed to open (>15%) mixed broadleaved and needleleaved	0.15
110	202	1.84	110.06	Mosaic forest or shrubland (50-70%) / grassland (20-50%)	0.16
120	8059	37.1	217.25	Mosaic grassland (50-70%) / forest or shrubland (20-50%)	0.33
140	3168	16.18	195.76	Closed to open (>15%) herbaceous vegetation (grassland, savannas or lichens/mosses)	0.29
150	35556	219.37	162.08	Sparse (<15%) vegetation (woody vegetation, shrubs, grassland)	0.24
190	7830	11.72	668.08	Artificial surfaces and associated areas (urban areas >50%)	1.00
200	19481	214.74	90.72	Bare areas	0.14

220	1609	46.72	34.44	Permanent snow and ice	0.05

ATab. 25: Absolute & relative DS&PS-density site Aosta Valley ascending west, layover and shadow areas excluded

Class	Frequency	Area [km²]	DS&PS-targets per km²	LCCS GlobCover global legend	relative DS&PS-density based on '190'
14	24374	51.03	477.64	Rainfed croplands	0.39
20	39774	140.07	283.95	Mosaic Cropland (50-70%) / Vegetation (grassland, shrubland, forest) (20-50%)	0.23
30	20703	46.88	441.58	Mosaic Vegetation (grassland, shrubland, forest) (50-70%) / Cropland (20-50%)	0.36
50	7681	35.55	216.08	Closed (>40%) broadleaved deciduous forest (>5m)	0.18
70	9202	93.75	98.16	Closed (>40%) needleleaved evergreen forest (>5m)	0.08
90	203	2.99	67.87	Open (15-40%) needleleaved deciduous or evergreen forest	0.06
100	3846	28.12	136.8	Closed to open (>15%) mixed broadleaved and needleleaved	0.11
120	3184	11.32	281.24	Mosaic grassland (50-70%) / forest or shrubland (20-50%)	0.23
140	1294	3.92	330.23	Closed to open (>15%) herbaceous vegetation (grassland, savannas or lichens/mosses)	0.27
150	13050	46.94	278.03	Sparse (<15%) vegetation (woody vegetation, shrubs, grassland)	0.23
190	6487	5.26	1232.7	Artificial surfaces and associated areas (urban areas >50%)	1.00
200	7049	30.92	227.94	Bare areas	0.18
220	8	0.21	38.67	Permanent snow and ice	0.03

I.II.II Piedmont sites – GlobCover 2009

ATab. 26: Absolute & relative DS&PS-density Domodossola (Piedmont) site

Class	Frequency	Area [km²]	DS&PS-targets per km²	LCCS GlobCover global legend	relative DS&PS-density based on '190'
14	30875	343.01	90.01	Rainfed croplands	0.27
20	48750	740.85	65.8	Mosaic Cropland (50-70%) / Vegetation (grassland, shrubland, forest) (20-50%)	0.20
30	23911	387.18	61.76	Mosaic Vegetation (grassland, shrubland, forest) (50-70%) / Cropland (20-50%)	0.18
50	25264	849.41	29.74	Closed (>40%) broadleaved deciduous forest (>5m)	0.09
70	5232	224.68	23.29	Closed (>40%) needleleaved evergreen forest (>5m)	0.07
90	1376	47.71	28.84	Open (15-40%) needleleaved deciduous or evergreen forest	0.09
100	4297	208.96	20.56	Closed to open (>15%) mixed broadleaved and needleleaved	0.06
110	147	12.05	12.2	Mosaic forest or shrubland (50-70%) / grassland (20-50%)	0.04
120	13638	421.95	32.32	Mosaic grassland (50-70%) / forest or shrubland (20-50%)	0.10
130	*2*	*0.03*	*59.34*	*Closed to open (>15%) (broadleaved or needleleaved, evergreen of deciduous) shrubland (<5m)*	*0.18*
140	5014	164.98	30.39	Closed to open (>15%) herbaceous vegetation (grassland, savannas or lichens/mosses)	0.09
150	7556	108.79	69.46	Sparse (>15%) vegetation	0.21
190	7794	23.16	336.48	Artificial surfaces and associated areas (urban areas >50%)	1.00
200	674	22.84	29.51	Bare areas	0.09
220	143	3.64	39.31	Permanent snow and ice	0.12

ATab. 27: Absolute & relative DS&PS-density Novara (Piedmont) site

Class	Frequency	Area [km²]	DS&PS-targets per km²	LCCS GlobCover global legend	relative DS&PS-density based on '190'
11	30995	1359.9	22.79	Post-flooding or irrigated croplands	0.07
14	23832	345.63	68.95	Rainfed croplands	0.22
20	46851	550.93	85.04	Mosaic Cropland (50-70%) / Vegetation (grassland, shrubland, forest) (20-50%)	0.27
30	21089	193.56	108.95	Mosaic Vegetation (grassland, shrubland, forest) (50-70%) / Cropland (20-50%)	0.34
50	22887	584.93	39.13	Closed (>40%) broadleaved deciduous forest (>5m)	0.12
70	627	13.23	47.38	Closed (>40%) needleleaved evergreen forest (>5m)	0.15
90	228	5.52	41.28	Open (15-40%) needleleaved deciduous or evergreen forest	0.13
100	257	7.34	35	Closed to open (>15%) mixed broadleaved and needleleaved	0.11
110	*1115*	*4.63*	*241.07*	*Mosaic forest or shrubland (50-70%) / grassland (20-50%)*	*0.76*
120	8370	142.43	58.76	Mosaic grassland (50-70%) / forest or shrubland (20-50%)	0.18
130	3446	19.99	172.39	Closed to open (>15%) (broadleaved or needleleaved, evergreen of deciduous) shrubland (<5m)	0.54
140	1710	30.42	56.21	Closed to open (>15%) herbaceous vegetation (grassland, savannas or lichens/mosses)	0.18
150	2491	15.8	157.65	Sparse (<15%) vegetation	0.49
190	46638	146.33	318.72	Artificial surfaces and associated areas (urban areas >50%)	1.00

ATab. 28: Absolute & relative DS&PS-density Omegna (Piedmont) site

Class	Frequency	Area [km²]	DS&PS-targets per km²	LCCS GlobCover global legend	relative DS&PS-density based on '190'
11	17547	461.21	38.05	Post-flooding or irrigated croplands	0.12
14	23110	210.57	109.75	Rainfed croplands	0.36
20	30139	251.13	120.01	Mosaic Cropland (50-70%) / Vegetation (grassland, shrubland, forest) (20-50%)	0.39
30	12934	151.2	85.54	Mosaic Vegetation (grassland, shrubland, forest) (50-70%) / Cropland (20-50%)	0.28
50	18753	526.65	35.61	Closed (>40%) broadleaved deciduous forest (>5m)	0.12
70	3772	52.68	71.6	Closed (>40%) needleleaved evergreen forest (>5m)	0.23
90	588	15.98	36.79	Open (15-40%) needleleaved deciduous or evergreen forest	0.12
100	2371	74.99	31.62	Closed to open (>15%) mixed broadleaved and needleleaved	0.10
110	409	5.06	80.91	Mosaic forest or shrubland (50-70%) / grassland (20-50%)	0.26
120	6798	171.16	39.72	Mosaic grassland (50-70%) / forest or shrubland (20-50%)	0.13
130	1361	8.84	154.02	Closed to open (>15%) (broadleaved or needleleaved, evergreen of deciduous) shrubland (<5m)	0.50
140	838	31.27	26.8	Closed to open (>15%) herbaceous vegetation (grassland, savannas or lichens/mosses)	0.09
150	*2579*	*7.47*	*345.4*	*Sparse (<15%) vegetation*	*1.13*
190	22405	73.21	306.05	Artificial surfaces and associated areas (urban areas >50%)	1.00
200	*21*	*0.13*	*157.3*	*Bare areas*	*0.51*

ATab. 29: Absolute & relative DS&PS-density Varallo (Piedmont) site

Class	Frequency	Area [km²]	DS&PS-targets per km²	LCCS GlobCover global legend	relative DS&PS-density based on '190'
14	21874	180.78	121	Rainfed croplands	0.38
20	46245	507.11	91.19	Mosaic Cropland (50-70%) / Vegetation (grassland, shrubland, forest) (20-50%)	0.29
30	20743	237.55	87.32	Mosaic Vegetation (grassland, shrubland, forest) (50-70%) / Cropland (20-50%)	0.27
50	16777	366.9	45.73	Closed (>40%) broadleaved deciduous forest (>5m)	0.14
70	2992	137.11	21.82	Closed (>40%) needleleaved evergreen forest (>5m)	0.07
90	798	26.13	30.54	Open (15-40%) needleleaved deciduous or evergreen forest	0.10
100	2332	110.4	21.12	Closed to open (>15%) mixed broadleaved and needleleaved	0.07
110	185	7.5	24.65	Mosaic forest or shrubland (50-70%) / grassland (20-50%)	0.08
120	10366	233.53	44.39	Mosaic grassland (50-70%) / forest or shrubland (20-50%)	0.14
140	11080	125.74	88.12	Closed to open (>15%) herbaceous vegetation (grassland, savannas or lichens/mosses)	0.28
150	11481	98.5	116.56	Sparse (<15%) vegetation	0.37
190	2267	7.11	319.03	Artificial surfaces and associated areas (urban areas >50%)	1.00
200	3668	42.07	87.2	Bare areas	0.27
220	1692	18.08	93.58	Permanent snow and ice	0.29

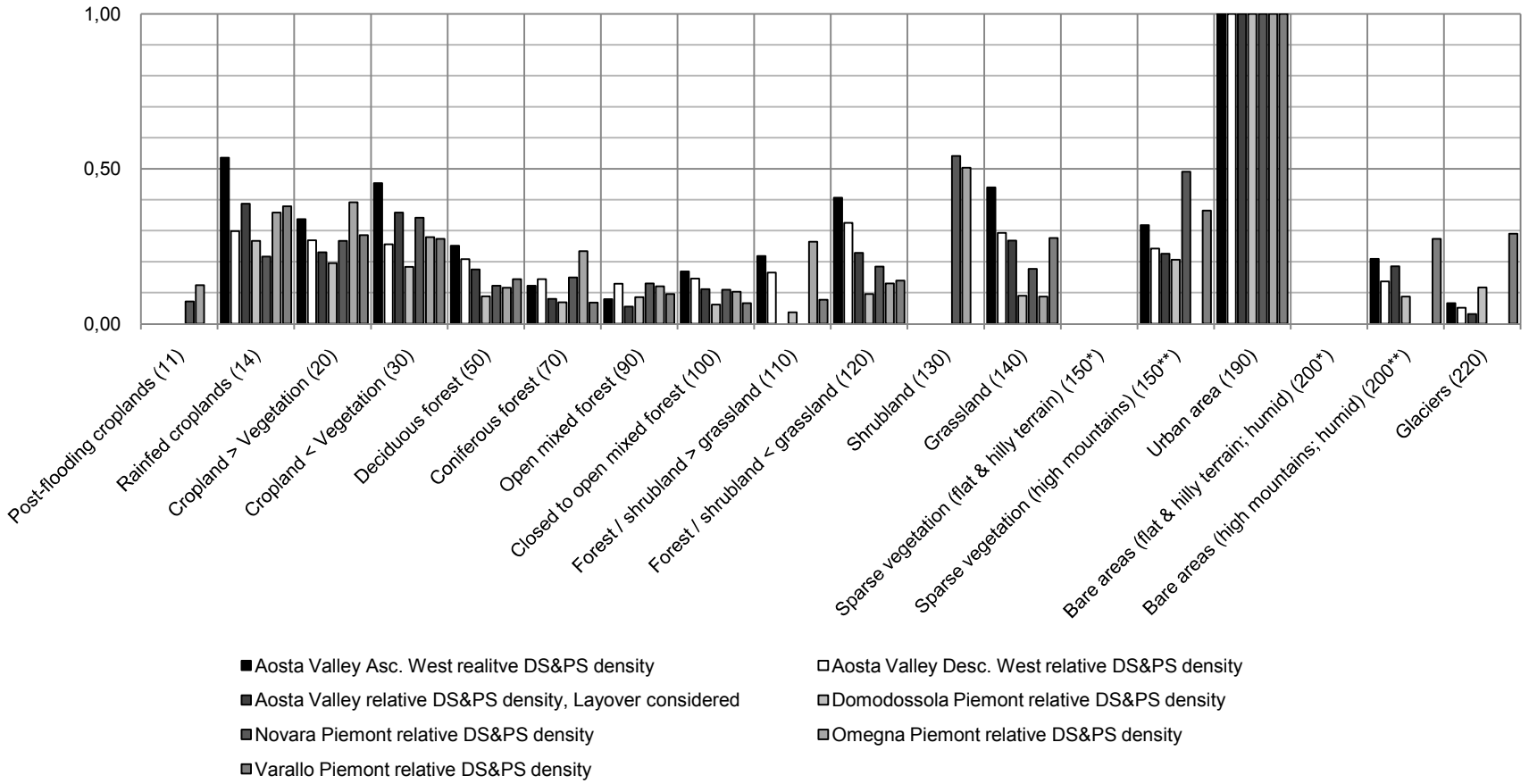

AFig. 3: GlobCover 2009 relative DS&PS-density. The numbers show the ID of the GlobCover land cover classification.

I.II.III Arithmetic mean and validation of relative DS&PS-density – GlobCover 2009

ATab. 30: Arithmetic mean of relative DS&PS-density of all suitable GlobCover sites (calculated using the data from ATab. 23 to 29)

Updated GlobCover 2009 land cover (class)	Arithmetic mean of relative DS&PS-density	Minimum of relative DS&PS-density	Maximum of relative DS&PS-density
Post-flooding croplands (11)	0.10	0.07	0.12
Rainfed croplands (14)	0.35	0.22	0.54
Cropland > Vegetation (20)	0.28	0.20	0.39
Cropland < Vegetation (30)	0.31	0.18	0.45
Deciduous forest (50)	0.16	0.09	0.25
Coniferous forest (70)	0.12	0.07	0.23
Open mixed forest (90)	0.10	0.06	0.13
Closed to open mixed forest (100)	0.11	0.06	0.17
Forest / shrubland > grassland (110)	0.15	0.04	0.26
Forest / shrubland < grassland (120)	0.22	0.10	0.41
Shrubland (130)	0.52	0.50	0.54
Grassland (140)	0.23	0.09	0.44
Sparse vegetation (high mountains) (150**)	0.31	0.21	0.49
Urban area (190)	1.00	1.00	1.00
Bare areas (high mountains; humid) (200**)	0.18	0.09	0.27
Glaciers (220)	0.11	0.03	0.29

ATab. 31 shows the result of the validation of the relative DS&PS-density method for using GlobCover 2009. Both the processed and estimated DS&PS-density as well as their difference are shown. Great differences are written in *italics*. Similarly to ATab. 20, the classes '110' and '150**' show large differences between the estimated and processed DS&PS-density, which is due to the small area of class '110' and the very high processed DS&PS-density of class '150**' compared to the other sites (also cf. chapter 5.1.4.2 b).

ATab. 31: Validation of relative DS&PS-density method at Ivrea (Piedmont) site: Multiplication of the mean values from ATab. 30 and the absolute PS-density of the reference class from the Omegna site (ATab. 28)

Updated GlobCover 2009 land cover (class)	Frequency	Area [km²]	DS&PS-targets per km²	Estimated DS&PS-targets per km²	Difference of estimated and processed DS&PS-density
Post-flooding croplands (11)	18022	891,71	20.21	29.97	9.76
Rainfed croplands (14)	22065	266,17	82.9	106.81	23.91
Cropland > Vegetation (20)	41540	432,82	95.98	86.44	-9.54
Cropland < Vegetation (30)	19263	166,43	115.74	93.87	-21.87
Deciduous forest (50)	23101	498,39	46.35	48.34	1.99
Coniferous forest (70)	263	8,06	32.65	37.83	5.18
Open mixed forest (90)	355	8,18	43.41	30.34	-13.07
Closed to open mixed forest (100)	239	7,61	31.41	33.45	2.04
Forest / shrubland > grassland (110)	*889*	*3,85*	*231.03*	*46.58*	*-184.45*
Forest / shrubland < grassland (120)	8418	132,02	63.76	65.99	2.23
Shrubland (130)	2133	11,33	188.23	159.78	-28.45
Grassland (140)	3040	30	101.35	71.31	-30.04

*Sparse vegetation (high mountains) (150**)*	*2424*	*10,46*	*231.79*	*94.26*	*-137.53*
Urban area (190)	28759	88,61	324.54	306.05	-18.49

II. CORINE 2006

II.I 'normal' PS

II.I.I Aosta Valley site – CORINE 2006

ATab. 32: Absolute & relative PS-density site Aosta Valley ascending east

Class	Frequency	Area [km²]	PS-targets per km²	CORINE CLC legend (label 3)	relative PS-density based on '112'
112	12673	14.45	876.88	Discontinuous urban fabric	1.00
121	1365	2.19	623.46	Industrial or commercial units	0.71
142	85	0.27	316.11	Sport and leisure facilities	0.36
221	466	2.4	194.13	Vineyards	0.22
231	6307	57.17	110.32	Pastures	0.13
242	725	3.28	221.13	Complex cultivation patterns	0.25
243	6472	49.58	130.54	Land principally occupied by agriculture, with significant areas of natural vegetation	0.15
311	2279	50.16	45.43	Broad-leaved forest	0.05
312	3753	248.5	15.1	Coniferous forest	0.02
313	2763	74.88	36.9	Mixed forest	0.04
321	16120	254.61	63.31	Natural grasslands	0.07
322	2366	43.52	54.37	Moors and heathland	0.06
324	15756	251.1	62.75	Transitional woodland-shrub	0.07
332	14849	241.79	61.41	Bare rocks	0.07
333	15254	136.47	111.78	Sparsely vegetated areas	0.13
335	198	49.9	3.97	Glaciers and perpetual snow	0.00

ATab. 33: Absolute & relative PS-density site Aosta Valley descending east

Class	Frequency	Area [km²]	PS-targets per km²	CORINE CLC legend (label 3)	relative PS-density based on '112'
112	12833	14.45	887.95	Discontinuous urban fabric	1.00
121	1362	2.19	622.09	Industrial or commercial units	0.70
142	70	0.27	260.33	Sport and leisure facilities	0.29
221	618	2.4	257.46	Vineyards	0.29
231	6298	57.17	110.17	Pastures	0.12
242	698	3.28	212.89	Complex cultivation patterns	0.24
243	6450	49.58	130.09	Land principally occupied by agriculture, with significant areas of natural vegetation	0.15
311	2049	50.16	40.85	Broad-leaved forest	0.05
312	5223	248.5	21.02	Coniferous forest	0.02
313	3406	74.88	45.49	Mixed forest	0.05
321	14081	254.61	55.3	Natural grasslands	0.06
322	2467	43.52	56.69	Moors and heathland	0.06
324	17628	251.1	70.2	Transitional woodland-shrub	0.08
332	14860	241.79	61.46	Bare rocks	0.07

333	11866	136.47	86.95	Sparsely vegetated areas	0.10
335	237	49.9	4.75	Glaciers and perpetual snow	0.01

ATab. 34: Absolute & relative PS-density site Aosta Valley ascending west

Class	Frequency	Area [km²]	PS-targets per km²	CORINE CLC legend (label 3)	relative PS-density based on '112'
111	2386	1.6	1487.0	Continuous urban fabric	1.75
112	16543	19.5	848.44	Discontinuous urban fabric	1.00
121	3961	5.5	720.49	Industrial or commercial units	0.85
124	159	0.4	395.38	Airports	0.47
131	104	0.4	263.08	Mineral extraction sites	0.31
133	188	0.46	410.97	Construction sites	0.48
221	320	1.72	185.53	Vineyards	0.22
222	574	2.55	225.29	Fruit trees and berry plantations	0.27
231	5973	58.1	102.8	Pastures	0.12
242	4754	16.81	282.73	Complex cultivation patterns	0.33
243	6815	68.42	99.61	Land principally occupied by agriculture, with significant areas of natural vegetation	0.12
311	138	7.16	19.27	Broad-leaved forest	0.02
312	2842	327.93	8.67	Coniferous forest	0.01
313	850	31.07	27.36	Mixed forest	0.03
321	21295	334.57	63.65	Natural grasslands	0.08
322	1231	62.86	19.58	Moors and heathland	0.02
324	8450	179.69	47.03	Transitional woodland-shrub	0.06
332	19102	408.71	46.74	Bare rocks	0.06
333	12815	148.79	86.13	Sparsely vegetated areas	0.10
335	341	78.55	4.34	Glaciers and perpetual snow	0.01

ATab. 35: Absolute & relative PS-density site Aosta Valley descending west

Class	Frequency	Area [km²]	PS-targets per km²	CORINE CLC legend (label 3)	relative PS-density based on '112'
111	2268	1.6	1413.4	Continuous urban fabric	1.73
112	15931	19.5	817.05	Discontinuous urban fabric	1.00
121	3802	5.5	691.56	Industrial or commercial units	0.85
124	98	0.4	243.69	Airports	0.30
131	98	0.4	247.91	Mineral extraction sites	0.30
133	178	0.46	389.11	Construction sites	0.48
221	287	1.72	166.39	Vineyards	0.20
222	472	2.55	185.25	Fruit trees and berry plantations	0.23
231	4954	58.1	85.27	Pastures	0.10
242	3586	16.81	213.27	Complex cultivation patterns	0.26
243	6119	68.6	89.2	Land principally occupied by agriculture, with significant areas of natural vegetation	0.11
311	335	7.16	46.77	Broad-leaved forest	0.06
312	3450	327.69	10.53	Coniferous forest	0.01
313	897	30.91	29.02	Mixed forest	0.04

321	10563	361.77	29.2	Natural grasslands	0.04
322	1324	69.17	19.14	Moors and heathland	0.02
324	7296	180.91	40.33	Transitional woodland-shrub	0.05
332	16884	466.92	36.16	Bare rocks	0.04
333	11213	161.7	69.35	Sparsely vegetated areas	0.08
335	438	107.75	4.06	Glaciers and perpetual snow	0.00

ATab. 36: Absolute & relative PS-density site Aosta Valley ascending west, layover and shadow areas excluded

Class	Frequency	Area [km²]	PS-targets per km²	CORINE CLC legend (label 3)	relative PS-density based on '112'
111	2386	1.6	1487.0	Continuous urban fabric	1.58
112	11305	11.99	943.15	Discontinuous urban fabric	1.00
121	3961	5.5	720.49	Industrial or commercial units	0.76
124	159	0.4	395.38	Airports	0.42
133	188	0.46	410.97	Construction sites	0.44
221	320	1.72	185.53	Vineyards	0.20
222	503	2.16	232.59	Fruit trees and berry plantations	0.25
231	2831	21.54	131.45	Pastures	0.14
242	3023	10.29	293.74	Complex cultivation patterns	0.31
243	3676	31.52	116.61	Land principally occupied by agriculture, with significant areas of natural vegetation	0.12
311	89	3.32	26.84	Broad-leaved forest	0.03
312	1397	120.09	11.63	Coniferous forest	0.01
313	440	16.01	27.48	Mixed forest	0.03
321	7178	78.48	91.46	Natural grasslands	0.10
322	210	5.64	37.22	Moors and heathland	0.04
324	4432	62.58	70.82	Transitional woodland-shrub	0.08
332	5206	87.21	59.69	Bare rocks	0.06
333	4131	32.46	127.25	Sparsely vegetated areas	0.13
335	20	3.98	5.02	Glaciers and perpetual snow	0.01

II.I.II Budapest site – CORINE 2006

The classes '222' and '242' are not considered, due to their small area. Additionally, comparison with optical data showed, that the class '242' was falsely classified in CORINE 2006. At the Budapest site this is class is only represented by one single polygon. Its correct land cover class would be urban area (→ relatively high PS-density), but the high number of trees caused the false classification in CORINE. Therefore, the class '242' is excluded.

ATab. 37: Absolute & relative PS-density Budapest site

Class	Frequency	Area [km²]	PS-targets per km²	CORINE CLC legend (label 3)	relative PS-density based on '112'
111	251095	13.76	18244.	Continuous urban fabric	1.97
112	832888	90.1	9244.5	Discontinuous urban fabric	1.00
121	314659	32.05	9817.7	Industrial or commercial units	1.06
122	142891	9.54	14984.	Road and rail networks and associated land	1.62

123	12956	2.89	4477.2	Port areas	0.48
131	394	0.36	1082.0	Mineral extraction sites	0.12
133	3983	1.15	3468.5	Construction sites	0.38
141	15033	7.18	2094.7	Green urban areas	0.23
142	24389	6.47	3767.9	Sport and leisure facilities	0.41
211	1075	2.16	498.46	Non-irrigated arable land	0.05
222	*130*	*0.78*	*167.26*	*Fruit trees and berry plantations*	*0.02*
231	2035	2.44	834.66	Pastures	0.09
242	*1951*	*0.45*	*4340.1*	*Complex cultivation patterns*	*0.47*
311	405	1.78	227.4	Broad-leaved forest	0.02
313	564	1.55	364.26	Mixed forest	0.04
324	768	0.92	836.03	Transitional woodland-shrub	0.09

II.I.III Bavaria site – CORINE 2006

The class '332' is excluded due to its very small area. Also the area of the class '322' is very small. But this class is mainly excluded due to its falsely classification in CORINE 2006. Due to its very high density of rocks (confirmed by visual comparison in Google Earth™), this area would correctly classified as bare rocks, which would explain the high PS-density.

ATab. 38: Absolute & relative PS-density Bavaria site

Class	Frequency	Area [km²]	PS-targets per km²	CORINE CLC legend (label 3)	relative PS-density based on '112'
111	7553	19.17	394	Continuous urban fabric	1.84
112	147348	687.14	214.44	Discontinuous urban fabric	1.00
121	20543	90.12	227.95	Industrial or commercial units	1.06
122	1528	9.8	155.87	Road and rail networks and associated land	0.73
124	2638	36.02	73.23	Airports	0.34
131	1368	17.91	76.36	Mineral extraction sites	0.36
132	162	1.34	121.25	Dump sites	0.57
133	154	2.68	57.42	Construction sites	0.27
141	2313	34.73	66.6	Green urban areas	0.31
142	2902	37.08	78.26	Sport and leisure facilities	0.36
211	38463	1826.6	21.06	Non-irrigated arable land	0.10
231	73617	1890.3	38.94	Pastures	0.18
242	22403	703.39	31.85	Complex cultivation patterns	0.15
243	11168	269.7	41.41	Land principally occupied by agriculture, with significant areas of natural vegetation	0.19
311	1832	59.55	30.76	Broad-leaved forest	0.14
312	41620	1729.4	24.07	Coniferous forest	0.11
313	20145	678.34	29.7	Mixed forest	0.14
321	1146	33.41	34.31	Natural grasslands	0.16
322	*611*	*6.29*	*97.14*	*Moors and heathland*	*0.45*
324	1786	123.39	14.47	Transitional woodland-shrub	0.07
332	*24*	*1.89*	*12.71*	*Bare Rocks*	*0.06*
333	623	6.76	92.2	Sparsely vegetated areas	0.43
411	1053	55.68	18.91	Inland marshes	0.09
412	1070	94.06	11.38	Peat bogs	0.05

II.I.IV North Germany site – CORINE 2006

The classes ‘331’ and ‘333’ are excluded due to their small area.

ATab. 39: Absolute & relative PS-density North Germany site

Class	Frequency	Area [km²]	PS-targets per km²	CORINE CLC legend (label 3)	relative PS-density based on ‘112’
111	3446	12.99	265.21	Continuous urban fabric	2.33
112	111389	978.72	113.81	Discontinuous urban fabric	1.00
121	16334	126.26	129.37	Industrial or commercial units	1.14
122	917	11.18	82	Road and rail networks and associated land	0.72
123	1838	24.74	74.29	Port areas	0.65
124	505	11.51	43.87	Airports	0.39
131	190	31.2	6.09	Mineral extraction sites	0.05
132	88	13.16	6.69	Dump sites	0.06
133	17	3.59	4.73	Construction sites	0.04
141	785	29.42	26.69	Green urban areas	0.23
142	2270	65.94	34.43	Sport and leisure facilities	0.30
211	20379	4373.7	4.66	Non-irrigated arable land	0.04
222	775	139.94	5.54	Fruit trees and berry plantations	0.05
231	10738	2279.0	4.71	Pastures	0.04
242	5098	770.02	6.62	Complex cultivation patterns	0.06
243	1790	329.17	5.44	Land principally occupied by agriculture, with significant areas of natural vegetation	0.05
311	977	525.74	1.86	Broad-leaved forest	0.02
312	1258	802.09	1.57	Coniferous forest	0.01
313	407	205.63	1.98	Mixed forest	0.02
321	35	27.91	1.25	Natural grasslands	0.01
322	22	16.14	1.36	Moors and heathland	0.01
324	17	13.02	1.31	Transitional woodland-shrub	0.01
331	*2*	*0.69*	*2.91*	*Beaches, dunes, sands*	*0.03*
333	*24*	*0.77*	*31.2*	*Sparsely vegetated areas*	*0.27*
411	39	13.55	2.88	Inland marshes	0.03
412	5	47.75	0.1	Peat bogs	0.00
423	9	21.41	0.42	Intertidal flats	0.00

II.I.V Aschau am Inn site – CORINE 2006

ATab. 40: Absolute & relative PS-density Aschau am Inn site

Class	Frequency	Area [km²]	PS-targets per km²	CORINE CLC legend (label 3)	relative PS-density based on ‘112’
112	11946	3.56	3354.55	Discontinuous urban fabric	1.00
211	7343	27.25	269.45	Non-irrigated arable land	0.08
231	3774	14.65	257.68	Pastures	0.08
242	11597	40.78	284.4	Complex cultivation patterns	0.08
243	130	1.23	105.67	Land principally occupied by agriculture, with significant areas of natural vegetation	0.03
311	155	1.43	108.07	Broad-leaved forest	0.03
312	600	25.18	23.82	Coniferous forest	0.01
313	558	6.53	85.46	Mixed forest	0.03

II.I.VI Netherlands site – CORINE 2006

The class '322' is not considered, as it consists of a very high number of very small sub areas, which are located very close to urban area. Therefore, the high PS-density of this class (in the case of the Netherlands site) is caused by its high number of buildings within its area, which is not common for this class at the other sites.

ATab. 41: Absolute & relative PS-density Netherlands site

Class	Frequency	Area [km²]	PS-targets per km²	CORINE CLC legend (label 3)	relative PS-density based on '112'
111	1009	12.99	77.68	Continuous urban fabric	2.79
112	21158	760.04	27.84	Discontinuous urban fabric	1.00
121	6504	160.74	40.46	Industrial or commercial units	1.45
122	696	47.62	14.61	Road and rail networks and associated land	0.52
123	4491	144.03	31.18	Port areas	1.12
124	72	9.21	7.82	Airports	0.28
131	5	0.38	13.32	Mineral extraction sites	0.48
132	6	2.55	2.35	Dump sites	0.08
133	324	75.78	4.28	Construction sites	0.15
141	593	55.62	10.66	Green urban areas	0.38
142	1077	120.16	8.96	Sport and leisure facilities	0.32
211	6746	2493.6	2.71	Non-irrigated arable land	0.10
222	73	13.08	5.58	Fruit trees and berry plantations	0.20
231	2102	578.62	3.63	Pastures	0.13
242	2345	484.68	4.84	Complex cultivation patterns	0.17
243	378	68.33	5.53	Land principally occupied by agriculture, with significant areas of natural vegetation	0.20
311	209	69.83	2.99	Broad-leaved forest	0.11
312	197	85.15	2.31	Coniferous forest	0.08
313	96	39.63	2.42	Mixed forest	0.09
321	138	97.25	1.42	Natural grasslands	0.05
322	*215*	*28.78*	*7.47*	*Moors and heathland*	*0.27*
324	7	6.77	1.03	Transitional woodland-shrub	0.04
331	23	28.83	0.8	Beaches, dunes, sands	0.03
411	63	53.42	1.18	Inland marshes	0.04
421	35	39.79	0.88	Salt marshes	0.03
423	65	180.15	0.36	Intertidal flats	0.01

II.I.VII Piedmont sites – CORINE 2006

Due to their small area, the classes '221' and '411' are excluded from the Domodossola data.

ATab. 42: Absolute & relative PS-density Domodossola (Piedmont) site

Class	Frequency	Area [km²]	PS-targets per km²	CORINE CLC legend (label 3)	relative PS-density based on '112'
111	1109	2.74	404.89	Continuous urban fabric	1.35
112	30090	100.04	300.77	Discontinuous urban fabric	1.00
121	4385	15.87	276.34	Industrial or commercial units	0.92
122	382	2.14	178.36	Road and rail networks and associated land	0.59

131	32	0.98	32.64	Mineral extraction sites	0.11
133	42	0.33	127.15	Construction sites	0.42
142	158	5.2	30.39	Sport and leisure facilities	0.10
211	1968	50.09	39.29	Non-irrigated arable land	0.13
221	*11*	*0.73*	*15.07*	*Vineyards*	*0.05*
231	1882	24.33	77.36	Pastures	0.26
242	3964	53.78	73.71	Complex cultivation patterns	0.25
243	15967	220.26	72.49	Land principally occupied by agriculture, with significant areas of natural vegetation	0.24
311	11183	1115.9	10.02	Broad-leaved forest	0.03
312	1226	285.23	4.3	Coniferous forest	0.01
313	3304	459.43	7.19	Mixed forest	0.02
321	9004	489.08	18.41	Natural grasslands	0.06
322	1828	146.98	12.44	Moors and heathland	0.04
324	5392	331.35	16.27	Transitional woodland-shrub	0.05
331	1553	15.34	101.26	Beaches, dunes, sands	0.34
332	2184	130.02	16.8	Bare rocks	0.06
333	2505	87.14	28.75	Sparsely vegetated areas	0.10
411	*11*	*0.56*	*19.49*	*Inland marshes*	*0.06*

At the Novara site the classes ‘332’ and ‘333’ are excluded, due to their small area.

ATab. 43: Absolute & relative PS-density Novara (Piedmont) site

Class	Frequency	Area [km²]	PS-targets per km²	CORINE CLC legend (label 3)	relative PS-density based on ‘112’
111	2269	4.9	462.76	Continuous urban fabric	1.32
112	55201	157.18	351.19	Discontinuous urban fabric	1.00
121	12199	43.76	278.8	Industrial or commercial units	0.79
122	1585	10.6	149.51	Road and rail networks and associated land	0.43
124	229	4.09	55.99	Airports	0.16
131	597	11.23	53.17	Mineral extraction sites	0.15
133	673	7.36	91.39	Construction sites	0.26
142	319	6.48	49.23	Sport and leisure facilities	0.14
211	17767	615.12	28.88	Non-irrigated arable land	0.08
213	12440	1364.9	9.11	Rice fields	0.03
221	370	5.94	62.32	Vineyards	0.18
222	462	18.36	25.17	Fruit trees and berry plantations	0.07
231	986	30.45	32.38	Pastures	0.09
242	8540	132.36	64.52	Complex cultivation patterns	0.18
243	14412	334.62	43.07	Land principally occupied by agriculture, with significant areas of natural vegetation	0.12
311	6148	444.01	13.85	Broad-leaved forest	0.04
312	22	2.78	7.93	Coniferous forest	0.02
313	383	38.51	9.94	Mixed forest	0.03
321	2930	49.79	58.85	Natural grasslands	0.17
322	461	14.55	31.68	Moors and heathland	0.09
324	2306	87.76	26.28	Transitional woodland-shrub	0.07
331	1733	21.18	81.82	Beaches, dunes, sands	0.23

332	*5*	*0.28*	*18.12*	*Bare rocks*	*0.05*
333	*769*	*4.95*	*155.31*	*Sparsely vegetated areas*	*0.44*

The classes ‘221’, ‘333’ and ‘411’ are excluded at the Omegna site, because of their small area.

ATab. 44: Absolute & relative PS-density Omegna (Piedmont) site

Class	Frequency	Area [km²]	PS-targets per km²	CORINE CLC legend (label 3)	relative PS-density based on ‘112’
111	1786	4.03	443.1	Continuous urban fabric	1.26
112	42563	120.69	352.65	Discontinuous urban fabric	1.00
121	7828	24.88	314.58	Industrial or commercial units	0.89
122	789	4.55	173.49	Road and rail networks and associated land	0.49
124	291	3.73	78.12	Airports	0.22
131	177	3.72	47.61	Mineral extraction sites	0.14
133	350	4.07	85.89	Construction sites	0.24
142	187	5.64	33.17	Sport and leisure facilities	0.09
211	5446	162.42	33.53	Non-irrigated arable land	0.10
213	5816	457.55	12.71	Rice fields	0.04
221	*10*	*1.79*	*5.59*	*Vineyards*	*0.02*
231	84	2.4	34.95	Pastures	0.10
242	6575	96.7	67.99	Complex cultivation patterns	0.19
243	13194	199.98	65.98	Land principally occupied by agriculture, with significant areas of natural vegetation	0.19
311	7097	612.32	11.59	Broad-leaved forest	0.03
312	22	16.89	1.3	Coniferous forest	0.00
313	1022	129.32	7.9	Mixed forest	0.02
321	1921	63.22	30.39	Natural grasslands	0.09
322	303	28.64	10.58	Moors and heathland	0.03
324	2212	78.7	28.11	Transitional woodland-shrub	0.08
331	1773	17.64	100.49	Beaches, dunes, sands	0.28
333	*154*	*3.11*	*49.53*	*Sparsely vegetated areas*	*0.14*
411	*10*	*0.56*	*17.72*	*Inland marshes*	*0.05*

At the Varallo site the class ‘211’ is excluded, due to its very small area compared to the corresponding class at the other sites.

ATab. 45: Absolute & relative PS-density Varallo (Piedmont) site

Class	Frequency	Area [km²]	PS-targets per km²	CORINE CLC legend (label 3)	relative PS-density based on ‘112’
111	249	0.56	443.99	Continuous urban fabric	1.48
112	6113	20.38	299.89	Discontinuous urban fabric	1.00
121	1410	5.23	269.74	Industrial or commercial units	0.90
122	346	1.49	232.02	Road and rail networks and associated land	0.77
211	*313*	*3.85*	*81.4*	*Non-irrigated arable land*	*0.27*
231	1570	18.57	84.55	Pastures	0.28

242	139	1.61	86.15	Complex cultivation patterns	0.29
243	5602	63.29	88.52	Land principally occupied by agriculture, with significant areas of natural vegetation	0.30
311	8105	518.4	15.63	Broad-leaved forest	0.05
312	1351	191.68	7.05	Coniferous forest	0.02
313	2612	294.58	8.87	Mixed forest	0.03
321	25759	377.49	68.24	Natural grasslands	0.23
322	2428	110.39	21.99	Moors and heathland	0.07
324	7671	238.3	32.19	Transitional woodland-shrub	0.11
331	1349	10.54	127.97	Beaches, dunes, sands	0.43
332	7636	144.89	52.7	Bare rocks	0.18
333	5674	75.48	75.17	Sparsely vegetated areas	0.25
335	123	14.62	8.42	Glaciers and perpetual snow	0.03

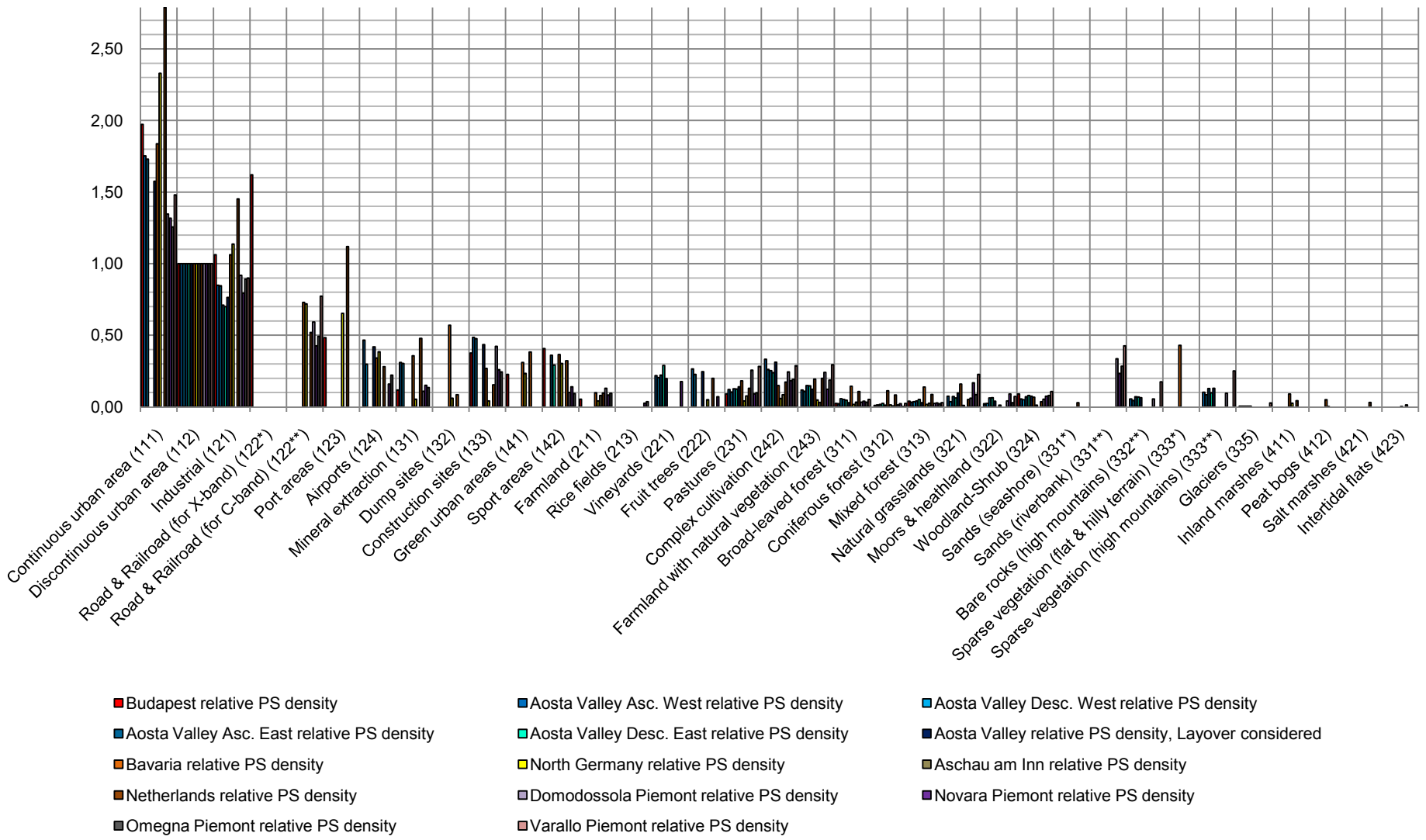

AFig. 4: CORINE 2006 relative PS-density. The numbers show the ID of the CORINE land cover classification.

II.I.VIII Arithmetic mean and validation of relative PS-density – CORINE 2006

ATab. 46: Arithmetic mean of relative PS-density of all suitable CORINE 2006 sites (calculated using the data from ATab. 32 to 45)

Updated CORINE 2006 land cover (class)	Arithmetic mean of relative PS-density	Minimum of relative PS-density	Maximum of relative PS-density
Continuous urban area (111)	1.76	1.26	2.79
Discontinuous urban area (112)	1.00	1.00	1.00
Industrial (121)	0.93	0.70	1.45
Road & Railroad (for X-band) (122*)	1.62	1.62	1.62
Road & Railroad (for C-band) (122**)	0.61	0.43	0.77
Port areas (123)	0.75	0.48	1.12
Airports (124)	0.32	0.16	0.47
Mineral extraction (131)	0.22	0.05	0.48
Dump sites (132)	0.24	0.06	0.57
Construction sites (133)	0.32	0.04	0.48
Green urban areas (141)	0.29	0.23	0.38
Sport areas (142)	0.27	0.09	0.41
Farmland (211)	0.08	0.04	0.13
Rice fields (213)	0.03	0.03	0.04
Vineyards (221)	0.22	0.18	0.29
Fruit trees (222)	0.18	0.05	0.27
Pastures (231)	0.13	0.04	0.28
Complex cultivation (242)	0.21	0.06	0.33
Farmland with natural vegetation (243)	0.15	0.03	0.30
Broad-leaved forest (311)	0.05	0.02	0.14
Coniferous forest (312)	0.03	0.00	0.11
Mixed forest (313)	0.04	0.02	0.14
Natural grasslands (321)	0.09	0.01	0.23
Moors & heathland (322)	0.05	0.01	0.09
Woodland-Shrub (324)	0.07	0.01	0.11
Sands (seashore) (331*)	0.03	0.03	0.03
Sands (riverbank) (331**)	0.32	0.23	0.43
Bare rocks (high mountains) (332**)	0.08	0.04	0.18
Sparse vegetation (flat & hilly terrain) (333*)	0.43	0.43	0.43
Sparse vegetation (high mountains) (333**)	0.13	0.08	0.25
Glaciers (335)	0.01	0.00	0.03
Inland marshes (411)	0.05	0.03	0.09
Peat bogs (412)	0.03	0.00	0.05
Salt marshes (421)	0.03	0.03	0.03
Intertidal flats (423)	0.01	0.00	0.01

Table 47 shows the result of the validation of the relative PS-density method for using CORINE 2006. (cf. chapter 5.1.4.2 c). The classes ‘111’ and ‘333**’ show large differences between the estimated and processed PS-density, due to their small area at the Ivrea site. The class ‘321’ shows a very high processed PS-density compared to the other sites. This causes a large difference between estimated and processed PS-density. The relatively large difference at the class ‘332**’ is due to the very small area of this class at the Ivrea site.

ATab. 47: Validation of relative PS-density method at Ivrea (Piedmont) site: Multiplication of the mean values from Tab. 46 and the absolute PS-density of the reference class from the Omegna site (ATab. 44)

Updated CORINE 2006 land cover (class)	Frequency	Area [km²]	Processed PS-targets per km²	Estimated PS-targets per km²	Difference of estimated and processed PS-density
Continuous urban area (111)	*1359*	*3.01*	*451.72*	*621.66*	*169.94*
Discontinuous urban area (112)	39610	113.3	349.61	352.65	3.04
Industrial (121)	8362	29.47	283.74	327.97	44.23
Road & Railroad (for C-band) (122**)	1256	6.77	185.63	214.33	28.7
Airports (124)	30	0.36	82.22	113.39	31.17
Mineral extraction (131)	590	8.33	70.81	78.90	8.09
Construction sites (133)	579	3.62	159.95	111.48	-48.47
Sport areas (142)	402	6.04	66.55	93.49	26.94
Farmland (211)	15421	495.94	31.09	29.92	-1.17
Rice fields (213)	7822	901.94	8.67	10.93	2.26
Vineyards (221)	301	4.88	61.69	76.87	15.18
Fruit trees (222)	462	18.36	25.17	62.33	37.16
Pastures (231)	1052	29.23	35.99	47.00	11.01
Complex cultivation (242)	6833	87.67	77.94	75.19	-2.75
Farmland with natural vegetation (243)	14676	277.89	52.81	53.24	0.43
Broad-leaved forest (311)	6172	398.11	15.5	17.33	1.83
Coniferous forest (312)	59	1.75	33.69	9.67	-24.02
Mixed forest (313)	320	23.6	13.56	15.17	1.61
Natural grasslands (321)	*5444*	*41.34*	*131.68*	*32.52*	*-99.16*
Moors & heathland (322)	653	10.11	64.6	16.17	-48.43
Woodland-Shrub (324)	2551	71.9	35.48	23.14	-12.34
Sands (riverbank) (331**)	630	8.7	72.39	112.97	40.58
Bare rocks (high mountains) (332**)	6	0.1	61.66	26.88	-34.78
Sparse vegetation (high mountains) (333)*	*619*	*3.65*	*169.38*	*44.74*	*-124.64*

II.II DS&PS

For the explanation of the excluded classes (*italic*) the reader is referred to the corresponding table in chapter I.I (only PS).

II.II.I Aosta Valley site – CORINE 2006

ATab. 48: Absolute & relative DS&PS-density site Aosta Valley ascending east

Class	Frequency	Area [km²]	DS&PS-targets per km²	CORINE CLC legend (label 3)	relative DS&PS-density based on '112'
112	17924	14.45	1240.2	Discontinuous urban fabric	1.00
121	2061	2.19	941.35	Industrial or commercial units	0.76
142	143	0.27	531.81	Sport and leisure facilities	0.43
221	1449	2.4	603.65	Vineyards	0.49
231	13621	57.17	238.26	Pastures	0.19
242	1466	3.28	447.13	Complex cultivation patterns	0.36
243	13466	49.58	271.6	Land principally occupied by agriculture, with significant areas of natural vegetation	0.22
311	5354	50.16	106.74	Broad-leaved forest	0.09

312	18138	248.5	72.99	Coniferous forest	0.06
313	7182	74.88	95.92	Mixed forest	0.08
321	79758	254.61	313.25	Natural grasslands	0.25
322	10883	43.52	250.08	Moors and heathland	0.20
324	57340	251.1	228.36	Transitional woodland-shrub	0.18
332	60566	241.79	250.49	Bare rocks	0.20
333	65992	136.47	483.57	Sparsely vegetated areas	0.39
335	595	49.9	11.92	Glaciers and perpetual snow	0.01

ATab. 49: Absolute & relative DS&PS-density site Aosta Valley descending east

Class	Frequency	Area [km²]	DS&PS -targets per km²	CORINE CLC legend (label 3)	relative DS&PS-density based on '112'
112	18160	14.45	1256.5	Discontinuous urban fabric	1.00
121	2108	2.19	962.82	Industrial or commercial units	0.77
142	145	0.27	539.25	Sport and leisure facilities	0.43
221	1818	2.4	757.38	Vineyards	0.60
231	13008	57.17	227.54	Pastures	0.18
242	1391	3.28	424.26	Complex cultivation patterns	0.34
243	13412	49.58	270.52	Land principally occupied by agriculture, with significant areas of natural vegetation	0.22
311	5298	50.16	105.62	Broad-leaved forest	0.08
312	20778	248.5	83.61	Coniferous forest	0.07
313	8320	74.88	111.12	Mixed forest	0.09
321	71238	254.61	279.79	Natural grasslands	0.22
322	11640	43.52	267.47	Moors and heathland	0.21
324	64145	251.1	255.46	Transitional woodland-shrub	0.20
332	64792	241.79	267.97	Bare rocks	0.21
333	56736	136.47	415.75	Sparsely vegetated areas	0.33
335	882	49.9	17.67	Glaciers and perpetual snow	0.01

ATab. 50: Absolute & relative DS&PS-density site Aosta Valley ascending west

Class	Frequency	Area [km²]	DS&PS -targets per km²	CORINE CLC legend (label 3)	relative DS&PS-density based on '112'
111	2888	1.6	1799.8	Continuous urban fabric	1.53
112	22982	19.5	1178.7	Discontinuous urban fabric	1.00
121	5668	5.5	1031.0	Industrial or commercial units	0.87
124	390	0.4	969.79	Airports	0.82
131	232	0.4	586.88	Mineral extraction sites	0.50
133	366	0.46	800.08	Construction sites	0.68
221	1196	1.72	693.4	Vineyards	0.59
222	1044	2.55	409.76	Fruit trees and berry plantations	0.35
231	10710	58.1	184.34	Pastures	0.16
242	8227	16.81	489.28	Complex cultivation patterns	0.42
243	13381	68.42	195.59	Land principally occupied by agriculture, with significant areas of natural vegetation	0.17
311	563	7.16	78.6	Broad-leaved forest	0.07

312	12151	327.93	37.05	Coniferous forest	0.03
313	2094	31.07	67.39	Mixed forest	0.06
321	108083	334.57	323.05	Natural grasslands	0.27
322	8299	62.86	132.02	Moors and heathland	0.11
324	35139	179.69	195.56	Transitional woodland-shrub	0.17
332	74500	408.71	182.28	Bare rocks	0.15
333	54236	148.79	364.53	Sparsely vegetated areas	0.31
335	843	78.55	10.73	Glaciers and perpetual snow	0.01

ATab. 51: Absolute & relative DS&PS-density site Aosta Valley descending west

Class	Frequency	Area [km²]	DS&PS-targets per km²	CORINE CLC legend (label 3)	relative DS&PS-density based on '112'
111	2925	1.6	1822.8	Continuous urban fabric	1.57
112	22632	19.5	1160.7	Discontinuous urban fabric	1.00
121	5366	5.5	976.05	Industrial or commercial units	0.84
124	303	0.4	753.46	Airports	0.65
131	192	0.4	485.69	Mineral extraction sites	0.42
133	325	0.46	710.46	Construction sites	0.61
221	1038	1.72	601.8	Vineyards	0.52
222	905	2.55	355.2	Fruit trees and berry plantations	0.31
231	8812	58.1	151.67	Pastures	0.13
242	6695	16.81	398.17	Complex cultivation patterns	0.34
243	12196	68.6	177.79	Land principally occupied by agriculture, with significant areas of natural vegetation	0.15
311	1151	7.16	160.69	Broad-leaved forest	0.14
312	12898	327.69	39.36	Coniferous forest	0.03
313	2486	30.91	80.43	Mixed forest	0.07
321	66290	361.77	183.24	Natural grasslands	0.16
322	8052	69.17	116.4	Moors and heathland	0.10
324	31846	180.91	176.04	Transitional woodland-shrub	0.15
332	66883	466.92	143.24	Bare rocks	0.12
333	48409	161.7	299.38	Sparsely vegetated areas	0.26
335	1146	107.75	10.64	Glaciers and perpetual snow	0.01

ATab. 52: Absolute & relative DS&PS-density site Aosta Valley ascending west, layover and shadow areas excluded

Class	Frequency	Area [km²]	DS&PS-targets per km²	CORINE CLC legend (label 3)	relative DS&PS-density based on '112'
111	2888	1.6	1799.8	Continuous urban fabric	1.39
112	15549	11.99	1297.2	Discontinuous urban fabric	1.00
121	5668	5.5	1031.0	Industrial or commercial units	0.79
124	390	0.4	969.79	Airports	0.75
133	366	0.46	800.08	Construction sites	0.62
221	1196	1.72	693.4	Vineyards	0.53
222	934	2.16	431.89	Fruit trees and berry plantations	0.33
231	5398	21.54	250.63	Pastures	0.19

242	5283	10.29	513.35	Complex cultivation patterns	0.40
243	7682	31.52	243.69	Land principally occupied by agriculture, with significant areas of natural vegetation	0.19
311	247	3.32	74.48	Broad-leaved forest	0.06
312	5495	120.09	45.76	Coniferous forest	0.04
313	1222	16.01	76.32	Mixed forest	0.06
321	33984	78.48	433.02	Natural grasslands	0.33
322	845	5.64	149.78	Moors and heathland	0.12
324	14898	62.58	238.07	Transitional woodland-shrub	0.18
332	20409	87.21	234.02	Bare rocks	0.18
333	14366	32.46	442.52	Sparsely vegetated areas	0.34
335	36	3.98	9.04	Glaciers and perpetual snow	0.01

II.II.II Piedmont sites – CORINE 2006

ATab. 53: Absolute & relative DS&PS-density Domodossola (Piedmont) site

Class	Frequency	Area [km²]	DS&PS-targets per km²	CORINE CLC legend (label 3)	relative DS&PS-density based on '112'
111	1487	2.74	542.89	Continuous urban fabric	1.39
112	38957	100.04	389.4	Discontinuous urban fabric	1.00
121	5877	15.87	370.36	Industrial or commercial units	0.95
122	571	2.14	266.61	Road and rail networks and associated land	0.68
131	54	0.98	55.08	Mineral extraction sites	0.14
133	63	0.33	190.73	Construction sites	0.49
142	240	5.2	46.16	Sport and leisure facilities	0.12
211	3113	50.09	62.14	Non-irrigated arable land	0.16
221	*19*	*0.73*	*26.03*	*Vineyards*	*0.07*
231	2928	24.33	120.36	Pastures	0.31
242	5908	53.78	109.86	Complex cultivation patterns	0.28
243	24555	220.26	111.48	Land principally occupied by agriculture, with significant areas of natural vegetation	0.29
311	20693	1115.9	18.54	Broad-leaved forest	0.05
312	3054	285.23	10.71	Coniferous forest	0.03
313	6901	459.43	15.02	Mixed forest	0.04
321	25882	489.08	52.92	Natural grasslands	0.14
322	5240	146.98	35.65	Moors and heathland	0.09
324	13043	331.35	39.36	Transitional woodland-shrub	0.10
331	2531	15.34	165.03	Beaches, dunes, sands	0.42
332	6379	130.02	49.06	Bare rocks	0.13
333	7013	87.14	80.48	Sparsely vegetated areas	0.21
411	*21*	*0.56*	*37.21*	*Inland marshes*	*0.10*

ATab. 54: Absolute & relative DS&PS-density Novara (Piedmont) site

Class	Frequency	Area [km²]	DS&PS-targets per km²	CORINE CLC legend (label 3)	relative DS&PS-density based on '112'
111	2850	4.9	581.25	Continuous urban fabric	1.29
112	70662	157.18	449.55	Discontinuous urban fabric	1.00

121	16457	43.76	376.11	Industrial or commercial units	0.84
122	2579	10.6	243.27	Road and rail networks and associated land	0.54
124	*456*	*4.09*	*111.49*	*Airports*	*0.25*
131	1116	11.23	99.38	Mineral extraction sites	0.22
133	1226	7.36	166.48	Construction sites	0.37
142	653	6.48	100.78	Sport and leisure facilities	0.22
211	27320	615.12	44.41	Non-irrigated arable land	0.10
213	20323	1364.9	14.89	Rice fields	0.03
221	639	5.94	107.63	Vineyards	0.24
222	758	18.36	41.29	Fruit trees and berry plantations	0.09
231	1975	30.45	64.86	Pastures	0.14
242	12699	132.36	95.94	Complex cultivation patterns	0.21
243	22726	334.62	67.92	Land principally occupied by agriculture, with significant areas of natural vegetation	0.15
311	10784	444.01	24.29	Broad-leaved forest	0.05
312	46	2.78	16.58	Coniferous forest	0.04
313	872	38.51	22.64	Mixed forest	0.05
321	5465	49.79	109.76	Natural grasslands	0.24
322	1180	14.55	81.1	Moors and heathland	0.18
324	4896	87.76	55.79	Transitional woodland-shrub	0.12
331	2977	21.18	140.56	Beaches, dunes, sands	0.31
332	*21*	*0.28*	*76.09*	*Bare rocks*	*0.17*
333	*1184*	*4.95*	*239.12*	*Sparsely vegetated areas*	*0.53*

ATab. 55: Absolute & relative DS&PS-density Omegna (Piedmont) site

Class	Frequency	Area [km²]	DS&PS-targets per km²	CORINE CLC legend (label 3)	relative DS&PS-density based on '112'
111	2301	4.03	570.87	Continuous urban fabric	1.26
112	54789	120.69	453.95	Discontinuous urban fabric	1.00
121	10273	24.88	412.84	Industrial or commercial units	0.91
122	1209	4.55	265.85	Road and rail networks and associated land	0.59
124	519	3.73	139.33	Airports	0.31
131	346	3.72	93.07	Mineral extraction sites	0.21
133	606	4.07	148.72	Construction sites	0.33
142	289	5.64	51.26	Sport and leisure facilities	0.11
211	8535	162.42	52.55	Non-irrigated arable land	0.12
213	9429	457.55	20.61	Rice fields	0.05
221	*52*	*1.79*	*29.09*	*Vineyards*	*0.06*
231	124	2.4	51.59	Pastures	0.11
242	9861	96.7	101.97	Complex cultivation patterns	0.22
243	19871	199.98	99.37	Land principally occupied by agriculture, with significant areas of natural vegetation	0.22
311	11961	612.32	19.53	Broad-leaved forest	0.04
312	61	16.89	3.61	Coniferous forest	0.01
313	1813	129.32	14.02	Mixed forest	0.03
321	4549	63.22	71.96	Natural grasslands	0.16
322	808	28.64	28.21	Moors and heathland	0.06
324	4259	78.7	54.12	Transitional woodland-shrub	0.12

331	2710	17.64	153.6	Beaches, dunes, sands	0.34
333	*330*	*3.11*	*106.13*	*Sparsely vegetated areas*	*0.23*
411	*22*	*0.56*	*38.98*	*Inland marshes*	*0.09*

ATab. 56: Absolute & relative DS&PS-density Varallo (Piedmont) site

Class	Frequency	Area [km²]	DS&PS -targets per km²	CORINE CLC legend (label 3)	relative DS&PS-density based on '112'
111	317	0.56	565.23	Continuous urban fabric	1.41
112	8166	20.38	400.6	Discontinuous urban fabric	1.00
121	1889	5.23	361.38	Industrial or commercial units	0.90
122	468	1.49	313.83	Road and rail networks and associated land	0.78
211	*533*	*3.85*	*138.61*	*Non-irrigated arable land*	*0.35*
231	2582	18.57	139.05	Pastures	0.35
242	236	1.61	146.26	Complex cultivation patterns	0.37
243	9109	63.29	143.93	Land principally occupied by agriculture, with significant areas of natural vegetation	0.36
311	14964	518.4	28.87	Broad-leaved forest	0.07
312	3187	191.68	16.63	Coniferous forest	0.04
313	5687	294.58	19.31	Mixed forest	0.05
321	51921	377.49	137.54	Natural grasslands	0.34
322	5915	110.39	53.58	Moors and heathland	0.13
324	16263	238.3	68.24	Transitional woodland-shrub	0.17
331	2097	10.54	198.92	Beaches, dunes, sands	0.50
332	16811	144.89	116.02	Bare rocks	0.29
333	11656	75.48	154.42	Sparsely vegetated areas	0.39
335	287	14.62	19.64	Glaciers and perpetual snow	0.05

Appendix 9: Absolute and relative PS(DS)-density of all sites

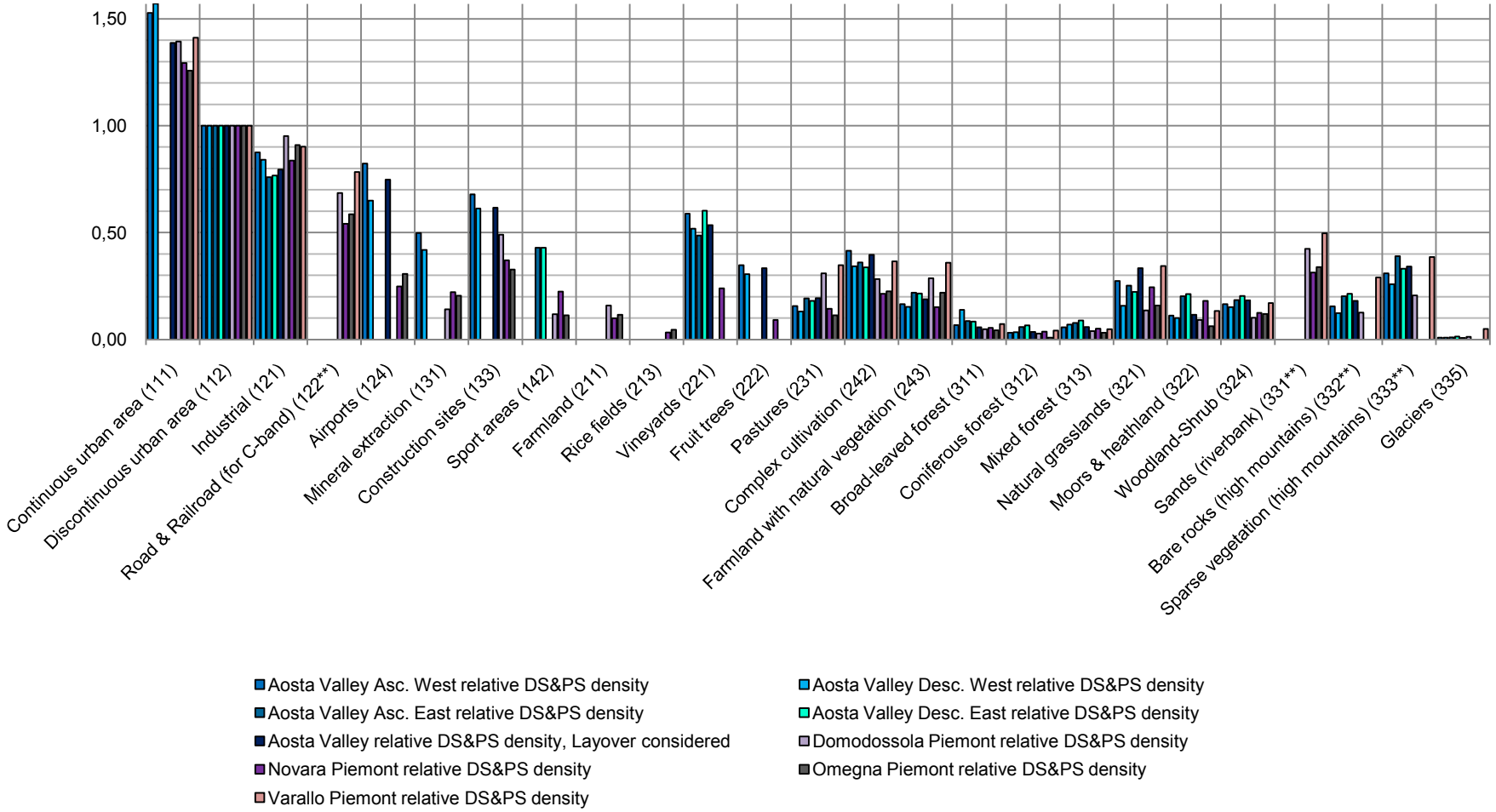

AFig. 5: CORINE 2006 relative DS&PS-density. The numbers show the ID of the CORINE land cover classification.

II.II.III Arithmetic mean and validation of relative DS&PS-density – CORINE 2006

ATab. 57: Arithmetic mean of relative DS&PS-density of all suitable CORINE sites (calculated using the data from ATab. 48 to 56)

Updated CORINE 2006 land cover (class)	Arithmetic mean of relative DS&PS-density	Minimum of relative DS&PS-density	Maximum of relative DS&PS-density
Continuous urban area (111)	1.41	1.26	1.57
Discontinuous urban area (112)	1.00	1.00	1.00
Industrial (121)	0.85	0.76	0.95
Road & Railroad (for C-band) (122**)	0.65	0.54	0.78
Airports (124)	0.55	0.25	0.82
Mineral extraction (131)	0.30	0.14	0.50
Construction sites (133)	0.52	0.33	0.68
Sport areas (142)	0.26	0.11	0.43
Farmland (211)	0.12	0.10	0.16
Rice fields (213)	0.04	0.03	0.05
Vineyards (221)	0.50	0.24	0.60
Fruit trees (222)	0.27	0.09	0.35
Pastures (231)	0.20	0.11	0.35
Complex cultivation (242)	0.33	0.21	0.42
Farmland with natural vegetation (243)	0.22	0.15	0.36
Broad-leaved forest (311)	0.07	0.04	0.14
Coniferous forest (312)	0.04	0.01	0.07
Mixed forest (313)	0.06	0.03	0.09
Natural grasslands (321)	0.24	0.14	0.34
Moors & heathland (322)	0.13	0.06	0.21
Woodland-Shrub (324)	0.16	0.10	0.20
Sands (riverbank) (331**)	0.39	0.31	0.50
Bare rocks (high mountains) (332**)	0.18	0.12	0.29
Sparse vegetation (high mountains) (333**)	0.32	0.21	0.39
Glaciers (335)	0.02	0.01	0.05

ATab. 58 shows the result of the validation of the relative DS&PS-density method for using CORINE 2006. (cf. chapter 5.1.4.2 d). The classes '221' and '333**' show large differences between the estimated and processed DS&PS-density, due to their small area at the Ivrea site. The class '321' shows a very high DS&PS-density compared to the other sites. This causes a large difference between estimated and processed DS&PS-density. The relatively large difference at the class '332**' is due to the very small area of this class at the Ivrea site.

ATab. 58: Validation of relative DS&PS-density method at Ivrea (Piedmont) site: Multiplication of the mean values from ATab. 57 and the absolute PS-density of the reference class from the Omegna site (ATab. 55)

Updated CORINE 2006 land cover (class)	Frequency	Area [km²]	Processed DS&PS-targets per km²	Estimated DS&PS-targets per km²	Difference of estimated and processed DS&PS-density
Continuous urban area (111)	1786	3.01	593.65	638.15	44.50
Discontinuous urban area (112)	51954	113.3	458.57	453.95	-4.62
Industrial (121)	11237	29.47	381.3	385.10	3.80
Road & Railroad (for C-band) (122**)	1877	6.77	277.4	294.48	17.08

Airports (124)	61	0.36	167.17	251.89	84.72
Mineral extraction (131)	1029	8.33	123.49	134.72	11.23
Construction sites (133)	943	3.62	260.51	234.19	-26.32
Sport areas (142)	778	6.04	128.79	119.26	-9.53
Farmland (211)	23417	495.94	47.22	56.61	9.39
Rice fields (213)	12562	901.94	13.93	17.82	3.89
Vineyards (221)	*510*	*4.88*	*104.52*	*224.72*	*120.20*
Fruit trees (222)	789	18.36	42.98	122.39	79.41
Pastures (231)	1991	29.23	68.12	89.16	21.04
Complex cultivation (242)	10161	87.67	115.91	148.15	32.24
Farmland with natural vegetation (243)	22175	277.89	79.8	98.70	18.90
Broad-leaved forest (311)	10429	398.11	26.2	32.75	6.55
Coniferous forest (312)	113	1.75	64.53	17.14	-47.39
Mixed forest (313)	675	23.6	28.61	26.18	-2.43
Natural grasslands (321)	*8912*	*41.34*	*215.57*	*107.08*	*-108.49*
Moors & heathland (322)	1248	10.11	123.47	61.04	-62.43
Woodland-Shrub (324)	4926	71.9	68.51	70.78	2.27
Sands (riverbank) (331**)	1200	8.7	137.89	178.33	40.44
Bare rocks (high mountains) (332**)	12	0.1	123.33	83.61	-39.72
Sparse vegetation (high mountains) (333)*	*946*	*3.65*	*258.86*	*144.05*	*-114.81*

III. Africover

The class 'Tree, Orchard (60%), Vegetated Urban Area (40%)' is not considered, due to its small area.

ATab. 59: Absolute & relative PS-density Cairo site for thresholding on the SCR

Africover class	Frequency	Area [km²]	PS-targets per km²	relative PS-density based on 'urban area'
Airport	1183	18.51	63.9	0.79
Bare rock	30714	184.16	166.78	2.06
Bare rock with thin sand layer	8619	111.44	77.34	0.96
Bare soil stony	26186	371.57	70.47	0.87
Bare soil stony (60%), Herbaceous Crop (40%)	3713	88.55	41.93	0.52
Bare soil stony (60%), Urban Area (40%)	2257	38.89	58.03	0.72
Herbaceous Crop	2293	610.11	3.76	0.05
Herbaceous Crop (60%), Bare soil stony (40%)	333	9.28	35.88	0.44
Herbaceous Crop (60%), Tree (40%)	546	137.3	3.98	0.05
Sand	923	35.36	26.1	0.32
Tree, Orchard	1015	159.11	6.38	0.08
Tree, Orchard (60%), Herbaceous Crop (40%)	390	83.25	4.68	0.06
Tree, Orchard (60%), Vegetated Urban Area (40%)	*172*	*1.43*	*120.02*	*1.48*
Urban Area	38983	482.24	80.84	1.00
Urban Area (60%), Bare soil stony (40%)	1408	15.83	88.96	1.10
Urban Area (60%), Sand (40%)	381	3.82	99.65	1.23

ATab. 60: Absolute & relative PS-density Cairo site for thresholding on the D_a

Africover class	Frequency	Area [km²]	PS-targets per km²	relative PS-density based on 'urban area'
Airport	1946	18.51	105.11	0.92
Bare rock	182817	184.16	992.71	8.66
Bare rock with thin sand layer	21592	111.44	193.76	1.69
Bare soil stony	46583	371.57	125.37	1.09
Bare soil stony (60%), Herbaceous Crop (40%)	5577	88.55	62.98	0.55
Bare soil stony (60%), Urban Area (40%)	3786	38.89	97.35	0.85
Herbaceous Crop	2499	610.11	4.1	0.04
Herbaceous Crop (60%), Bare soil stony (40%)	436	9.28	46.98	0.41
Herbaceous Crop (60%), Tree (40%)	552	137.3	4.02	0.04
Sand	1107	35.36	31.3	0.27
Tree, Orchard	1083	159.11	6.81	0.06
Tree, Orchard (60%), Herbaceous Crop (40%)	463	83.25	5.56	0.05
Tree, Orchard (60%), Vegetated Urban Area (40%)	*213*	*1.43*	*148.62*	*1.30*
Urban Area	55262	482.24	114.6	1.00
Urban Area (60%), Bare soil stony (40%)	2088	15.83	131.92	1.15
Urban Area (60%), Sand (40%)	574	3.82	150.13	1.31

ATab. 61: Absolute & relative PS-density Cairo site for combination of thresholding on the SCR and thresholding on the D_a

Africover class	Frequency	Area [km²]	PS-targets per km²	relative PS-density based on 'urban area'
Airport	2961	18.51	159.94	0.86
Bare rock	207595	184.16	1127.26	6.05
Bare rock with thin sand layer	28931	111.44	259.62	1.39
Bare soil stony	68166	371.57	183.45	0.98
Bare soil stony (60%), Herbaceous Crop (40%)	8790	88.55	99.26	0.53
Bare soil stony (60%), Urban Area (40%)	5740	38.89	147.59	0.79
Herbaceous Crop	4383	610.11	7.18	0.04
Herbaceous Crop (60%), Bare soil stony (40%)	703	9.28	75.74	0.41
Herbaceous Crop (60%), Tree (40%)	997	137.3	7.26	0.04
Sand	1966	35.36	55.6	0.30
Tree, Orchard	1880	159.11	11.82	0.06
Tree, Orchard (60%), Herbaceous Crop (40%)	789	83.25	9.48	0.05
Tree, Orchard (60%), Vegetated Urban Area (40%)	*360*	*1.43*	*251.2*	*1.35*
Urban Area	89839	482.24	186.3	1.00
Urban Area (60%), Bare soil stony (40%)	3258	15.83	205.84	1.10
Urban Area (60%), Sand (40%)	935	3.82	244.55	1.31

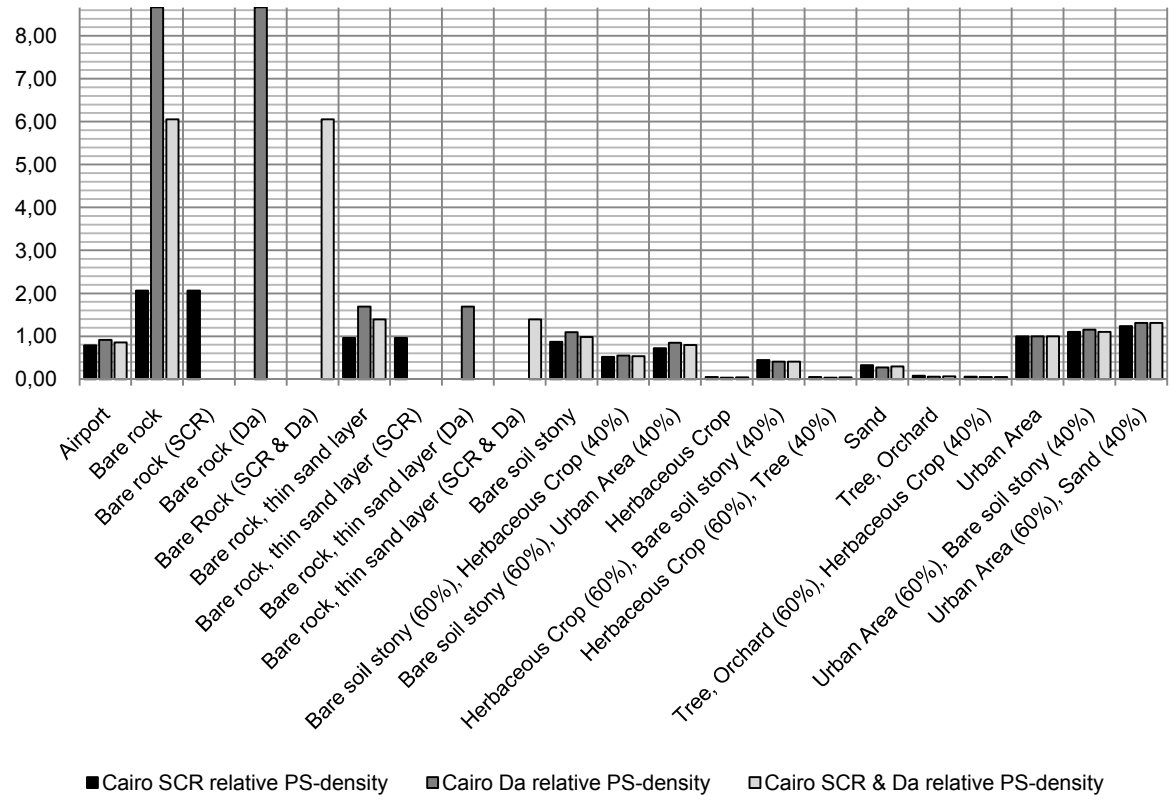

AFig. 6: Africover relative PS-density.

ATab. 62: Arithmetic mean of relative PS-density of all suitable Africover data

Updated Africover	Arithmetic mean of relative PS-density	Minimum of relative PS-density	Maximum of relative PS-density
Airport	0.86	0.79	0.92
Bare rock	5.59	2.06	8.66
Bare rock (SCR)	2.06	2.06	2.06
Bare rock (D_a)	8.66	8.66	8.66
Bare Rock (SCR & D_a)	6.05	6.05	6.05
Bare rock, thin sand layer	1.35	0.96	1.69
Bare rock, thin sand layer (SCR)	0.96	0.96	0.96
Bare rock, thin sand layer (D_a)	1.69	1.69	1.69
Bare rock, thin sand layer (SCR & D_a)	1.39	1.39	1.39
Bare soil stony	0.98	0.87	1.09
Bare soil stony (60%), Herbaceous Crop (40%)	0.53	0.52	0.55
Bare soil stony (60%), Urban Area (40%)	0.79	0.72	0.85
Herbaceous Crop	0.04	0.04	0.05
Herbaceous Crop (60%), Bare soil stony (40%)	0.42	0.41	0.44
Herbaceous Crop (60%), Tree (40%)	0.04	0.04	0.05
Sand	0.30	0.27	0.32
Tree, Orchard	0.07	0.06	0.08
Tree, Orchard (60%), Herbaceous Crop (40%)	0.05	0.05	0.06
Urban Area	1.00	1.00	1.00
Urban Area (60%), Bare soil stony (40%)	1.12	1.10	1.15
Urban Area (60%), Sand (40%)	1.29	1.23	1.31

Appendix 10: Implementation of the NDVI based PS-estimation method

This appendix shows the implementation of the NDVI-PS-percentage method. In the first step, the NDVI of an optical image of the site is calculated according equation 47. Next, this NDVI raster is multiplied by 100 (*Times*) and transformed to integer values (*Int*) to be able to transfer it to a polygon. This is done in a ArcGIS® model. Then, the generated polygon of the NDVI values is exported to a geodatabase.

Using *Select by location* all polygon cells containing at least one PS-target are selected and saved to the aforementioned geodatabase.

Then, at both tables (NDVI polygon of the entire site & the NDVI values containing at least one PS-target) the NDVI values are divided by 100, to get the original NDVI values by the following SQL query applied in Access®:

```
UPDATE cairo_le71760392001078edc00_ndvi_polygon100 SET cai-
ro_le71760392001078edc00_ndvi_polygon100.GRIDCODE = [GRIDCODE]/100;
```

In the next step, at both tables the column containing the NDVI values (GRIDCODE) is exported to a text file (point as decimal delimiter).

The following IDL procedure determines the frequency of each NDVI value within the site and the frequency of NDVI raster cells containing at least one PS-target.

```
PRO ndvi_ps_percentage2
; 1. Satellite image (NDVI)
; Read file containing the NDVI values of the entire site using the
;template "test_template"
ndvi_image_struct=read_ascii(filepath('cairo_le71760392001078edc00_ndvi_pol
ygon.txt', subdir=['Dissertation/Cairo/NDVI_image']),
;template=test_template)
ndvi_image=ndvi_image_struct.field1
; sorting ascending
ndvi_image_sort=ndvi_image[sort(ndvi_image)]
; determine position of the uinque values
ndvi_image_uniq_pos=uniq(ndvi_image_sort)
; unique values
ndvi_image_uniq=ndvi_image_sort[ndvi_image_uniq_pos]
; determine frequency of the unique values
; determine size of array ndvi_image_uniq_pos
testsize_image = where(ndvi_image_uniq_pos GT -1, size_ndvi_image_uniq_pos)
print, "number of unique image ndvi values:", size_ndvi_image_uniq_pos
image_freq = fltarr(size_ndvi_image_uniq_pos)
; calculate frequency values
; calculate 1. position
image_freq [0] = ndvi_image_uniq_pos[0] + 1
; calculate remaining values
for i=0,(size_ndvi_image_uniq_pos-2) do image_freq[i+1] =
ndvi_image_uniq_pos[i+1]-ndvi_image_uniq_pos[i]
; generate histogram
image_hist = fltarr(2,size_ndvi_image_uniq_pos)
; column NDVI values
image_hist[0,*] = ndvi_image_uniq
; column frequency
```

```
image_hist[1,*] = image_freq
; write file to disk
openw, lun, 'cairo_le71760392001078edc00_ndvi_polygon_frequency.txt',
/get_lun
printf, lun, image_hist
close, lun
free_lun, lun

; 2. PS-points (NDVI)
; same procedure as above
ndvi_ps_struct=read_ascii(filepath('cairo_le71760392001078edc00_ndvi_polygo
n100_withcatPS.txt', subdir=['Dissertation/Cairo/PS_points']),
;template=test_template)
ndvi_ps=ndvi_ps_struct.field1
ndvi_ps_sort=ndvi_ps[sort(ndvi_ps)]
ndvi_ps_uniq_pos=uniq(ndvi_ps_sort)
ndvi_ps_uniq=ndvi_ps_sort[ndvi_ps_uniq_pos]
testsize_ps = where(ndvi_ps_uniq_pos GT -1, size_ndvi_ps_uniq_pos)
print, "number of unique PS ndvi values:", size_ndvi_ps_uniq_pos
ps_freq = fltarr(size_ndvi_ps_uniq_pos)
ps_freq [0] = ndvi_ps_uniq_pos[0] + 1
for i=0,(size_ndvi_ps_uniq_pos-2) do ps_freq[i+1] = ndvi_ps_uniq_pos[i+1]-
ndvi_ps_uniq_pos[i]
ps_hist = fltarr(2,size_ndvi_ps_uniq_pos)
ps_hist[0,*] = ndvi_ps_uniq
ps_hist[1,*] = ps_freq
openw, lun,
'cairo_le71760392001078edc00_ndvi_polygon_with_catPS_frequency.txt',
/get_lun
printf, lun, ps_hist
close, lun
free_lun, lun
END
```

Then, at both generated text files the decimal delimiter is replaced to ‘comma’ to enable the import to Microsoft® Excel®. Not each NDVI value contains a PS-target. Therefore, only NDVI values that are saved in both text files are chosen (the one containing all NDVI values of the entire site & the file containing only the NDVI values of the cells with at least one PS-target).

Then, for each single NDVI value the percentage of cells containing at least one PS-target is calculated to get the NDVI-PS-percentage. In the next step, all NDVI values that occur less than ten times within the site are excluded to avoid falsely high percentage values caused by a very small number of cells with at least one PS-target.

The result is again exported to a text file (point as decimal delimiter) and following IDL procedure is applied to generate the plot of the NDVI-PS-percentage (cf. chapter 5.3.2)

```
PRO ndvi_ps_percentage2_plot
ndvi_ps_percentage_struct=read_ascii(filepath('cairo_LE71760392001142SGS00_
ndvi_PS_perc.txt', subdir=['Dissertation/Cairo/PS_NDVI_probability']))
ndvi_ps_percentage=ndvi_ps_percentage_struct.field1
iplot, ndvi_ps_percentage
END
```

Appendix 11: OSM

ATab. 63: OSM road types with widths and rail road types with gauges

OSM road type	Road width [m]
Motorway	2 x 11.5
Trunk	2 x 7.50
Primary	7.50
Secondary	6.50
Tertiary	5.50
Unclassified	5.50
Residential	5.50
Service	2.75
OPENSTREETMAP WIKI 2008, WIKIPEDIA 2011a	

OSM rail road type	gauge [m]
Rail	1.435
Tram	1.0
Light rail	1.0
Disused, rail still exists	1.435
Narrow gauge	1.0
Only over ground tracks were considered (OPENSTREETMAP WIKI 2011, WIKIPEDIA 2011b).	

Appendix 12: Implementation of the TM & OSM based PS-estimation method

This appendix briefly describes the implementation of the TM and OSM based PS-estimation method theoretically described in chapter 5.3. The procedure was implemented in a model of ArcGIS®. In the first step of the model a random raster with an extent equal to the one of the topographic map is created. The cell size of this raster is equal to the spatial resolution of the SAR sensor used. Then, each cell value of the random raster is multiplied (*Times*) by 1,000,000 and transferred to an integer value (*Int*) to get a single polygon for each raster cell in the succeeding *raster to polygon* conversion. The next step is *intersection* of possible PS-objects (buildings, roads, railroads, etc.; previously extracted from the TM and OSM data) with the cells of the polygon raster (see above). Then, a *spatial join* is applied to get all polygon cells that contain at least one possible PS-object (e.g. part of a building).

After that, the function *feature to point* is used to transform all previously selected polygon cells to points (estimated PS). Then, the Euclidean distance between the estimated PS is calculated according to equation 52 and classified regarding the applicability of PS-InSAR processing as described in chapter 5.3.2.1. The tool *point distance* calculates the Euclidean distance between each estimated PS and stores the results in a *.dbf table. In the next step, the *Average Nearest Neighbor* tool is applied to analyze the distribution of the estimated PS.

The area of the site for the later PS-density calculation according equation 46 is done by calculating the area for each single raster cell and then adding up the results with *summary statistics*.

The vertical distance to the nearest estimated PS is calculated as follows. First, the tool *near* is applied to get the feature identification number (FID) of the nearest PS and the horizontal distance to it. Then, based on a DEM (e.g. SRTM) the elevation value is assigned to each estimated PS using the function *spot* (3D Analyst). After *copying* the point file of the estimated PS, a *join* of the copy and the original of the point shapefile is applied. This join is based on the *Near_FID* of the copy and the *FID* of the original point file (It is important to follow the mentioned order and to keep all records). Then, the joined shapefile is exported and reloaded to ArcMap® to fix the join. The last step is the calculation of the vertical distance to the nearest PS using following equation in the *FieldCalculator* with '`Abs()`' modulus: `Abs([Spot] - [Spot_1])`.